

Decarbonylation of Carboxylic Acids over Supported Metal Catalysts

A Dissertation

Presented to

the faculty of the School of Engineering and Applied Science

University of Virginia

In Partial Fulfillment

of the requirement for the Degree

Doctor of Philosophy in Chemical Engineering

by

Juan A. Lopez-Ruiz

September 2014

Abstract

Removal of oxygen from biomass-derived feedstocks such as carbohydrates and vegetable oil is often needed to produce chemicals and fuels. In this study, oxygen was removed from the model compounds heptanoic acid and propanoic acid by either decarboxylation, which yields carbon dioxide (CO₂) and an alkane, and/or decarbonylation, which forms carbon monoxide (CO), water (H₂O), and a linear alkene. Although decarbonylation produces an α -olefin as a primary product, the double bond can be isomerized to form an internal olefin or be hydrogenated to form an alkane. Recent work on decarboxylation/decarbonylation of carboxylic acids over transition metal catalysts is often performed in the presence of dihydrogen to inhibit catalyst deactivation, however, paraffins are the major product in those systems.

The effects of metal type, support composition, metal loading, reaction phase, acid concentration, and conversion on activity, selectivity, and stability are presented. We studied the liquid- and gas-phase decarbonylation of carboxylic acids on Pt, Pd, and Rh nanoparticles supported on carbon and silica supports in a continuous-flow fixed-bed reactor at temperatures ranging from 533 to 573 K. The liquid-phase turnover frequency (TOF) of heptanoic acid conversion over Pt at 573 K was fairly constant, 0.0050 s⁻¹, as the catalyst dispersion and metal loading was varied. The liquid-phase TOF of Pd at 573 K was 0.00070 s⁻¹ and was independent of support composition, weight loading, and acid concentration. A shift in product selectivity from decarboxylation products, paraffin and CO₂, to decarbonylation products, olefins and CO, as previously discussed in the literature was most likely a result of changes in conversion. However, the decarboxylation products observed in the current study were likely formed in secondary side reactions such as water-gas shift (WGS) and hydrogenation.

Low conversion and high acid concentration experiments in liquid-phase and gas-phase operation suggest that the main reaction path for heptanoic acid and propanoic acid conversion is the decarbonylation reaction. Some direct decarboxylation was observed when operating in the gas-phase at very low concentrations of acid. The reaction was zero order in acid during the liquid-phase operation and high partial

pressures during gas-phase operation, but was observed to be negative order in acid at very low partial pressures.

Characterization of catalysts after reaction revealed metal sintering, loss of surface area and loss of exposed metal during the liquid-phase operation. X-ray diffraction and electron microscopy revealed Pd sintering on a carbon support when operating in the liquid-phase at high acid concentration, but negligible Pd sintering when acid concentration was below 0.10 M. Palladium nanoparticles were more stable on the silica support during the liquid-phase operation. Furthermore, Pd sintering was negligible during the gas-phase experiments regardless of the support composition and acid concentration. Nevertheless, N₂ physisorption and H₂ chemisorption revealed a loss of surface area and metal exposed during the liquid- and gas-phase operation, even when metal sintering was not observed. Evidently, there was blocking of active sites and/or the porous structure by strong absorption of side products or carbonaceous species.

A Pt catalyst recovered from the liquid-phase reaction could not be regenerated after air calcination and H₂ reduction at mild temperatures, and/or hot wash in acid. However, catalyst regeneration after gas-phase operation was successful. *In situ* treatment at 623 K with N₂ and H₂ of the spent catalyst recovered the initial catalytic activity. This suggested that the main cause for catalyst deactivation in the gas-phase was deposition of organic molecules onto the active sites.

Keywords

Decarbonylation; Decarboxylation; Deoxygenation; Carboxylic Acid; Heptanoic Acid; Propanoic acid; Pt/C; Pd/C; Pt/SiO₂; Rh/SiO₂; Pd/SiO₂ ; α -Olefin; Olefin; Paraffin; Ketonization; 1-Hexene; Hexane; 7-Tridecanone; Ethylene; Ethane; 3-Pentanone.

Acknowledgment

I thank my advisor, Robert J. Davis, for his mentoring and patience during my graduate studies. In addition, I would like to thank all of the Davis group members, past and present, with whom I have interacted through the years. I would like to acknowledge the financial support provided by the Center for Biorenewable Chemicals (CBiRC) and BP, the collaboration with the University of New Mexico and the Neurock Lab at the University of Virginia, and all the discussions with Dr. John Shabaker, Dr. Drew Braden, Dr. Matthew Neurock, Dr. Corneliu Buda, Dr. Glen Allen, Dr. Abhaya Datye, and Dr. Hien Pham. I also would like to thank Dr. Brent Shanks, Dr. Peter Keeling, and Ms. Tonia McCarley from CBiRC.

Many thanks to my classmates for their support and camaraderie over the past years, in particular to Edward Wong and Joseph Basconi. I express my gratitude also to the staff of the Chemical Engineering Department, Ms. Vickie Falconer, Ms. Kim Doerr, Ms. Teresa Morris, Mr. Rick Buchanan, and Ms. Jennifer Davis. I would like to thank the Department of Material Science for their help with the catalyst characterization, in particular to Mr. Richard White and Matthew Schneider.

Many thanks to Dean Aaron Laushway and the Office of the Dean of students for their continuous support. Best regards goes to the Teaching Resources Center (TRC) and its supporting staff, in particular to Dr. Michael Palmer.

Last but not least, I thank both my Spanish and American families for their overwhelming love and support that has helped me reach this point. In particular I would like to thank my mother, Maria Luisa Ruiz-Fernandez, my sisters, Maria Luisa Lopez-Ruiz and Patricia Lopez-Ruiz, my father, Torcuato Lopez-Garcia, my grandmother, Maria del Carmen Fernandez-Leyva, my mother-in-law, Lisa Fisher, my father-in-law, Steven Fisher, my brother-in-law, Ross Fisher, my aunt, Carmen Ruiz-Fernandez, my uncle, Manolo Ruiz-Lopez, and my cousins, Manolo Ruiz-Ruiz and Francisco Javier Ruiz-Ruiz.

To my wife, Morgan Z. Fisher, whose love and support gave me the strength to complete the
Ph.D.

Table of Content

Chapter 1: Introduction	1
1.1.Motivation.....	1
1.2.Effect of Metal	3
1.3.Effect of support	4
1.4.Effect of concentration.....	7
1.5.Catalyst deactivation and regeneration	8
1.6.Reaction kinetics and mechanism	8
1.7.Focus of this work.....	9
1.8.References.....	10
Chapter 2. Decarbonylation of Heptanoic Acid over Carbon-Supported Platinum Nanoparticles.....	14
2.1. Abstract.....	14
2.2. Introduction.....	15
2.3. Experimental Methods.....	18
2.3.1. Catalyst synthesis.....	18
2.3.2. Dihydrogen chemisorption.....	18
2.3.3. Dinitrogen physisorption.....	18
2.3.4. X-ray diffraction	19
2.3.5. Electron microscopy	19
2.3.6. Catalytic conversion of heptanoic acid	19

2.3.7. Turnover frequency and selectivity calculations.....	22
2.3.8. Mass transfer limitations.....	23
2.4. Results and Discussion.....	24
2.4.1. Effect of carbonaceous support.....	24
2.4.2. Effect of reduction temperature	27
2.4.3. Effect of metal loading.....	32
2.4.4. Effect of flow rate	37
2.4.5. Effect of pressure	40
2.4.6. Catalyst deactivation	42
2.5. Conclusions.....	47
2.6. Acknowledgement.....	48
2.7. References.....	49
Chapter 3. Reactivity and Stability of Supported Pd Nanoparticles during the Liquid-Phase and Gas-Phase Decarbonylation of Heptanoic Acid	53
Abstract.....	53
3.1.Introduction.....	54
3.2.Experimental Methods	56
3.2.1. Catalyst synthesis.....	56
3.2.2. Dihydrogen chemisorption.....	56
3.2.3. Dinitrogen physisorption.....	57
3.2.4. X-ray diffraction	57

3.2.5. Electron microscopy	57
3.2.6. Catalytic conversion of heptanoic acid	57
3.2.7. Post-mortem catalyst characterization	59
3.2.8. Calculations of rates	59
3.3.Results and Discussion.....	60
3.3.1. Effect of support and impregnation method during the liquid-phase operation.....	60
3.3.2. Effect of metal loading and reaction pressure.....	68
3.3.3. Effect of liquid-phase conversion on product selectivity.....	73
3.3.4. Gas-phase operation.....	74
3.4.Conclusions.....	80
3.5.Acknowledgement	81
3.6.References.....	81









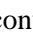





Chapter 4. Mechanistic Insights on the Decarbonylation and Decarboxylation of Propanoic Acid over

Palladium Catalysts	86
Abstract.....	86
4.1. Introduction.....	87
4.2. Experimental Methods.....	90
4.2.1. Catalyst synthesis.....	90
4.2.2. Dihydrogen chemisorption.....	90
4.2.3. Dinitrogen physisorption.....	91
4.2.4. X-ray diffraction	91

4.2.5. Electron microscopy	91
4.2.6. Catalytic conversion of propanoic acid.....	91
4.2.7. Post-mortem catalyst characterization	94
4.2.8. Calculation of rates	94
4.3.Results and Discussion.....	96
4.3.1. Effect of metal.....	96
4.3.2. Effect of support.....	103
4.3.3. Effect of reaction temperature on TOF and extent of deactivation.....	105
4.3.4. Effect of propanoic acid concentration	110
4.3.5. Propanoic anhydride as potential reaction intermediate	113
4.4.Conclusions.....	115
4.5.Acknowledgement.....	116
4.6.References.....	116
Chapter 5. Conclusions and Future Work.....	121
5.1.Conclusions.....	121
5.2. Future work and recommendations.....	123
5.2.1. Auto-sampling.....	123
5.2.2. Co-feeding dihydrogen	124
5.2.3. Bimetallic catalysts	124
5.2.4. Reactive Distillation.....	126

5.3.References.....	126
Appendix A. Sample calculation of Weisz-Prater Criterion.....	131
Appendix B. Gas chromatography calibrations	138
Appendix C. Effect of heptanoic acid concentration	143
Appendix D. Catalyst deactivation during the decarbonylation of propanoic acid	145
Appendix E. Catalyst regeneration	148

List of Figures

- Figure 2.1. Schematic of the reactor system. TC represents a thermocouple, GC represents a gas chromatograph, PG represents a pressure gauge, and PC represents a back pressure regulator. 21
- Figure 2.2. Comparison of the XRD patterns of 5 wt% Pt supported on Norit carbon, Vulcan carbon and SiC reduced at 623 K under $100 \text{ cm}^3\text{min}^{-1}$ of H_2 at a heating rate of 5 K min^{-1} .  represents features of SiC support. The patterns were offset for clarity. 27
- Figure 2.3. TEM images of fresh 3 wt% Pt/Norit C catalyst reduced at four different temperatures. A was reduced at 623 K, B was reduced at 673 K, C was reduced at 773 K, and D was reduced at 873 K. 29
- Figure 2.4. Effect of reduction temperature ( represents 623 K,  represents 673 K,  represents 773 K, and  represents 873 K) on heptanoic acid conversion over 3 wt% Pt/Norit C. The reactions conditions were 573 K, 37 bar, and $0.01 \text{ cm}^3\text{min}^{-1}$ of feed composed of 95 wt% heptanoic acid and 5 wt% dodecane. 30
- Figure 2.5. Effect of reduction temperature ( represents 623 K,  represents 673 K,  represents 773 K, and  represents 873 K) on the olefin (left) and CO (right) selectivity over time during the conversion of heptanoic acid over 3 wt% Pt/Norit C. The reactions conditions were 573 K, 37 bar, and $0.01 \text{ cm}^3\text{min}^{-1}$ of feed composed of 95 wt% heptanoic acid and 5 wt% dodecane. Olefin selectivity is relative to liquid products only and CO selectivity is relative to $\text{CO} + \text{CO}_2$ 31
- Figure 2.6. Effect of Pt weight loading supported on Norit C on product selectivity and conversion at 573 K, 37 bar, and $0.01 \text{ cm}^3\text{min}^{-1}$ of feed composed of 95 wt% heptanoic acid and 5 wt% dodecane. The product selectivity (%) is represented with color bars and can be read on the left axis.  represents 1-hexene,  represents 2 and 3-hexenes,  represents hexane,  represents 7-tridecanone, and  represents the

unknown products. The black squares represent conversion (%) and can be read on the right axis. These results were recorded after 20 h of reaction. 35

Figure 2.7. TEM images of fresh Pt/Norit C catalysts reduced at identical conditions but with four different Pt loadings. A has 1 wt% loading, B has 3 wt% loading, C has 5 wt% loading, and D has 10 wt% loading. 36

Figure 2.8. Dependence of conversion of heptanoic acid at different flow rates over 10 wt% Pt/Norit C at 573 K and 37 bar. These results were recorded after 20 h of reaction. The W/F was calculated as the weight of catalyst used divided by the mass flow rate. 37

Figure 2.9. Dependence of decarbonylation product selectivity on conversion over 10 wt% Pt/Norit C at 573 K and 37 bar. ■ represents the selectivity to decarbonylation products, olefins, in the liquid product. ◆ represents the selectivity to decarbonylation product, CO, in the gas product. ▲ represents the selectivity to α -olefins in the liquid product. These results were recorded after 20 h of reaction. 39

Figure 2.10. Effect of reaction pressure and feed flow rate on catalyst activity and product distribution over Pt/Norit C with different loadings of Pt during the conversion of heptanoic acid at 573 K. The feed composition was 95 wt% heptanoic acid and 5 wt% dodecane. The color bars can be read on the left axis and represents the product distribution. □ represents 1-hexene, ▨ represents 2-3-hexenes, ▩ represents hexane, ▩▩ represents 7-tridecanone, and ■ represents the unknown products. The black squares represent conversion (%) and can be read on the right axis. These results were recorded after 20 h of reaction. Figure A was run in liquid phase (37 bar) conditions and flow rate of $0.01 \text{ cm}^3\text{min}^{-1}$. Figure B was run in gas phase (1 bar) conditions and a flow rate of $0.01 \text{ cm}^3\text{min}^{-1}$. Figure C was run in gas phase (1 bar) conditions and a flow rate of $0.05 \text{ cm}^3\text{min}^{-1}$ 41

Figure 2.11. Effect of deactivation on catalyst activity and product distribution over 10 wt% Pt/Norit C during the conversion of heptanoic acid at 573 K and a feed flow rate of $0.01 \text{ cm}^3\text{min}^{-1}$ composed of 95






wt% heptanoic acid and 5 wt% dodecane. The bars with patterns represents the product distribution and can be read on the left axis.  represents 1-hexene,  represents 2-3-hexenes,  represents hexane,  represents 7-tridecanone, and  represents the unknown products. The black squares represent conversion (%) and can be read on the right axis. These results were recorded after 20 h of reaction. 43

Figure 2.12. TEM images of spent Pt/Norit C catalysts. The catalysts were prepared by IWI and reduced with H₂ at 623 K at a heating rate of 5 K min⁻¹. A represents a spent sample of 1 wt% Pt, B represents a spent sample of 5 wt% Pt, and C represent a spent sample of 10 wt% Pt. The spent samples were first run in liquid-phase operation until steady-state operation and then they were run in gas-phase operation until deactivation. At that point in time, the spent samples were recovered from the reactor and treated as described in the Experimental Methods section. The spent catalysts were collected after a total of 80 h under reaction conditions. 44

Figure 2.13. Comparison of the XRD patterns of Norit C support, fresh 10 wt% Pt/Norit C after reduction, and spent 10 wt% Pt/Norit C after reaction. The spent sample was first run in liquid-phase operation until steady-state operation and then it was run in gas-phase operation until deactivation. At that point, the spent sample was recovered from the reactor and treated as described in the Experimental Methods section. The spent catalyst was collected after a total of 80 h under reaction conditions. The patterns were offset for clarity. 46

Figure 2.14. Schematic depiction of working hypothesis for catalyst sintering. 47

Figure 2.15. Reaction network for the decarbonylation/decarboxylation of heptanoic acid over supported Pt at low conversion levels. 48

Figure 3.1. Comparison of the XRD patterns of 5 wt% Pd/Norit C, 5 wt% Pd/Vulcan C, and 5 wt% Pd/SiO₂ prepared by alcohol reduction (AR) before (fresh) and after (spent) liquid-phase reaction at 573 K. The

patterns were offset for clarity. The spent samples were recovered from the reactor and treated as described in the Experimental Methods section. 63

Figure 3.2. High-angle annular dark field-STEM images of fresh (left) and spent (right) catalysts during the liquid-phase decarbonylation of heptanoic acid at 573 K. 64





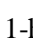
Figure 3.3. Effect of support on product selectivity and conversion during the liquid-phase decarbonylation of heptanoic acid at 573 K, and $0.01 \text{ cm}^3\text{min}^{-1}$ of liquid feed composed of 95 wt% heptanoic acid and 5 wt% dodecane. The product selectivity (%) is represented with color bars and can be read on the left axis.  represents 1-hexene,  represents 2 and 3-hexenes,  represents hexane,  represents 7-tridecanone, and  represents the unknown products. The black squares represent conversion (%) and can be read on the right axis. The background conversion of the carbon supports was removed for clarity. These results were recorded after 20 h of reaction. 66



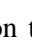


Figure 3.4. Effect of Pd weight loading on Norit C on product selectivity and conversion during the liquid-phase decarbonylation of heptanoic acid at 573 K, and $0.01 \text{ cm}^3\text{min}^{-1}$ of liquid feed composed of 95 wt% heptanoic acid and 5 wt% dodecane. The product selectivity (%) is represented with color bars and can be read on the left axis.  represents 1-hexene,  represents 2 and 3-hexenes,  represents hexane,  represents 7-tridecanone, and  represents the unknown products. The black squares represent conversion (%) and can be read on the right axis. The background conversion of the carbon supports was removed for clarity. These results were recorded after 20 h of reaction. 67

Figure 3.5. Comparison of the XRD patterns of 1, 5, and 20 wt% Pd/Norit C prepared by incipient wetness impregnation (IWI) before (fresh) and after (spent) liquid-phase reaction at 573 K. The patterns were offset for clarity. The spent samples were recovered from the reactor and treated as described in the Experimental Methods section. 69

Figure 3.6. Bright field HRTEM images of fresh (left) and spent (right) Pd/Norit C samples after the liquid-phase decarbonylation of heptanoic acid at 573 K. The spent samples were recovered from the reactor and treated as described in the Experimental Methods section. 70

Figure 3.7. Dependence of product selectivity on liquid-phase conversion of heptanoic acid over 10 wt% Pd/Norit C at 573 K and 37 bar. ■ represents the selectivity to olefins (1-, 2- and 3-hexenes) decarbonylation products, olefins, in the liquid product. ◆ represents the carbon oxide selectivity to CO. ▲ represents the selectivity to α -olefin relative to all olefins in the liquid product. These results were recorded after 20 h of reaction. 72

Figure 3.8. Time evolution of the (a) conversion and (b) CO selectivity represented by and (c) product selectivity during the gas-phase decarbonylation of heptanoic acid over 10 wt% Pd/Norit C at 573 K and $0.05 \text{ cm}^3 \text{ min}^{-1}$ of liquid feed composed by 95 wt% heptanoic acid (6.6 M) and 5 wt% dodecane. The product selectivity in (c) is represented with color bars where □ represents 1-hexene, ▨ represents 2 and 3-hexenes, ▩ represents hexane, ▨ represents 7-tridecanone, and ■ represents the unknown products. 75

Figure 3.9. Comparison of the XRD patterns of 10 wt% Pd/Norit C run at 573 K after different reaction conditions. The patterns were offset for clarity. 77

Figure 3.10. Bright field HRTEM images of 10 wt% Pd/Norit C fresh (left), spent during liquid-phase operation, and spent during the gas-phase operation at 573 K. The spent samples were recovered from the reactor and treated as described in the Experimental Methods section. 78

Figure 3.11. Comparison of the XRD patterns of 20 wt% Pd/Norit C after the liquid-phase operation at 573 K and different acid concentrations. The patterns were offset for clarity. The spent samples were recovered from the reactor and treated as described in the Experimental Methods section. 79

Figure 3.12. BF-HRTEM images of 20 wt% Pd/Norit C after the liquid-phase operation at 573 K and different acid concentrations. The spent samples were recovered from the reactor and treated as described in the Experimental Methods section..... 80

Figure 4.1. Schematic of the reactor system. TC refers to temperature controller, PG refers to pressure gauge, PC refers to the back pressure regulator..... 92

Figure 4.2. Comparison of the XRD patterns of 5 wt% Rh/SiO₂, 10 wt% Pt/SiO₂, 5 wt% Pd/SiO₂, and 20 wt% Pd/Carbon before (fresh) and after (spent) reaction at 573 K. The patterns were offset for clarity. The spent samples were recovered from the reactor and treated as described in the Experimental Methods section. The spent catalysts were collected after 25 h under reaction conditions. 98

Figure 4.3. TEM images of fresh (left) and spent at 573 K (right) of 5 wt% Rh/SiO₂, 10 wt% Pt/SiO₂, 5 wt% Pd/SiO₂, and 20 wt% Pd/Carbon, respectively. The spent samples were recovered from the reactor and treated as described in the Experimental Methods section. The spent catalysts were collected after 25 h under reaction conditions. 99

Figure 4.4. Time evolution of the (a) deoxygenation conversion, (b) CO selectivity during the deoxygenation of propanoic acid at 573 K over 5 wt% Rh/SiO₂, 10 wt% Pt/SiO₂, and 5 wt% Pd/SiO₂, run at 1 bar, and 0.05 cm³min⁻¹ of liquid feed composed of 95 wt% propanoic acid and 5 wt% octane. The time evolution of the deoxygenation product selectivity is represented in (c) for 5 wt% Rh/SiO₂, (d) for 10 wt% Pt/SiO₂, and (e) for 5 wt% Pd/SiO₂..... 101

Figure 4.5. Determination of initial rates (mol h⁻¹) by extrapolation to t = 0 h. ● represents 5 wt% Rh/SiO₂, ◆ represents 10 wt% Pt/SiO₂, and ■ represents 5 wt% Pd/SiO₂. The reactions conditions were 573 K and 1 bar, and 0.05 cm³min⁻¹ of liquid feed composed of 95 wt% propanoic acid and 5 wt% octane. 102

Figure 4.6. Time evolution of the (a) deoxygenation conversion, (b) CO selectivity, and (c) deoxygenation product selectivity during the deoxygenation of propanoic acid at 573 K over 20 wt% Pd/Carbon run at 1 bar, and $0.05 \text{ cm}^3\text{min}^{-1}$ of liquid feed composed of 95 wt% propanoic acid and 5 wt% octane. 104

Figure 4.7. TEM images of spent 20 wt% Pd/Carbon (left) and spent 5 wt% Pd/SiO₂ (right) at 553 (top) and 533 K (bottom). The spent samples were recovered from the reactor and treated as described in the Experimental Methods section. The spent catalysts were collected after 25 h under reaction conditions. 106

Figure 4.8. Time evolution of the (a) deoxygenation conversion and (b) CO selectivity during the deoxygenation of propanoic acid at 533 K over 5 wt% Pd/SiO₂ and 20 wt% Pd/Carbon run at 1 bar, and $0.05 \text{ cm}^3\text{min}^{-1}$ of liquid feed composed of 95 wt% propanoic acid and 5 wt% octane. The time evolution of the deoxygenation product selectivity is represented in (c) for over 5 wt% Pd/SiO₂ and (d) for 20 wt% Pd/Carbon. 108

Figure 4.9. Arrhenius-type plots of the initial rates for propanoic acid conversion over (a) 5 wt% Pd/SiO₂ and (b) 20 wt% Pd/Carbon. 109

Figure 4.10. Effect of partial pressure of propanoic acid (P_{PAC}) on initial TOF over 20 wt% Pd/C at 1 bar of total pressure and 533 K. The average P_{PA} was determined from the initial and final P_{PA} . The dotted lines are not linear fits, they are meant to guide the reader. 110

Figure 4.11. Effect of partial pressure on site time yield (STY) during the deoxygenation of propanoic acid over 20 wt% Pd/C at 533 K. The initial partial pressure of propanoic acid was (a) 1.00, (b) 0.10, and (c) 0.05 bar. ■ represents ethylene, ▲ represents ethane, ◆ represents 3-pentanone, ◊ represents CO, and ▽ represents CO₂. The STY was calculated using the Pd dispersion of the fresh catalysts. 112

Figure 4.12. Deoxygenation of propanoic anhydride at (a) 1.00 bar for the high initial partial pressure experiment and (b) 0.025 bar for the low initial partial pressure experiment over 20 wt% Pd/Carbon at 533

K and 1 bar. ■ represents ethylene, ▲ represents ethane, ◆ represents 3-pentanone, ● represents propanoic acid, ◊ represents CO, and ▽ represents CO ₂ . The STY was calculated using the Pd dispersion of the fresh catalysts.....	114
Figure B.1. Calibration curve for 1-hexene	138
Figure B.2. Calibration curve for hexane.....	138
Figure B.3. Calibration curve for 7-tridecanone	139
Figure B.4. Calibration curve for heptanoic acid.....	139
Figure B.5. Calibration curve for CO ₂	140
Figure B.6. Calibration curve for CO	140
Figure B. 7. Calibration curve for propanoic acid	141
Figure B. 8. Calibration curve for 3-pentanone	141
Figure B. 9. Calibration curve for ethane.....	142
Figure B. 10. Calibration curve for ethylene	142
Figure D. 1. Catalytic conversion of propanoic anhydride diluted (33 mol %) with ethylene (A) and 3-pentanone (B) over 20 wt% Pd/Norit C at 573 K and 1 bar. ■ represents ethylene, ▲ represents ethane, ◆ represents 3-pentanone, ● represents propanoic acid, ◊ represents CO, and ▽ represents CO ₂ . <i>The STY was calculated using the Pd dispersion of the fresh catalysts.</i>	146

- Figure E. 1. Thermogravimetric analysis of spent 5 wt% Pd/SiO₂ with Air up to 1295 K. ● represents Weight (%) and can be read on the left hand axis. ● represents Deriv. Weight (% K⁻¹) and can be read on the right hand axis. *The spent catalyst was recovered after the decarbonylation of propanoic acid at 533 K and 1 bar.* 148
- Figure E. 2. TEM images of spent 5 wt% Pd/SiO₂ after TGA analysis with Air flowing at 100 cm³ min⁻¹ at 1475 K (A), 1173 K (B), 1073 K (C), 873 K (D), 773 K (E), and 623 K (D) (left) and spent 5 wt% Pd/SiO₂ (right) at 553 (top) and 533 K (bottom). 149
- Figure E. 3. Thermogravimetric analysis of spent 20 wt% Pd/Norit C with Air (top), He (middle), and H₂ (bottom) up to 1095 K. ● represents Weight (%) and can be read on the left hand axis. ● represents Deriv. Weight (% K⁻¹) and can be read on the right hand axis. 150
- Figure E. 4. TEM images of 20 wt% Pd/Norit C after regeneration at 623 K with and N₂ plus H₂ treatment (A) and H₂ treatment (B)..... 151

List of Tables

Table 1.1. Summary of literature results during the liquid-phase reaction obtained using a semibatch reactor	5
Table 1.2. Summary of literature results obtained using a fixed-bed continuous flow reactor.....	6
Table 2.1. Summary of the characterization results for 5 wt% Pt on different supports.	25
Table 2.2. Effect of support on the reaction of heptanoic acid over Pt nanoparticles.....	26
Table 2.3. Result of the characterization of 3 wt% Pt/Norit C reduced at 4 different temperatures.....	28
Table 2.4. Effect of metal dispersion on the decarbonylation/decarboxylation of heptanoic acid over 3 wt% Pt/Norit C.....	32
Table 2.5. Effect of Pt loading on heptanoic acid reaction over Pt/Norit C at 553 K and 573 K.	33
Table 3.1. Summary of the catalyst characterization and reactivity results for Pd catalysts synthesized by alcohol reduction (AR) during the liquid-phase reaction at 573 K.....	61
Table 3.2. Summary of catalysts characterization and reactivity results for Pd catalysts synthesized by incipient wetness impregnation (IWI) during the liquid-phase reaction at 573 K.....	62
Table 4.1. Summary of the catalyst characterization and reactivity results for silica-supported Rh and Pt catalysts.....	97
Table 4.2. Summary of catalysts characterization and reactivity results for Pd catalysts.....	97
Table A.1. Summary of transport phenomena analysis	137

Table C.1. Summary of reactivity results for 20 wt% Pd/NoritC operated at different acid concentrations at 573 K and liquid-phase conditions.....	144
Table D. 1. Result of reactivity of propanoic anhydride (33 mol%) co-fed with ethylene (67 mol%) or 3-pentanone (67 mol%) over 20 wt% Pd/Norit C at 533 K.	146
Table E. 1. Result of reactivity of propanoic anhydride over 20 wt% Pd/Norit C at 533 K after regeneration with N ₂ and H ₂ treatments.....	152

List of Schemes

Scheme 1.1. Deoxygenation reactions of carboxylic acids.....	2
Scheme 1.2. Hydrogenation/dehydrogenation of decarbonylation/decarboxylation products.....	2
Scheme 1.3. Ketonization of heptanoic acid scheme.....	3
Scheme 2.1. Decarbonylation and decarboxylation of heptanoic acid	15
Scheme 2.2. Ketonization of heptanoic acid.....	16
Scheme 2.3. Hydrogenation of 1-hexene	17
Scheme 2.4. Water-gas shift (WGS) reaction.....	39
Scheme 3.1. Decarbonylation and decarboxylation of heptanoic acid	54
Scheme 3.2. Ketonization of heptanoic acid.....	55
Scheme 3.3. Some possible side reactions during the conversion of heptanoic acid.....	74
Scheme 4.1. Decarbonylation and decarboxylation of propanoic acid	87
Scheme 4.2. Ketonization of propanoic acid	88
Scheme 4.3. Propanoic anhydride as a reaction intermediate for the decarbonylation of propanoic acid.....	113
Scheme D. 1. Formation of 3-pentanone through a coupling reaction of propanyl and ethylene.....	147
Scheme D. 2. Formation of propanoic acid through the dimerization of 3-pentanone. R' represents CH ₂ -CH ₃ and R'' represents CH ₃	147

Abbreviations

<i>Abbreviation</i>	<i>Full Meaning</i>	<i>Description</i>
<i>AR</i>	Alcohol reduction	Impregnation method used to deposit metal precursors on the surface of the support.
<i>BET</i>	Brunauer-Emmett-Teller	Method used to determine the specific surface area of the catalyst evaluated by N ₂ physisorption.
<i>BJH</i>	Barrett-Joyner-Halenda	Method used to determine the pore size of the catalyst evaluated by N ₂ physisorption.
<i>Conv.</i>	Conversion	Formation rates of the major products with respect to the feed rate of reagents.
<i>Disp.</i>	Metal dispersion	Number of surface metal atoms available with respect to the total number of metal atoms in the catalyst.
<i>D_P</i>	Metal particle size	Metal particle size determined by TEM, XRD, and/or H ₂ chemisorption.
<i>E_A</i>	Apparent activation energy	Apparent activation energy determined using the Arrhenius equation.
<i>Fract.</i>	Fraction of metal exposed	Number of surface metal atoms available with respect to the total number of metal atoms in the catalyst.
<i>IWI</i>	Inicipient wetness impregnation	Impregnation method used to deposit metal precursors on the surface of the support.
<i>r_A</i>	Reaction rate	Moles of product formed or reagent consumed per unit of time.
<i>STY</i>	Site time yield	Rate of formation of individual products with respect to the number of surface metal atoms evaluated by H ₂ chemisorption.
<i>S_i</i>	Product selectivity	Moles of a product formed divided by the total moles of all identified products.
<i>TEM</i>	Transmission electron microscopy	
<i>TOF</i>	Turnover frequency	Rate of formation of all products with respect to the number of surface metal atoms evaluated by H ₂ chemisorption.
<i>XRD</i>	X-ray diffraction	

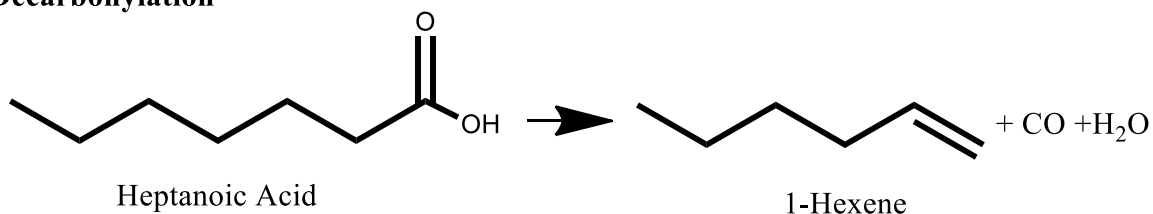
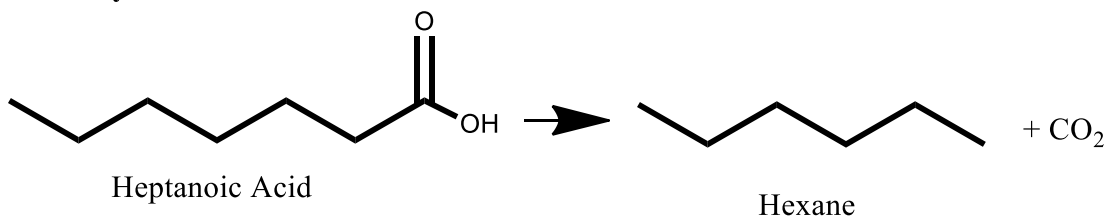
Chapter 1: Introduction

Portions of this Introduction Chapter are based on the content of Chapters 2, 3, and 4.

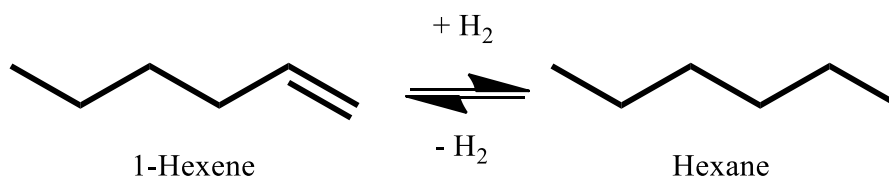
1.1. Motivation

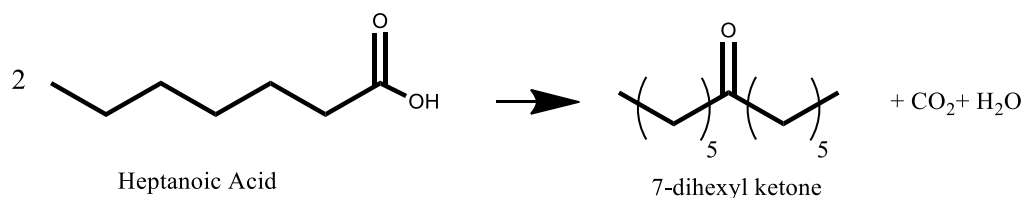
The world is now approaching a great turning point like never before. Societies all over the world are encouraged to utilize renewable energies such as solar, wind, hydroelectricity, and biomass [1]. One of the major driving forces to use renewable energy is to secure access to energy at an affordable price, which is complicated since the world demand for energy is constantly growing due to the increased consumption in the developing world. Another driving force to develop clean and renewable energy sources is the threat of climate change that results from the anthropogenic emission of CO₂ into the atmosphere [1]. Biomass represents an alternative to fossil fuels as an abundant carbon-neutral resource. However, it represents a chemical challenge because biomass requires a set of oxygen removal reactions to convert over-functionalized molecules into oxygen-free hydrocarbons [2]. Therefore, new renewable conversion technologies need to be developed using biomass as feedstock to meet the growing energy, fuel, and chemical demand of the 21st century.

Conversion of biomass feedstocks to oxygen-free hydrocarbons can be accomplished reactions such as dehydration, ketonization, decarbonylation and decarboxylation [2]. This set of reactions is collectively known as deoxygenation. Decarbonylation and decarboxylation reactions are of special interest because they represent a novel method for production of fuels from carbon neutral renewable resources such as vegetable oils and animal fats. The carbonyl group is removed from the fatty acid structure via production of CO₂, and/or CO, thus producing a linear alkane or alkene present at the fatty acid alkyl group, as shown in Scheme 1.1.

Decarbonylation**Decarboxylation****Scheme 1.1. Deoxygenation reactions of carboxylic acids**

A special family of alkenes is the α -olefin and it usually refers to linear hydrocarbons with four or more carbon atoms and a double bond at the primary or alpha (α) position, which enhances the reactivity of the molecule. It is an appealing organic chemical raw material that has received a lot of attention in recent years because of its application in the polymer industry. However, most of the work done in the decarbonylation/decarboxylation literature is often performed in the presence of dihydrogen to inhibit catalyst deactivation but is highly selective towards the production of paraffin, the saturated linear hydrocarbon [3–17]. Under these conditions, hydrogenation of α -olefins can also take place, especially over supported Pt and Pd supported catalyst (see Scheme 1.2).

**Scheme 1.2. Hydrogenation/dehydrogenation of decarbonylation/decarboxylation products**



Scheme 1.3. Ketonization of heptanoic acid scheme

Gaertner *et al.* showed that ketonization can play a key role in upgrading fatty acids into fine chemicals [18]. This process allows the coupling of two carboxylic acids into a larger ketone with the simultaneous removal of oxygen in the form of CO_2 and H_2O , as depicted in Scheme 1.3. Gaertner *et al.* also theorized that ketonization could be an intermediate step in the deoxygenation reaction [19], and in the presence of a transition metal, the ketone could further react to form olefins, mostly α -olefins, and CO. The ketonization reaction is often referred to as ketonic decarboxylation.

1.2. Effect of Metal

In 1982, Maier *et al.* studied the decarboxylation of fatty acid for production of fuel-like hydrocarbons [20]. In their work, they showed that supported metal catalysts, especially palladium (Pd) and nickel (Ni), are highly selective towards deoxygenation products however, the use of hydrogen as reaction gas was essential. Murzin and co-workers studied several other supported metals such as ruthenium (Ru), platinum (Pt), iridium (Ir), osmium (Os), and rhodium (Rh), and it was concluded that the most promising transition metals are Pd and Pt, which achieved more than 90% selectivity towards alkane and alkene production when supported on carbon [14]. Nickel has also been extensively studied for deoxygenation, but it is not an attractive metal because it particularly favors alkane production and cracking [6,10,12,21].

Relatively little has been reported on the conversion of fatty acids to olefins, with generally poor results achieved in terms of catalyst efficiency and selectivity towards terminal olefin formation in the product [3]. Because the different studies were run at different concentrations of H_2 , conversion levels,

amounts of catalyst, time on stream, and the results such as turnover frequency (TOF), conversions, and product selectivities were not always reported, it is still unclear which metals are more selective towards the formation of alpha-olefins. Furthermore, TOF values were not always provided because of a lack of catalyst characterization and/or proper data analysis [4]. Therefore, the field would benefit from a greater understanding of the different behaviors of the metals under H₂-free conditions to determine which one is more selective towards the formation of α -olefins. Some of the literature results are summarized in Tables 1.1 and 1.2 for studies performed using a semibatch reactor and continuous flow fixed-bed reactor, respectively.

1.3. Effect of support

Snåre *et al.* showed that Pt, Rh, and Pd nanoparticles displayed very different activity and product distribution when supported on alumina instead of carbon during liquid-phase operation [3]. Ford *et al.* showed that when Pd nanoparticles were supported on carbon instead of silica, the TOF of the reaction increased an order of magnitude, from 0.055 to 0.206 s⁻¹, for the liquid-phase deoxygenation of succinic acid at 573 K [17]. However, Lugo-José *et al.* showed a TOF decrease of an order of magnitude when Pd nanoparticles were supported over carbon instead of silica, from 0.0053 to 0.0002 s⁻¹, for the gas-phase deoxygenation of propanoic acid at 573 K.

Although seemingly contradictory, it is very difficult to explain these behaviors because the catalysts were run under completely different conditions and they were not completely characterized before and after reaction. Therefore, various supports will be used in this work to deposit transition metal nanoparticles. These supported catalysts will be then tested under identical conditions and characterized before and after reaction to explain differences in behaviors (if any).

Table 1.1. Summary of literature results during the liquid-phase reaction obtained using a semibatch reactor.

Catalyst	Temp (K)	[Acid]	H ₂	Conversion (%)	Product Selectivity		TOF (s ⁻¹)	Ref.	
					Paraffin	CO ₂			
1 wt% Pd/C	573	0.14 M	-	33.4 (after 6 h)	52 (after 6 h)	-	-	[3]	
	573	0.15 M	1 vol%	23 (after 5.5 h)	-	-	0.01	[9]	
	573	-	(17.5 bar)	68	49	-	0.030	[14]	
				100	52	-	0.076	[14]	
				99	54	-	0.110	[14]	
			96	51	-	0.012	[14]		
4 wt% Pd/C	543						0.13	[5]	
	573	-	-	-	-	-	1.1	[5]	
	603						1.7	[5]	
5 wt% Pd/C	573	0.14 M	-	100 (after 6 h)	95 (after 6 h)	-	-	[3]	
	573	-	-	41	-	-	0.067	[10]	
	633	-	1290 kPa	49	-	-	0.078	[10]	
	633	-	70 kPa	62	-	-	0.126	[10]	
	573	1.6 M	-	22 (after 6 h)	80 (at 30% conversion)	-	0.01	[11]	
	573	-	(15 atm)	5 vol%	-	-	95	0.083	[15]
				10 vol%	-	-	92	0.053	[15]
				10 vol%	-	-	92	0.018	[16]
573	-	(15 atm)	5 vol%	-	-	89	0.076	[16]	
573	0.19 M	(15 atm)	5 vol%	-	-	95	0.21	[17]	
5 wt% Pd/SiO₂	573	0.19 M	5 vol% (15 atm)	-	-	49	0.089	[17]	
						66	0.055	[17]	
5 wt% Pd/Al₂O₃	573	0.19 M	5 vol% (15 atm)	-	-	84	0.029	[17]	
10 wt% Pd/C	573	0.14 M	-	48 (after 6 h)	60 (after 6 h)	-	-	[3]	
5 wt% Pt/C	573	0.14 M	-	86 (after 6 h)	87 (after 6 h)	-	-	[3]	
1 wt% Rh/C	573	0.14 M	-	18 (after 6 h)	18 (after 6 h)	-	-	[3]	

Table 1.2. Summary of literature results obtained using a fixed-bed continuous-flow reactor.

Catalyst	Temp (K)	Reaction Phase	[Acid]	H ₂	Conversion (%)	Product Selectivity		TOF (s ⁻¹)	Ref.
						Paraffin	CO ₂		
5 wt% Pd/C	528	Liquid	0.22 M	-	23 (after 60 min)	94 (at 80% conversion)	-	-	[6]
	543	Liquid	0.44 M	-	6 (after 60 min)	82-86	-	-	[6]
	543	Liquid	0.35 M	-	3 (after 30 min)	82 (at 70% conversion)	-	-	[6]
	543	Liquid	0.22 M	-	4 (after 30 min)	78 (at 70% conversion)	-	-	[6]
	558	Liquid	0.22 M	-	41 (after 60 min)	98 (at 80% conversion)	-	-	[6]
	573	Liquid	0.22 M	-	44 (after 60 min)	98 (at 80% conversion)	-	-	[6]
1.1 wt% Pd/SiO₂	473	Gas	0.01 bar	0.2 bar	7.0	-	-	0.011	[22]
4.0 wt% Pd/SiO₂	473	Gas	0.01 bar	0.2 bar	11 4.0	-	-	0.0053 0.0053	[22]
2.1 wt% Pt/SiO₂	473	Gas	0.01 bar	0.2 bar	5.0	-	-	0.0020	[22]
2.1 wt% Rh/SiO₂	473	Gas	0.01 bar	0.2 bar	4.0	-	-	0.00083	[22]
5.0 wt% Pd/C	473	Gas	0.01 bar	0.2 bar	2.0	-	-	0.00017	[22]
2.3 wt% Pd/TiO₂	473	Gas	0.01 bar	0.2 bar	3.3	-	-	0.0022	[22]
0.5 wt% Pd/SiO₂	523	Gas	0.02 bar	0.98 bar	<10	-	-	0.0094	[23]
0.5 wt% Pt/SiO₂	523	Gas	0.02 bar	0.98 bar	<10	-	-	0.00064	[23]

1.4. Effect of concentration

Most of the experiments with carboxylic acid deoxygenation over Pd catalysts involved a long chain hydrocarbon as solvent [3,8,9,11,12,15–17,22–25] and co-feeding H₂ [9,10,14–17,22,23,25] to enhance the TOF and the stability of the catalyst. Under these conditions, liquid-phase TOF values reported over Pd ranged from 0.01 to 0.96 s⁻¹ for batch reaction at 573 K [10,11,15,16] and from 0.027 to 0.004 s⁻¹ for fixed-bed operation at 543 K [4,6].

Mäki-Arvela *et al.* showed that when the concentration of lauric acid decreases from 0.44 to 0.22 mol L⁻¹ the steady state reaction rates did not change [6]. Similarly, Snåre *et al.* reported a zero order regime at concentrations between 0.15 and 1.5 mol L⁻¹ [8]. However, Bartosz *et al.* showed that the reaction rate increases when the concentration of fatty acid decreases from 0.6 to 0.15 mol L⁻¹ [7]. Furthermore, Immer *et al.* showed that as the concentration of fatty acid decreases, the decarboxylation rate decays rapidly whereas the decarbonylation rate increases [16]. This led to a switchover in product selectivity from paraffins and CO₂ (typical of decarboxylation) to olefins and CO (typical of decarbonylation) which led to a decrease in total deoxygenation rate. However, when the concentration of fatty acid was lowered, the decarbonylation rate decreased and the decarboxylation rate increased and the product switchover was reversed [16]. More recently, Lugo-José *et al.* showed that during gas-phase reaction of propanoic acid at 1 bar and 473 K, there were two reaction orders as a function of the propanoic acid partial pressure, zero at high partial pressures and 0.5 at low partial pressures [22]. While the zero reaction order regime that Lugo-José *et al.* reported is in agreement with Mäki-Arvela *et al.* [6] results, the 0.5 reaction order regime at low partial pressures is in disagreement with the findings of Immer *et al.* [16].

Whereas the literature results seem to be inconsistent and sometimes contradictory, differences in acid concentrations, reactor configuration, and reaction phase, could account for some of the differences observed among studies. The field would benefit from understanding the effect of acid concentration on catalyst stability, activity, and product distribution, during the liquid- and gas-phase reaction.

1.5. Catalyst deactivation and regeneration

Catalyst deactivation during the deoxygenation of carboxylic acids has been widely reported in the literature. Snåre *et al.* [12] and Mäki-Arvela *et al.* [6] suggested that deactivation of Pd/carbon originated from poisoning of the metal by the reactants and products (especially CO), as well as by coking. Furthermore, Simakova *et al.* reported that deactivating aromatics are formed in reactions performed under H₂-scarce conditions [9]. However, Ping *et al.* concluded that the observed deactivation did not result from coke formation, but from deposition of organic molecules onto the active sites [24]. In that study, Ping *et al.* regained the catalytic activity of Pd/SiO₂ after hot extraction with solvent and subsequent reduction in H₂ at 573 K [24]. The initial concentration of carboxylic acid was also proposed to influence catalyst deactivation. Mäki-Arvela *et al.* observed that deactivation was more extensive with higher initial concentration of carboxylic acid [6].

Whereas it is clear that a metal catalyst could deactivate during reaction and, in some cases, the catalytic activity can be recovered using mild regeneration methods, the lack of catalyst characterization after reaction and/or regeneration makes it difficult to understand the deactivation mechanism. The field would benefit from using standard characterization techniques of deactivated catalysts to determine the deactivation mechanism and regeneration of the catalyst.

1.6. Reaction kinetics and mechanism

Whereas most of the previous studies concluded that decarboxylation is the main reaction of carboxylic acid over Pd catalysts, more recent studies showed that decarbonylation is in fact the main reaction [22,25]. However, some of these studies showed that the formation rate of alkenes did not match that of CO [4,11].

As mentioned earlier, Immer *et al.* showed that as the concentration of fatty acids decreases, the decarboxylation rate decayed rapidly whereas the decarbonylation rate increased [16]. This led to a switchover in product selectivity from paraffins and CO₂ to olefins and CO which led to a decrease in total deoxygenation rate. However, when the concentration of fatty acid was decreased, the

decarbonylation rate decreased and the decarboxylation rate increased and the product switchover was reversed [16]. This implies a complex relationship exists between the metal surface and surrounding environment.

Although Snåre *et al.* reported a zero order regime at concentrations between 0.15 and 1.5 mol L⁻¹, first order kinetics were used to estimate activation barriers [8]. In the same study, Snåre *et al.* reported catalyst deactivation during their kinetic study, but they did not account for it when obtaining activation barriers or reaction orders. As mentioned above, Lugo-José *et al.* showed that during gas-phase reaction of propanoic acid at 1 bar and 473 K, there were two reaction orders as a function of the propanoic acid partial pressure, zero at high partial pressures and 0.5 at low partial pressures [22]. While the zero reaction order regime that Lugo-José *et al.* reported is in agreement with Mäki-Arvela *et al.* [6] results, the 0.5 reaction order regime at low partial pressures is in disagreement with the findings of Immer *et al.* [16] Although seemingly contradictory, the differences in reaction mechanism and reaction order reported in the literature could be the result of performing the experiments on deactivated catalysts and/or under different reaction conditions such as conversion, acid concentration, and reaction phase. The field would strongly benefit from developing a fundamental understanding of how to perform reaction kinetics under reaction conditions that deactivate catalysts.

1.7. Focus of this work

While there is already extensive work on the decarbonylation/decarboxylation of fatty acids, the differences in reaction conditions between studies have led to conflicting results, especially in terms of turnover frequency (TOF), catalyst stability, and reaction mechanism. In light of the previous discussion, this thesis addresses the following topics:

1. The effect of metal and support on catalyst activity and product selectivity
2. The effect of reaction conditions on catalyst stability and product selectivity
3. The reaction mechanism and possible reaction intermediates at different reaction conditions

Chapter 2 presents a study of the decarbonylation of heptanoic acid with a goal of forming α -olefins over Pt nanoparticles during the liquid- and gas-phase operation at different conversion levels. Chapter 3 focuses on the stability of Pd nanoparticles during the liquid- and gas-phase conversion of heptanoic acid. Chapter 4 provides an in depth investigation of gas-phase decarbonylation unveils mechanistic insights on the decarbonylation of propanoic acid over silica- and carbon-supported Pt, Rh and Pd nanoparticles.

In this work, a laboratory scale continuous flow fixed bed reactor system was designed and built to study the liquid- and gas-phase deoxygenation reaction over different transition metal catalysts with two different carboxylic acids, heptanoic and propanoic acid. The reagents, diluents, and reaction products were analyzed using gas chromatography. A flame ionization detector (FID) was used to analyze condensable products (mainly hexane, 1-hexene, hexenes, 7-tridecanone, and 3-tridecanone), unreacted reagents (mainly heptanoic acid and propanoic acid), internal standard (octane and dodecane), and diluents (hexane and tetradecane). A thermal conductivity detector (TCD) was used to analyze products that cannot be condensed at room temperature (mainly CO, CO₂, ethylene, and ethane) and gaseous external standards (N₂ and methane).

A variety of characterization techniques were used to study the fresh catalysts, used catalysts and regenerated catalysts, including X-ray diffraction (XRD), transmission electron microscopy (TEM), N₂ physisorption, H₂ chemisorption, and thermogravimetric analysis (TGA).

1.8. References

- [1] 2008, National Research council. America's Energy Future. Summary of a meeting 2008.
- [2] Ragauskas, A. J., Williams, C. K., Davison, B. H., Britovsek, G., Cairney, J., Eckert, C. A., Frederick, W. J., Hallett, J. P., Leak, D. J., Liotta, C. L., Mielenz, J. R., Murphy, R., Templer, R., and Tschaplinski, T., 2006, "The path forward for biofuels and biomaterials.," *Science*, **311**(5760), pp. 484–9.

- [3] Snåre, M., Kubičková, I., Mäki-Arvela, P., Eränen, K., and Murzin, D. Y., 2006, "Heterogeneous Catalytic Deoxygenation of Stearic Acid for Production of Biodiesel," *Ind Eng Chem Res*, **45**(45), pp. 5708–5715.
- [4] Lestari, S., Mäki-Arvela, P., Bernas, H., Simakova, O., Sjöholm, R., Beltramini, J., Lu, G. Q. M., Myllyoja, J., Simakova, I., and Murzin, D. Y., 2009, "Catalytic Deoxygenation of Stearic Acid in a Continuous Reactor over a Mesoporous Carbon-Supported Pd Catalyst," *Energ Fuel*, **23**(8), pp. 3842–3845.
- [5] Lestari, S., Simakova, I., Tokarev, A., Mäki-Arvela, P., Eränen, K., and Murzin, D. Y., 2008, "Synthesis of Biodiesel via Deoxygenation of Stearic Acid over Supported Pd / C Catalyst," *Catal Lett*, **122**(3-4), pp. 247–251.
- [6] Mäki-Arvela, P., Snåre, M., Eränen, K., Myllyoja, J., and Murzin, D. Y., 2008, "Continuous decarboxylation of lauric acid over Pd/C catalyst," *Fuel*, **87**(17-18), pp. 3543–3549.
- [7] Rozmysłowicz, B., Mäki-Arvela, P., Lestari, S., Simakova, O. A., Eränen, K., Simakova, I. L., Murzin, D. Y., and Salmi, T. O., 2010, "Catalytic Deoxygenation of Tall Oil Fatty Acids Over a Palladium-Mesoporous Carbon Catalyst: A New Source of Biofuels," *Top Catal*, **53**(15-18), pp. 1274–1277.
- [8] Snåre, M., Kubičková, I., Mäki-Arvela, P., Eränen, K., Wärnä, J., and Murzin, D. Y., 2007, "Production of diesel fuel from renewable feeds: Kinetics of ethyl stearate decarboxylation," *Chem Eng J*, **134**, pp. 29–34.
- [9] Simakova, I., Rozmysłowicz, B., Simakova, O. A., Mäki-Arvela, P., Simakov, A., and Murzin, D. Y., 2011, "Catalytic Deoxygenation of C18 Fatty Acids Over Mesoporous Pd / C Catalyst for Synthesis of Biofuels," *Top Catal*, **54**(8-9), pp. 460–466.

- [10] Kubičková, I., Snåre, M., Eränen, K., Mäki-Arvela, P., and Murzin, D., 2005, "Hydrocarbons for diesel fuel via decarboxylation of vegetable oils," *Catal Today*, **106**(1-4), pp. 197–200.
- [11] Mäki-Arvela, P., Kubičková, I., Snåre, M., Eränen, K., and Murzin, D. Y., 2007, "Catalytic Deoxygenation of Fatty Acids and Their Derivatives," *Energ Fuel*, **21**(1), pp. 30–41.
- [12] Snåre, M., Kubičková, I., Mäki-Arvela, P., Chichova, D., Eränen, K., and Murzin, D. Y., 2008, "Catalytic deoxygenation of unsaturated renewable feedstocks for production of diesel fuel hydrocarbons," *Fuel*, **87**(6), pp. 933–945.
- [13] Lestari, S., Mäki-Arvela, P., Simakova, I., Beltramini, J., Lu, G. Q. M., and Murzin, D. Y., 2009, "Catalytic Deoxygenation of Stearic Acid and Palmitic Acid in Semibatch Mode," *Catal Lett*, **130**(1-2), pp. 48–51.
- [14] Simakova, I., Simakova, O., Mäki-Arvela, P., Simakov, A., Estrada, M., and Murzin, D. Y., 2009, "Deoxygenation of palmitic and stearic acid over supported Pd catalysts: Effect of metal dispersion," *Appl Catal A-Gen*, **355**, pp. 100–108.
- [15] Immer, J. G., and Lamb, H. H., 2010, "Fed-Batch Catalytic Deoxygenation of Free Fatty Acids," *Energ Fuel*, **130**(10), pp. 5291–5299.
- [16] Immer, J. G., Kelly, M. J., and Lamb, H. H., 2010, "Catalytic reaction pathways in liquid-phase deoxygenation of C18 free fatty acids," *Appl Catal A-Gen*, **375**(1), pp. 134–139.
- [17] Ford, J. P., Immer, J. G., and Lamb, H. H., 2012, "Palladium Catalysts for Fatty Acid Deoxygenation: Influence of the Support and Fatty Acid Chain Length on Decarboxylation Kinetics," *Top Catal*, **55**(3-4), pp. 175–184.

- [18] Gaertner, C. A., Serrano-Ruiz, J. C., Braden, D. J., and Dumesic, J. A., 2010, “Ketonization Reactions of Carboxylic Acids and Esters over Ceria–Zirconia as Biomass-Upgrading Processes,” *Ind Eng Chem Res*, **49**(13), pp. 6027–6033.
- [19] Gaertner, C. A., Serrano-Ruiz, J. C., Braden, D. J., and Dumesic, J. A., 2009, “Catalytic coupling of carboxylic acids by ketonization as a processing step in biomass conversion,” *J Catal*, **266**(1), pp. 71–78.
- [20] Maier, W. F., Roth, W., Thies, I., v. Rague Schleyer, P., Ragukschleyer, P., and Schleyer, R., 1982, “Gas Phase Decarboxylation of Carboxylic Acids,” *Chem Ber*, **115**, pp. 808–812.
- [21] Simakova, I., Simakova, O., Mäki-Arvela, P., and Murzin, D. Y., 2010, “Decarboxylation of fatty acids over Pd supported on mesoporous carbon,” *Catal Today*, **150**(1-2), pp. 28–31.
- [22] Lugo-José, Y. K., Monnier, J. R., and Williams, C. T., 2014, “Gas-Phase, Catalytic Hydrodeoxygenation of Propanoic Acid, Over Supported Group VIII Noble Metals: Metal and Support Effects,” *Appl Catal A-Gen*, **469**, pp. 410–418.
- [23] Alotaibi, M. A., Kozhevnikova, E. F., and Kozhevnikov, I. V., 2012, “Deoxygenation of propionic acid on heteropoly acid and bifunctional metal-loaded heteropoly acid catalysts: Reaction pathways and turnover rates,” *Appl Catal A-Gen*, **447-448**, pp. 32–40.
- [24] Ping, E. W., Pierson, J., Wallace, R., Miller, J. T., Fuller, T. F., and Jones, C. W., 2011, “On the nature of the deactivation of supported palladium nanoparticle catalysts in the decarboxylation of fatty acids,” *Appl Catal A-Gen*, **396**(1-2), pp. 85–90.
- [25] Boda, L., Onyestyák, G., Solt, H., Lónyi, F., Valyon, J., and Thernesz, A., 2010, “Catalytic hydroconversion of tricaprylin and caprylic acid as model reaction for biofuel production from triglycerides,” *Appl Catal A-Gen*, **374**(1-2), pp. 158–169.

Chapter 2. Decarbonylation of Heptanoic Acid over Carbon-Supported Platinum Nanoparticles

This chapter appears in: Juan A. Lopez-Ruiz and Robert J. Davis, “Decarbonylation of Heptanoic Acid over Carbon-Supported Platinum Nanoparticles” *Green Chem*, 2014, **16**, 683–694, Copyright (2014) RSC Green Chemistry

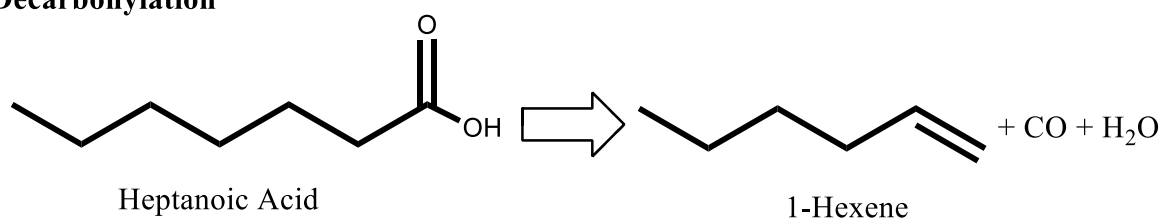
Abstract

The decarbonylation and decarboxylation of heptanoic acid over carbon-supported Pt nanoparticles were studied in a continuous flow fixed bed reactor at 573 K and 37 bar for liquid-phase operation and 1 bar for gas-phase operation. Under liquid-phase conditions, the TOF over Pt supported on Norit carbon was 0.0052 s^{-1} and independent of Pt loading. At very low conversions, approaching zero, the product selectivity was consistent with decarbonylation as the primary reaction, producing mostly hexenes and CO. As conversion increased from 1% to 5% at 37 bar, substantial amounts of hexane and CO_2 were observed, presumably from secondary side reactions such as water-gas shift (WGS) and hydrogenation instead of direct decarboxylation. The terminal olefin was observed with high selectivity (57%) only during gas-phase operation (1 bar) which facilitated transport of the olefin away from the Pt that also catalyzed double bond isomerization. Some sintering of the Pt metal particles during reaction of heptanoic acid was observed by X-ray diffraction analysis of the spent catalyst. Catalyst regeneration studies were performed over spent catalyst but they failed to restore any catalytic activity.

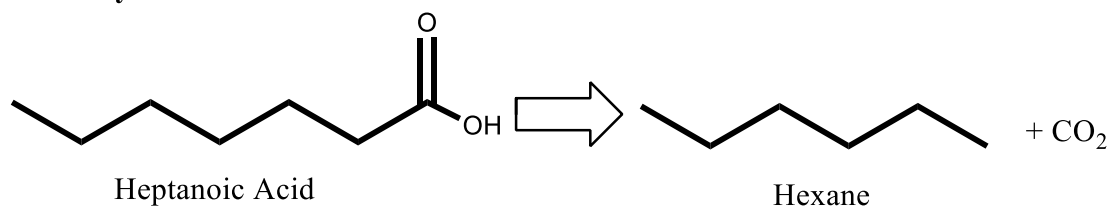
2.1. Introduction

Deoxygenation refers to a broad class of chemical reactions involving the removal of oxygen from organic compounds that can be accomplished by reactions such as dehydration, decarbonylation and decarboxylation. Carboxylic acids found in vegetable oils and animal fats can be readily converted to fuels and chemicals by decarbonylation and decarboxylation reactions. For example, linear organic acids are converted to linear alkenes and linear alkanes by decarbonylation and decarboxylation, respectively, as shown for the reaction of heptanoic acid in Scheme 2.1. Recent work on decarbonylation and decarboxylation of carboxylic acids over transition metal catalysts is often performed in the presence of dihydrogen to inhibit catalyst deactivation, but the reactions are highly selective towards the production of paraffins because of the rapid hydrogenation of any alkenes formed in the process [1,2]. Terminal alkenes formed by decarbonylation are appealing organic materials because of their application in the polymer industry. Therefore, an effective catalyst for decarbonylation prevents both hydrogenation of product α -olefin as well as the double bond isomerization to form internal olefins.

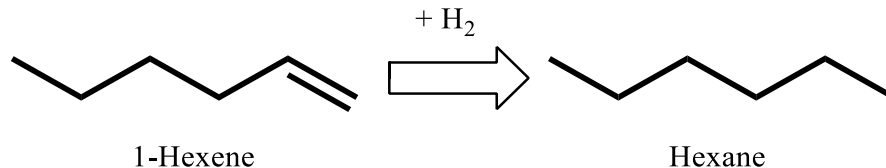
Decarbonylation



Decarboxylation



Scheme 2.1. Decarbonylation and decarboxylation of heptanoic acid



Scheme 2.3. Hydrogenation of 1-hexene

As mentioned above, hydrogenation is an important side reaction that can also take place over supported metal catalysts (see Scheme 2.3). Because hydrogenation of α -olefins forms less valuable paraffins, sources of hydrogen in the reaction need to be minimized. Some studies on decarboxylation and decarbonylation include H₂ not only to maximize the selectivity towards the formation of paraffins (typically for fuel components), but also to influence the deoxygenation rate [9,10]. Snåre *et al.* showed that reaction under low H₂ conditions formed coke [10]. Olefins can also be formed from the decarboxylation of unsaturated fatty acids that had been dehydrogenated earlier in the reactor [9].

In this study, we studied systematically the decarbonylation and decarboxylation of heptanoic acid over a wide variety of carbon-supported Pt catalysts in a steady-state, fixed bed flow reactor to elucidate the reaction path and evaluate the turnover frequency of the reaction. In particular, the influences of Pt dispersion, Pt loading, carbon support and reaction phase on the conversion of heptanoic acid and selectivity to various products were explored.

2.2. Experimental Methods

2.2.1. Catalyst synthesis

The catalysts were prepared by an incipient wetness impregnation method using aqueous solutions of tetraammineplatinum (II) nitrate, $(\text{NH}_3)_4\text{Pt}(\text{NO}_3)_2$ (Sigma Aldrich) to obtain 1, 3, 5, and 10 wt% Pt loadings. Norit activated carbon (ROX 0.9), SiC (SICAT β -SiC), and Vulcan carbon (VXC72R) were used as supports for the metal particles. Prior to impregnation, Norit C and SiC support particles were crushed and sieved between 180 μm and 425 μm . Vulcan C powder was used as received. After impregnation of the desired Pt precursor solution, the catalyst was dried in air at 393 K overnight. The dried solids were then reduced in H_2 (GT&S 99.999%) flowing at 100 $\text{cm}^3 \text{min}^{-1}$. The temperature of reduction was increased at 5 K min^{-1} from room temperature to the desired value, which ranged from 623 to 873 K, and held isothermally for 3 h. The catalyst was then cooled, exposed to air, and stored in a vial.

2.2.2. Dihydrogen chemisorption

The metal dispersion was measured by H_2 chemisorption performed on a Micromeritics ASAP 2020 adsorption system. The catalyst was evacuated at 573 K for 10 h under vacuum followed by heating to 623 K at a rate of 5 K min^{-1} after which it was reduced with flowing H_2 (GT&S 99.999%) at 623 K for 2 h.

Following reduction, the catalyst sample was evacuated at 623 K and cooled to 308 K in vacuum. The chemisorption of H_2 was performed at 308 K over the pressure range of 40 to 450 Torr. The amount of metal on the surface was evaluated by the total amount of H_2 adsorbed extrapolated to zero pressure, assuming a stoichiometric relationship between H_2 to metal (H_2 : Pt) of 1:2 (i.e. $\text{H}/\text{Pt} = 1$).

2.2.3. Dinitrogen physisorption

The specific surface area and pore size were measured by N_2 physisorption using a Micromeritics ASAP 2020. The samples were evacuated for 180 min at 373 K prior to the N_2 physisorption, after

which adsorption isotherms were measured at 77 K. The Brunauer-Emmett-Teller (BET) and the Barrett-Joyner-Halenda (BJH) methods were used to determine the specific surface area and the pore size, respectively.

2.2.4. X-ray diffraction

Powder X-ray diffraction (XRD) analysis was carried out on a X'Pert Pro MPD with monochromatic Cu K α -radiation ($\lambda=1.54056 \text{ \AA}$) using a step size of $1/4^\circ$ and a time step of 1 s. Diffraction angles were measured from $2\theta = 20^\circ$ to 100° . The Scherrer equation was used to estimate the particle size as described in Patterson *et al.* [11].

2.2.5. Electron microscopy

Transmission electron microscopy (TEM) was performed on a FEI Titan operated at 300 keV in EFTEM mode. Energy dispersive X-ray spectroscopy (EDS) was used to obtain elemental analysis of the nanoparticles. Catalyst samples were deposited on a SPI lacey-carbon coated Cu grid after being dispersed in methanol [12]. Fresh (after catalyst synthesis) and spent (after exposure to reaction conditions) catalyst samples were imaged to determine the effect of reaction conditions on particle morphology. The spent samples were recovered from the reactor, washed with 25 mL of methanol and sonicated in a methanol solution for 30 min to remove reactant and products from the surface of the catalyst. After sonication, the solids were recovered by filtration and dried overnight in air at 400 K.

2.2.6. Catalytic conversion of heptanoic acid

The decarbonylation/decarboxylation of fatty acids can be a challenging reaction, mainly because of low reaction rates and rapid catalyst deactivation [2]. Furthermore, saturated fatty acids with more than 9 carbons in the aliphatic chain have a high melting point. This physical property makes operation in a continuous mode particularly challenging since the entire pumping system as well as the reactor must be heated. In this study, heptanoic acid was selected as the reactant because it is a

liquid at room temperature, therefore eliminating the need to pre-heat the lines and the pumping system.

Decarbonylation/decarboxylation reactions are often performed in a solvent with H_2 simultaneously fed to the reactor to extend catalyst life. Under these conditions, the fatty acid could be hydrogenated before deoxygenation, leading to the formation of alcohols and other products, which can react with the acid substrate to form esters [2–4,7–9,13,14]. To avoid undesirable side reactions, neither solvent nor H_2 was cofed with the heptanoic acid. Dodecane was used as an internal standard because it has a similar boiling point to heptanoic acid and is thermally stable. The amount of dodecane was minimized (5 wt%) to avoid hydrogen transfer from it to the products [9].

The main organic products from converting heptanoic acid were expected to be 6 carbon hydrocarbons, hexane, 1, 2, and 3-hexene, and the ketonization product 7-dihexyl ketone (a symmetrical ketone). These compounds were therefore monitored by gas chromatography. Gas chromatography calibration curves can be found in Appendix B.

The catalytic decarboxylation/decarbonylation of heptanoic acid (Sigma Aldrich 99.0 %) was performed in a 1/4" OD x 8" length x 0.035" wall thickness stainless steel fixed bed reactor. After loading the catalyst in the reactor, the system was first flushed for 30 min with $100 \text{ cm}^3\text{min}^{-1}$ of N_2 (GT&S 99.999%) at 40 bar to remove any dioxygen from the system and to perform a leak test. Then, the temperature was increased to the desired reduction temperature, 623 – 873 K, under $100 \text{ cm}^3\text{min}^{-1}$ of N_2 at 5 K min^{-1} at 1 bar. The temperature was held isothermally for 2 h as the catalyst was reduced in H_2 (GT&S 99.999%) flowing at $100 \text{ cm}^3\text{min}^{-1}$ at atmospheric pressure. The reactor was finally cooled to the reaction temperature, 573 K, and pressurized to 37 bar in $100 \text{ cm}^3\text{min}^{-1}$ of N_2 (GT&S 99.999%). The feed mixture was composed of 95 wt% heptanoic acid (Sigma Aldrich 99.00 %) and 5 wt% dodecane (Sigma Aldrich anhydrous 99.00 %). The feed was pumped into the reactor containing 0.25 g of catalyst using a syringe pump (ISCO 500D) operating at different liquid flow rates (0.005 , 0.01 , or $0.05 \text{ cm}^3\text{min}^{-1}$). The acid feed passed through a heated zone before entering the catalytic

reactor. The reactor was operated in an upflow mode because gases were generated in the reaction. Figure 2.1 shows a schematic of the reactor system.

The outlet of the reactor was connected to a condenser, maintained at room temperature, and samples of the liquid and gas products were collected approximately every 150 min. The liquid sample was analyzed by a gas chromatograph (GC 7890 A) equipped with a ZB-FFAP column (length 45 m x 0.538 mm) and a flame ionization detector. The presence of dodecane as an internal standard allowed for quantification of the products.

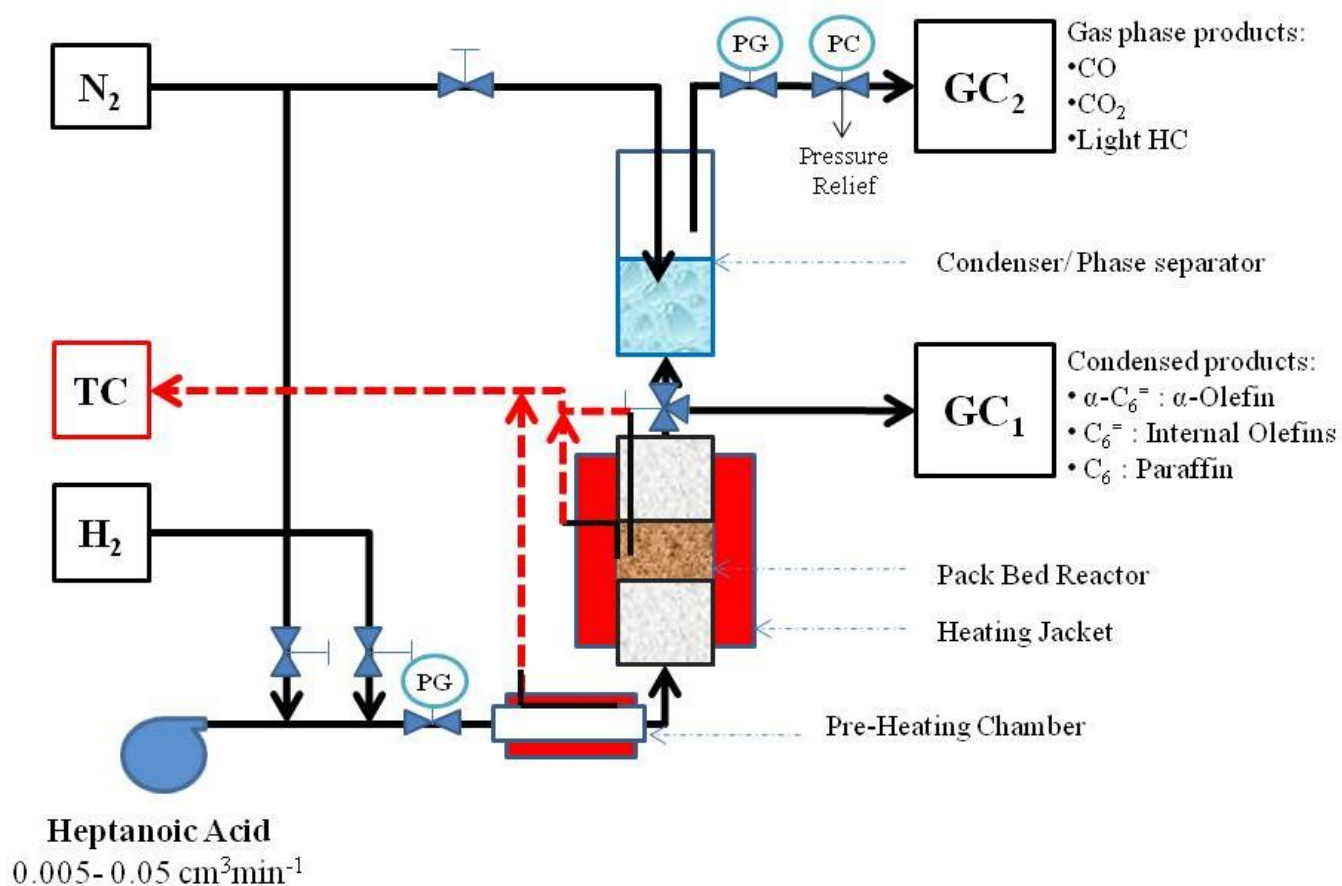


Figure 2.1. Schematic of the reactor system. TC represents a thermocouple, GC represents a gas chromatograph, PG represents a pressure gauge, and PC represents a back pressure regulator.

The product gas was continuously removed from the condenser by an N₂ (GT&S 99.999%) purge gas, which was fed to an on-line gas chromatograph (HP 5890 Series II) equipped with a packed column, ShinCarbon ST 80/100, and a thermal conductivity detector (TCD) for detection of N₂, CO, CO₂, and light hydrocarbons (if any). The N₂ purge gas was also used to maintain pressure in the system and was the internal standard for GC analysis.

A series of control experiments was performed to determine the background conversion of the system at our typical reaction conditions (573 K, 37 or 1 bar, and 0.01 cm³min⁻¹ of liquid feed composed of 95 wt% heptanoic acid and 5 wt% dodecane). In the absence of catalyst, no conversion of heptanoic acid was observed. However, when Norit carbon and Vulcan carbon supports were used, a background conversion of 2 - 3% was detected. No conversion was observed over SiC.

2.2.7. Turnover frequency and selectivity calculations

The turnover frequency (TOF) was defined by Boudart as the number of revolutions of the catalytic cycle per unit time [15]. In this work the TOF was calculated as the rate of formation of the products referred to the number of surface Pt atoms. The main components in the liquid products were hexane (C6), 1-hexene (α -C6), 2 and 3-hexenes (i-hexenes, i-C6), 7-tridecanone (ketone), and minor amounts of heavier unknown products (which accounted for \approx 3 % of the total detected liquid product). The TOF was therefore calculated as [(rate of production (mol s⁻¹) of C6 + α -C6 + i-C6 + 2 x moles of ketone + others) / (mol of surface Pt counted by H₂ chemisorption)]. The major gas products observed were CO and CO₂. The product selectivity was defined as the moles of a product formed divided by the total moles of all identified products present in the same phase (liquid or gas), i.e. selectivity of 1-hexene [(rate of α -C6) / (rate of all C6 products + 2x moles of 7-tridecanone + moles of unknowns)] and selectivity of CO [(rate of CO) / (rate of CO + rate of CO₂)]. Selectivities of liquid and gas products were calculated independently. The TOF associated with the Pt was based on measured rates after subtracting the background conversion from the support and normalized by the dispersion of Pt evaluated on a freshly prepared catalyst.

2.2.8. Mass transfer limitations

The mass transfer characteristics were estimated using the Weisz-Prater criterion for internal transport limitations (Φ_I), Equation 2.1, and the analogous expression for external transport limitations (Φ_E), Equation 2.2, assuming first order reaction [16]. In Equations 2.1 and 2.2, r_{obs} is the observed rate, R_p is the radius of the support particle, ρ_p is the density of the catalyst pellet, D_{EA} is the effective

$$\Phi_I = \frac{r_{obs} R_p^2 \rho_p}{D_{EA} C_{AS}} < 1 \quad \text{Equation 2.1}$$

$$\Phi_E = \frac{r_{obs} R_p \rho_p}{k_A C_{AB}} < 0.15 \quad \text{Equation 2.2}$$

diffusivity, k_A is the external mass transfer coefficient, C_{AS} is the surface concentration, and C_{AB} is the bulk concentration of heptanoic acid [16,17].

The effective diffusivity (D_{EA}) was estimated using a porosity (ϵ_p) of 0.5 and a tortuosity (τ) of 3 as recommended in Davis and Davis [17]. The self-diffusion coefficient (D_{AA}) for heptanoic acid was calculated using the Stokes-Einstein equation for analysis of the liquid-phase and using gas kinetic theory for analysis of the gas-phase reaction. Because the average Pt particle size was ≈ 2 nm or greater, it was assumed for this analysis that the size of the pore in which the catalytic reaction takes place is at least 2 nm, which was used to calculate the Knudsen diffusivity (D_{KA}) for the gas-phase operation. The external mass transfer coefficient (k_A) was obtained using a mass transfer correlation for fluid-solid interface for packed bed reactors obtained from Cussler [18].

Using the highest observed rates, Φ_I was calculated to be much less than 1 for the liquid and gas phase reactions (0.005 and 0.012, respectively) and Φ_E was much less than 0.15 for the liquid and gas phase reactions (0.004 and 0.001, respectively) for a catalyst particle size of 425 μm . The criteria

suggest that the system was not mass transfer limited with respect to the reactant. Detailed calculations of the mass transfer criteria can be found in Appendix A.

2.3. Results and Discussion

2.3.1. Effect of carbonaceous support

Carbon is a widely used support for transition metals in deoxygenation reactions because of its high surface area (700 – 1500 m²g⁻¹) and relative inertness [1,2,19–24]. Carbon supports are available in different particle sizes, surface areas, and pore size distributions. Most carbon supports are difficult to pelletize, which may account for why so many of the earlier studies in the field were performed in batch systems. Operation of a fixed bed reactor system with a fine powder can develop a very large pressure drop across the catalyst bed. Therefore, we chose to explore some of the pelletized carbons as supports for Pt nanoparticles.

Three different carbonaceous supports were tested in this study, each having very different physical properties. Norit carbon is a high surface area support that can be purchased in pellet form, which can be easily crushed to the desired particle size. However, it has many small pores that might influence the transport rates of products out of the pellets and therefore affect the side reactions. Vulcan carbon is nonporous, but has a much smaller surface area than Norit carbon. Furthermore, the as-received Vulcan carbon could not be easily pelletized. Preliminary tests of Vulcan carbon powder in our fixed bed reactor revealed a very large pressure drop when we tried to pump liquid reactant through the bed. Therefore, Vulcan carbon was only used as a support for Pt in experiments with gaseous heptanoic acid. Silicon carbide is a macroporous support that was obtained in pellet form. However, it has a much lower surface area than Norit carbon.

Table 2.1. Summary of the characterization results for 5 wt% Pt on different supports.

Support	Dispersion (%)	Surface Area (m²g⁻¹)	Pore Size (nm)	Pt Particle Size (nm)
Norit Carbon	31 ^a	1428	N.D. ^b	3.7 ^a
Vulcan Carbon	-	217	7.3	21 ^c
SiC	-	26	20	40 ^c

^a Result estimated from H₂ chemisorption

^b Not determined, both micropores and mesopores are present on this sample

^c Result obtained using XRD patterns and Scherrer equation

Catalysts composed of 5 wt% Pt supported on the various carbon supports were characterized using N₂ physisorption, H₂ chemisorption, and XRD, and the results are summarized in Table 2.1. While a high Pt dispersion of 31 % was obtained on Norit carbon, very large Pt particles were formed on Vulcan carbon and SiC. The diffraction peaks in Figure 2.2 observed at about 39.5° , 45.5° , 57° , and 79.5° are attributed to the (111), (200), (220), and (311) reflections of Pt [25]. Analysis of the peak width by the Scherrer equation gave an average Pt crystallite size of 21 and 40 nm for Pt supported on Vulcan C and SiC, respectively. The lack of a Pt diffraction pattern associated with Pt/Norit C was consistent with the high metal dispersion revealed by H₂ chemisorption.

The three catalysts were tested under the same reaction conditions (573 K, 0.25 g of catalyst, and a flow rate of 0.01 cm³min⁻¹) and their performance is summarized in Table 2.2.

Table 2.2. Effect of support on the reaction of heptanoic acid over Pt nanoparticles.

Support	Pressure (bar)	Conversion (%)	Selectivity (%)				
			α -Olefin	i-Olefin	Paraffin	Ketones	Others
Norit Carbon	37	10.3	5.65	61.0	28.4	0.6	4.3
	1	11.1	26.4	55.6	15.3	3.4	0.4
Vulcan Carbon	1	3.5	14.1	64.7	18.5	0.2	2.6
SiC	37	1.6	2.5	19.9	54.7	3.5	19.5
	1	0.5	22.7	0.0	18.6	58.7	0.0

The reaction was run at 573 K, 37 bar for liquid-phase experiments and 1 bar for gas-phase experiments, with 0.25 g of catalyst and a flow rate of 0.01 cm³min⁻¹ composed of 95 wt% heptanoic acid and 5 wt% dodecane.

The most obvious conclusion from Table 2.2 is the highest conversion of heptanoic acid over Pt/Norit C, presumably because of the highest metal dispersion. The results in Table 2.2 also show an effect of the reaction phase on the product selectivity. For Pt/Norit C and Pt/SiC, the selectivity towards the formation of α -olefin was increased in gas-phase reaction at 1 bar compared to the liquid-phase reaction at 37 bar. On Pt/Norit C, internal olefins were the majority product at both liquid-phase and gas-phase conditions. However, the product distribution on Pt/SiC shifted from mostly paraffin (hexane) to mostly ketone after moving from the liquid-phase conditions into the gas-phase. Given the lack of success with preparing highly dispersed Pt on Vulcan C and SiC after reduction at 623 K, and the unfavorable product distributions on Pt/Vulcan C and Pt/SiC, we decided to focus our efforts on studying the behavior of Pt/Norit C.

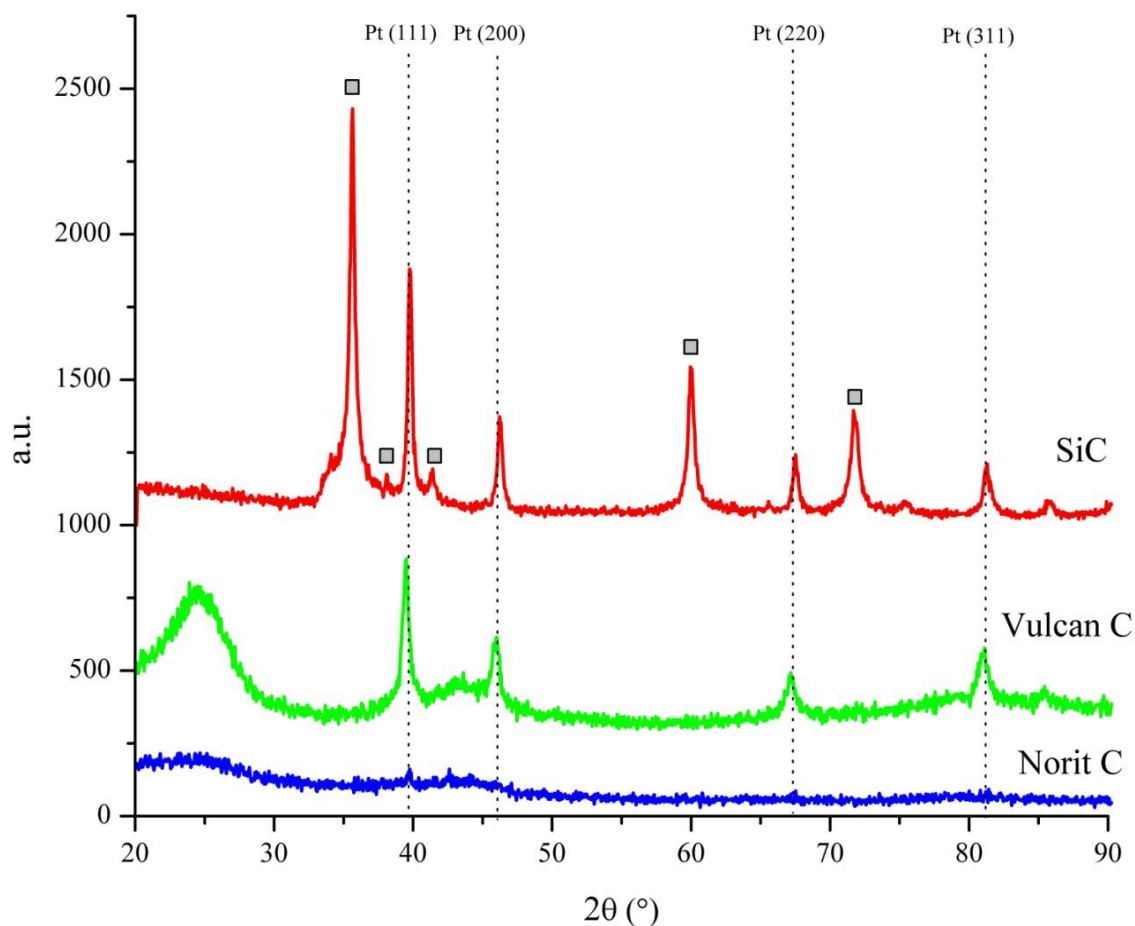


Figure 2.2. Comparison of the XRD patterns of 5 wt% Pt supported on Norit carbon, Vulcan carbon and SiC reduced at 623 K under $100 \text{ cm}^3 \text{ min}^{-1}$ of H_2 at a heating rate of 5 K min^{-1} . ■ represents features of SiC support. The patterns were offset for clarity.

2.3.2. Effect of reduction temperature

Simakova *et al.* [26] previously showed that Pd catalysts with different but high metal dispersions can exhibit different activities and product distributions. However, those catalysts with high dispersions approached similar activity after prolonged reaction times [26].

To obtain different Pt metal dispersions on 3 wt% Pt/Norit C, we reduced the same catalyst at four different temperatures (625, 673, 773 and 873 K) and tested them in the reaction of heptanoic

acid. Table 2.3 summarizes the results of the catalyst characterization by chemisorption, physisorption and electron microscopy.

Although the dihydrogen uptake decreased on the samples reduced at elevated temperatures, electron microscopy revealed very little growth of the small particles (from 2 to 3 nm). These contrasting findings could be the result of some Pt migrating outside of the Norit C pores to form large particles on the external surface. It should be noted that a wider Pt particle size distribution was observed by microscopy, which is consistent with Pt migration on the sample. Figure 2.3 shows the images of the catalysts obtained by TEM.

Table 2.3. Result of the characterization of 3 wt% Pt/Norit C reduced at 4 different temperatures

Reduction Temperature (K)	Metal Dispersion (%)	Pt Particle Size (nm)		Surface Area (m ² g ⁻¹)
		Chemisorption	TEM	
623	49	2.3	1.9 ± 0.2	1477
673	21	5.3	2.1 ± 0.5	1348
773	13	8.9	2.5 ± 0.8	1495
873	13	8.4	3.1 ± 1.0	1374

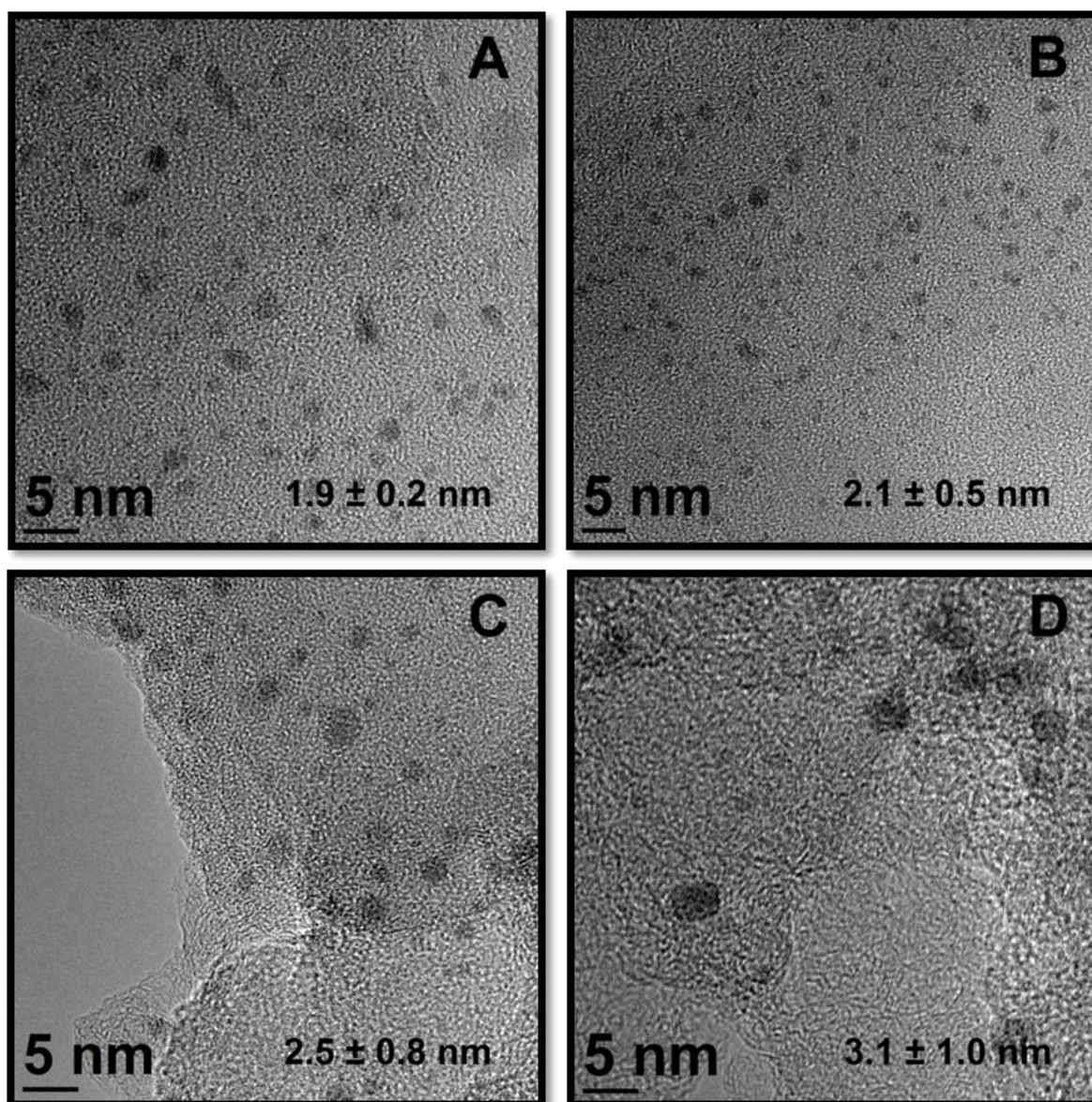


Figure 2.3. TEM images of fresh 3 wt% Pt/Norit C catalyst reduced at four different temperatures. A was reduced at 623 K, B was reduced at 673 K, C was reduced at 773 K, and D was reduced at 873 K.

Conversion of heptanoic acid and product distribution over the catalyst reduced at different temperatures were monitored for 35 h, and the results are presented in Figures 2.4 and 2.5. The catalytic activity and product distribution of the four catalysts did not reach steady state until about 15 to 20 h of reaction. Because of this induction period, the cause of which is unknown, the results in all of the subsequent tables are reported after at least 15 to 20 h of reaction.

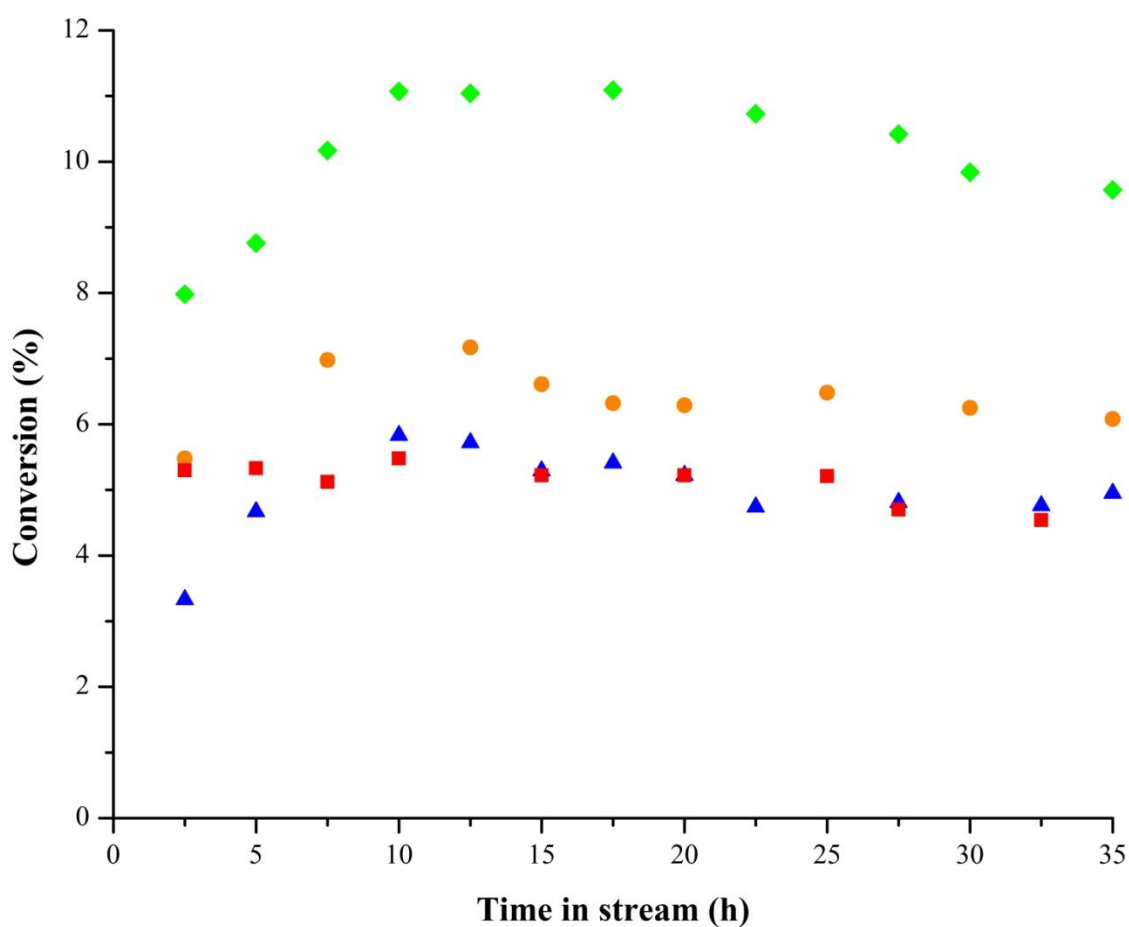


Figure 2.4. Effect of reduction temperature (◆ represents 623 K, ● represents 673 K, ▲ represents 773 K, and ■ represents 873 K) on heptanoic acid conversion over 3 wt% Pt/Norit C. The reactions conditions were 573 K, 37 bar, and $0.01 \text{ cm}^3\text{min}^{-1}$ of feed composed of 95 wt% heptanoic acid and 5 wt% dodecane.

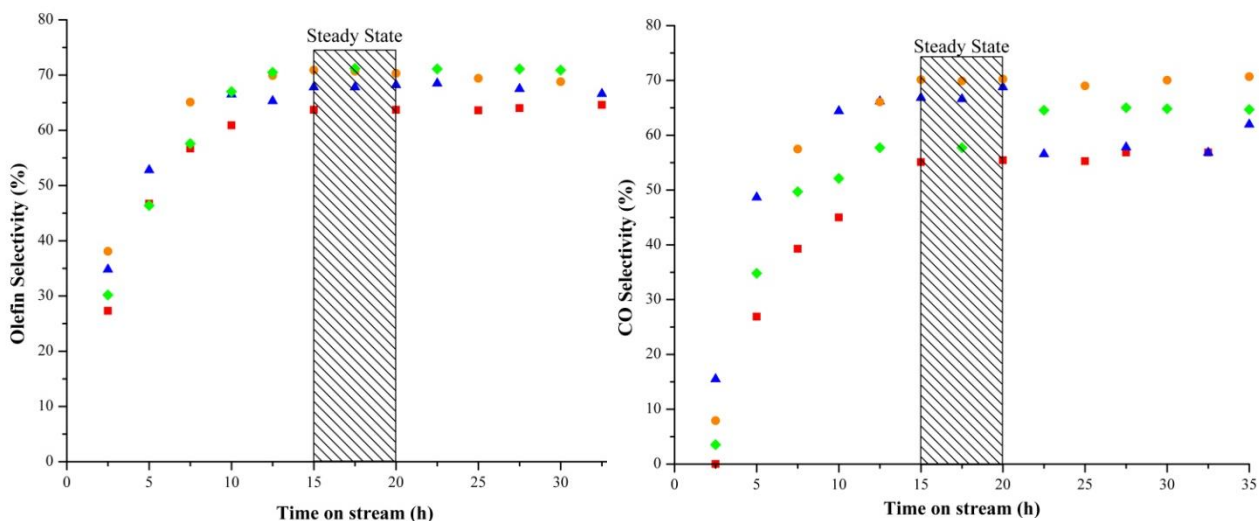


Figure 2.5. Effect of reduction temperature (◆ represents 623 K, ● represents 673 K, ▲ represents 773 K, and ■ represents 873 K) on the olefin (left) and CO (right) selectivity over time during the conversion of heptanoic acid over 3 wt% Pt/Norit C. The reactions conditions were 573 K, 37 bar, and $0.01 \text{ cm}^3\text{min}^{-1}$ of feed composed of 95 wt% heptanoic acid and 5 wt% dodecane. Olefin selectivity is relative to liquid products only and CO selectivity is relative to CO + CO₂.

As expected, increasing the reduction temperature decreased the Pt dispersion, which negatively affected the conversion. However, the TOF associated with the four catalysts was relatively constant at 0.0052 s^{-1} (Table 2.4). The constancy of the TOF suggests that the system was not mass transfer limited since the Koros-Nowak (or Madon-Boudart) criterion is obeyed at this one reaction temperature, which is consistent with the conclusion from mass transfer criteria discussed earlier [27].

Table 2.4 shows that the product distributions in the liquid (olefins and paraffin) and gas (CO and CO₂) over the four catalysts were different. Although this finding differs from the literature, it could be a result of the different conversion levels achieved by each catalyst [26]. Furthermore, the selectivity towards the formation of α -olefin was very low and was most likely due to rapid double bond isomerization over the Pt at the reaction temperature.

Table 2.4. Effect of metal dispersion on the decarbonylation/decarboxylation of heptanoic acid over 3 wt% Pt/Norit C.

Reduction Temperature (K)	Dispersion (%)	TOF (s ⁻¹)	Conversion ^a (%)	Product Selectivity (%)					
				Liquid					Gas
				α -Olefin	i-Olefins	Paraffin	Ketone	Others	CO
623	49	0.0052	9.1	5.2	63.2	27.7	1.2	2.7	58
673	21	0.0051	3.8	5.0	62.9	28.2	1.4	2.5	69
773	13	0.0052	2.4	4.8	61.1	31.5	0.5	1.6	67
873	13	0.0051	2.5	5.0	54.7	34.0	4.0	2.3	55

The reactions conditions were 573 K, 37 bar, 0.01 cm³min⁻¹ of feed composed of 95 wt% heptanoic acid and 5 wt% dodecane. Results were recorded after 20 h of reaction.

^a Background conversion has been removed

2.3.3. Effect of metal loading

Given the non-uniformity of the Pt particle size distribution formed by varying the reduction rate, we decided to test the performance of heptanoic acid conversion over catalysts with different Pt loadings but reduced at the same temperature. Therefore, four catalysts with different metal loadings of 1, 3, 5, and 10 wt% Pt were synthesized and tested at two different reaction temperatures. The results from characterization and reaction testing are summarized in Table 2.5 and Figure 2.6.

Table 2.5. Effect of Pt loading on heptanoic acid reaction over Pt/Norit C at 553 K and 573 K.

Loading (wt % Pt/C)	Dispersion (%)	Pt Particle Size (nm)		Conversion ^a (%)		TOF ^a (s ⁻¹)	
		Chemisorption	TEM	553 K	573K	553 K	573 K
		1.0	28	4.0	1.8 ± 0.4	0.7	1.7
3.0	49	2.3	1.9 ± 0.2	-	9.1	-	0.0052
5.0	31	3.7	1.9 ± 0.3	4.4	8.2	0.0024	0.0045
10.0	39	2.9	2.1 ± 0.5	10.1	24.3	0.0021	0.0051

The catalysts were tested at 37 bar and 0.01 cm³min⁻¹ of feed composed of 95 wt% heptanoic acid and 5 wt% dodecane. Results were recorded after 20 h of reaction.

As expected, the conversion of heptanoic acid increased with the amount of surface Pt in the reactor. The TOF at 553 and 573 K was constant at each temperature over the four different metal loadings tested with an average value of 0.0022 s⁻¹ and 0.0052 s⁻¹, respectively. Furthermore, the TOF obtained at 573 K matched the one obtained over 3 wt% Pt/Norit C reduced at different temperatures (Table 2.4).

Increasing the Pt loading did not considerably increase the Pt particle size but instead increased the number of particles per unit of area, as shown by the TEM images in Figure 2.7. The average Pt particle size obtained by TEM was relatively constant at a value of about 2 nm for all the samples, while the value estimated by H₂ chemisorption varied between 2.3 and 4.0 nm (Table 2.5). Again, this difference might be due to some large Pt particles on the external surface of the pellets that were not observed by microscopy but were accounted for by H₂ chemisorption.

As shown in Figure 2.6, the product selectivity changed as the metal loading and therefore the conversion increased. For example, the overall selectivity towards the formation of olefins decreased at higher conversion; interestingly the relatively low selectivity of α -olefin relative to all olefins (1, 2, and 3-hexenes) remained constant (Figure 2.6).

Due to a lack of reported TOF values for the decarboxylation/decarbonylation reactions over Pt catalysts, we compared our TOF values to those reported for Pd. In general, the TOF obtained with Pt in this study was lower than the TOF reported in the literature for Pd. For example, TOF values over Pd ranged from 0.01 to 0.96 s⁻¹ for batch reaction at 573 K [22–24,28] and from 0.027 to 0.004 s⁻¹ for fixed-bed operation at 543 K [2,13]. As mentioned in the Experimental Methods section, Norit C revealed a low level of background conversion ($\approx 2\%$) at our reaction conditions (573 K, and 0.01 cm³min⁻¹ of feed), which contributed significantly to the observed conversion at low Pt loadings or low Pt dispersions. If the background conversion were not accounted for properly, the TOF for Pt would be artificially inflated. Likewise, for Pd catalysts with low loadings or low dispersions, it is possible that some background conversion on the support could contribute to the high TOF reported in the literature [22,26]. Furthermore, most of the experiments with Pd involved co-feeding H₂ and diluting the fatty acid with long chain hydrocarbons, which have been reported to enhance the TOF and the stability of the catalyst [9,10].

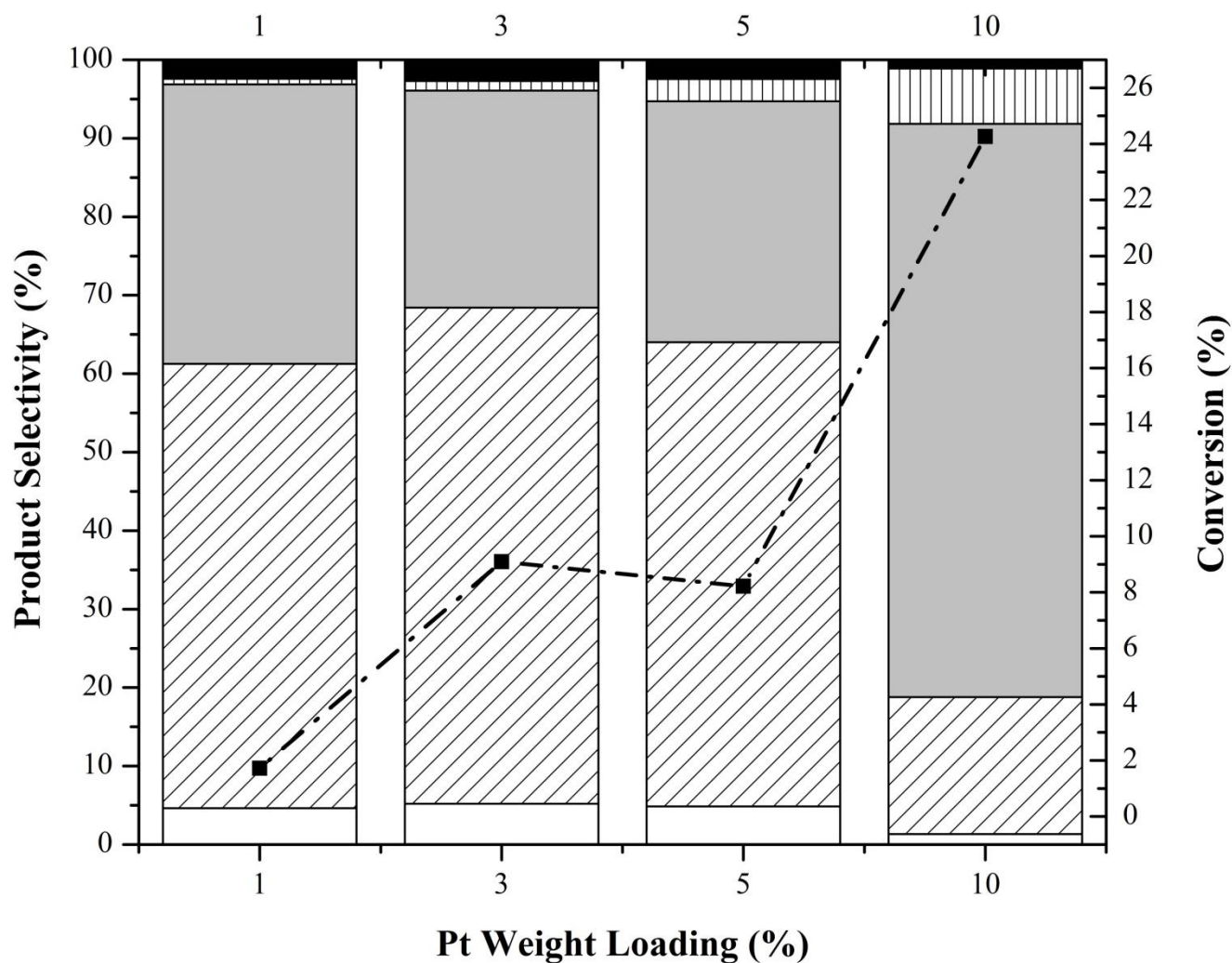


Figure 2.6. Effect of Pt weight loading supported on Norit C on product selectivity and conversion at 573 K, 37 bar, and $0.01 \text{ cm}^3\text{min}^{-1}$ of feed composed of 95 wt% heptanoic acid and 5 wt% dodecane. The product selectivity (%) is represented with color bars and can be read on the left axis. \square represents 1-hexene, ▨ represents 2 and 3-hexenes, ▩ represents hexane, ▧ represents 7-tridecanone, and \blacksquare represents the unknown products. The black squares represent conversion (%) and can be read on the right axis. These results were recorded after 20 h of reaction.

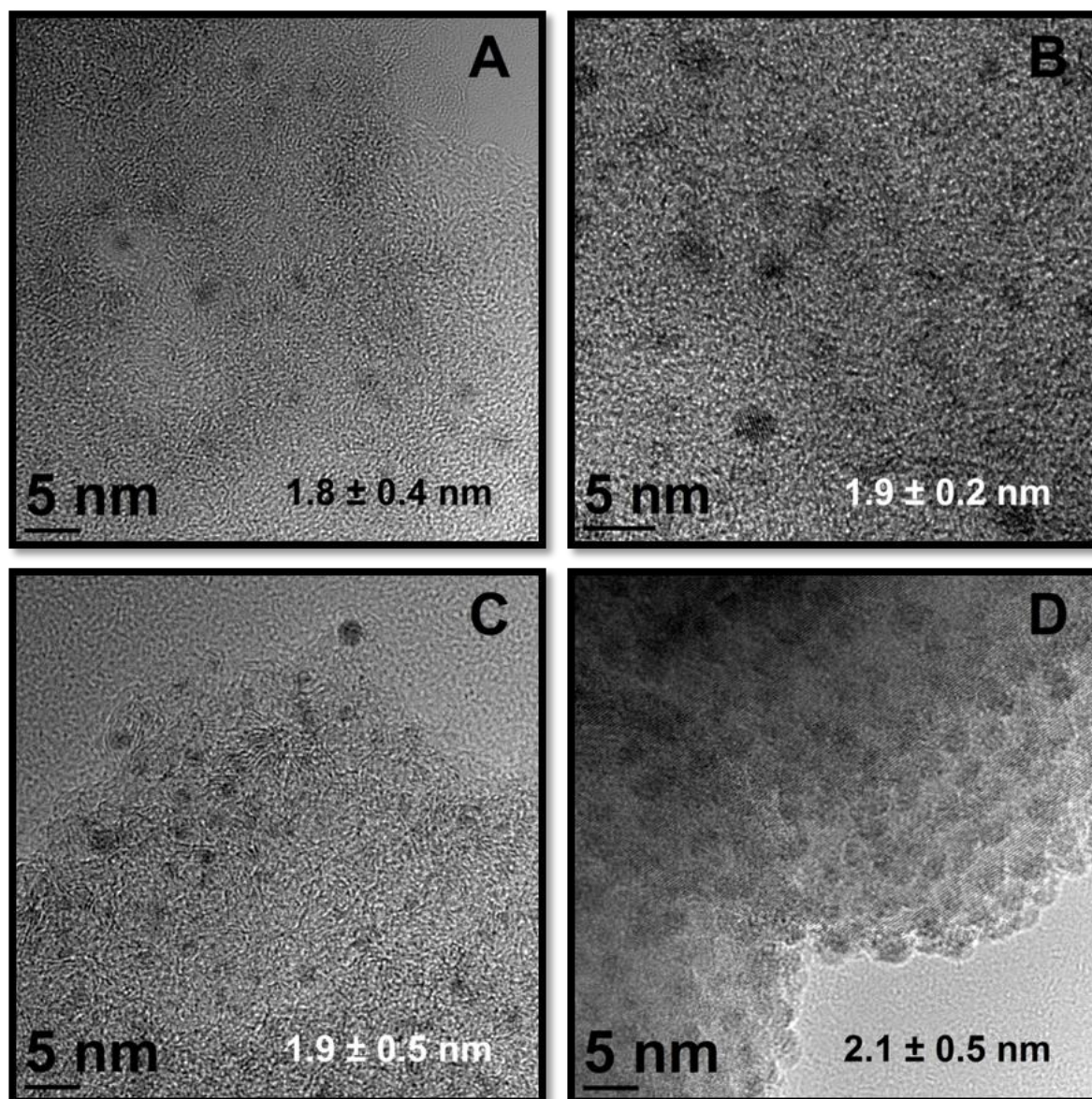


Figure 2.7. TEM images of fresh Pt/Norit C catalysts reduced at identical conditions but with four different Pt loadings. A has 1 wt% loading, B has 3 wt% loading, C has 5 wt% loading, and D has 10 wt% loading.

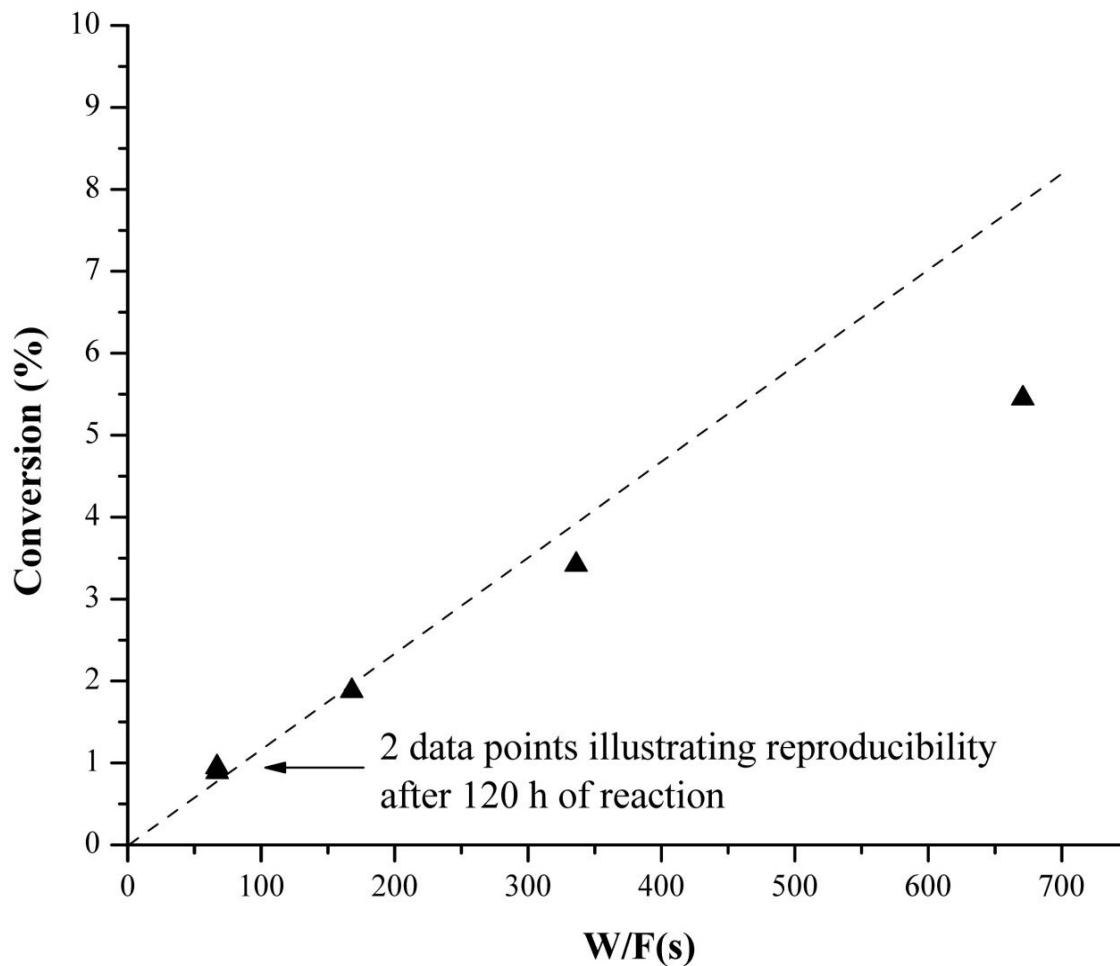


Figure 2.8. Dependence of conversion of heptanoic acid at different flow rates over 10 wt% Pt/Norit C at 573 K and 37 bar. These results were recorded after 20 h of reaction. The W/F was calculated as the weight of catalyst used divided by the mass flow rate.

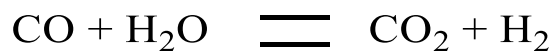
2.3.4. Effect of flow rate

To minimize the impact of support activity on the results, we chose to study a 10 wt% Pt/Norit C catalyst at various flow rates of heptanoic acid to explore the influence of conversion on the product distribution. The feed flow rate was varied from 0.005 to 0.05 $\text{cm}^3\text{min}^{-1}$ over a period of 120 h (\approx 2200 turnovers) to obtain a range of conversion values. Figure 2.8 shows the relationship between space time and conversion, which was fairly linear at low conversion. At higher conversions, however, the catalyst appeared to be less active than expected, which might be evidence for inhibition

by product CO on the Pt sites. The conversion at very short space time was reproduced after 120 h of reaction, confirming that a long term deactivation process was not significant during the course of this particular experiment. If the Pt metal nanoparticles sintered under reaction conditions, particle growth must have occurred during the initial induction period.

Figure 2.9 shows a very strong correlation of the product selectivity to conversion. Extrapolation of the product selectivity for gaseous products (CO + CO₂) to zero conversion indicates 80% of the gas product is CO. Likewise, extrapolation of the liquid-phase products to zero conversion results in 80% selectivity to olefins. Evidently, the initial reaction of heptanoic acid under these conditions is mainly decarbonylation. The very low selectivity to α -olefins was the result of rapid isomerization of the double bond in 1-hexene over Pt to form 2- and 3-hexenes.

With increasing conversion, the selectivity for CO decreased more extensively than the selectivity for olefins, suggesting there is a side reaction that converts CO into CO₂. A likely side reaction is the water-gas shift (WGS) reaction shown in Scheme 2.4, which is believed to play an important role in the decarbonylation/decarboxylation reactions, not only for converting CO into CO₂, but for providing a source of H₂ that can hydrogenate the olefins into paraffin [23,24]. In contrast, Lestari *et al.* theorized that CO is actually formed from CO₂ in the reverse water-gas shift reaction, rather than by direct decarbonylation reaction of fatty acids [29]. Our results in Figure 2.9 clearly support the idea that decarbonylation was the primary reaction on Pt metal nanoparticles under our experimental conditions. The fact that the fraction of olefins in the liquid products exceeded the fraction of CO in the gaseous products at increasing conversions (Figure 2.9) suggests that the WGS reaction occurs more readily than the hydrogenation of olefins using H₂ produced by WGS. Figure 2.9 also shows that selectivity of α -olefins (1-hexene) in the liquid product was always less than about 10%, even at very low conversions. Evidently, the double bond isomerization of 1-hexene to 2- and 3-hexenes was rapid over Pt catalysts in the liquid-phase conversion of heptanoic acid at 573 K.



Scheme 2.4. Water-gas shift (WGS) reaction

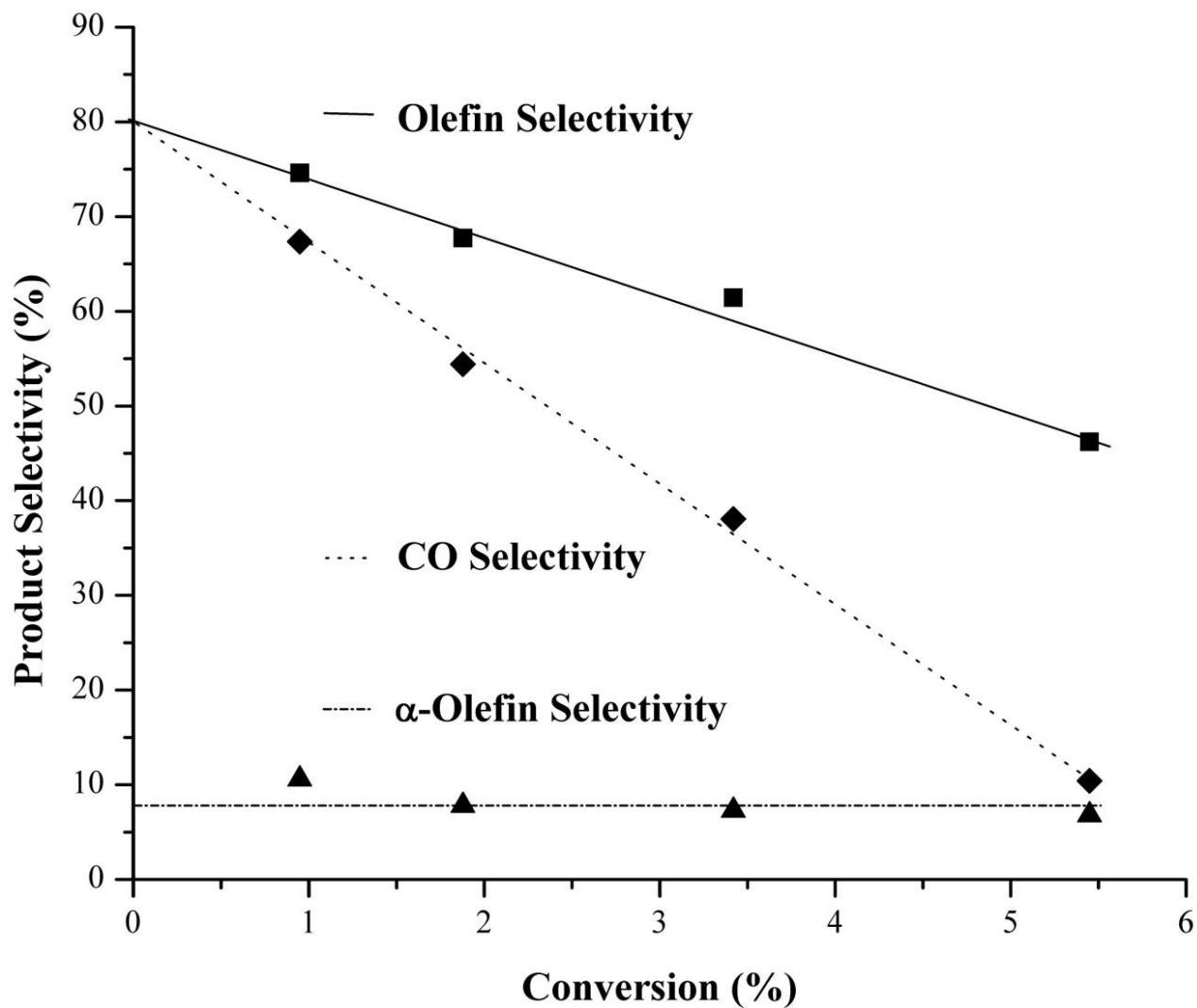


Figure 2.9. Dependence of decarbonylation product selectivity on conversion over 10 wt% Pt/Norit C at 573 K and 37 bar. ■ represents the selectivity to decarbonylation products, olefins, in the liquid product. ♦ represents the selectivity to decarbonylation product, CO, in the gas product. ▲ represents the selectivity to α -olefins in the liquid product. These results were recorded after 20 h of reaction.

2.3.5. Effect of pressure

Previous studies showed that the formation rate of alkene did not match that of CO [2,22]. Our results clearly show that reactions of the primary products, α -olefin, CO (and presumably H₂O), proceed at rates that are quite rapid. The formation of CO₂ and H₂ via the water-gas shift reaction, which is then followed by hydrogenation of olefin to paraffin, might account for the product distribution at higher conversion. Although the conversion of heptanoic acid was not mass transfer limited with respect to the acid, it is possible that rapid conversion of the primary products in the catalyst pores might be limited by mass transfer rates out of the catalyst particles. To increase the effective diffusivity and external mass transfer coefficient of the molecules, we performed exactly the same reaction experiments at 1 bar pressure, which allows the major products and heptanoic acid to remain in the gas-phase.

Figure 2.10 compares the performance of Pt/Norit C with different metal loadings and system pressures. For operation with liquid-phase reactant (37 bar), the main products at high conversions (> 20%) were hexane and CO₂. At lower conversions, mostly olefins were produced, although they were mainly 2 and 3 hexenes formed from double bond isomerization of 1-hexene. When the reaction was run at low pressure (1 bar) resulting in gas-phase conditions in the reactor, the selectivity towards the formation of α -olefin was higher than that in the liquid-phase. Moreover, higher metal loadings in the catalyst pores facilitated subsequent conversion of the α -olefin to the internal olefins, even at low pressure. Figure 2.10 also shows that lowering the conversion by increasing the reactant flow rate improved selectivity to α -olefin, which is expected when α -olefin is a primary product of decarbonylation.

It should be noted that the conversion of heptanoic acid over the three different Pt catalysts did not correlate with the surface Pt when operated in the gas-phase, which contrasts the direct relation observed in the liquid-phase, as reported in Figure 2.10 and Table 2.5. We attribute the observed behavior of Pt catalysts in gas phase operation to significant deactivation, which is discussed in the next section.

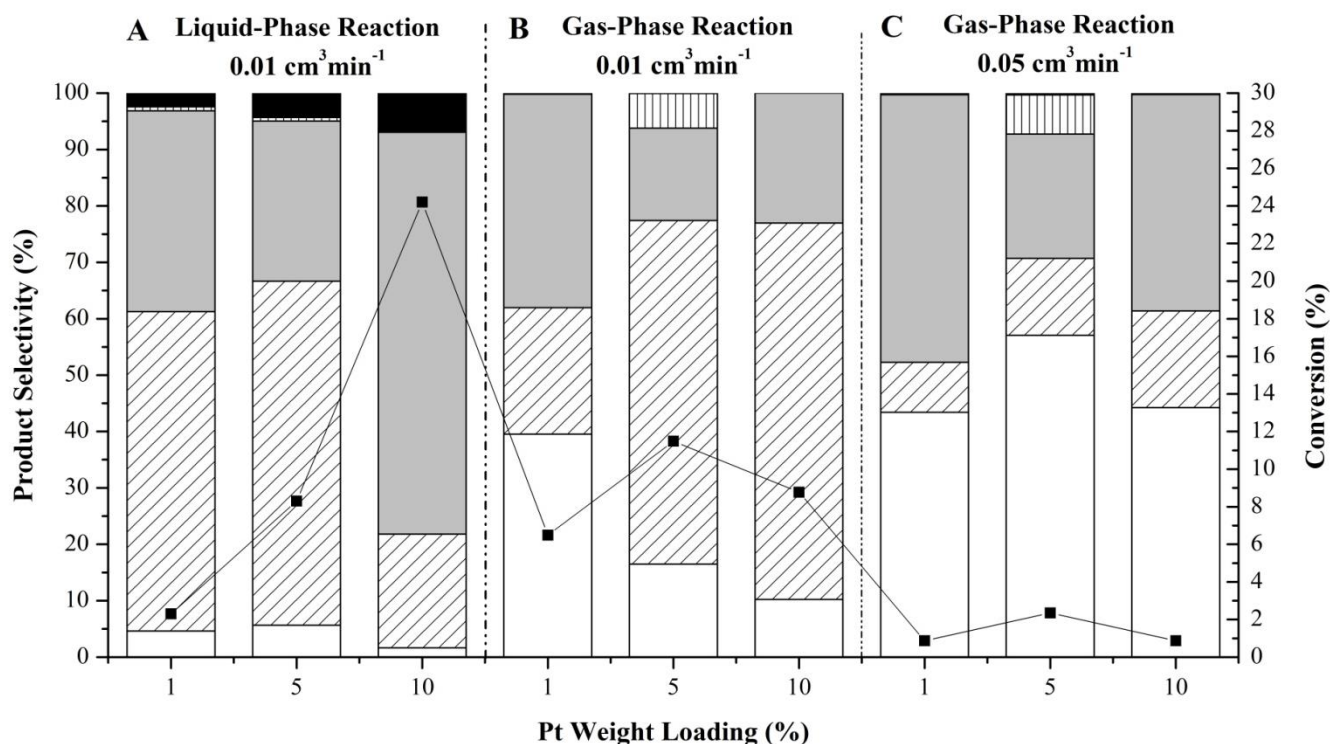


Figure 2.10. Effect of reaction pressure and feed flow rate on catalyst activity and product distribution over Pt/Norit C with different loadings of Pt during the conversion of heptanoic acid at 573 K. The feed composition was 95 wt% heptanoic acid and 5 wt% dodecane. The color bars can be read on the left axis and represents the product distribution. □ represents 1-hexene, ▨ represents 2-3-hexenes, ▩ represents hexane, ▤ represents 7-tridecanone, and ■ represents the unknown products. The black squares represent conversion (%) and can be read on the right axis. These results were recorded after 20 h of reaction. Figure A was run in liquid phase (37 bar) conditions and flow rate of 0.01 cm³min⁻¹. Figure B was run in gas phase (1 bar) conditions and a flow rate of 0.01 cm³min⁻¹. Figure C was run in gas phase (1 bar) conditions and a flow rate of 0.05 cm³min⁻¹.

2.3.6. Catalyst deactivation

Catalyst deactivation during the deoxygenation of carboxylic acids has been widely reported in the literature. Snåre *et al.* [10] and Mäki-Arvela *et al.* [13] suggested that deactivation originated from poisoning of the metal by the reactants, products (especially CO), and coking. Furthermore, Simakova *et al.* reported that deactivating aromatics are formed in reactions performed under H₂-scarce conditions [30]. The initial concentration of carboxylic acid is also proposed to influence catalyst deactivation. Mäki-Arvela *et al.* observed that deactivation was more extensive with higher initial concentration of carboxylic acid [13].

Ping *et al.* imaged Pd nanoparticles supported on silica with TEM before and after reaction [31]. The catalyst did not show a significant increase in metal particle size after reaction indicating negligible metal sintering occurred. Since most of the catalyst activity was regained after hot extraction with solvent and subsequent reduction in H₂ at 573 K, the authors concluded that the observed deactivation resulted from deposition of organic molecules onto the active sites [31].

Figure 2.11 summarized catalyst performance after several changes in reaction conditions to study the deactivation phenomenon. Although our studies revealed stable operation of Pt/Norit C up to 120 h of operation with the liquid-phase reactant, we observed significant deactivation during gas-phase operation at 1 bar. For this series of experiments, the catalyst was assumed to be at steady state after prolonged liquid-phase reaction. At this point, the pressure was lowered to 1 bar to begin operation in the gas phase. Although the conversion decreased after the phase change, catalyst deactivation continued to lower conversion with time. After 40 h of gas-phase operation, the catalyst deactivated to half its activity at the time of the phase change. The pressure was then increased to return to liquid-phase operation. After 20 h of steady state operation in liquid-phase conditions, the catalyst activity remained low, indicating the liquid-phase flow was unable to recover the original activity.

The deactivated catalyst was finally exposed to flowing heptanoic acid at 350 K at 1 bar for 24 h to remove possible products from the surface. The reactor was then flushed with N₂ and heated at 5 K

min^{-1} to reaction temperature. Since the catalyst activity was not regained by this treatment, the catalyst was also re-reduced in flowing H_2 at 623 K and 1 bar for 4 h, but again the activity was not recovered. A mild oxidation treatment of the catalyst in air at 623 K and 1 bar for 4 h followed by a re-reduction in flowing H_2 at 623 K and 1 bar for 4 h also did not re-activated the catalyst. Clearly, the mode of deactivation was not easily reversed by standard regeneration methods.

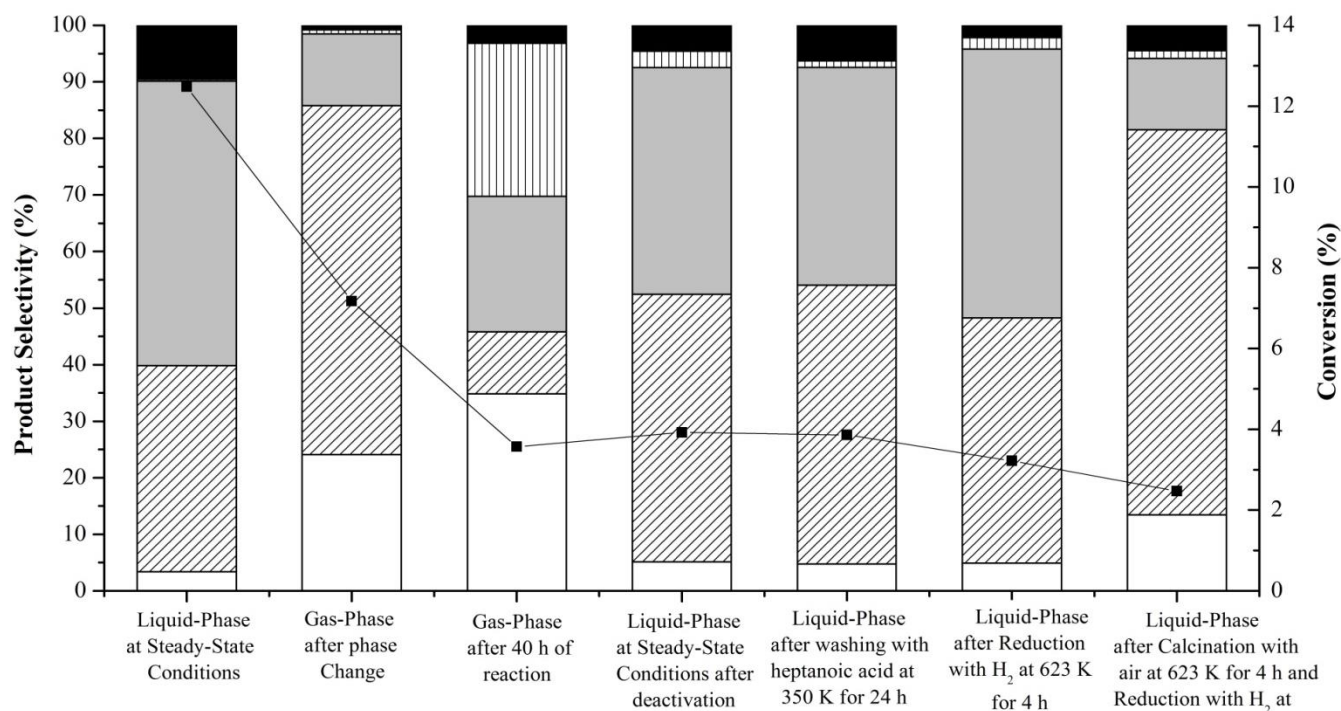


Figure 2.11. Effect of deactivation on catalyst activity and product distribution over 10 wt% Pt/Norit C during the conversion of heptanoic acid at 573 K and a feed flow rate of $0.01 \text{ cm}^3 \text{ min}^{-1}$ composed of 95 wt% heptanoic acid and 5 wt% dodecane. The bars with patterns represents the product distribution and can be read on the left axis. \square represents 1-hexene, \square represents 2-3-hexenes, \square represents hexane, \square represents 7-tridecanone, and \blacksquare represents the unknown products. The black squares represent conversion (%) and can be read on the right axis. These results were recorded after 20 h of reaction.

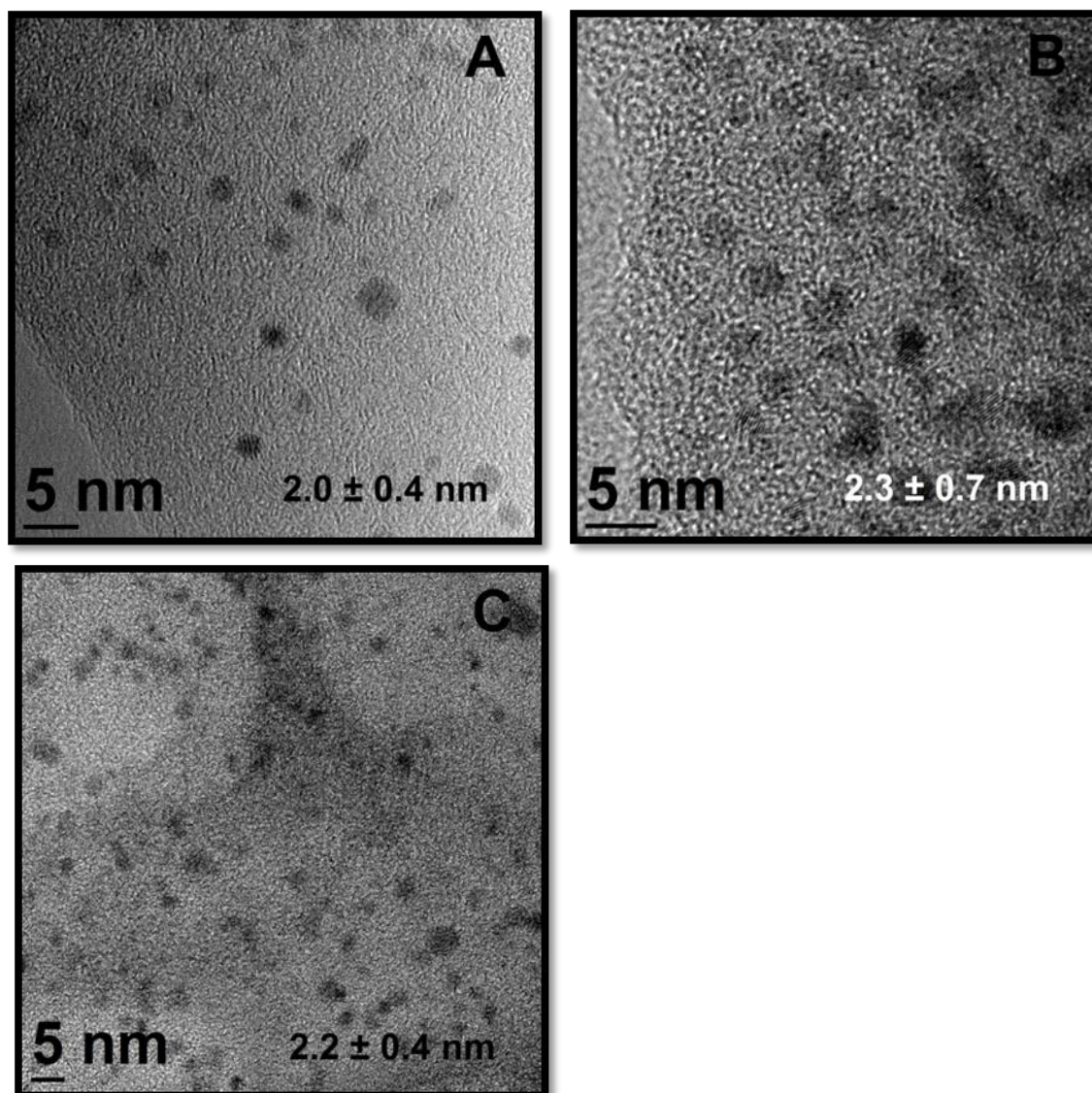


Figure 2.12. TEM images of spent Pt/Norit C catalysts. The catalysts were prepared by IWI and reduced with H_2 at 623 K at a heating rate of 5 K min^{-1} . A represents a spent sample of 1 wt% Pt, B represents a spent sample of 5 wt% Pt, and C represent a spent sample of 10 wt% Pt. The spent samples were first run in liquid-phase operation until steady-state operation and then they were run in gas-phase operation until deactivation. At that point in time, the spent samples were recovered from the reactor and treated as described in the Experimental Methods section. The spent catalysts were collected after a total of 80 h under reaction conditions.

Figure 2.12 shows high magnification TEM images of three Pt/Norit C catalysts with different weight loadings after 80 h of reaction in gas-phase operation conditions, and they did not reveal substantial particle growth compared to the fresh samples shown in Figure 2.7. In contrast, XRD patterns of the catalyst before and after reaction presented in Figure 2.13 suggested the presence of some large Pt particles on the spent catalysts. The resulting average particle size of the spent catalyst was estimated with the Scherrer equation to be 19 nm. The migration and sintering of Pt would explain why the various attempts at catalyst regeneration were unsuccessful. The sintering of Pt particles was not observed in Figure 2.12 because the images were associated with very thin areas of the sample to obtain good contrast for imaging. We speculate that the large Pt particles reside outside the small pores of the carbon support. Indeed, the small Pt particles of 2 to 3 nm observed in Figure 2.12 probably reside inside the highly porous structure Norit C which likely inhibited particle growth inside the pores.

Figure 2.14 presents a schematic depicting of our working hypothesis for deactivation of the Pt particles during reaction. What is apparently unknown at this point is why gas-phase operation facilitates deactivation compared to liquid-phase operation. We hypothesize that some organic species are strongly absorbed on the Pt particles after gas-phase operation.

Although metal sintering observed by XRD might occur very early during the reaction, which might account for the lower TOF reported here for Pt (which is based on dispersion of a freshly prepared catalyst), the constancy of TOF in liquid-phase operation with metal loading suggests that most of the Pt remained highly dispersed. Nevertheless a difference in metal particle size between the fresh catalyst and the spent catalyst might explain the rather low TOF reported in this work, which is based on initial Pt dispersion.

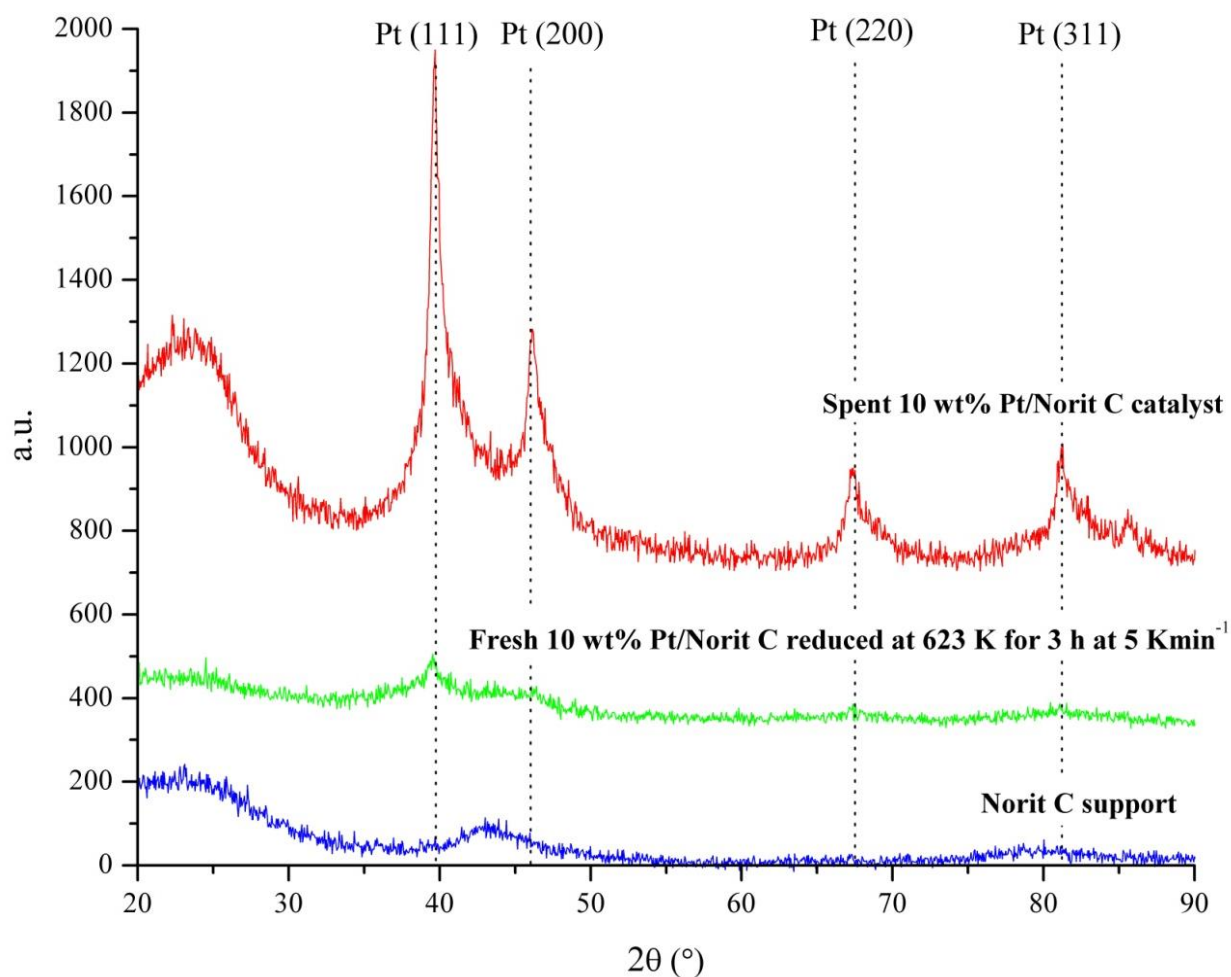


Figure 2.13. Comparison of the XRD patterns of Norit C support, fresh 10 wt% Pt/Norit C after reduction, and spent 10 wt% Pt/Norit C after reaction. The spent sample was first run in liquid-phase operation until steady-state operation and then it was run in gas-phase operation until deactivation. At that point, the spent sample was recovered from the reactor and treated as described in the Experimental Methods section. The spent catalyst was collected after a total of 80 h under reaction conditions. The patterns were offset for clarity.

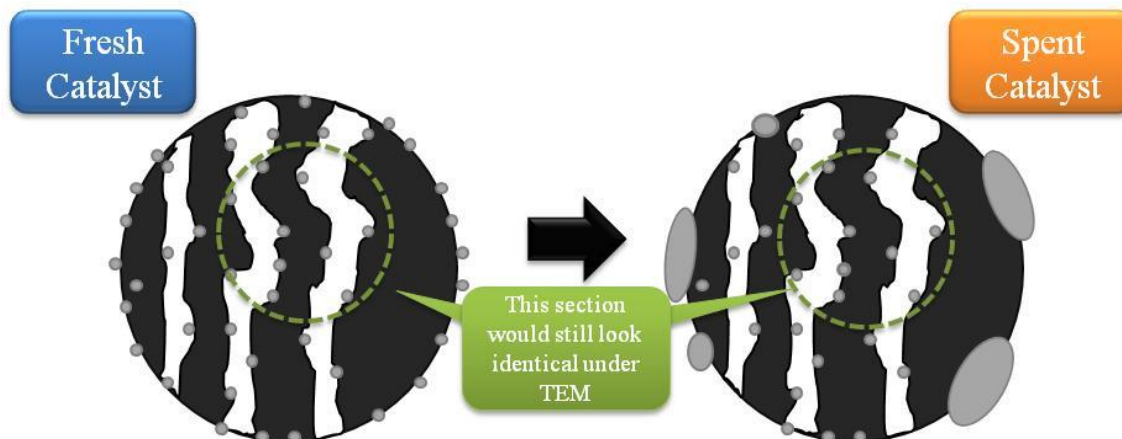


Figure 2.14. Schematic depiction of working hypothesis for catalyst sintering.

2.4. Conclusions

Platinum nanoparticles were supported on Norit carbon, Vulcan carbon and silicon carbide, characterized by chemisorption, X-ray diffraction and electron microscopy, and evaluated in the conversion of heptanoic acid at 573 K. Results from characterization and reactivity confirmed that highly dispersed Pt was formed in Norit carbon (dispersion \approx 49%) after a mild reduction treatment at 623 K. Similar treatment of Pt/Vulcan carbon and Pt/SiC resulted in the formation of much larger particles of Pt. Variations of Pt dispersion, Pt loading and reactor space time were used to explore the influence of conversion on product distribution during heptanoic acid conversion over Pt/Norit C. In summary, decarbonylation of heptanoic acid was the primary reaction to produce olefin, CO and water. Rapid conversion of α -olefin to internal olefin was observed in liquid-phase operation, even at low conversion. Higher selectivity to α -olefin product was achieved by operation in the gas phase, presumable because of the greater rate of mass transfer of product molecules out of the catalyst pores. Although various criteria indicated the rate of heptanoic acid conversion was not limited by mass transfer, subsequent reactions of the products could be. Higher conversion of heptanoic acid in liquid-phase operation also was accompanied by sequential conversion of CO to CO₂, presumably via water-gas shift reaction. In addition, hydrogenation of olefin was observed at higher conversion as expected from H₂ generated by the WGS reaction. A summary of the reaction network observed here is provided in Figure 2.15.

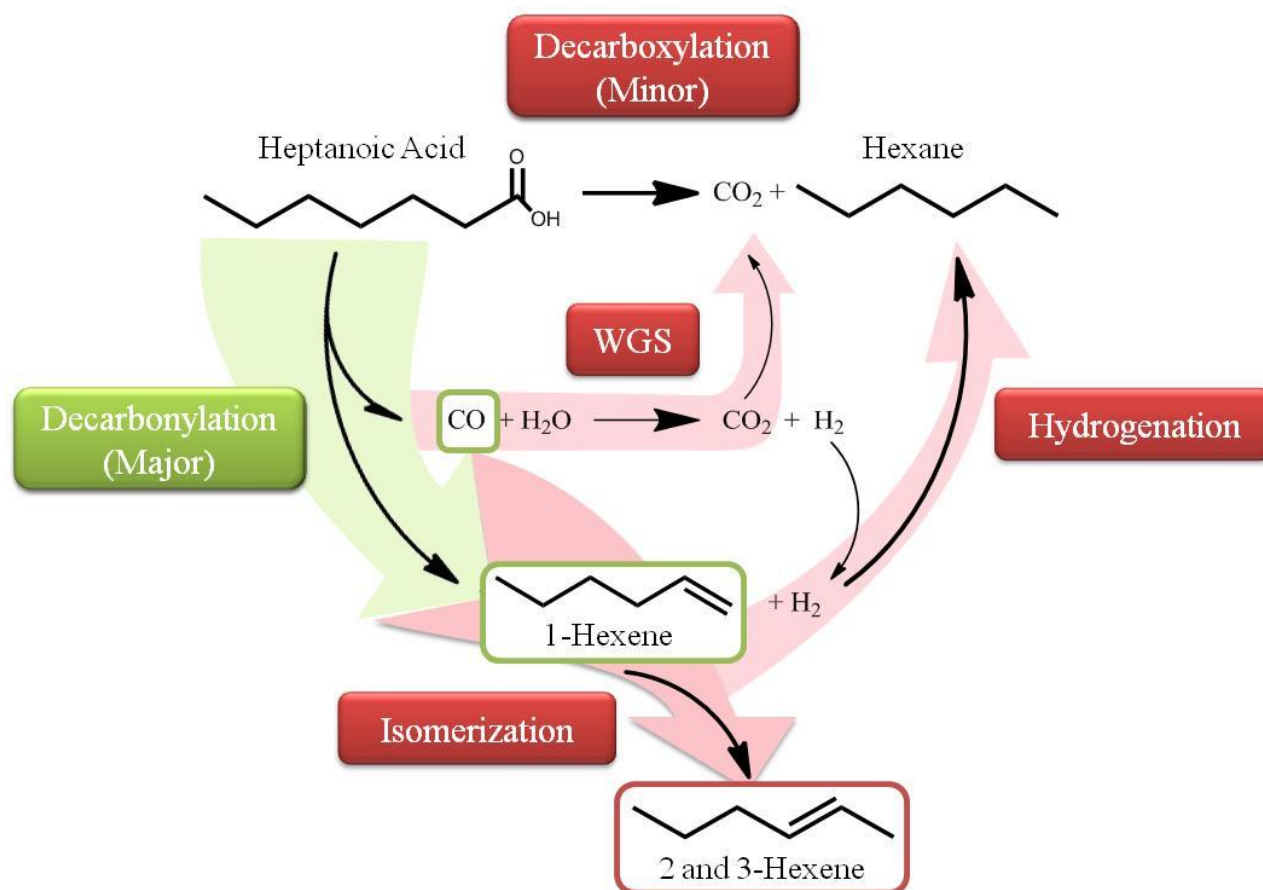


Figure 2.15. Reaction network for the decarbonylation/decarboxylation of heptanoic acid over supported Pt at low conversion levels.

2.5.Acknowledgement

This material is based upon work supported by the National Science Foundation (NSF) under Award No. EEC-0813570. Any opinions, findings, and conclusions or recommendations expressed in this material are those of the author(s) and do not necessarily reflect the views of the NSF. We acknowledge discussions with Professor Matthew Neurock at the University of Virginia, Dr. Hien Pham and Professor Abhaya Datye at the University of New Mexico. We also gratefully acknowledge the help of Mr. Richard White and Mr. Matthew Schneider at the University of Virginia for their help with the TEM.

2.6. References

- [1] Snåre, M., Kubičková, I., Mäki-Arvela, P., Eränen, K., and Murzin, D. Y., 2006, “Heterogeneous Catalytic Deoxygenation of Stearic Acid for Production of Biodiesel,” *Ind Eng Chem Res*, **45**(45), pp. 5708–5715.
- [2] Lestari, S., Mäki-Arvela, P., Bernas, H., Simakova, O., Sjöholm, R., Beltramini, J., Lu, G. Q. M., Myllyoja, J., Simakova, I., and Murzin, D. Y., 2009, “Catalytic Deoxygenation of Stearic Acid in a Continuous Reactor over a Mesoporous Carbon-Supported Pd Catalyst,” *Energ Fuel*, **23**(8), pp. 3842–3845.
- [3] Miller, J. A., Nelson, J. A. J. A., and Byrne, M. P., 1993, “A Highly Catalytic and Selective Conversion of Carboxylic Acids to 1-Alkenes of One Less Carbon Atom,” *J Org Chem*, **58**(1), pp. 18–20.
- [4] Maier, W. F., Roth, W., Thies, I., v. Rague Schleyer, P., Ragukschleyer, P., and Schleyer, R., 1982, “Gas Phase Decarboxylation of Carboxylic Acids,” *Chem Ber*, **115**, pp. 808–812.
- [5] Morgan, T., Grubb, D., Santillan-Jimenez, E., Crocker, M., and Crocker, E. S. M., 2010, “Conversion of Triglycerides to Hydrocarbons Over Supported Metal Catalysts,” *Top Catal*, **53**(11-12), pp. 820–829.
- [6] Santillan-Jimenez, E., Morgan, T., Lacny, J., Mohapatra, S., and Crocker, M., 2012, “Catalytic deoxygenation of triglycerides and fatty acids to hydrocarbons over carbon-supported nickel,” *Fuel*, **103**(September), pp. 1010–1017.
- [7] Renz, M., 2005, “Ketonization of Carboxylic Acids by Decarboxylation: Mechanism and Scope,” *Eur J Org Chem*, **2005**(6), pp. 979–988.

- [8] Gaertner, C. A., Serrano-Ruiz, J. C., Braden, D. J., and Dumesic, J. A., 2009, "Catalytic coupling of carboxylic acids by ketonization as a processing step in biomass conversion," *J Catal*, **266**(1), pp. 71–78.
- [9] Snåre, M., Kubičková, I., Mäki-Arvela, P., Eränen, K., Wärnå, J., and Murzin, D. Y., 2007, "Production of diesel fuel from renewable feeds : Kinetics of ethyl stearate decarboxylation," *Chem Eng J*, **134**, pp. 29–34.
- [10] Snåre, M., Kubičková, I., Mäki-Arvela, P., Chichova, D., Eränen, K., and Murzin, D. Y., 2008, "Catalytic deoxygenation of unsaturated renewable feedstocks for production of diesel fuel hydrocarbons," *Fuel*, **87**(6), pp. 933–945.
- [11] Patterson, A. L., 1939, "The Scherrer Formula for X-Ray Particle Size Determination," *Phys Rev*, **56**, pp. 978–982.
- [12] Pham, H. N., Pagan-Torres, Y. J., Serrano-Ruiz, J. C., Wang, D., Dumesic, J. A., and Datye, A. K., 2011, "Improved hydrothermal stability of niobia-supported Pd catalysts," *Appl Catal A-Gen*, **397**(1-2), pp. 153–162.
- [13] Mäki-Arvela, P., Snåre, M., Eränen, K., Myllyoja, J., and Murzin, D. Y., 2008, "Continuous decarboxylation of lauric acid over Pd/C catalyst," *Fuel*, **87**(17-18), pp. 3543–3549.
- [14] Gaertner, C. A., Serrano-Ruiz, J. C., Braden, D. J., and Dumesic, J. A., 2010, "Ketonization Reactions of Carboxylic Acids and Esters over Ceria–Zirconia as Biomass-Upgrading Processes," *Ind Eng Chem Res*, **49**(13), pp. 6027–6033.
- [15] Boudart, M., 1995, "Turnover Rates in Heterogeneous Catalysis," *Chem Rev*, **95**, pp. 661–666.

- [16] Weisz, P. B., and Prater, C. D., 1954, "Interpretation of Measurements in Experimental Catalysis," *Adv Catal*, **6**, pp. 143–196.
- [17] Davis, M. E., and Davis, R. J., 2012, *Fundamentals of Chemical Reaction Engineering*, Dover Publications, Mineola, New York.
- [18] Cussler, E. L., 2009, *Diffusion: Mass Transfer in Fluid Systems*, Cambridge University Press, New York.
- [19] Simakova, I., Simakova, O., Mäki-Arvela, P., and Murzin, D. Y., 2010, "Decarboxylation of fatty acids over Pd supported on mesoporous carbon," *Catal Today*, **150**(1-2), pp. 28–31.
- [20] Lestari, S., Simakova, I., Tokarev, A., Mäki-Arvela, P., Eränen, K., and Murzin, D. Y., 2008, "Synthesis of Biodiesel via Deoxygenation of Stearic Acid over Supported Pd / C Catalyst," *Catal Lett*, **122**(3-4), pp. 247–251.
- [21] Bernas, H., Eränen, K., Simakova, I., Leino, A.-R., Kordás, K., Myllyoja, J., Mäki-Arvela, P., Salmi, T., and Murzin, D. Y., 2010, "Deoxygenation of dodecanoic acid under inert atmosphere," *Fuel*, **89**(8), pp. 2033–2039.
- [22] Mäki-Arvela, P., Kubičková, I., Snåre, M., Eränen, K., and Murzin, D. Y., 2007, "Catalytic Deoxygenation of Fatty Acids and Their Derivatives," *Energ Fuel*, **21**(1), pp. 30–41.
- [23] Immer, J. G., Kelly, M. J., and Lamb, H. H., 2010, "Catalytic reaction pathways in liquid-phase deoxygenation of C18 free fatty acids," *Appl Catal A-Gen*, **375**(1), pp. 134–139.
- [24] Immer, J. G., and Lamb, H. H., 2010, "Fed-Batch Catalytic Deoxygenation of Free Fatty Acids," *Energ Fuel*, **130**(10), pp. 5291–5299.

- [25] Su, B., Wang, K., Cheng, T., and Tseng, C., 2012, "Preparation of PtSn / C electrocatalysts with improved activity and durability toward oxygen reduction reaction by alcohol-reduction process," *Mater Chem Phys*, **135**(2-3), pp. 395–400.
- [26] Simakova, I., Simakova, O., Mäki-Arvela, P., Simakov, A., Estrada, M., and Murzin, D. Y., 2009, "Deoxygenation of palmitic and stearic acid over supported Pd catalysts: Effect of metal dispersion," *Appl Catal A-Gen*, **355**, pp. 100–108.
- [27] Madon, R. J., and Boudart, M., 1982, "Experimental Criterion for the Absence of Artifacts in the Measurements of Rates of Heterogeneous Catalytic Reactions," *Ind Eng Chem Fundam*, (21), pp. 438–447.
- [28] Kubičková, I., Snåre, M., Eränen, K., Mäki-Arvela, P., and Murzin, D., 2005, "Hydrocarbons for diesel fuel via decarboxylation of vegetable oils," *Catal Today*, **106**(1-4), pp. 197–200.
- [29] Lestari, S., Mäki-Arvela, P., Simakova, I., Beltramini, J., Lu, G. Q. M., and Murzin, D. Y., 2009, "Catalytic Deoxygenation of Stearic Acid and Palmitic Acid in Semibatch Mode," *Catal Lett*, **130**(1-2), pp. 48–51.
- [30] Simakova, I., Rozmysłowicz, B., Simakova, O. A., Mäki-Arvela, P., Simakov, A., and Murzin, D. Y., 2011, "Catalytic Deoxygenation of C18 Fatty Acids Over Mesoporous Pd / C Catalyst for Synthesis of Biofuels," *Top Catal*, **54**(8-9), pp. 460–466.
- [31] Ping, E. W., Pierson, J., Wallace, R., Miller, J. T., Fuller, T. F., and Jones, C. W., 2011, "On the nature of the deactivation of supported palladium nanoparticle catalysts in the decarboxylation of fatty acids," *Appl Catal A-Gen*, **396**(1-2), pp. 85–90.

Chapter 3. Reactivity and Stability of Supported Pd Nanoparticles during the Liquid-Phase and Gas-Phase Decarbonylation of Heptanoic Acid

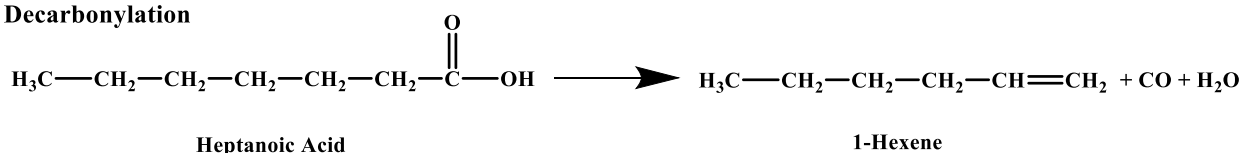
Abstract

The liquid-phase and gas-phase decarbonylation of heptanoic acid over carbon- and silica-supported Pd nanoparticles was studied in a continuous flow fixed bed reactor at 573 K. The liquid-phase turnover frequency (TOF) under steady state conditions (>20 h) was very low at $\approx 0.00070 \text{ s}^{-1}$, presumably because of deposition of carbonaceous species and in some cases sintering of the metal particles, as revealed by H_2 chemisorption, X-ray diffraction and electron microscopy. The steady-state rate was independent of the support composition, synthesis method, Pd loading (1 to 20 wt%), and acid concentration (0.1 to 6.6 M). Although the gas-phase reaction led to deactivation of the supported Pd catalysts, extrapolation of the rate to initial time gave a TOF of $\approx 0.035 \text{ s}^{-1}$ at 573 K. The liquid- and gas-phase reactions at low conversion levels were selective towards the formation of decarbonylation products such as CO and hexenes. Higher conversion levels resulted in the subsequent conversion of the primary decarbonylation products. *Postmortem* analysis of the catalysts revealed that concentrated, liquid-phase heptanoic acid at 573 K severely sintered the Pd nanoparticles supported on carbon but not those supported on silica. The Pd nanoparticles were able to maintain the high dispersion on carbon when exposed to low concentrations of liquid-phase heptanoic acid or gaseous heptanoic acid at 573 K.

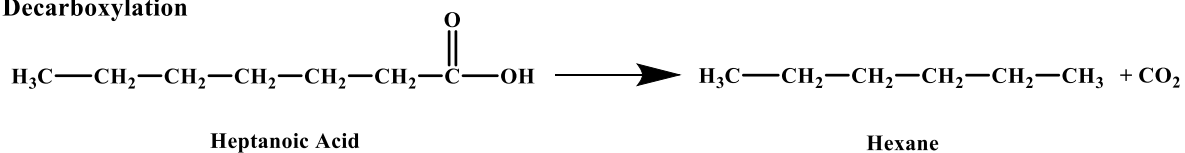
3.1. Introduction

Biomass is an abundant, carbon-neutral alternative resource to fossil fuels for the production of fuels and chemicals. Processing of biomass presents a chemical challenge because it often contains excess oxygen that needs to be removed [1]. Dehydration, ketonization, decarbonylation and decarboxylation comprise a set of transformations collectively regarded as deoxygenation reactions. Organic acids, such as carboxylic acids, are biomass-derived molecules that can be readily converted to hydrocarbons by deoxygenation reactions. As shown in Scheme 3.1, linear carboxylic acids can be converted into linear olefins and paraffins by decarbonylation and decarboxylation, respectively. Ketonization is also an important reaction for the production of fine chemicals and fuels [2,3] in which two carboxylic acid molecules couple to form a symmetrical ketone, CO₂, and H₂O, as depicted in Scheme 3.2.

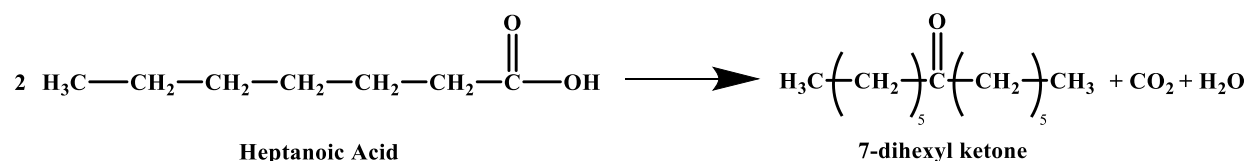
Decarbonylation



Decarboxylation



Scheme 3.1. Decarbonylation and decarboxylation of heptanoic acid



Scheme 3.2. Ketonization of heptanoic acid

In our previous work, we studied the decarbonylation of heptanoic acid over Pt nanoparticles and reported low α -olefin selectivities because of olefin isomerization and sequential hydrogenation when the reaction was run at modest conversions [4]. At low conversions, however, decarbonylation was the primary reaction path [4]. Whereas Boda *et al.* [5] and Lugo-José *et al.* [6,7] also reported that decarbonylation was the main deoxygenation reaction over Pd catalysts, much of the deoxygenation literature [8–22] reports decarboxylation occurs when performing experiments in the presence of dihydrogen and solvent to inhibit catalyst deactivation and maximize the selectivity towards the formation of paraffins [17]. Discriminating between competing reaction paths based solely on the hydrocarbon products that are formed is difficult because alkenes are readily hydrogenated in the presence of H₂ and Pd. Nevertheless, Maier *et al.* speculated the active site on a Pd catalyst to be a Pd/H complex [23]. Interestingly, quantum chemical studies by Lamb *et al.* explored a potential mechanistic path to decarboxylate butanoic acid on a model Pd (111) surface [24], whereas Heyden and co-workers revealed a path to decarboxylate propanoic acid on Pd (111) [25,26].

Support composition and metal particle size have also been reported to affect the catalyst activity. For example, Lugo-José *et al.* studied the gas-phase decarbonylation of propanoic acid and reported an increase in TOF by a factor of ≈ 32 when Pd nanoparticles were supported on silica instead of carbon [6], but Ford *et al.* reported a decrease in TOF of ≈ 3 fold when Pd nanoparticles were supported on silica instead of carbon during the liquid-phase operation [22]. In a different study, Lugo-José *et al.* reported during the gas-phase deoxygenation of propanoic acid at 473 K a constant TOF over Pd nanoparticles with sizes between 3.0 to 12 nm, but the TOF decreased by a factor of 3 when Pd nanoparticles of 1.9 nm were used instead [7]. In contrast, Simakova *et al.* reported an increase in TOF as the Pd nanoparticle size

decreased from 6.1 to 2.3 nm during the liquid-phase deoxygenation of palmitic and stearic acid at 573 K [19].

Given the diversity of results reported for the conversion of carboxylic acids over supported Pd catalysts, which seem to depend on both catalyst type and reaction conditions, we studied systematically the decarbonylation and decarboxylation of heptanoic acid over a wide variety of supported Pd catalysts in a continuous-flow fixed-bed reactor. The effects of support type, Pd impregnation method, Pd weight loading, conversion, reaction phase, and acid concentration on the activity, product selectivity, and catalyst stability were examined.

3.2. Experimental Methods

3.2.1. Catalyst synthesis

The catalysts were prepared by incipient wetness impregnation (IWI) using aqueous solutions of tetraamminepalladium (II) nitrate, $(\text{NH}_3)_4\text{Pd}(\text{NO}_3)_2$ (Sigma Aldrich) to obtain 1, 5, 10, and 20 wt% Pd loadings on Norit activated carbon (ROX 0.9), respectively. Prior to impregnation, Norit carbon particles were crushed and sieved between 180 μm and 425 μm . After impregnation of the desired metal precursor solution, the catalyst was dried in air at 393 K overnight. Palladium (II) acetate, $\text{Pd}(\text{OCOCH}_3)_2$, was used to prepare catalysts by the alcohol reduction (AR) method, as described by Benavidez *et al.* [27], to obtain a 5 wt% loading on Norit activated carbon, Vulcan carbon (XC-72), and Davisil silica 636. Vulcan carbon and Davisil silica were used as received. The dried solids were reduced with H_2 (GTS-Welco 99.999%) flowing at 100 $\text{cm}^3 \text{min}^{-1}$. The temperature of reduction was increased at 1 K min^{-1} from room temperature to 623 K, and held isothermally for 3 h. The catalysts were then cooled, exposed to air, and stored in a vial.

3.2.2. Dihydrogen chemisorption

The metal dispersion was measured by H_2 chemisorption performed on a Micromeritics ASAP 2020 system. The catalyst was evacuated at 573 K for 10 h under vacuum followed by heating to 623

K at a rate of 1 K min⁻¹ after which it was reduced with flowing H₂ (GTS-Welco 99.999%) at 623 K for 3 h. Following reduction, the catalyst sample was evacuated at 573 K and cooled in vacuum to 373 K to prevent β -phase hydride formation during chemisorption. The amount of metal on the surface was evaluated by the total amount of H₂ adsorbed extrapolated to zero pressure, assuming a stoichiometric relationship between H₂ to metal of 1:2 (i.e. H/Pd = 1).

3.2.3. Dinitrogen physisorption

The specific surface area and pore size were measured by N₂ physisorption using a Micromeritics ASAP 2020. The samples were evacuated for 180 min at 373 K prior to the N₂ physisorption, after which adsorption isotherms were measured at 77 K. The Brunauer-Emmett-Teller (BET) and the Barrett-Joyner-Halenda (BJH) methods were used to determine the specific surface area and the pore size, respectively.

3.2.4. X-ray diffraction

Powder X-ray diffraction (XRD) analysis from $2\theta = 20$ to 90° was carried out on a X'Pert Pro MPD with monochromatic Cu K α -radiation ($\lambda=1.54056 \text{ \AA}$) using a step size of $1/4^\circ$ and a time step of 1 s.

3.2.5. Electron microscopy

Transmission electron microscopy (TEM) was performed on a FEI Titan operated at 300 keV in bright field mode and on a JEOL 2010F operated at 200 KeV in STEM high-angle annular dark-field (HAADF) mode. Catalyst samples were deposited on a SPI holey-carbon coated Cu grid after being dispersed in ethanol [28].

3.2.6. Catalytic conversion of heptanoic acid

The catalytic decarbonylation/decarboxylation of heptanoic acid (Sigma Aldrich $\geq 99.50\%$) was performed in a fixed bed tubular reactor described previously [4]. The reactor was composed of a 2

μm pore size frit that immobilized 50 to 500 mg of catalyst pellets supported on a glass wool plug. Fresh catalyst was used for each experiment due to the irreversible deactivation of the catalyst as described in our previous work with Pt catalysts. After loading the reactor, the system was purged for 60 min with $200\text{ cm}^3\text{ min}^{-1}$ of N_2 (GTS-Welco 99.999%) at atmospheric pressure to remove dioxygen from the system and the pressure was increased to 45 bar to perform a leak test and then depressurized. The temperature was then increased at 1 K min^{-1} to the desired reduction temperature, 623 K, under $100\text{ cm}^3\text{ min}^{-1}$ of H_2 (GTS-Welco 99.999%) and held isothermally for 3 h at atmospheric pressure. The reactor was finally cooled to the desired reaction temperature, 573 K, and purged for 60 min in $200\text{ cm}^3\text{ min}^{-1}$ of N_2 (GTS-Welco 99.999%). Then, the pressure was increased to the desired reaction condition, 40 bar, with $200\text{ cm}^3\text{ min}^{-1}$ of N_2 (GTS-Welco 99.999%).

For the “pure” acid experiments, the feed mixture was composed of 95 wt% heptanoic acid (Sigma Aldrich $\geq 99.50\%$) and 5 wt% dodecane (Sigma Aldrich anhydrous 99.00%) as an internal standard. Tetradecane (Sigma Aldrich anhydrous 99.90%) was used as a diluent to prepare feeds with different heptanoic acid concentration (50, 25, 10, 7.5, 5, and 2.5 mol%). The feed was then pumped in the reaction system using a syringe pump (ISCO 500D) operating at different liquid flow rates (0.01 to $1.0\text{ cm}^3\text{ min}^{-1}$). The acid feed mixtures passed through a heated zone before entering the catalytic reactor. A more detailed explanation of reaction set up and schematic can be found in section 2.2.6 and Figure 2.1, respectively.

The outlet of the reactor was connected to an air cooled condenser maintained at room temperature to remove the condensable products, such as hexane, 1-hexene, hexenes, 7-tridecanone, dodecane, tetradecane, and unreacted heptanoic acid, from the product stream. The liquid-phase sample was analyzed by a gas chromatograph (GC 7890 A) equipped with a ZB-FFAP column (length $45\text{ m} \times 0.538\text{ mm}$) and a flame ionization detector (FID). The product gas was continuously removed from the condenser using $5\text{ cm}^3\text{ min}^{-1}$ N_2 (GTS-Welco 99.999%) as a purge gas. The outlet gas of the condenser was fed to an on-line gas chromatograph (HP 5890 Series II) equipped with a packed column, ShinCarbon ST 80/100, and a thermal conductivity detector (TCD) for detection of

N₂, CO, CO₂ and any other light hydrocarbons (if any). Gas chromatography calibrations can be found in Appendix B.

A series of control experiments was performed to determine the background conversion of the system at our typical reaction conditions (573 K, 1 bar, 250 mg of catalyst, and 0.01 cm³ min⁻¹ of liquid feed composed of 95 wt% heptanoic acid and 5 wt% dodecane). In the absence of catalyst, no conversion of heptanoic acid was observed. However, when Norit or Vulcan carbon support were used, a background conversion was detected of ≈ 2 and 1 %, respectively. No conversion was observed over the silica support.

3.2.7. Postmortem catalyst characterization

The spent samples were recovered from the reactor, washed with 25 mL of methanol and sonicated in a methanol solution for 30 min to remove weakly adsorbed reactant and products from the surface of the catalyst. After sonication, the solids were recovered by filtration and dried overnight in air at 400 K. The spent samples were characterized by H₂ chemisorption, N₂ physisorption, XRD, and TEM to determine the effect of reaction conditions on the catalyst structure and adsorption capacity.

3.2.8. Calculations of rates

As described in our previous work, the turnover frequency (TOF) was calculated as the rate of formation of the products referred to the number of surface metal atoms evaluated on a freshly prepared catalyst [4]. The main components in the gas-phase were CO and CO₂, whereas 1-hexene, 2- and 3-hexenes (i-hexenes), hexane, 7-tridecanone, and heptanoic acid were the main products in the liquid-phase. Some minor amounts of heavier unknown products were also detected in the liquid-phase products (which accounted for $\approx 0.4\%$ of the total detected liquid product).

The liquid-phase TOF was calculated using the rate of formation of the products after 20 h of reaction, after which the liquid-phase reaction was at a steady state, normalized to the number of

surface metal atoms evaluated on a fresh catalyst. The liquid-phase TOF was therefore calculated as [(rate of production after 20 h of reaction (mol s^{-1}) hexane + 1-hexene + i-hexenes + 2 x moles of 7-tridecanone) / (mol of surface metal on a fresh catalyst counted by H_2 chemisorption)].

During gas-phase operation, the catalyst deactivated exponentially with time during the first 3 h of reaction. Thus, an initial TOF was calculated by extrapolating the log of the reaction rate to $t = 0$ h. The initial TOF was calculated as [(rate of production (mol s^{-1}) of hexane + 1-hexene + i-hexenes + 2 x moles of 7-tridecanone) / (mol of surface metal on a fresh catalyst counted by H_2 chemisorption)].

The deoxygenation conversion is defined here as the formation rates of the major products divided by the feed rate of reagent. Thus, the deoxygenation conversion was calculated as [(rate of production (mol s^{-1}) of hexane + 1-hexene + i-hexenes + 2 x moles of 7-tridecanone) / (moles of heptanoic acid fed (mol s^{-1}))].

The product selectivity was defined as the moles of a product formed divided by the total moles of products present in the same phase (liquid or gas). Three different sets of product selectivity were calculated, the selectivity to carbon oxides (CO and CO_2), i.e. CO selectivity [(rate of CO) / (rate of CO + rate of CO_2)], the selectivity of α -olefin relative to all olefin produced for 1-hexene and hexenes, i.e. relative α -olefin selectivity [(rate of 1-hexene) / (rate of 1-hexene + i-hexenes)], and the selectivity to deoxygenation products for mainly hexane, 1-hexene, i-hexenes, and 7-tridecanone, i.e. selectivity of hexane [(rate of hexane) / (rate of hexane + 1-hexene + i-hexenes + 2 x moles of 7-tridecanone)].

3.3. Results and Discussion

3.3.1. Effect of support and impregnation method during the liquid-phase operation

In our previous study [4], low metal dispersion was achieved with 5 wt% Pt synthesized by an incipient wetness impregnation (IWI) method on low surface area supports such as Vulcan carbon and silicon carbide. For this reason, we decided to use an alcohol reduction (AR) method to deposit Pd nanoparticles on Vulcan carbon and silica. Since high dispersion of metal can be achieved with

Norit carbon as support, Pd was added to Norit carbon by either incipient wetness impregnation or alcohol reduction to test the influence of preparation method.

Table 3.1. Summary of the catalyst characterization and reactivity results for Pd catalysts synthesized by alcohol reduction (AR) during the liquid-phase reaction at 573 K.

Catalysts	Pd Dispersion^a (%)	Pd Particle Size^b (nm)	Surface Area^c (m ² g ⁻¹)	Pore Size^d (nm)	Liquid-Phase TOF^e (s ⁻¹)	CO Selectivity^f (%)
5 wt% Pd/Norit C	20	2.2 ± 1.0	1460	N.D.	0.00069	71
5 wt% Pd/Vulcan C	11	3.0 ± 1.5	210	8.8	0.00071	91
5 wt% Pd/SiO₂	43	2.0 ± 0.5	500	6.2	0.00069	69

^a Result estimated from H₂ chemisorption of the fresh catalyst sample, using nominal Pd loading

^b Result estimated from TEM of the fresh catalyst sample

^c Result estimated using N₂ physisorption and the BET method on the fresh catalyst sample

^d Result estimated using N₂ physisorption and the BJH method on the fresh catalyst sample

^e Result estimated using rates of heptanoic acid conversion after 20 h of reaction

^f Result estimated using rates of carbon oxide formation after 20 h of reaction.

N.D. Not determined, both micropores and mesopores are present on this sample

Table 3.2. Summary of catalysts characterization and reactivity results for Pd catalysts synthesized by incipient wetness impregnation (IWI) during the liquid-phase reaction at 573 K.

Catalyst	Reaction Temperature (K)	Pd Dispersion^a (%)	Pd Particle Size^b (nm)	Surface Area^c (m² g⁻¹)	Liquid-Phase TOF^d (s⁻¹)	CO Selectivity^e (%)
1 wt% Pd/Norit C	Fresh 573	25 0	1.9 ± 0.5 -	1460 495	- 0.00071	- 70
5 wt% Pd/Norit C	Fresh 573	25 0	2.0 ± 0.4 -	1450 510	- 0.00069	- 67
10 wt% Pd/Norit C	Fresh 573	25 1.2	2.4 ± 0.5 -	1400 540	- 0.00069	- 60
20 wt% Pd/Norit C	Fresh 573	24 1.7	2.5 ± 0.5 -	1460 530	- 0.00068	- 54

^a Result estimated from H₂ chemisorption of the fresh catalyst sample, using nominal Pd loading

^b Result estimated from electron microscopy

^c Result estimated using N₂ physisorption and the BET method on the fresh and spent catalyst samples

^d Result estimated using rates of heptanoic acid conversion after 20 h of reaction

^e Result estimated using rates of carbon oxide formation after 20 h of reaction

Catalysts composed of 5 wt% Pd loaded on the various supports were characterized by N₂ physisorption, H₂ chemisorption, XRD, and TEM, and the results are summarized in Tables 3.1 and 3.2 for the catalysts synthesized by AR and IWI, respectively. The Pd nanoparticle size on all the catalysts was about 2 to 3 nm as evaluated by TEM. Although the dispersion of Pd on Pd/SiO₂ (43%) was consistent with the observed particle size evaluated by TEM (2.0 ± 0.5 nm) the dispersion of Pd/Norit C samples (20 – 25%) and Pd/Vulcan C (11%) was lower than those expected from the particle size observed by TEM. Therefore, the catalysts were examined by X-ray diffraction.

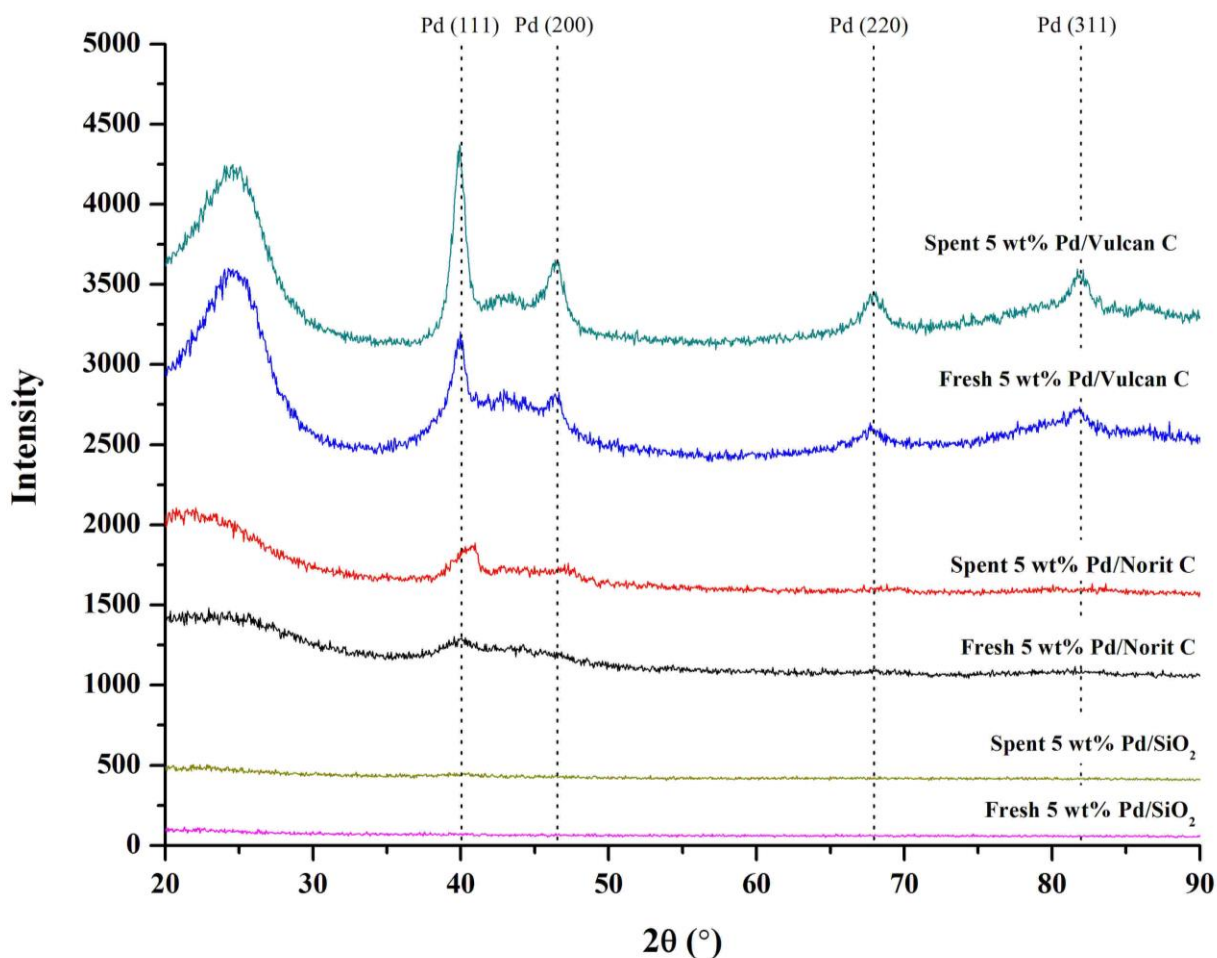


Figure 3.1. Comparison of the XRD patterns of 5 wt% Pd/Norit C, 5 wt% Pd/Vulcan C, and 5 wt% Pd/SiO₂ prepared by alcohol reduction (AR) before (fresh) and after (spent) liquid-phase reaction at 573 K. The patterns were offset for clarity. The spent samples were recovered from the reactor and treated as described in the Experimental Methods section.

Figure 3.1 provides evidence for Pd crystallites on Vulcan C, even before reaction, which likely accounts for the low dispersion of Pd measured by H₂ chemisorption. Evidently, the particle size evaluated by TEM did not account for the small number of larger metal crystallites. We assume the discrepancy between the TEM particle size and metal dispersion of Pd on Norit C samples can be explained in the same way. After liquid-phase reaction, both of the carbon catalysts had much intense diffraction peaks associated with Pd most likely the result of metal sintering that occurred under the

liquid-phase reaction conditions, as reported for Pt catalysts [4]. Whereas TEM micrographs showed highly dispersed Pd nanoparticles before reaction on all the supports, growth of Pd particles was observed on all the carbon-based catalysts (Figure 3.2), more so for Pd/Vulcan C.

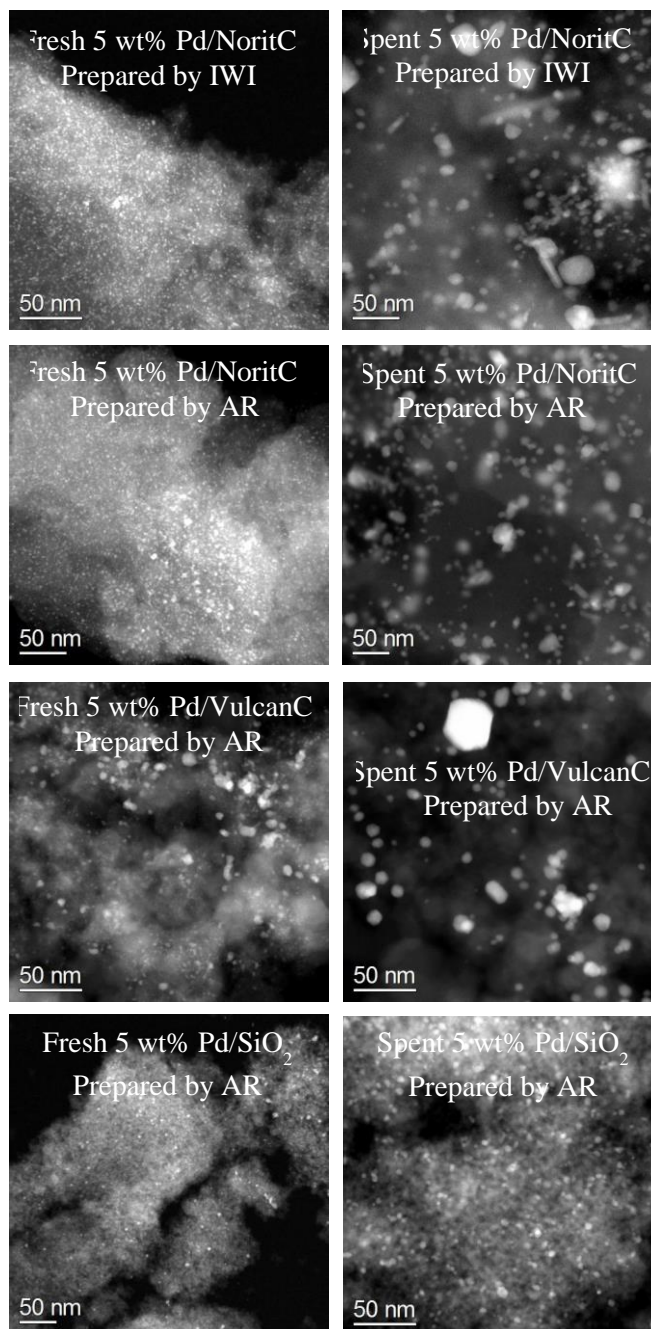


Figure 3.2. High-angle annular dark field STEM images of fresh (left) and spent (right) catalysts during the liquid-phase decarbonylation of heptanoic acid at 573 K.

Interestingly, the silica-supported catalyst still showed highly dispersed Pd nanoparticles, as depicted in Figure 3.2. This result suggests that silica might be a better support than carbon for stabilizing metal particles under the harsh reaction conditions. Since all of the catalysts had very low rate after 20 h of liquid-phase ($\text{TOF} \approx 0.00070 \text{ s}^{-1}$), the large variation in final metal particle size does not explain the deactivation.

Figures 3.3 and 3.4a shows the liquid-phase product selectivity after 20 h of reaction for the 5 wt% Pd catalyst synthesized by AR and IWI, respectively. The two 5 wt% Pd/Norit C catalysts exhibited similar conversion level and product selectivity during reaction of heptanoic acid, with the main liquid-phase products being hexane and hexenes. Evidently, the impregnation method and metal precursor did not influence the catalytic performance or stability of the resulting Pd nanoparticles. The variation of conversion with 5 wt% Pd sample in Figure 3.3 was likely the result of the different initial dispersion of the catalysts, with Pd/Vulcan C having the lowest dispersion. Nevertheless, the major liquid-phase product over all of the samples were hexenes and hexane.

Because silica is unstable at high temperatures in the presence of high concentration of water (a product of the reaction) [29], and high dispersion of Pd was not successfully prepared on Vulcan C, we focused additional efforts on the performance of Pd/Norit C.

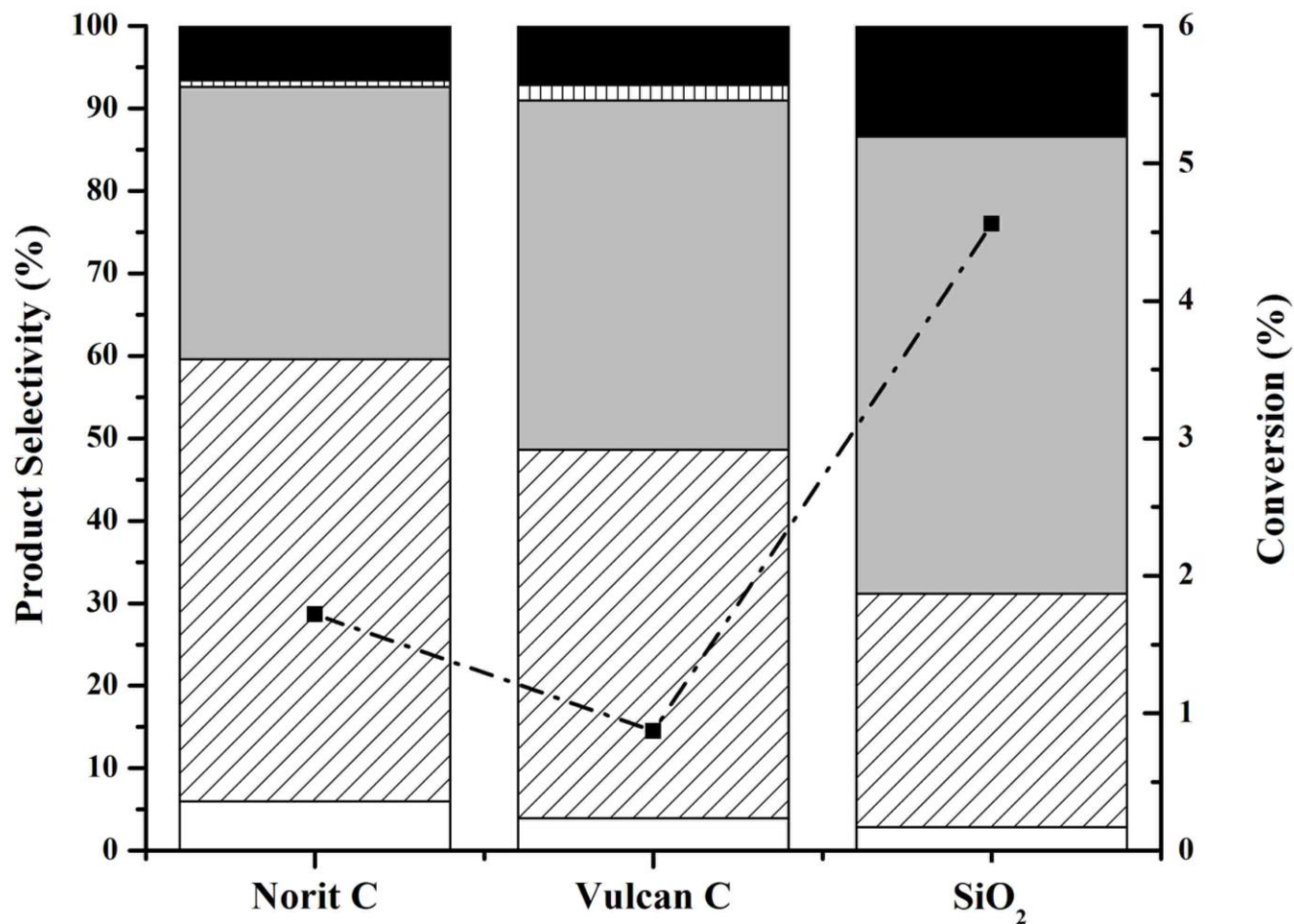


Figure 3.3. Effect of support on product selectivity and conversion during the liquid-phase decarbonylation of heptanoic acid at 573 K, and $0.01 \text{ cm}^3\text{min}^{-1}$ of liquid feed composed of 95 wt% heptanoic acid and 5 wt% dodecane. The product selectivity (%) is represented with color bars and can be read on the left axis. \square represents 1-hexene, ▨ represents 2 and 3-hexenes, ▤ represents hexane, ▧ represents 7-tridecanone, and \blacksquare represents the unknown products. The black squares represent conversion (%) and can be read on the right axis. The background conversion of the carbon supports was removed for clarity. These results were recorded after 20 h of reaction.

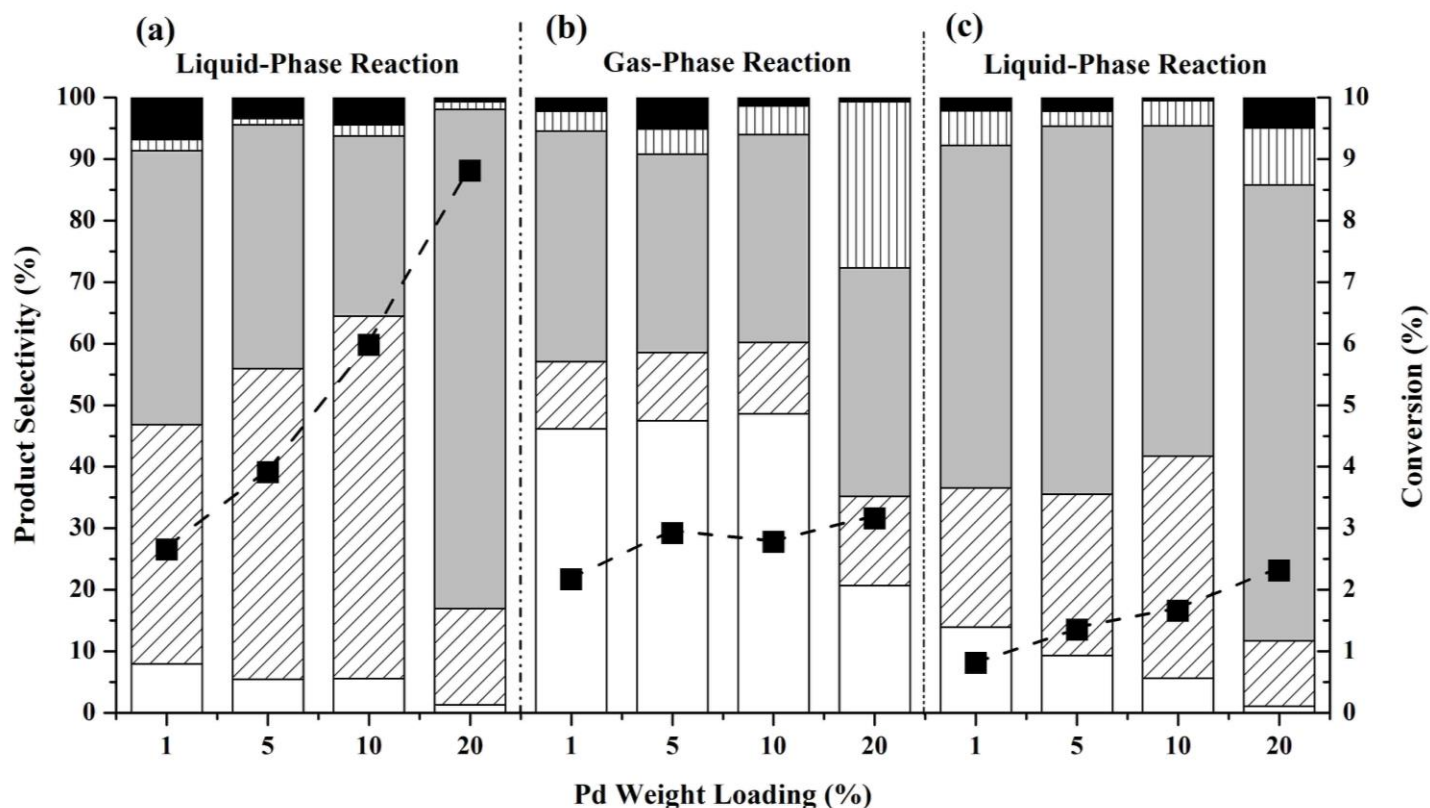


Figure 3.4. Effect of Pd weight loading on Norit C on product selectivity and conversion during the liquid-phase decarbonylation of heptanoic acid at 573 K, and $0.01 \text{ cm}^3 \text{ min}^{-1}$ of liquid feed composed of 95 wt% heptanoic acid and 5 wt% dodecane. The product selectivity (%) is represented with color bars and can be read on the left axis. \square represents 1-hexene, ▨ represents 2 and 3-hexenes, ▒ represents hexane, ▤ represents 7-tridecanone, and \blacksquare represents the unknown products. The black squares represent conversion (%) and can be read on the right axis. The background conversion of the carbon supports was removed for clarity. These results were recorded after 20 h of reaction.

3.3.2. Effect of metal loading and reaction pressure

In a previous study, we reported the liquid-phase TOF for Pt/Norit C to be independent of Pt loading at a value of $\approx 0.005 \text{ s}^{-1}$ [4]. As reported in Tables 3.1 and 3.2, Pd/Norit C converted heptanoic acid in the liquid-phase with a TOF of $\approx 0.0007 \text{ s}^{-1}$, which is about an order of magnitude less than that for Pt/Norit C under identical conditions [4]. Because of the low activity of Pd in the liquid-phase reaction, the metal loading of Pd was increased to 20 wt% to minimize the relative contribution of the Norit C support to the catalytic evaluation. The results from the catalyst characterization and reaction testing of the higher loaded samples are summarized in Table 3.2.

The catalyst characterization of the fresh catalysts synthesized by IWI revealed that the surface area ($\approx 1500 \text{ m}^2 \text{ g}^{-1}$) and Pd dispersion ($\approx 25\%$) was independent of Pd loading. The characterization of the spent catalysts revealed a severe loss of surface area to $\approx 500 \text{ m}^2 \text{ g}^{-1}$ and almost a complete loss of exposed Pd measured by H_2 chemisorption. Apparently the evacuation step for surface area determination and the reduction step for H_2 chemisorption were not sufficient to regenerate the high surface area and chemisorption capacity of the fresh catalyst. These results were consistent with the observations previously reported by Simakova *et al.* [19], Immer *et al.* [20], and Ping *et al.* [30] during the decarboxylation of carboxylic acids over Pd catalysts. We suspect that adsorption of carbonaceous materials in the pores and on the Pd is the major cause of deactivation, as previously reported by Ping *et al.* [30,31], because the reaction over Pd/SiO₂ was also very low after 20 h of reaction but there was minor Pd particle growth. Figures 3.5 and 3.6 show the XRD patterns and electron micrographs, respectively, of the Pd/Norit C catalysts with various Pd loadings before and after reaction. Significant Pd particle growth was observed at every loading on Norit C, as revealed by the micrographs in Figure 3.6. The XRD patterns are consistent with the growth of particles on the higher loaded samples (5 to 20 wt%). The lack of significant Pd diffraction features on the 1 wt% Pd sample was likely because of the low metal loading.

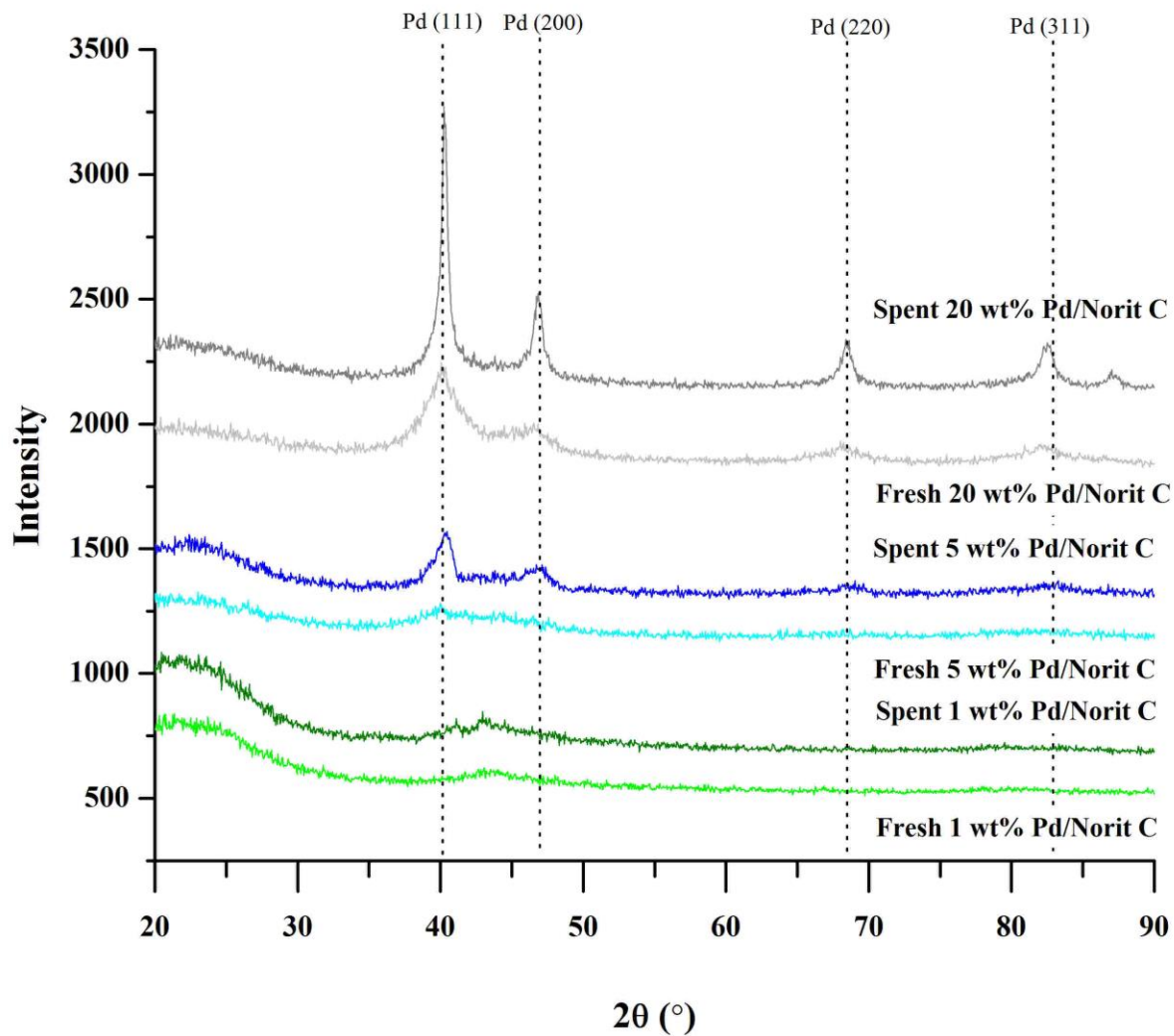


Figure 3.5. Comparison of the XRD patterns of 1, 5, and 20 wt% Pd/Norit C prepared by incipient wetness impregnation (IWI) before (fresh) and after (spent) liquid-phase reaction at 573 K. The patterns were offset for clarity.

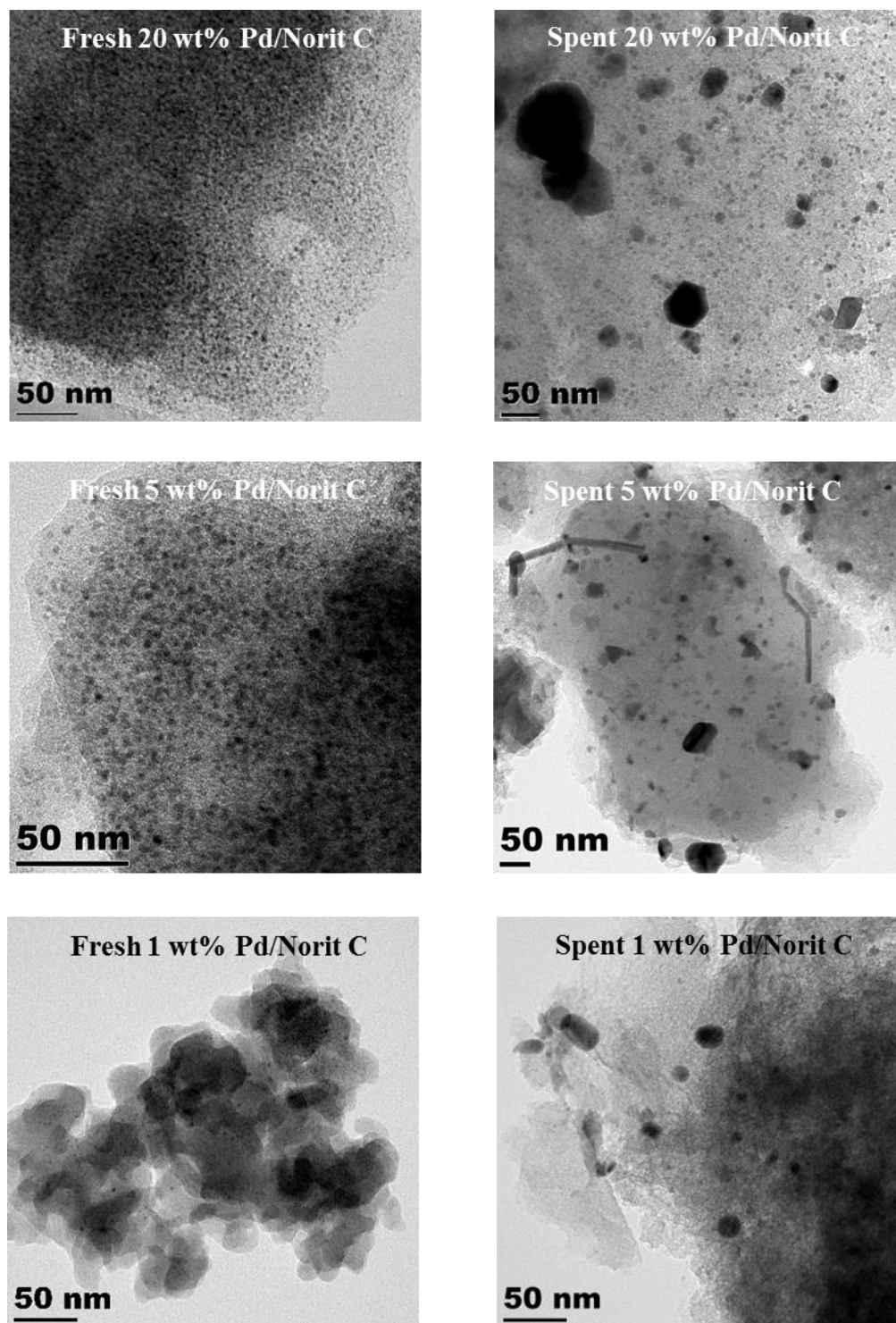


Figure 3.6. Bright field HRTEM images of fresh (left) and spent (right) Pd/Norit C samples after the liquid-phase decarbonylation of heptanoic acid at 573 K.

The product distribution during the liquid-phase conversion of heptanoic acid over Pd catalysts with low weight loading favored the formation of hexenes (1-, 2- and 3-hexenes) and CO, but was difficult to distinguish from that attributed to the carbon support (Figure 3.4a). The catalyst with the highest weight loading (20 wt% Pd) showed a different product distribution favoring the formation of hexane and CO₂. As the liquid-phase conversion increased because of the added Pd, the selectivity towards the formation of 1-hexene decreased. This observation was consistent with our previous work performed on Pt/Norit C, in which we found rapid bond isomerization of terminal olefins over the Pt at our reaction conditions [4].

After 25 h of liquid-phase operation, the system was depressurized to allow for operation with gas-phase heptanoic acid. During the gas-phase operation (Figure 3.4b), the selectivity towards the α -olefin was higher than that observed during the liquid-phase experiments, but the catalyst deactivated, as previously reported [4]. The deactivation was more severe with catalysts having higher Pd loading (10 and 20 wt% Pd). After operating in gas-phase for 25 h, the system was re-pressurized to liquid-phase reaction conditions (Figure 3.4c). The catalytic activity of the various Pd catalysts did not recover to their initial steady state liquid-phase levels, indicating an irreversible change of the catalysts during the gas-phase operation.

The reported values for turnover frequency (TOF) of carboxylic acid conversion over Pd generally ranged 0.01 to 0.96 s⁻¹ for batch reaction at 573 K [15,16,20,21] and from 0.027 to 0.004 s⁻¹ for fixed-bed operation at 543 K [8,10]. Although these values are substantially greater than those reported in this work, differences in reaction conditions such as not co-feeding H₂ and feeding nearly pure carboxylic acid might account for the differences in TOF. For example, Murzin and co-workers [9,10,14–16,19] as well as Lamb and co-workers [20–22] studied the liquid-phase conversion of carboxylic acids in the presence of H₂ over Pd catalysts and reported TOFs from 0.01 to 0.1 s⁻¹ at 573 K. Characterization of our spent catalysts revealed substantial loss in H₂ chemisorption capacity, suggesting our reaction conditions generally deactivated the catalyst.

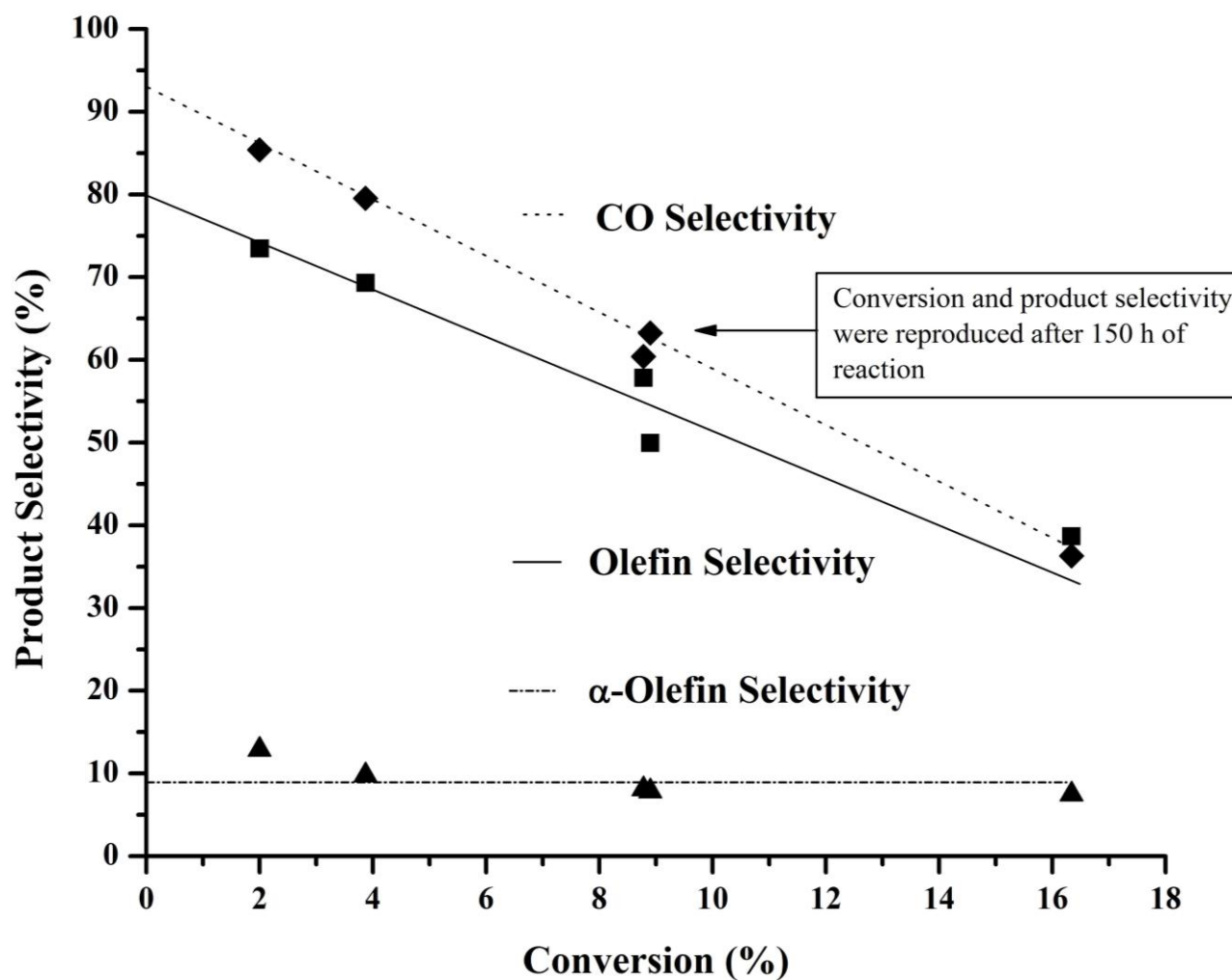


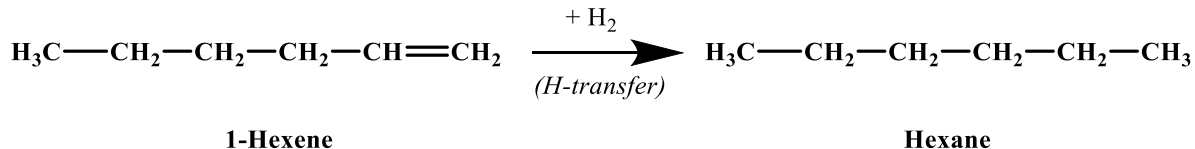
Figure 3.7. Dependence of product selectivity on liquid-phase conversion of heptanoic acid over 10 wt% Pd/Norit C at 573 K and 37 bar. ■ represents the selectivity to olefins (1-, 2- and 3-hexenes) decarbonylation products, olefins, in the liquid product. ◆ represents the carbon oxide selectivity to CO. ▲ represents the selectivity to α -olefin relative to all olefins in the liquid product. These results were recorded after 20 h of reaction.

3.3.3. Effect of liquid-phase conversion on product selectivity

To minimize the impact of support activity on the results, we studied the liquid-phase conversion of heptanoic acid at 573 K over 10 wt% Pd/Norit C at various space velocities to explore the influence of conversion on the product distribution. With a constant loading of catalyst, the feed flow rate was varied from 0.005 to 0.05 cm³min⁻¹ over a period of 150 h (\approx 370 turnovers) to obtain a range of conversion values. At the end of experiment, the catalyst returned to the initial reaction condition to check for deactivation. Figure 3.7 summarizes the effect of conversion on product selectivity achieved by varying the space velocity. The reproducibility of the initial conversion (\approx 9%) to that achieved at identical conditions after 150 h of reaction confirms that long term deactivation was not significant during the course of the experiment.

Figure 3.7 shows a very strong correlation of the product selectivity to conversion. Extrapolation of the product selectivities to zero conversion indicates \approx 90% of the carbon oxides is CO and 80% of the liquid-phase products are hexenes. Therefore, the main reaction path during the liquid-phase conversion of heptanoic acid over Pd/Norit C at 573 K is decarbonylation, which is consistent with previously reported results over Pt/Norit C [4]. Figure 3.7 also shows a low selectivity to α -olefin, between 7 and 12%, across the conversion range. As discussed earlier, metal-catalyzed double bond isomerization of 1-hexene to 2- and 3-hexenes occurs rapidly on Pd.

The selectivity for hexenes was lower than that selectivity for CO, indicating there was a side reaction that hydrogenated hexenes into hexane. In previous work with heptanoic acid decarbonylation over supported Pt [4], a higher olefin selectivity compared to CO selectivity was observed, with the loss of CO being attributed to the water-gas shift reaction. Scheme 3.3 shows some possible side reactions that take place during the conversion of heptanoic acid. Since the water-gas shift activity of Pd is less than that of Pt, as reported by Grenoble and Estadt [32], we suspect the hydrogen involved in the hydrogenation of the hexenes to hexane in the current work originated from the absorption and decomposition of the organic acid on the catalyst.

Hydrogenation**Scheme 3.3. Some possible side reactions during the conversion of heptanoic acid**

Nevertheless, the results in Figure 3.7 clearly support the idea that decarbonylation is the primary reaction of heptanoic acid on Pd under our experimental conditions. The fact that the fraction of CO exceeds the fraction of hexenes at low conversions suggests that olefin hydrogenation occurs readily on the catalysts and is independent of the water-gas shift reaction.

3.3.4. Gas-phase operation

Because liquid-phase heptanoic acid causes growth of Pd particles on the carbon support, we decided to explore the gas-phase conversion over 10 wt% Pd/Norit C without exposing the catalyst to liquid acid. The reactivity results summarized in Figure 3.8 reveal that the catalyst deactivated severely during the first 2 h of reaction (Figure 3.8a), and that the deactivation was followed by changes in product selectivity. Initially, we observed an acid conversion of 16.5%, with the CO selectivity (Figure 8b) being similar to that of hexenes (Figure 3.8c). The 1-hexene selectivity was very low, $\approx 5\%$, indicating rapid double bond isomerization.

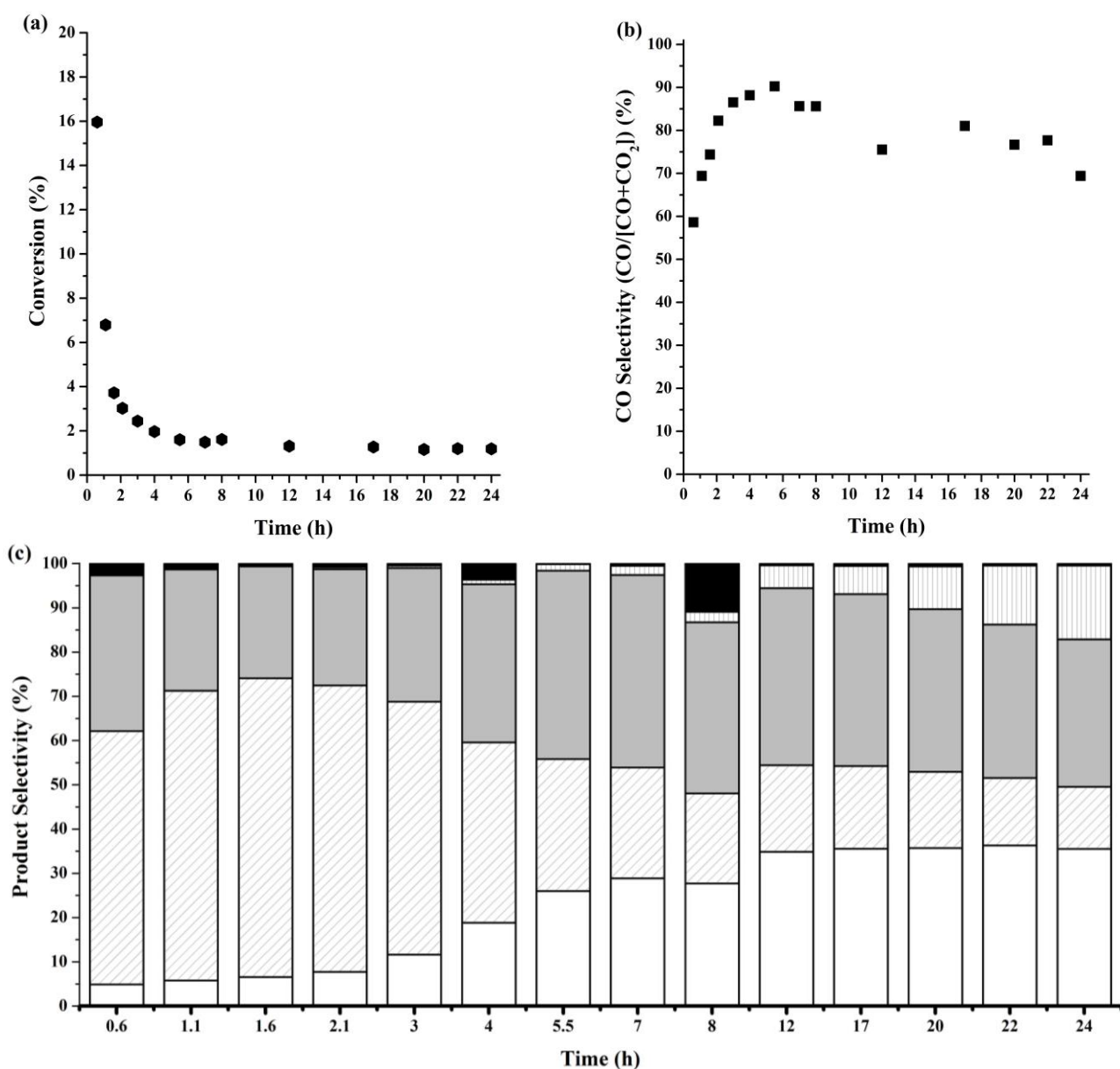


Figure 3.8. Time evolution of the (a) conversion and (b) CO selectivity represented by and (c) product selectivity during the gas-phase decarbonylation of heptanoic acid over 10 wt% Pd/Norit C at 573 K and 0.05 cm³ min⁻¹ of liquid feed composed by 95 wt% heptanoic acid (6.6 M) and 5 wt% dodecane. The product selectivity in (c) is represented with color bars where \square represents 1-hexene, ▨ represents 2 and 3-hexenes, ▩ represents hexane, ▤ represents 7-tridecanone, and \blacksquare represents the unknown products.

As the catalyst deactivated, the CO selectivity increased to a maximum of 90% before decreasing to 70% by the end of the experiment (Figure 3.8b). Similarly, the hexenes selectivity increased to 70% before decreasing to 50%. The decrease of CO selectivity at long times was most likely the result of the ketonization reaction, which was observed after 4 h of reaction. Ketonization of heptanoic acid produces CO₂ and 7-tridecanone (Scheme 3.2). The hexane produced during the reaction could not be produced entirely by direct decarboxylation because of the lack of CO₂ produced relative to CO as provided in Figures 3.8b and 3.8c. Evidently, some hydrogenation of hexenes to hexane occurred. Regarding the olefin selectivity, up to 35% terminal olefin was observed after long times on stream (Figure 3.8c), which is consistent with decarbonylation followed by some double bond isomerization.

Extrapolation of the conversion to $t = 0$ h allows for an estimation of the initial rate unaffected by deactivation. Using this method, we obtained a gas-phase TOF = 0.035 s⁻¹, which was ≈ 50 times faster than that of the liquid-phase TOF and similar to the values reported by others. As speculated in the previous section and suggested by the *postmortem* catalyst characterization with H₂ chemisorption, the liquid-phase TOF reported here was very likely affected by severe catalyst deactivation, which explains the order of magnitude difference between the liquid-phase TOF reported here and the literature [9,10,14–16,19–22].

Lugo-José *et al.* reported a TOF of 0.00017 s⁻¹ for the gas-phase decarbonylation of propanoic acid over Pd/C at 473 K and an activation barrier of ≈ 72 kJ mol⁻¹ [6]. The Arrhenius equation was used to extrapolate their rate to 573 K and revealed a TOF of ≈ 0.0042 s⁻¹. While this extrapolated value is an order of magnitude lower than the initial gas-phase Pd TOF reported here, it is similar to our final gas-phase Pd TOF of 0.0011 s⁻¹. This may suggest that the catalysts of Lugo-José *et al.* [6] suffered from some deactivation even though H₂ (20 vol%) was fed during that study.

Figures 3.9 and 3.10 compare the X-ray diffraction patterns and electron micrographs, respectively, of the spent catalysts from the gas-phase reaction. Even though the catalyst deactivated severely during the first 2 h of reaction, XRD and TEM revealed that the Pd nanoparticles remained

well dispersed after the gas-phase reaction. Evidently, sintering of Pd on the carbon support occurs only when operating in the liquid-phase acid. Severe deactivation occurred during gas-phase operation, not because of sintering, but presumably because of strongly held side products or carbonaceous species on the metal surface.

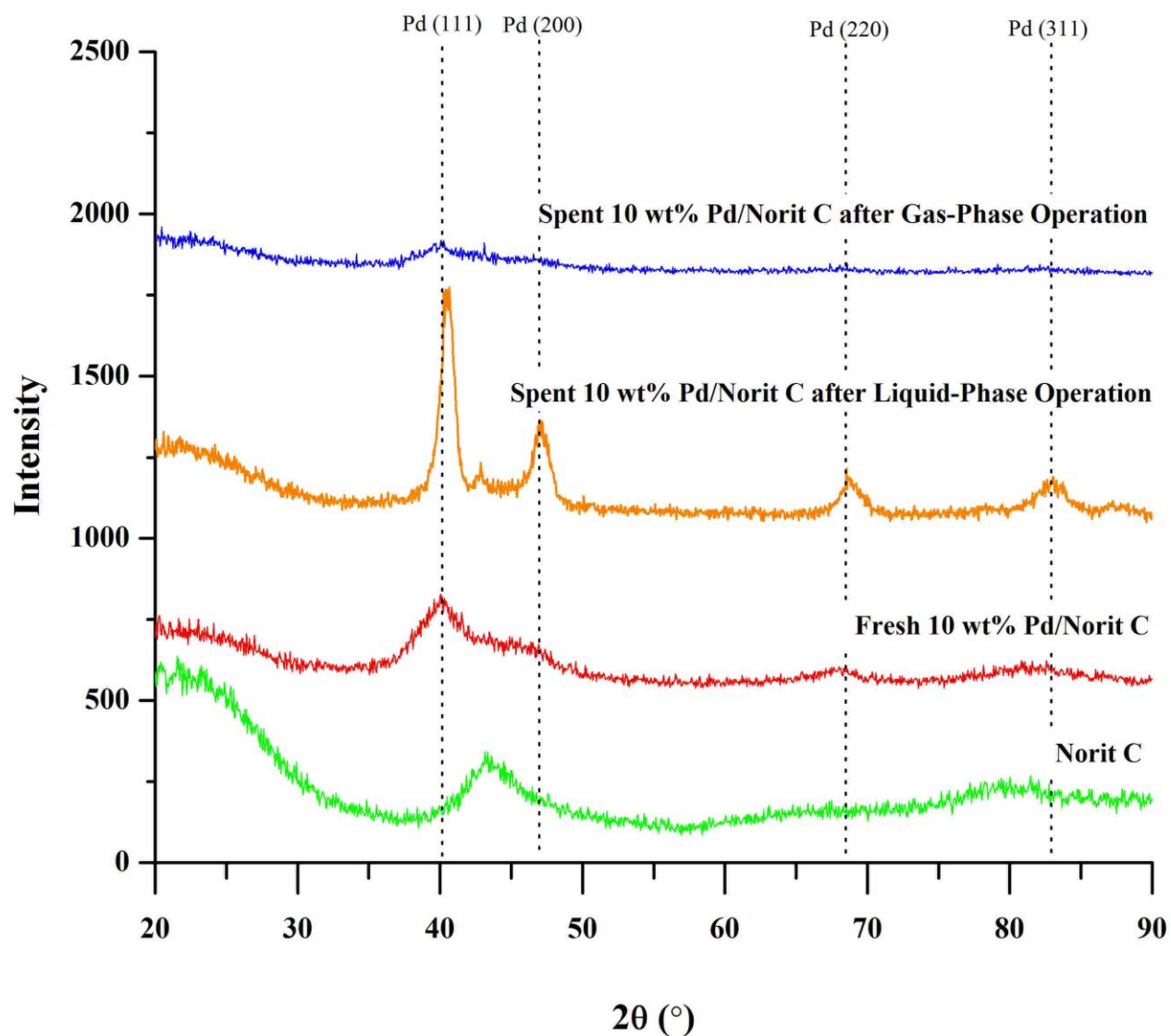


Figure 3.9. Comparison of the XRD patterns of 10 wt% Pd/Norit C run at 573 K after different reaction conditions. The patterns were offset for clarity.

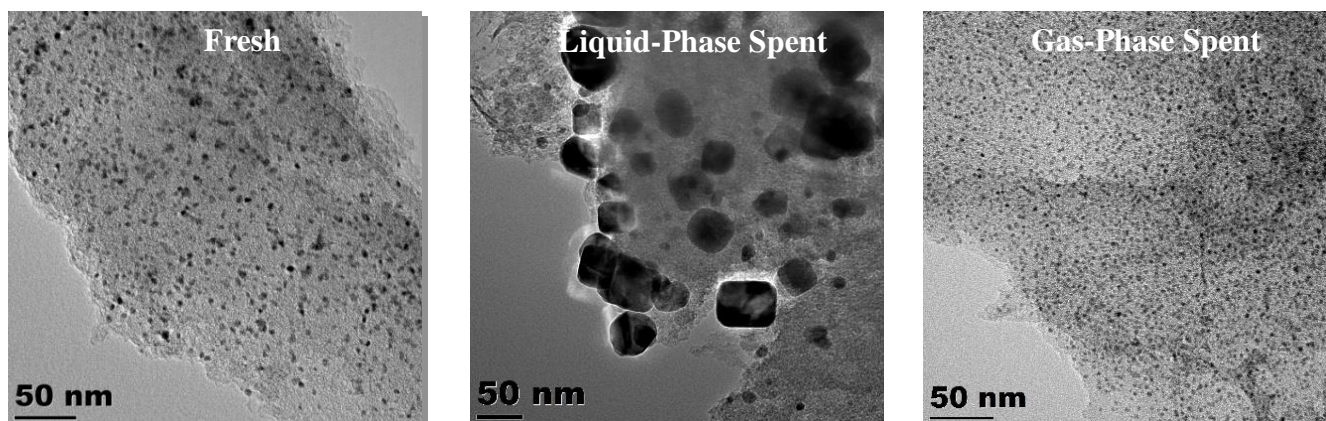


Figure 3.10. Bright field HRTEM images of 10 wt% Pd/Norit C fresh (left), spent during liquid-phase operation, and spent during the gas-phase operation at 573 K.

Since gas-phase operation apparently prevented severe Pd particle growth, we decided to investigate the stability of Pd particles in various concentrations of liquid heptanoic acid. Figures 3.11 and 3.12 present results from exposing 20 wt% Pd/Norit C to progressively lower liquid concentrations of reacting acid at 573 K. After 20 h of reaction, the catalyst in dilute acid (.019 M) appeared to be more dispersed than that in concentrated acid (1.1-6.6 M), confirming the hypothesis that concentrated liquid acid is detrimental to Pd particles dispersion on carbon. Interestingly, the liquid-phase steady state TOF at 573 K ($\approx 0.0007 \text{ s}^{-1}$) was independent of acid concentration from 0.1 to 6.6 M. The effect of acid concentration on the product selectivity can be found in Appendix C.

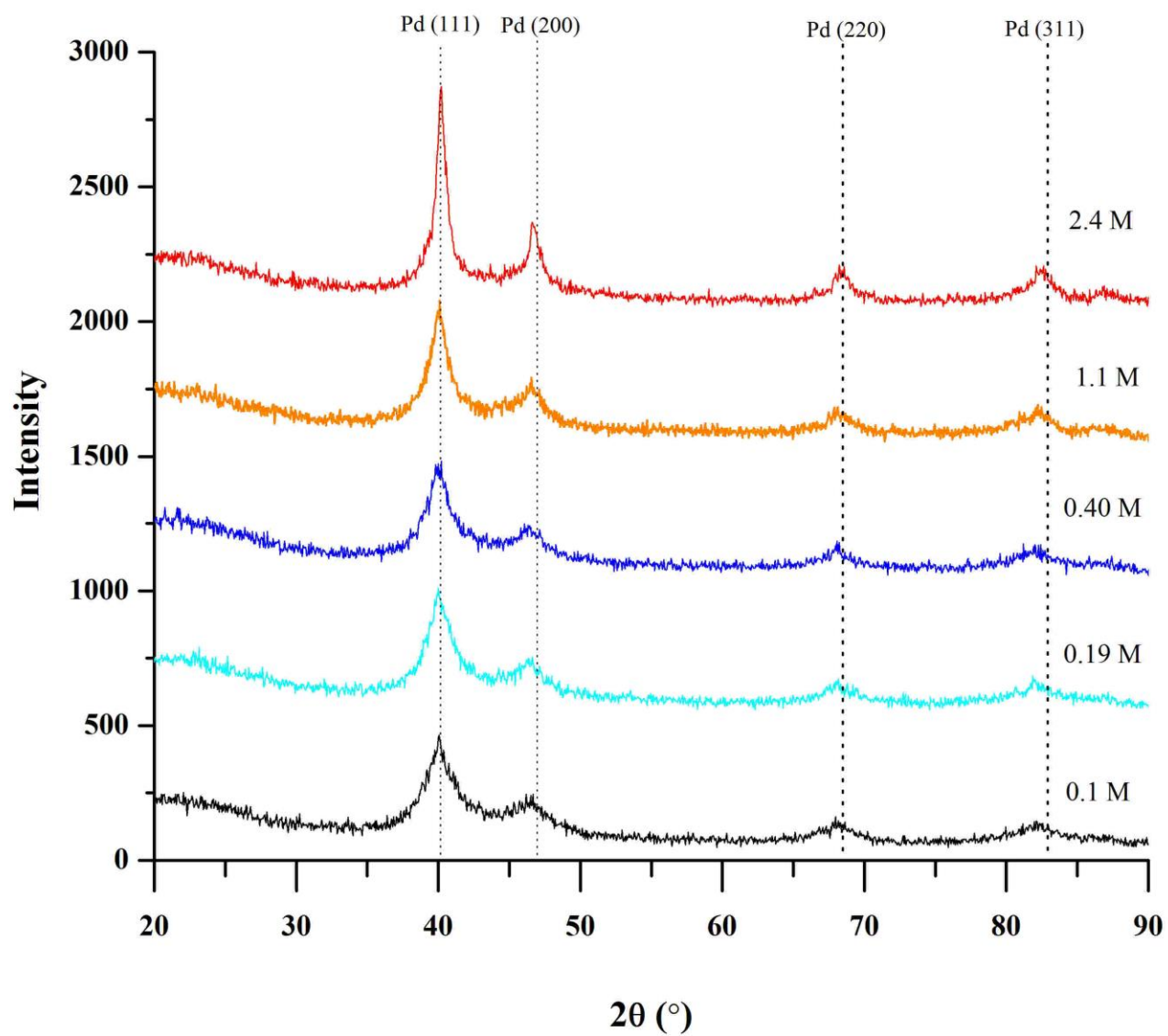


Figure 3.11. Comparison of the XRD patterns of 20 wt% Pd/Norit C after the liquid-phase operation at 573 K and different acid concentrations. The patterns were offset for clarity.

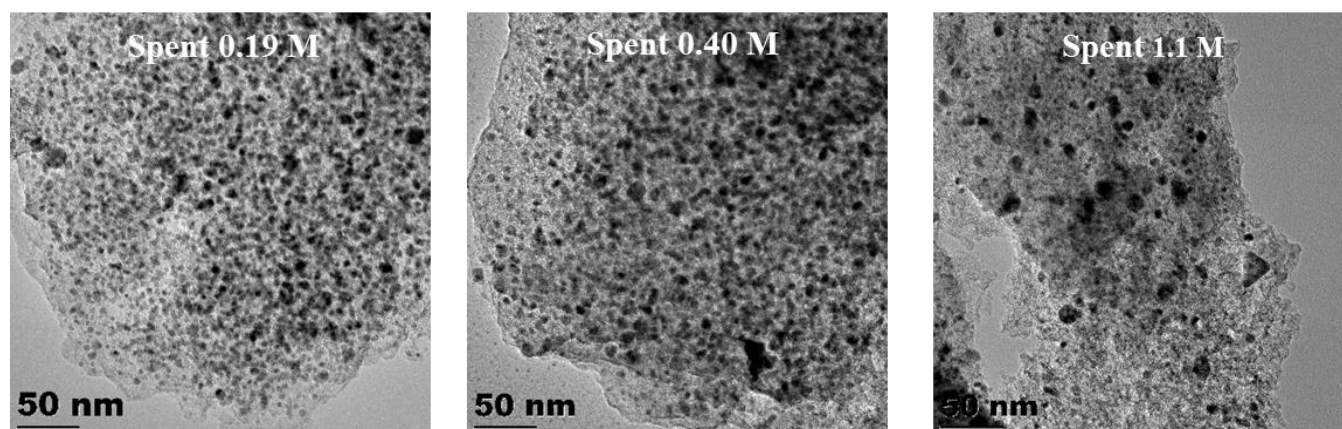


Figure 3.12. Bright field HRTEM images of 20 wt% Pd/Norit C after the liquid-phase operation at 573 K and different acid concentrations.

3.4. Conclusions

Palladium nanoparticles were supported on Davisil silica 636, Vulcan carbon and Norit carbon, characterized by H₂ chemisorption, N₂ physisorption, X-ray diffraction, electron microscopy (before and after reaction,) and evaluated in the liquid- and gas-phase conversion of heptanoic acid at 573 K. Decarbonylation was the primary reaction of heptanoic acid on Pd, producing hexene, CO and water (not measured). In liquid-phase operation, some hydrogenation of the olefins to hexane and conversion of CO to CO₂ was observed, especially at higher conversions. Rapid conversion of α -olefin to internal olefin was also observed in the liquid- and gas-phase operation at high conversion. A steady-state TOF of 0.00070 s⁻¹ at 573 K was obtained for the liquid-phase conversion of heptanoic acid over Pd, which was independent of synthesis method, support composition, Pd loading, and acid concentration. The very low TOF was a result of severe catalyst deactivation. Operation in gas-phase allowed for extrapolation of rates to initial time in an effort to evaluate the TOF on a fresh catalyst surface. An initial gas-phase TOF of 0.035 s⁻¹ was estimated from the initial rate at 573 K over supported Pd.

Postmortem characterization of the catalysts revealed a decrease of surface area and almost complete loss of H₂ chemisorption capacity after the liquid-phase operation, which accounts for the low steady-state rate under those conditions. X-ray diffraction and electron microscopy revealed that Pd

nanoparticles supported on carbon sintered substantially during the liquid-phase operation in nearly pure acid. In contrast, carbon-supported Pd nanoparticles were quite stable during gas-phase reaction. Likewise, the sintering of carbon-supported Pd nanoparticles in the liquid-phase was less significant at low acid concentrations. Silica-supported Pd nanoparticles maintained a high dispersion during the liquid-phase operation at high acid concentrations.

3.5. Acknowledgement

This material is based upon work supported by the National Science Foundation (NSF) under Award No. EEC-0813570. Any opinions, findings, and conclusions or recommendations expressed in this material are those of the author(s) and do not necessarily reflect the views of the NSF. We acknowledge discussions with Professor Matthew Neurock at the University of Virginia. We also gratefully acknowledge Mr. Matthew Schneider at the University of Virginia for his help with the bright field TEM.

3.6. References

- [1] Ragauskas, A. J., Williams, C. K., Davison, B. H., Britovsek, G., Cairney, J., Eckert, C. A., Frederick, W. J., Hallett, J. P., Leak, D. J., Liotta, C. L., Mielenz, J. R., Murphy, R., Templer, R., and Tschaplinski, T., 2006, "The path forward for biofuels and biomaterials.," *Science*, **311**(5760), pp. 484–9.
- [2] Renz, M., 2005, "Ketonization of Carboxylic Acids by Decarboxylation: Mechanism and Scope," *Eur J Org Chem*, **2005**(6), pp. 979–988.
- [3] Gaertner, C. A., Serrano-Ruiz, J. C., Braden, D. J., and Dumesic, J. A., 2009, "Catalytic coupling of carboxylic acids by ketonization as a processing step in biomass conversion," *J Catal*, **266**(1), pp. 71–78.

- [4] Lopez-Ruiz, J. A., and Davis, R. J., 2014, "Decarbonylation of heptanoic acid over carbon-supported platinum nanoparticles," *Green Chem*, **16**(2), pp. 683–694.
- [5] Boda, L., Onyestyák, G., Solt, H., Lónyi, F., Valyon, J., and Thernesz, A., 2010, "Catalytic hydroconversion of tricaprylin and caprylic acid as model reaction for biofuel production from triglycerides," *Appl Catal A-Gen*, **374**(1-2), pp. 158–169.
- [6] Lugo-José, Y. K., Monnier, J. R., and Williams, C. T., 2014, "Gas-Phase, Catalytic Hydrodeoxygenation of Propanoic Acid, Over Supported Group VIII Noble Metals: Metal and Support Effects," *Appl Catal A-Gen*, **469**, pp. 410–418.
- [7] Lugo-José, Y. K., Monnier, J. R., Heyden, A., and Williams, C. T., 2014, "Hydrodeoxygenation of propanoic acid over silica-supported palladium: effect of metal particle size," *Catal Sci Technol*.
- [8] Lestari, S., Mäki-Arvela, P., Bernas, H., Simakova, O., Sjöholm, R., Beltramini, J., Lu, G. Q. M., Myllyoja, J., Simakova, I., and Murzin, D. Y., 2009, "Catalytic Deoxygenation of Stearic Acid in a Continuous Reactor over a Mesoporous Carbon-Supported Pd Catalyst," *Energ Fuel*, **23**(8), pp. 3842–3845.
- [9] Lestari, S., Simakova, I., Tokarev, A., Mäki-Arvela, P., Eränen, K., and Murzin, D. Y., 2008, "Synthesis of Biodiesel via Deoxygenation of Stearic Acid over Supported Pd / C Catalyst," *Catal Lett*, **122**(3-4), pp. 247–251.
- [10] Mäki-Arvela, P., Snåre, M., Eränen, K., Myllyoja, J., and Murzin, D. Y., 2008, "Continuous decarboxylation of lauric acid over Pd/C catalyst," *Fuel*, **87**(17-18), pp. 3543–3549.
- [11] Rozmysłowicz, B., Mäki-Arvela, P., Lestari, S., Simakova, O. A., Eränen, K., Simakova, I. L., Murzin, D. Y., and Salmi, T. O., 2010, "Catalytic Deoxygenation of Tall Oil Fatty Acids Over a

- Palladium-Mesoporous Carbon Catalyst : A New Source of Biofuels,” *Top Catal*, **53**(15-18), pp. 1274–1277.
- [12] Snåre, M., Kubičková, I., Mäki-Arvela, P., Eränen, K., Wärnå, J., and Murzin, D. Y., 2007, “Production of diesel fuel from renewable feeds: Kinetics of ethyl stearate decarboxylation,” *Chem Eng J*, **134**, pp. 29–34.
- [13] Snåre, M., Kubičková, I., Mäki-Arvela, P., Eränen, K., and Murzin, D. Y., 2006, “Heterogeneous Catalytic Deoxygenation of Stearic Acid for Production of Biodiesel,” *Ind Eng Chem Res*, **45**(45), pp. 5708–5715.
- [14] Simakova, I., Rozmysłowicz, B., Simakova, O. A., Mäki-Arvela, P., Simakov, A., and Murzin, D. Y., 2011, “Catalytic Deoxygenation of C18 Fatty Acids Over Mesoporous Pd / C Catalyst for Synthesis of Biofuels,” *Top Catal*, **54**(8-9), pp. 460–466.
- [15] Kubičková, I., Snåre, M., Eränen, K., Mäki-Arvela, P., and Murzin, D., 2005, “Hydrocarbons for diesel fuel via decarboxylation of vegetable oils,” *Catal Today*, **106**(1-4), pp. 197–200.
- [16] Mäki-Arvela, P., Kubičková, I., Snåre, M., Eränen, K., and Murzin, D. Y., 2007, “Catalytic Deoxygenation of Fatty Acids and Their Derivatives,” *Energ Fuel*, **21**(1), pp. 30–41.
- [17] Snåre, M., Kubičková, I., Mäki-Arvela, P., Chichova, D., Eränen, K., and Murzin, D. Y., 2008, “Catalytic deoxygenation of unsaturated renewable feedstocks for production of diesel fuel hydrocarbons,” *Fuel*, **87**(6), pp. 933–945.
- [18] Lestari, S., Mäki-Arvela, P., Simakova, I., Beltramini, J., Lu, G. Q. M., and Murzin, D. Y., 2009, “Catalytic Deoxygenation of Stearic Acid and Palmitic Acid in Semibatch Mode,” *Catal Lett*, **130**(1-2), pp. 48–51.

- [19] Simakova, I., Simakova, O., Mäki-Arvela, P., Simakov, A., Estrada, M., and Murzin, D. Y., 2009, “Deoxygenation of palmitic and stearic acid over supported Pd catalysts: Effect of metal dispersion,” *Appl Catal A-Gen*, **355**, pp. 100–108.
- [20] Immer, J. G., and Lamb, H. H., 2010, “Fed-Batch Catalytic Deoxygenation of Free Fatty Acids,” *Energ Fuel*, **130**(10), pp. 5291–5299.
- [21] Immer, J. G., Kelly, M. J., and Lamb, H. H., 2010, “Catalytic reaction pathways in liquid-phase deoxygenation of C18 free fatty acids,” *Appl Catal A-Gen*, **375**(1), pp. 134–139.
- [22] Ford, J. P., Immer, J. G., and Lamb, H. H., 2012, “Palladium Catalysts for Fatty Acid Deoxygenation: Influence of the Support and Fatty Acid Chain Length on Decarboxylation Kinetics,” *Top Catal*, **55**(3-4), pp. 175–184.
- [23] Maier, W. F., Roth, W., Thies, I., v. Rague Schleyer, P., Ragukschleyer, P., and Schleyer, R., 1982, “Gas Phase Decarboxylation of Carboxylic Acids,” *Chem Ber*, **115**, pp. 808–812.
- [24] Lamb, H. H., Sremaniak, L., and Whitten, J. L., 2012, “Reaction pathways for butanoic acid decarboxylation on the (111) surface of a Pd nanoparticle,” *Surf Sci*, **607**(111), pp. 130–137.
- [25] Lu, J., Behtash, S., and Heyden, A., 2012, “Theoretical Investigation of the Reaction Mechanism of the Decarboxylation and Decarbonylation of Propanoic Acid on Pd (111) Model Surfaces,” *J Phys Chem C*, **116**(116), pp. 14328–14341.
- [26] Lu, J., Behtash, S., Faheem, M., and Heyden, A., 2013, “Microkinetic modeling of the decarboxylation and decarbonylation of propanoic acid over Pd(111) model surfaces based on parameters obtained from first principles,” *J Catal*, **305**, pp. 56–66.

- [27] Benavidez, A. D., Burton, P. D., Nogales, J. L., Jenkins, A. R., Ivanov, S. A., Miller, J. T., Karim, A. M., and Datye, A. K., 2014, "Improved selectivity of carbon-supported palladium catalysts for the hydrogenation of acetylene in excess ethylene," *Appl Catal A-Gen*, **482**, pp. 108–115.
- [28] Pham, H. N., Pagan-Torres, Y. J., Serrano-Ruiz, J. C., Wang, D., Dumesic, J. A., and Datye, A. K., 2011, "Improved hydrothermal stability of niobia-supported Pd catalysts," *Appl Catal A-Gen*, **397**(1-2), pp. 153–162.
- [29] Pham, H. N., Anderson, A. E., Johnson, R. L., Schmidt-Rohr, K., and Datye, A. K., 2012, "Improved hydrothermal stability of mesoporous oxides for reactions in the aqueous phase.," *Angew Chem Int Ed Engl*, **51**(52), pp. 13163–7.
- [30] Ping, E. W., Pierson, J., Wallace, R., Miller, J. T., Fuller, T. F., and Jones, C. W., 2011, "On the nature of the deactivation of supported palladium nanoparticle catalysts in the decarboxylation of fatty acids," *Appl Catal A-Gen*, **396**(1-2), pp. 85–90.
- [31] Ping, E. W., Wallace, R., Pierson, J., Fuller, T. F., and Jones, C. W., 2010, "Highly dispersed palladium nanoparticles on ultra-porous silica mesocellular foam for the catalytic decarboxylation of stearic acid," *Micropor Mesopor Mat*, **132**(1-2), pp. 174–180.
- [32] Grenoble, D. C., and Estadt, M. M., 1981, "The chemistry and catalysis of the water gas shift reaction: 1. The kinetics over supported metal catalysts," *J Catal*, **67**(1), pp. 90–102.

Chapter 4. Mechanistic Insights on the Decarbonylation and Decarboxylation of Propanoic Acid over Palladium Catalysts

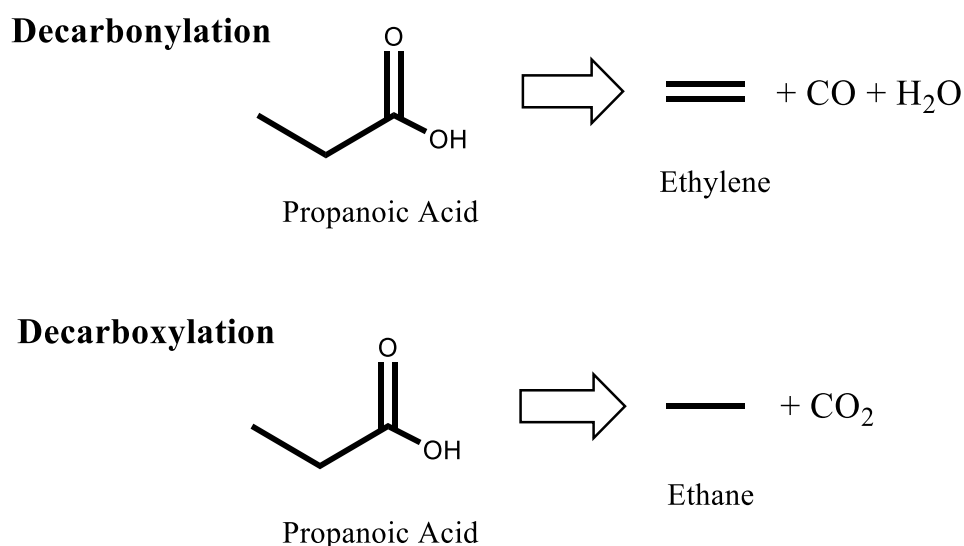
Abstract

The decarbonylation and decarboxylation of gaseous propanoic acid over Pd nanoparticles supported on silica and carbon were studied in a continuous flow fixed bed reactor operated at 1 bar and temperatures ranging from 533 to 573 K. Silica-supported Pt, and Rh nanoparticles were also studied for comparison. The initial turnover frequency at 573 K was 0.043, 0.027, and 0.007 s⁻¹ for silica-supported Pd, Pt, and Rh nanoparticles, respectively, confirming the highest specific activity of Pd catalyst. The observed apparent activation energy of propanoic acid conversion over Pd was approximately 130 kJ mol⁻¹ and was independent of support. At partial pressures of propanoic acid ranging from 0.1 to 1 bar, the order of the reaction in acid was zero and the primary reaction was decarbonylation. At acid pressures lower than 0.1 bar, the reaction order with respect to acid was negative and the primary reaction was decarboxylation. Conversion of propanoic anhydride at low partial pressure proceeded by decarbonylation, which suggests that propanoic anhydride may be a surface intermediate in the high pressure decarbonylation of propanoic acid. All the metal catalysts deactivated very rapidly during the first 3 h of reaction, which was accompanied by a change in product selectivity. Although X-ray diffraction and electron microscopy revealed that the size of the metal nanoparticles was relatively unchanged by the reaction conditions, results from N₂ and H₂ adsorption were consistent with deposition of carbonaceous species on the metal surface and in the catalysts pores being responsible for deactivation.

4.1. Introduction

By 2030, the world population is expected to reach 8.3 billion. Fossil fuels will not likely be able to sustain the growth in energy demand to support this population, so new sources of energy need to be developed [1]. According to the BP Energy Outlook 2030, the US is expected to reach energy independence by 2030, but it will need to increase the production of renewable and biorenewable energy by 194%. Thus, renewable energy is projected to be the fastest growing energy in the US, which should to grow by 7.6% per annum to meet $\approx 6\%$ of total energy demand by 2030. New renewable conversion technologies need to be developed to meet this scenario using biomass as feedstock.

The production of energy, fuels, and chemicals from biomass feedstocks, which usually possess a high content of oxygen, represents a chemical challenge and requires a set of oxygen removal reactions to produce oxygen-free hydrocarbons [2]. This set of reactions is collectively known as deoxygenation, which can be accomplished by reactions such as dehydration, ketonization, decarbonylation and decarboxylation. Organic acids that are found in vegetable oils and animal fats can be readily converted to hydrocarbon fuels and chemicals by deoxygenation reactions. For example, linear organic acids are converted to linear alkenes and linear alkanes by decarbonylation and decarboxylation, respectively, as shown for the reaction of propanoic acid in Scheme 4.1.



Scheme 4.1. Decarbonylation and decarboxylation of propanoic acid

showed catalyst deactivation was more severe under low H₂ conditions, which favored coke formation [10]. Also, Snåre *et al.* [10], Mäki-Arvela *et al.* [11] and Bartosz *et al.* [12] showed that when deoxygenation reactions were run under solvent free or concentrated acid conditions, the catalyst deactivation was more severe. Furthermore, the concentration of the organic acid has been reported to influence the deoxygenation rate and the reaction mechanism. For example, Bartosz *et al.* showed that the reaction rate increased when the concentration of acid decreased from 0.6 to 0.15 mol L⁻¹ [12]. In addition, Immer *et al.* showed that as the concentration of acid decreased, the decarboxylation rate decayed rapidly whereas the decarbonylation rate increased [13]. In contrast, Mäki-Arvela *et al.* showed that when the concentration of the fatty acid decreased from 0.44 to 0.22 mol L⁻¹ the steady state reaction rates and product selectivities did not change [11].

Because the presence of H₂ and solvent favor the production of CO₂ and alkanes [5,10–23], researchers often conclude decarboxylation is the primary reaction in these systems. Recent studies that test catalysts in the absence of dihydrogen and/or solvent revealed that the primary reaction path is decarbonylation producing olefins and CO [24–27]. For example, Lopez-Ruiz and Davis showed that during the dihydrogen-free liquid-phase decarbonylation of heptanoic acid over Pt/Norit carbon, the formation of decarboxylation products (alkane and CO₂) was caused by the sequential conversion of CO to CO₂ and hydrogenation of olefins, presumably via water–gas shift and alkene hydrogenation, respectively, when the reaction was run at high conversions [25]. At low conversions, decarbonylation was the main reaction path in both liquid- and gas-phase operation. To explore the importance of catalyst composition and reaction conditions on the conversion of carboxylic acids, we studied systematically the decarbonylation and decarboxylation of propanoic acid over a variety of silica-supported Pd, Pt, and Rh and carbon-supported Pd catalysts in a continuous flow fixed bed reactor. In particular, the influences of metal type, support composition, temperature, and acid concentration on the rate and selectivity were explored. Density functional theoretical calculations were used to elucidate the most energetically favorable reaction path and metal site requirements for decarbonylation and decarboxylation reactions.

4.2. Experimental Methods

4.2.1. Catalyst synthesis

The catalysts were prepared by an incipient wetness impregnation method using aqueous solutions of tetraamminepalladium (II) nitrate, $(\text{NH}_3)_4\text{Pd}(\text{NO}_3)_2$ (Sigma Aldrich) to obtain 5 and 20 wt% Pd loadings on Davisil SiO_2 636 and Norit activated carbon (ROX 0.9), respectively. Tetraammineplatinum (II) nitrate, $(\text{NH}_3)_4\text{Pt}(\text{NO}_3)_2$ (Sigma Aldrich) and rhodium (III) nitrate, $\text{Rh}(\text{NO}_3)_3$ (Sigma Aldrich) were used to obtain a 10 wt% Pt and a 5 wt% Rh on Davisil SiO_2 636. Prior to impregnation, Norit carbon particles were crushed and sieved between 180 μm and 425 μm , whereas Davisil SiO_2 was used as received. After impregnation of the desired metal precursor solution, the catalyst was dried in air at 393 K overnight. The dried SiO_2 solids were then calcined for 3 h at 623 K in air (GTS-Welco MED) flowing at $100 \text{ cm}^3 \text{ min}^{-1}$ followed by reduction for 3 h at 623 K in H_2 (GTS-Welco 99.999%) flowing at $100 \text{ cm}^3 \text{ min}^{-1}$. The dried, metal impregnated, carbon solids were directly reduced in H_2 (GTS-Welco 99.999%) flowing at $100 \text{ cm}^3 \text{ min}^{-1}$ without previous calcination. The temperature ramp for the calcination and reduction step was 1 K min^{-1} . After reduction, the catalysts were cooled, exposed to air, and stored in a vial.

4.2.2. Dihydrogen chemisorption

The metal dispersion was measured by H_2 chemisorption performed on a Micromeritics ASAP 2020 adsorption system. The catalyst was evacuated at 573 K for 10 h followed by a reduction with flowing H_2 (GTS-Welco 99.999%) at 573 K for 3 h. Then, the catalyst sample was evacuated at 573 K and cooled in vacuum to 308 K for the Pt and Rh catalysts, and to 373 K for the Pd catalysts (to prevent β -phase hydride formation). The amount of metal on the surface was evaluated by the total amount of H_2 adsorbed extrapolated to zero pressure, assuming a stoichiometric relationship between H_2 to surface metal of 1:2 (i.e. $\text{H}/\text{Pt} = 1$) for the case of Pt and Pd. Hip *et al.* reported that Rh

nanoparticles can exhibit high values of H/Rh that range from 1.2 to 2 [28]. Therefore, we assumed a stoichiometric relationship of H/Rh equal to 1.6.

4.2.3. Dinitrogen physisorption

The specific surface area was measured by N₂ physisorption using a Micromeritics ASAP 2020. The samples were first evacuated for 180 min at 373 K, after which N₂ adsorption isotherms were measured at 77 K. The Brunauer-Emmett-Teller (BET) method was used to determine the specific surface area.

4.2.4. X-ray diffraction

Powder X-ray diffraction (XRD) analysis from $2\theta = 20$ to 100° was carried out on a X'Pert Pro with monochromatic Cu K α -radiation ($\lambda=1.54056 \text{ \AA}$) using a step size of $1/4^\circ$ and a time step of 1 s.

4.2.5. Electron microscopy

Transmission electron microscopy (TEM) was performed on a FEI Titan operated at 300 keV in EFTEM mode. Energy dispersive X-ray spectroscopy (EDS) was used to obtain elemental analysis of the nanoparticles. Catalyst samples were deposited on SPI lacey-carbon coated Cu grids after being dispersed in ethanol [29].

4.2.6. Catalytic conversion of propanoic acid

As shown in our previous work [25], steady state decarbonylation of pure carboxylic acids in the liquid-phase was characterized by low rates and double-bond isomerization of the product α -olefin. Although the gas-phase reaction was more selective towards the formation of α -olefin, the catalyst deactivated rapidly. To study the reaction path and compare results to those derived from theoretical methods, we chose to evaluate the gas-phase conversion of propanoic acid as a probe reaction for decarbonylation and decarboxylation. The major products CO, CO₂, ethane, ethylene, and 3-pentano-

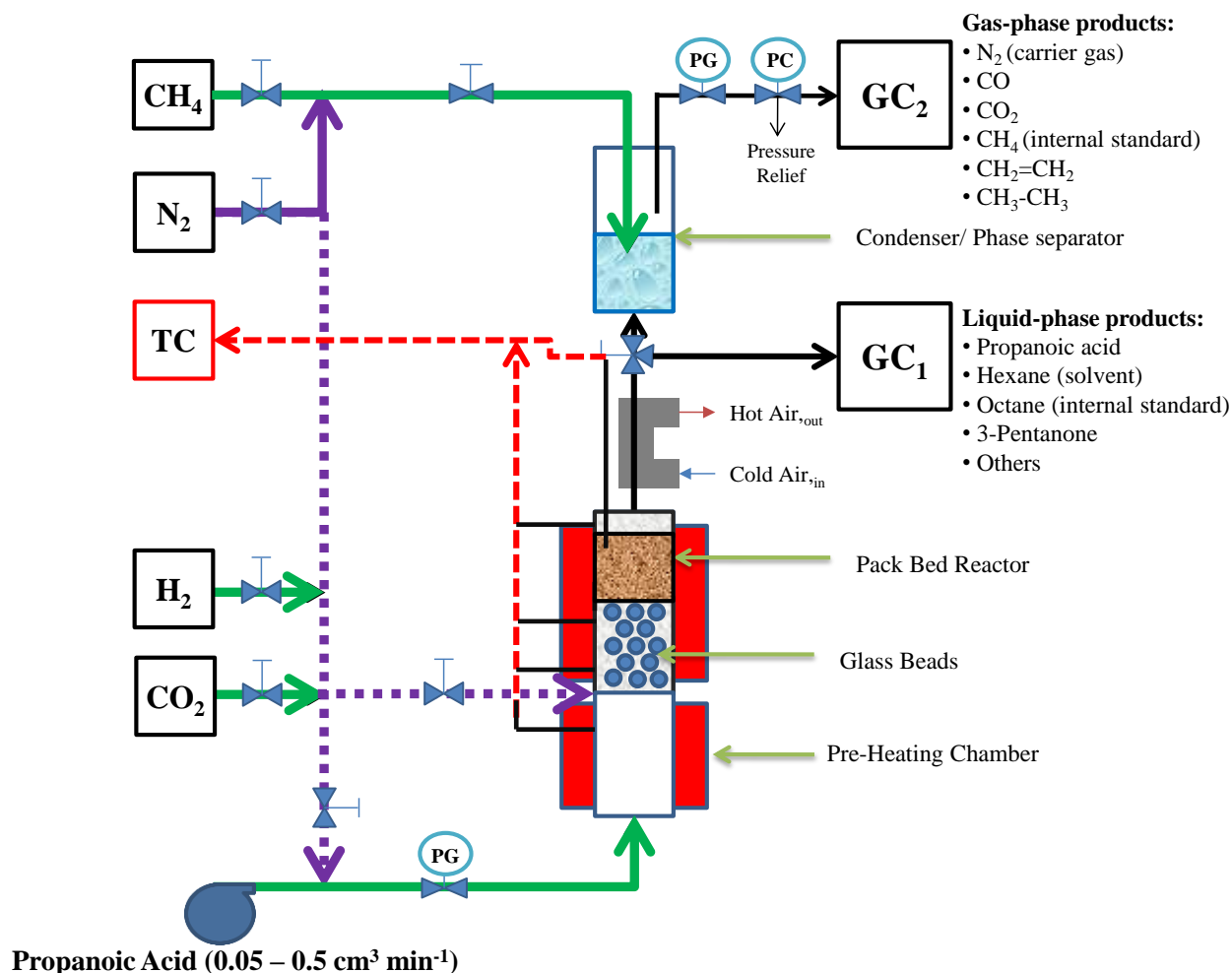


Figure 4.1. Schematic of the reactor system. TC refers to temperature controller, PG refers to pressure gauge, PC refers to the back pressure regulator.

-ne were monitored by gas chromatography. Octane (5 wt%) was used as an internal standard for analysis of the liquid-phase products.

The catalytic decarboxylation/decarbonylation of propanoic acid (Sigma Aldrich $\geq 99.50\%$) was performed in a 1/4" OD x 8" length x 0.035" wall thickness titanium tubing fixed bed tubular reactor. The reactor was composed of a 2 μm pore size frit that immobilized 50 to 500 mg of catalyst pellets and 500 mg of glass beads (Sigma Aldrich 16-25 U.S. sieve) supported on a glass wool plug. Because the catalyst deactivated significantly during a run, fresh catalyst was used for each experiment. After loading the reactor, the system was purged for 60 min with 200 cm³ min⁻¹ of N₂ (GTS-Welco

99.999%) at atmospheric pressure to remove any dioxygen from the system and the pressure was increased to 20 bar to perform a leak test. Then, the temperature was increased to the desired reduction temperature, 573 K, under $100 \text{ cm}^3 \text{ min}^{-1}$ of H_2 (GTS-Welco 99.999%) at 1 K min^{-1} and held isothermally for 3 h at atmospheric pressure. The reactor was finally cooled to the desired reaction temperature, 533 - 573 K, and purged with $200 \text{ cm}^3 \text{ min}^{-1}$ of N_2 (GTS-Welco 99.999%) at atmospheric pressure. For the pure acid experiments, the feed mixture was composed of 95 wt% propanoic acid (Sigma Aldrich $\geq 99.50\%$) and 5 wt% octane (Sigma Aldrich anhydrous 99.00%). Hexane (Sigma Aldrich anhydrous 99.90%) was used as a diluent to prepare feeds with different propanoic acid concentrations (66, 35, 20, 10, 7.5, 5, and 2.5 mol%). Feed mixtures containing hexane, propanoic anhydride, and/or 3-pentanone were dried over molecular sieves 3\AA (Sigma Aldrich) for 24 h prior to loading into the feed pump. The feed was then pumped to the reaction system using a syringe pump (ISCO 500D) operating at specified liquid flow rates (0.05 to $0.50 \text{ cm}^3 \text{ min}^{-1}$). The acid feed mixtures passed through a heated zone before entering the catalytic reactor. Figure 4.1 shows a schematic of the reactor system.

The outlet of the reactor was connected to an air cooled condenser maintained at room temperature to remove the condensable products, such as 3-pentanone, hexane, octane, and unreacted reagent, from the product stream. Samples of the liquid- and gas-phase products were collected approximately every 30 min. The liquid-phase sample was analyzed by a gas chromatograph (GC 7890 A) equipped with a ZB-FFAP column (length $45 \text{ m} \times 0.538 \text{ mm}$) and a flame ionization detector (FID). The product gas was continuously removed from the condenser using $10 \text{ cm}^3 \text{ min}^{-1}$ N_2 (GTS-Welco 99.999%) as a purge gas and $1 \text{ cm}^3 \text{ min}^{-1}$ CH_4 (GTS-Welco 99.999%) as internal standard. The outlet gas of the condenser was analyzed an on-line gas chromatograph (HP 5890 Series II) equipped with a packed column, ShinCarbon ST 80/100, and a thermal conductivity detector (TCD) for detection of N_2 , CO , CO_2 , CH_4 , ethane, ethylene, and any other light hydrocarbons (if any).

A series of control experiments was performed to determine the background conversion of the system at our typical reaction conditions (573 K , 1 bar , and $0.05 \text{ cm}^3 \text{ min}^{-1}$ of liquid feed composed of

95 wt% propanoic acid and 5 wt% octane). In the absence of catalyst, no conversion of propanoic acid was observed. However, when Norit carbon support was used, a background conversion of $\approx 0.4\%$ was found. We did not account for this small background conversion in our calculations of turnover frequency because it decreased over time and a high metal loading of Pd was used with the Norit carbon sample. No conversion of propanoic acid was observed over Davisil SiO₂ at standard conditions. Palladium nanoparticles supported on Norit carbon (20 wt%) and Davisil SiO₂ (5 wt%) were tested at our typical reaction conditions for the reverse water-gas shift by co-feeding the reagents at a molar ratio of 1:1 (i.e. 1 mol of CO₂ per 1 mol of H₂). In addition, ethane dehydrogenation (pure ethane or 1:1 ratio of ethane to CO₂) was tested over Pd at our standard conditions. None of these reactions occurred at our reaction conditions, indicating that the observed ethylene and CO detected during reaction formed by the direct decarbonylation of propanoic acid.

4.2.7. Post-mortem catalyst characterization

The spent catalysts were recovered from the reactor, washed with 25 mL of methanol and sonicated in a methanol solution for 30 min to remove reactant and products from the surface of the catalyst. After sonication, the solids were recovered by filtration and dried overnight in air at 400 K. The spent samples were characterized by H₂ chemisorption, N₂ physisorption, XRD, and TEM.

4.2.8. Calculation of rates

The turnover frequency (TOF) is defined as the number of revolutions of the catalytic cycle per unit time [30]. In this work, the TOF was calculated as the rate of formation of the products referred to the number of surface metal atoms evaluated on a freshly prepared catalyst. The main hydrocarbon components in the gas-phase were ethane and ethylene, whereas 3-pentanone and propanoic acid were the main components in the liquid-phase. Some minor amounts of heavier unknown products were also detected in the liquid-phase products (which accounted for $\approx 0.4\%$ of the total detected liquid product), but were neglected in the analysis.

Because all the catalysts deactivated exponentially during the first 3 h of reaction, an initial TOF was calculated by extrapolating the log of the reaction rate to $t = 0$ h. The initial TOF was therefore calculated as [(rate of production (mol s^{-1}) of ethane + ethylene + 2 x moles of 3-pentanone) / (mol of surface metal on a fresh catalyst counted by H_2 chemisorption)].

To probe the deactivation, final TOF was calculated using the rate of formation of the products after 20 h of reaction and the number of surface metal atoms evaluated from H_2 chemisorption on a spent catalyst. The final TOF was therefore calculated as [(rate of production after 20 h of reaction (mol s^{-1}) of ethane + ethylene + 2 x moles of 3-pentanone) / (mol of surface metal on a spent catalyst counted by H_2 chemisorption)].

The deoxygenation conversion is defined here as the formation rates of the major products divided by the feed rate of reagent. Thus, the deoxygenation conversion for propanoic acid was calculated as [(rate of production (mol s^{-1}) of ethane + ethylene + 2 x moles of 3-pentanone) / (moles of propanoic acid fed (mol s^{-1}))].

To appropriately compare the productivity of the catalysts, we reported the time evolution of the site time yield (STY) [30] of individual products based on the number of surface sites counted by H_2 chemisorption of the fresh catalyst.

Two different sets of product selectivities were calculated, the selectivity of carbon oxides for CO and CO_2 , and the selectivity to deoxygenation products for mainly ethylene, ethane, and 3-pentanone. The product selectivity was defined as the moles of a product formed divided by the total moles of all identified products, i.e. selectivity of ethylene [(rate of ethylene) / (rate of ethylene + rate of ethane + 2 x moles of 3-pentanone + moles of unknowns)] and selectivity of CO [(rate of CO) / (rate of CO + rate of CO_2)].

4.3. Results and Discussion

4.3.1. Effect of metal

The decarbonylation and decarboxylation of propanoic acid over 5 wt% Rh, 10 wt% Pt, and 5 wt% Pd supported on Davisil silica were performed at 573 K and 1 bar. Results from characterization of the fresh catalyst and catalysts after reaction (spent) are summarized in Tables 4.1 and 4.2 along with the calculated turnover frequencies of propanoic acid conversion. Figures 4.2 and 4.3 compare the X-ray diffraction patterns and electron micrographs of the fresh and spent catalysts. Results from all the characterization methods confirmed a high fraction of exposed metal ($\geq 49\%$) on the fresh catalysts, with negligible sintering of the metals during reaction. The lower hydrogen uptake on the spent catalysts was likely the result of carbonaceous species deposited on the catalysts during the propanoic acid reactions. Indeed, severe deactivation of the catalysts was observed over the first several hours of reaction, as depicted in Figure 4.4 a.

The reactivity pattern of propanoic acid over Rh, Pt, and Pd, particles is summarized in Figure 4.4. Decarbonylation was the major reaction path observed initially since CO was the major carbon oxide gas product (Figure 4.4b), as already reported in our previous study [25]. If decarbonylation and decarboxylation were the only two reactions to occur, the CO selectivity (Figure 4.4b) would be equal to the ethylene selectivity (Figures 4.4c-e) according to reaction stoichiometry (Scheme 4.1). For the three catalyst tested, decarbonylation slowed dramatically as the catalyst deactivated whereas low rates of ketonization, and perhaps, some decarboxylation were observed. The selectivity of carbon oxides shifted from CO to CO₂ after long time on stream mainly because of ketonization. As shown in Figures 4.4c-e, the ethane produced could not be produced entirely by direct decarboxylation. Evidently some hydrogenation of ethylene to ethane occurred, with the greatest hydrogenation rate observed over Pd during the initial 2 h of reaction.

Table 4.1. Summary of the catalyst characterization and reactivity results for silica-supported Rh and Pt catalysts.

Catalysts	Reaction Temperature (K)	Fraction of Metal Exposed ^a (%)	Metal Particle Size (nm)		Initial TOF ^b (s ⁻¹)	Final TOF ^c (s ⁻¹)
			Chemisorption ^a	TEM		
5 wt% Rh/SiO₂	Fresh	78	1.3	1.5 ± 0.5	-	-
	573	15	-	1.8 ± 0.7	0.027	0.006
10 wt% Pt/SiO₂	Fresh	50	2.0	1.9 ± 0.2	-	-
	573	16	-	2.1 ± 0.4	0.007	0.002

^a Result estimated from H₂ chemisorption

^b Result estimated using extrapolated reaction rates of propanoic acid to time 0 h

^c Result estimated using reaction rates of propanoic acid at the end of the experiment 20 h

Table 4.2. Summary of catalysts characterization and reactivity results for Pd catalysts

Catalyst	Reaction Temperature (K)	Fraction of Pd Exposed ^a (%)	Pd Particle Size ^b (nm)	Surface Area ^c (m ² g ⁻¹)	Initial TOF ^d (s ⁻¹)	Final TOF ^e (s ⁻¹)
5 wt% Pd/SiO₂	Fresh	49	2.0 ± 0.8	460	-	-
	573	19	2.1 ± 0.5	395	0.043	0.0035
	553	19	2.5 ± 0.8	405	0.016	0.0007
	533	24	2.3 ± 0.6	410	0.0055	0.0005
20 wt% Pd/Carbon	Fresh	31	1.9 ± 0.9	1100	-	-
	573	7	2.1 ± 0.8	310	0.035	0.0045
	553	7	2.1 ± 0.6	560	0.013	0.0025
	533	10	2.2 ± 0.5	930	0.0043	0.0011

^a Result estimated from H₂ chemisorption

^b Result estimated from electron microscopy

^c Result estimated from N₂ physisorption

^d Result estimated using extrapolated reaction rates of propanoic acid to time 0 h

^e Result estimated using reaction rates of propanoic acid at the end of the experiment 20 h

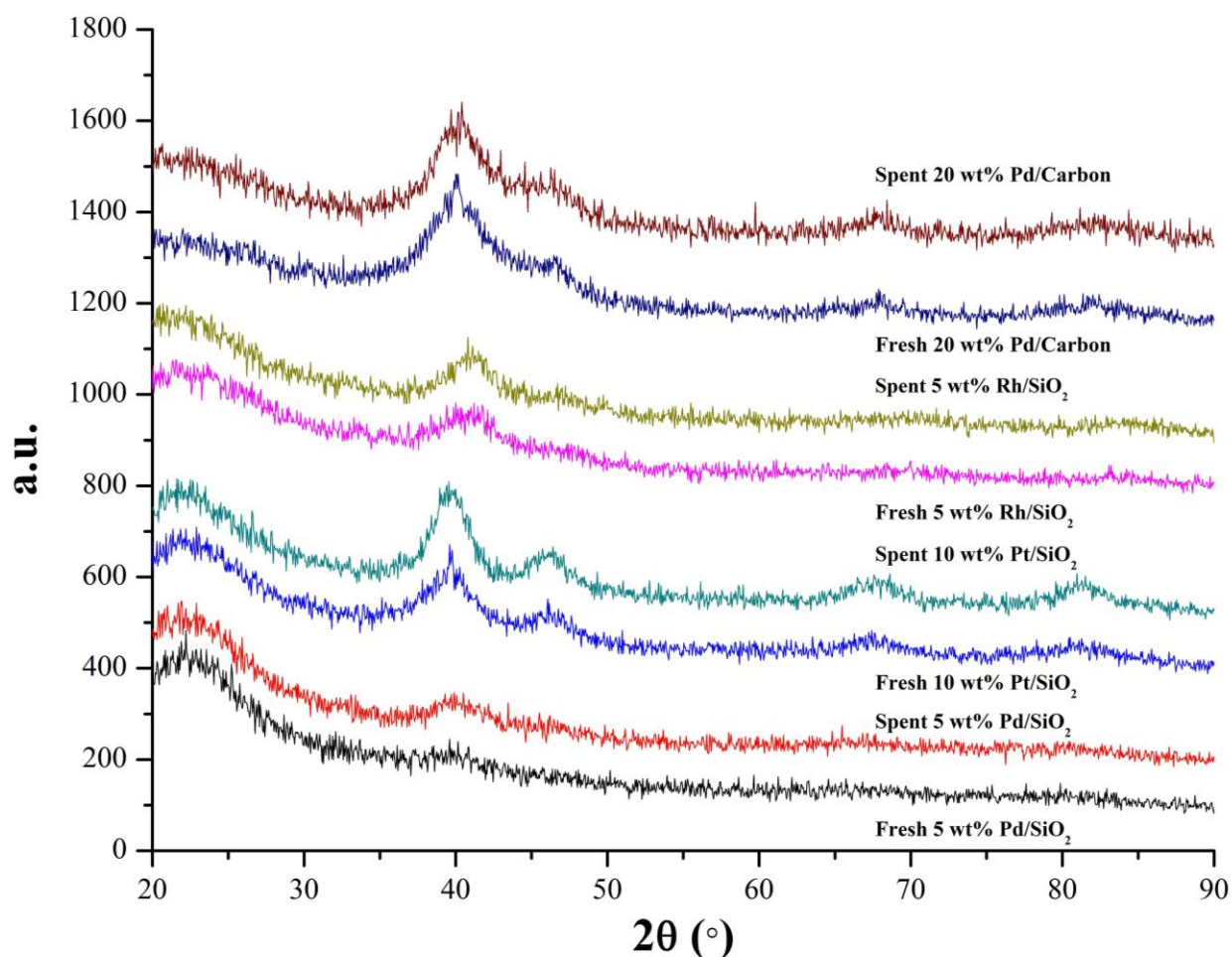


Figure 4.2. Comparison of the XRD patterns of 5 wt% Rh/SiO₂, 10 wt% Pt/SiO₂, 5 wt% Pd/SiO₂, and 20 wt% Pd/Carbon before (fresh) and after (spent) reaction at 573 K. The patterns were offset for clarity. The spent samples were recovered from the reactor and treated as described in the Experimental Methods section. The spent catalysts were collected after 25 h under reaction conditions.

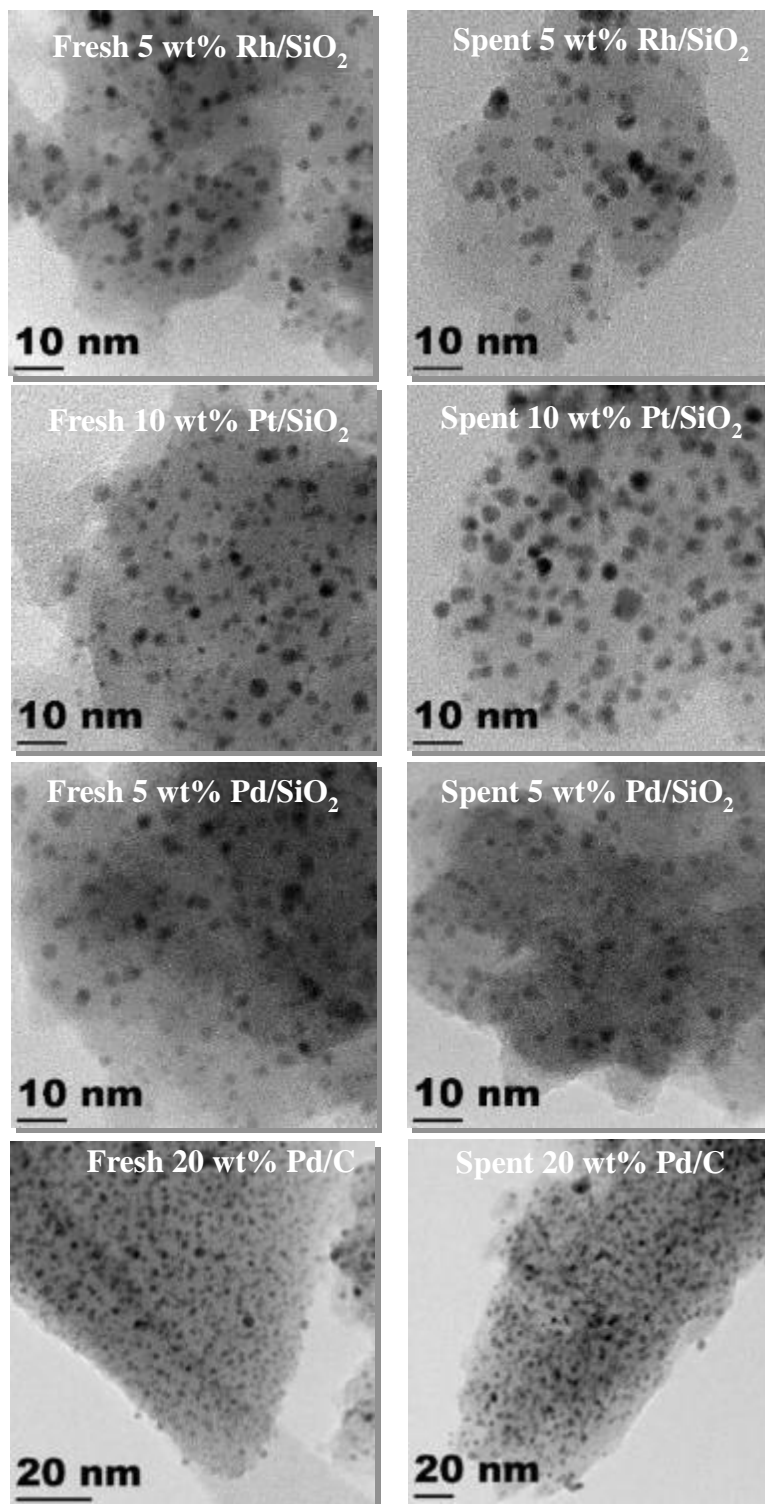
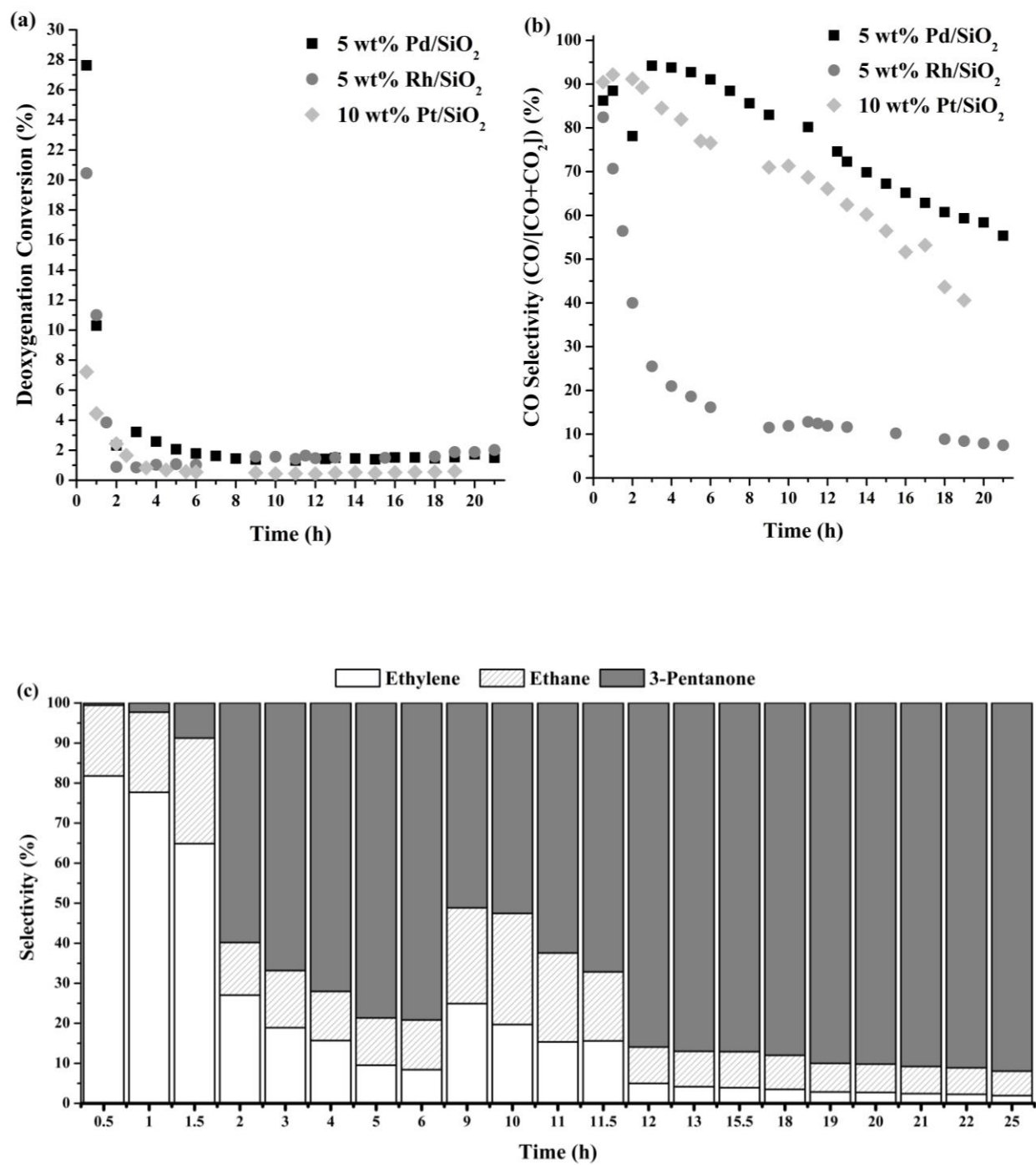


Figure 4.3. TEM images of fresh (left) and spent at 573 K (right) of 5 wt% Rh/SiO₂, 10 wt% Pt/SiO₂, 5 wt% Pd/SiO₂, and 20 wt% Pd/Carbon, respectively. The spent catalysts were collected after 25 h under reaction conditions.



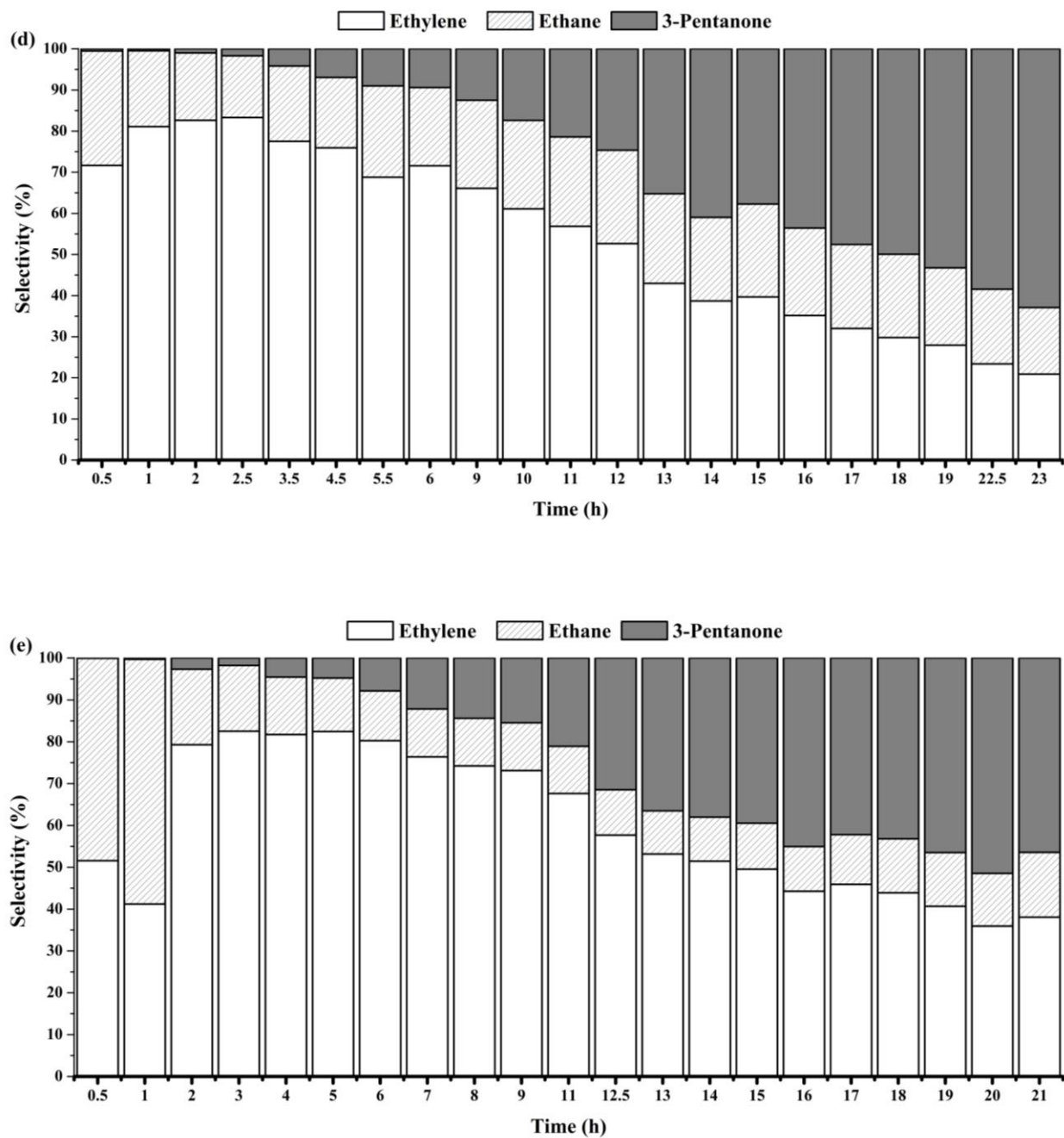


Figure 4.4. Time evolution of the (a) deoxygenation conversion, (b) CO selectivity during the deoxygenation of propanoic acid at 573 K over 5 wt% Rh/SiO₂, 10 wt% Pt/SiO₂, and 5 wt% Pd/SiO₂, run at 1 bar, and 0.05 cm³min⁻¹ of liquid feed composed of 95 wt% propanoic acid and 5 wt% octane. The time evolution of the deoxygenation product selectivity is represented in (c) for 5 wt% Rh/SiO₂, (d) for 10 wt% Pt/SiO₂, and (e) for 5 wt% Pd/SiO₂.

Figure 4.5 presents a semi-log plot of the measured rates at early time for the different catalysts. Extrapolation of the rates to $t = 0$ h allows for an estimation of the initial rate unaffected by deactivation. The initial TOF in Tables 4.1 and 4.2 calculated from extrapolated initial rates shows that Pd was the most active metal with an initial TOF of 0.043 s^{-1} . After long time on stream, the final TOF over Rh was slightly higher than that over Pd, primarily because of the slightly higher ketonization rate on the deactivated catalysts.

Murzin and co-workers [11,15,17–19,21] as well as Lamb and co-workers [13,22,23] studied the liquid-phase conversion of carboxylic acids in the presence of H_2 over Pd catalysts and reported TOFs from 0.01 to 0.1 s^{-1} , which are in the range of the values reported here.

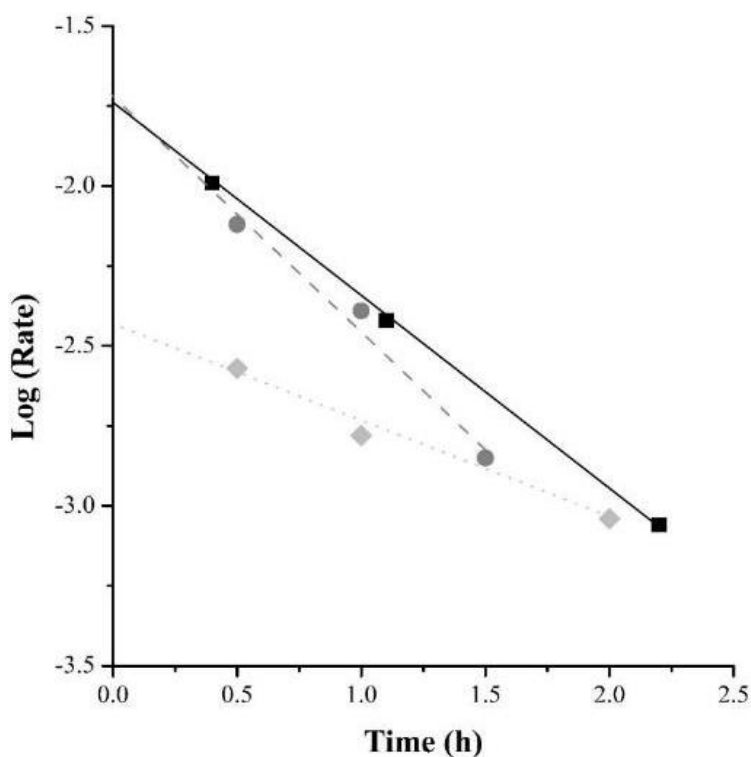


Figure 4.5. Determination of initial rates (mol h^{-1}) by extrapolation to $t = 0$ h. ● represents 5 wt% Rh/SiO₂, ◆ represents 10 wt% Pt/SiO₂, and ■ represents 5 wt% Pd/SiO₂. The reactions conditions were 573 K and 1 bar, and $0.05 \text{ cm}^3\text{min}^{-1}$ of liquid feed composed of 95 wt% propanoic acid and 5 wt% octane.

4.3.2. Effect of support

Carbon is a widely used support for transition metals in deoxygenation reactions because of its high surface area (700 – 1500 m²g⁻¹). [5,13–15,19,22,31,32] Ford *et al.* showed that when Pd nanoparticles were supported on carbon instead of silica, the TOF of the reaction increased by an order of magnitude from 0.055 to 0.206 s⁻¹, for the liquid-phase deoxygenation of succinic acid at 573 K [23]. In contrast, Lugo-José *et al.* showed the TOF to decrease by an order of magnitude when Pd nanoparticles were supported on carbon instead of silica from 0.0053 to 0.0002 s⁻¹, for the gas-phase deoxygenation of propanoic acid at 473 K. Because the catalysts were not characterized after reaction in both instances, we cannot account for the different results. Therefore, we decided to investigate the influence of support on Pd-catalyzed propanoic conversion.

Prior work in our lab with heptanoic acid conversion showed that Norit carbon had a low level of background activity [25]. Therefore, we prepared a Norit carbon-supported Pd catalyst with a high metal loading (20 wt%) to minimize the relative contribution of background conversion associated with this support. Catalysts composed of 5 and 20 wt% Pd supported on Davisil silica and Norit carbon, respectively, were tested for the decarbonylation of propanoic acid at 573 K and 1 bar. The catalysts were characterized using N₂ physisorption, H₂ chemisorption, XRD, and TEM before and after reaction, and the results are summarized in Table 4.2. Post mortem analysis by H₂ chemisorption revealed that a greater fraction of the Pd metal was unavailable for chemisorption on the carbon supported sample. Likewise, the surface area of the carbon-supported catalyst decreased by more than a factor of 3 whereas the surface area of the silica-supported catalyst was only slightly reduced by reaction. The significant loss of carbon surface area suggests the pores of that support were filled with side products from the reaction, consistent with a severe loss in H₂ adsorption capacity. Figures 4.2 and 4.3 show the X-ray diffraction patterns and electron micrographs of the 20 wt% Pd/C catalysts before and after reaction. The lack of evidence for significant Pd particle growth evaluated by XRD and TEM confirms that the loss of catalytic activity during the first 3 h of reaction is primarily the

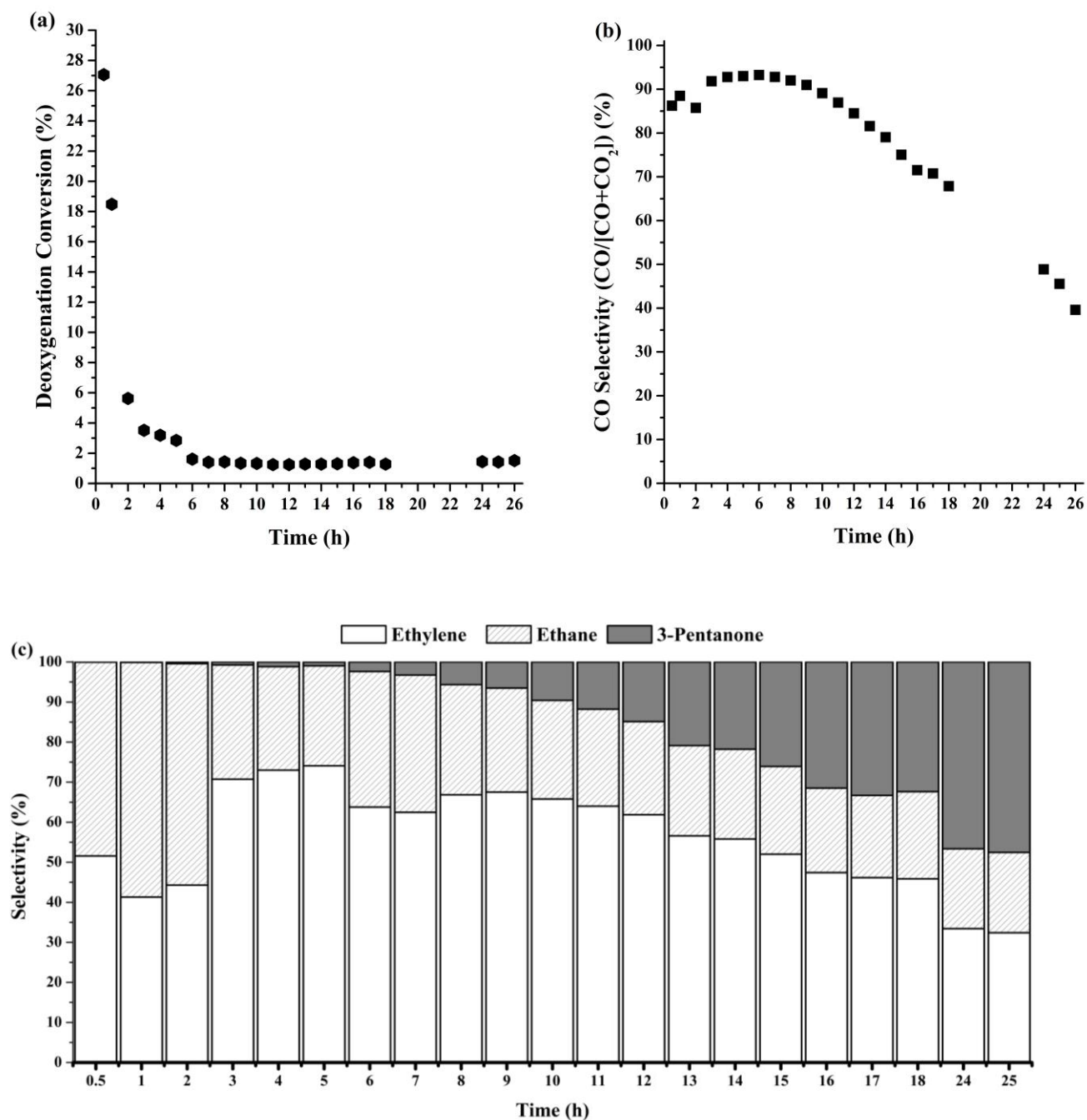


Figure 4.6. Time evolution of the (a) deoxygenation conversion, (b) CO selectivity, and (c) deoxygenation product selectivity during the deoxygenation of propanoic acid at 573 K over 20 wt% Pd/Carbon run at 1 bar, and 0.05 cm³min⁻¹ of liquid feed composed of 95 wt% propanoic acid and 5 wt% octane.

result of deposition of carbonaceous species and heavy oxygenates in the pores and on the metal, as proposed by Ping *et al* [33].

The initial TOF at 573 K was 0.043 and 0.035 s⁻¹ for Pd/SiO₂ and Pd/C respectively, indicating little effect of support on the propanoic acid conversion. The deactivation and product selectivity during propanoic acid conversion over 20 wt% Pd/C at 573 K is summarized in Figure 4.6, which illustrates a similar overall performance to 5 wt% Pd/SiO₂ (Figure 4.4).

4.3.3. Effect of reaction temperature on TOF and extent of deactivation

According to the results summarized in Table 4.2, the loss of surface area of the carbon supported catalyst was less severe during reactions carried out at lower temperatures. After reaction at 533 K, the surface area decreased by only 16% for Pd/carbon (Table 4.2). Likewise, the hydrogen adsorption capacity was less affected by reaction at lower temperatures (533 K) than at higher temperatures (573 K). Figure 4.7 illustrates a lack of severe metal particle growth during reaction at the lower temperatures of 553 and 533 K.

Figure 4.8 presents the time evolution of the catalysts performance for 5 wt% Pd/SiO₂ and 20 wt% Pd/C, respectively, and shows that the catalysts still deactivated at the lower reaction temperature. The selectivity to ketonization at 533 K (Figures 4.8c and 4.8d) was lower at all times compared to the same reaction performed at 573 K (Figures 4.4e and 4.6c). The CO selectivity (Figure 4.8b) was greater than 80% for all 35 h of reaction over 5 wt% Pd/SiO₂, indicating decarbonylation was the main reaction path. Whereas decarbonylation was also the main reaction over carbon-supported Pd, the lower selectivity to ethylene compared to that over silica-supported Pd (Figure 4.8c) suggests a greater rate of hydrogenation over 20 wt% Pd/C (Figure 4.8d).

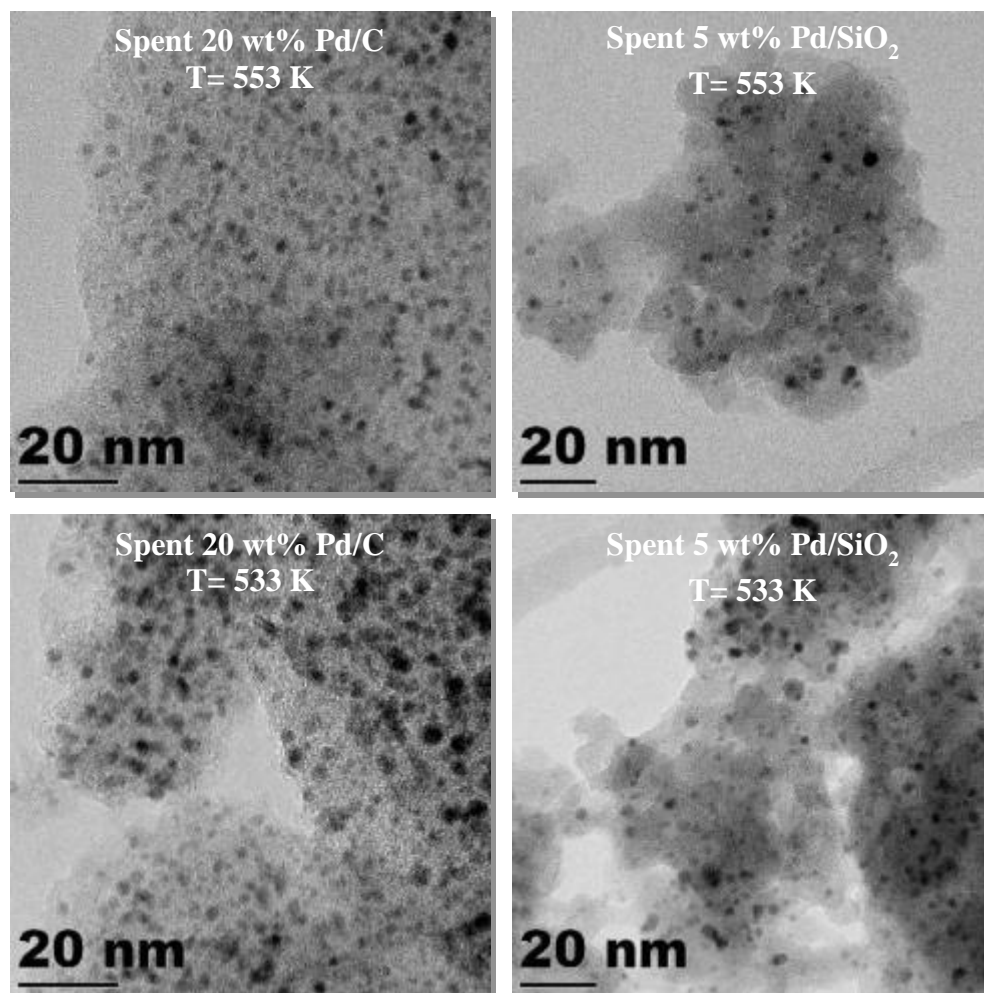
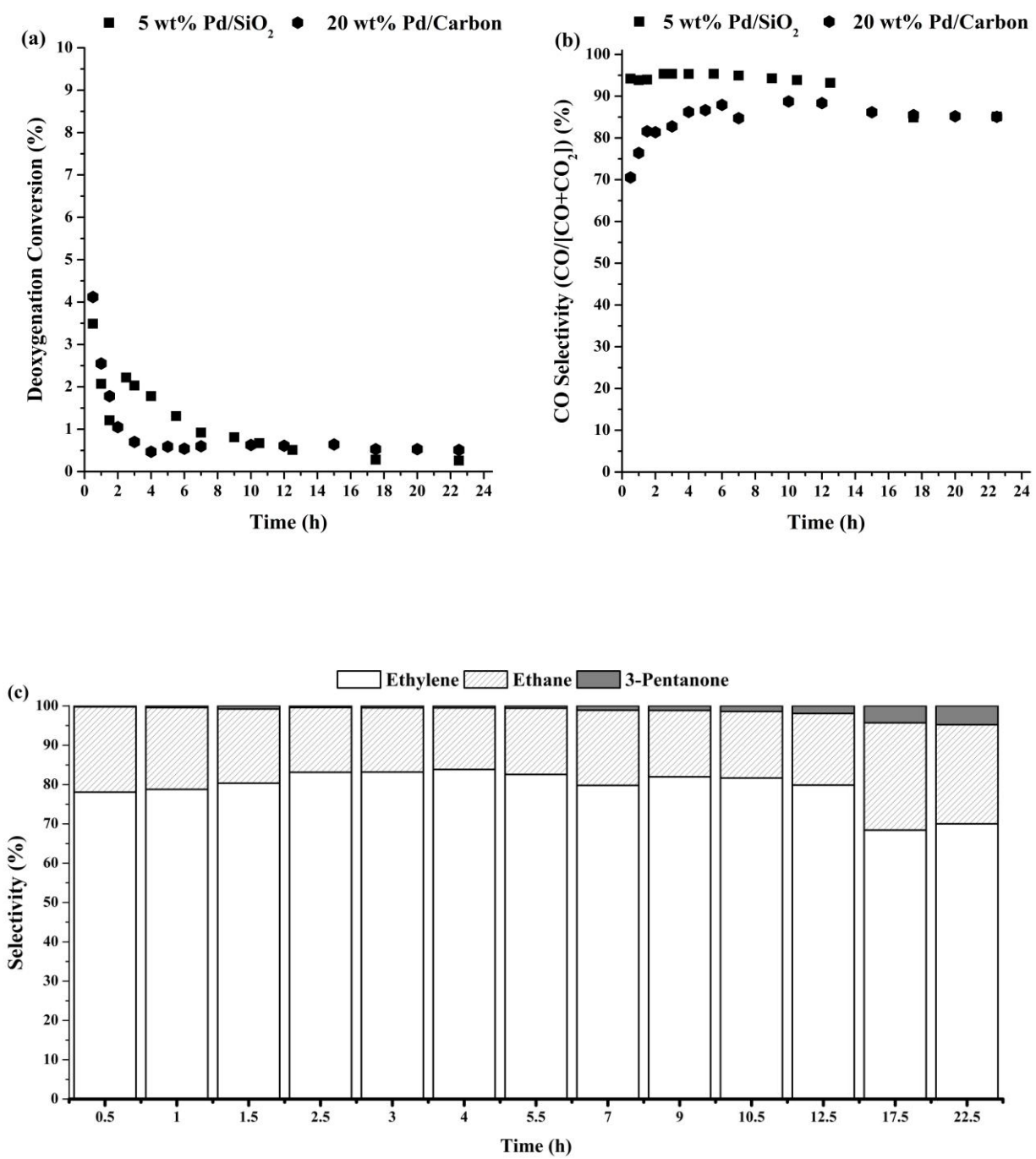


Figure 4.7. TEM images of spent 20 wt% Pd/Carbon (left) and spent 5 wt% Pd/SiO₂ (right) at 553 (top) and 533 K (bottom). The spent samples were recovered from the reactor and treated as described in the Experimental Methods section. The spent catalysts were collected after 25 h under reaction conditions.



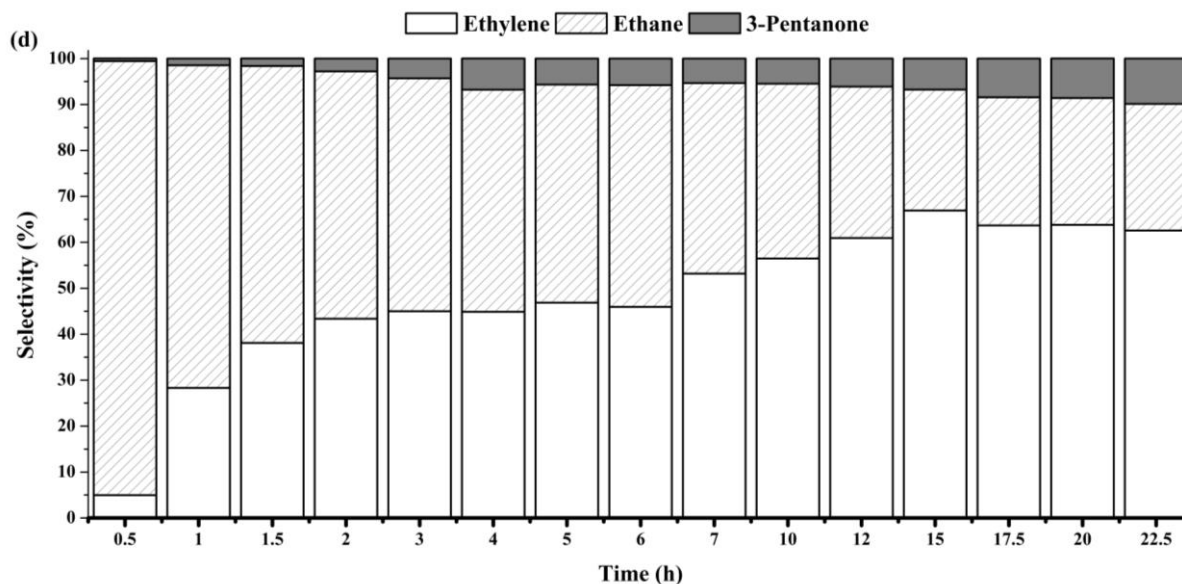


Figure 4.8. Time evolution of the (a) deoxygenation conversion and (b) CO selectivity during the deoxygenation of propanoic acid at 533 K over 5 wt% Pd/SiO₂ and 20 wt% Pd/Carbon run at 1 bar, and 0.05 cm³min⁻¹ of liquid feed composed of 95 wt% propanoic acid and 5 wt% octane. The time evolution of the deoxygenation product selectivity is represented in (c) for over 5 wt% Pd/SiO₂ and (d) for 20 wt% Pd/Carbon.

Figure 4.9 presents the temperature dependence of the rate in an Arrhenius plot and reveals an overall activation energy, E_A , of 131 and 132 kJ mol⁻¹ for 5 wt% Pd/SiO₂ and 20 wt% Pd/C, respectively. The similarity of TOF and E_A for both of the catalysts confirms a lack of any significant influence of the support on the rate of propanoic acid conversion.

Values of E_A equal to 35 and 70 kJ mol⁻¹ have been reported previously over similar Pd catalysts [26,27], but the reported values might be influenced by catalyst deactivation, the presence of co-fed H₂, structure sensitivity of the reaction, and/or support effects. Our value of $E_A \approx 130$ kJ mol⁻¹ is significantly higher but is consistent with elementary step barriers associated with Pd-catalyzed decarbonylation and decarboxylation as calculated by DFT [34].

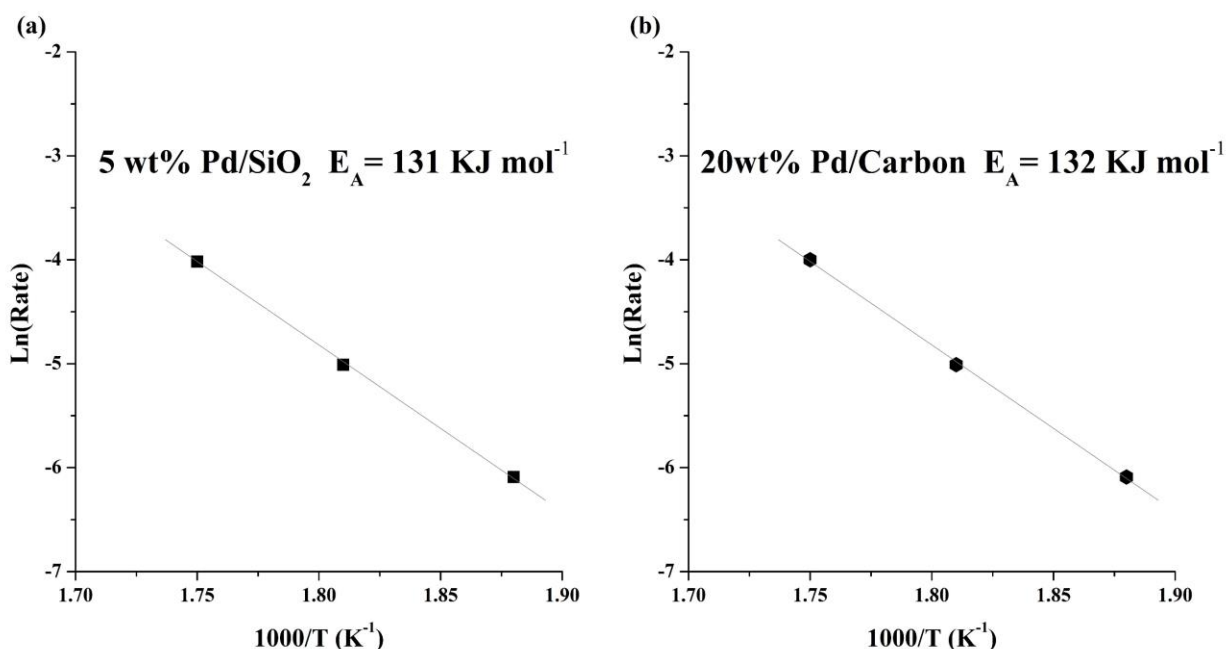


Figure 4.9. Arrhenius-type plots of the initial rates for propanoic acid conversion over (a) 5 wt% Pd/SiO₂ and (b) 20 wt% Pd/Carbon.

Lugo-José *et al.* [26] and Alotaibi *et al.* [27] reported a TOF of 0.0053 s^{-1} at 473 K and 0.0094 at 523 K, respectively, for the gas-phase decarbonylation of propanoic acid over Pd/SiO₂. As shown in Table 4.2, these values were higher compared to our reported values at 533 K, 0.0055 and 0.0043 s^{-1} for Pd supported on silica and carbon, respectively. Lugo-José *et al.* [26] and Alotaibi *et al.* [27] co-fed H₂ during reaction, 20 and 98 vol% respectively, which might have inhibited the catalyst deactivation. These results are consistent with our *post mortem* catalyst characterization. Whereas we reported a 62% loss of exposed Pd after reaction at 573 K over Pd/SiO₂ (Table 4.2), Alotaibi *et al.* reported only a 21% loss of fraction of exposed Pd after reaction at 573 K over Pd/SiO₂.

The catalyst was successfully regenerated after a mild H₂ treatment at 623 K. The catalyst regeneration was monitored by thermogravimetric analysis and electron microscopy and is further discussed in Appendix E.

4.3.4. Effect of propanoic acid concentration

As mentioned in the Introduction, the influence of acid concentration on the rate and product selectivity during reactions over supported Pd catalysts is not straight forward. Some researchers claim a switchover in product selectivity from paraffins and CO₂ to olefins and CO as the deoxygenation rate decreased [13]. Decreasing the concentration of fatty acid also decreased the decarbonylation rate and possibly caused a switchover to favor decarboxylation [13]. More recently, Lugo-José *et al.* showed that during gas-phase reaction of propanoic acid at 1 bar and 473 K over supported Pd, the reaction order was a function of the propanoic acid partial pressure, being zero at high partial pressures and 0.5 at low partial pressures [26].

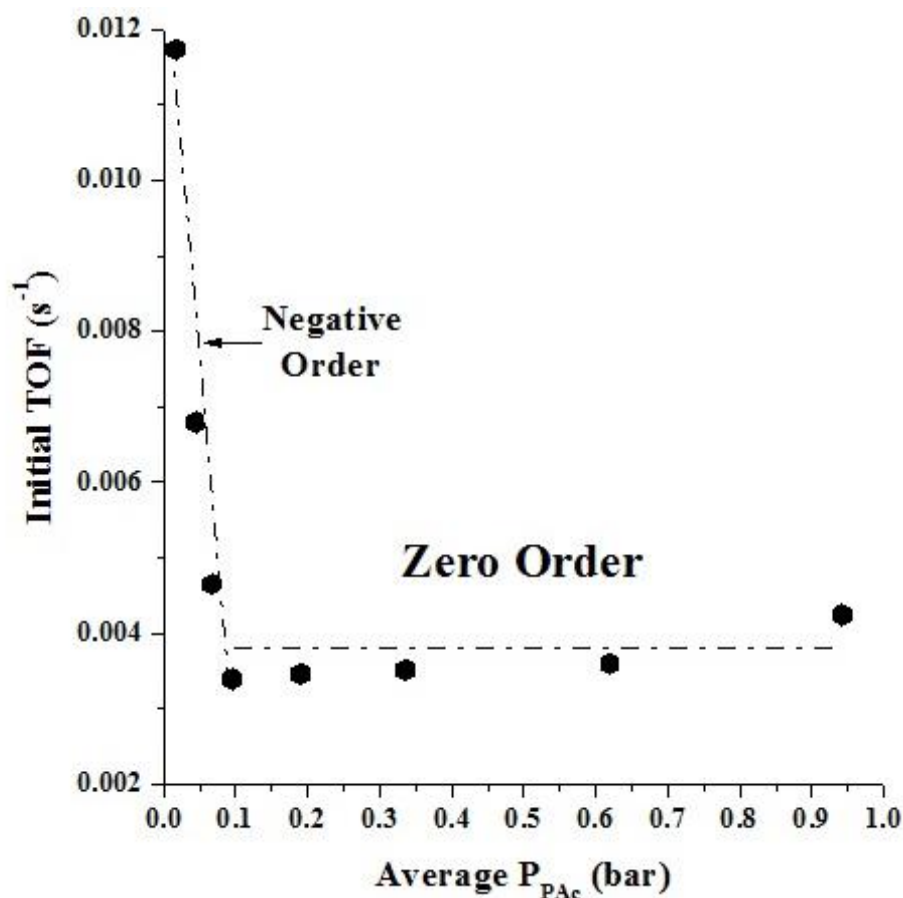


Figure 4.10. Effect of partial pressure of propanoic acid (P_{PAc}) on initial TOF over 20 wt% Pd/C at 1 bar of total pressure and 533 K. The average P_{PA} was determined from the initial and final P_{PA} . The dotted lines are not linear fits, they are meant to guide the reader.

To explore the kinetics of the reaction, the effect of the propanoic acid partial pressure (P_{PAC}) on the rate of conversion was explored over 20 wt% Pd/C at 1 bar and 533 K. The TOF for propanoic acid conversion as a function of partial pressure is presented in Figure 4.10. The constant TOF at compositions above 10 mol% propanoic acid is consistent with zero order reaction kinetics. Below 10 mol%, the increasing TOF with decreasing partial pressure suggests the reaction is negative order in acid.

Figure 4.11 compares the site time yields (STY) of the carbon oxides (CO and CO₂) and deoxygenation products (ethylene, ethane, and 2-pentanone) as a function of time during reaction at high and low partial pressures of propanoic acid. At high partial pressure (zero order regime), the main carbon oxide is initially CO whereas at low partial pressure (negative order regime), the main carbon oxide is initially CO₂, indicating a change from decarbonylation at high partial pressure to decarboxylation at low partial pressure. However, ethane was initially the main deoxygenation product at both high and low partial pressures experiments, because of the hydrogenation of ethylene, as explained earlier.

Density functional theory explains the switchover in initial reaction mechanism at different P_{PAC} and the change in reaction mechanism as the catalyst deactivates by the effect of surface coverage and size of metal ensemble. According to unpublished DFT calculations by the Neurock group, decarboxylation requires an ensemble of 5-7 Pd atoms whereas decarbonylation requires an ensemble of only 2-3 Pd atoms. At high values of P_{PAC} (zero order), the Pd surface is saturated by propanoic acid groups, propanoate and/or propanyl groups, and there are few unoccupied adjacent Pd atoms next to the adsorbed propanoic acid to carry out the decarboxylation reaction. Therefore, decarbonylation is likely to be the main reaction that can take place high P_{PAC} since it only requires 2-3 Pd atoms. At low pressures of acid, the reaction is no longer zero order and the surface is presumably not fully covered by propanoic acid groups, thus allowing for the direct decarboxylation of the adsorbed acid. However, as the catalyst deactivated at low pressures of acid by adsorption of carbonaceous species, the probability of finding unoccupied adjacent Pd atoms decreased, which in

turn shut down direct decarboxylation. The direct decarboxylation reaction, which requires ensembles of only 2-3 atoms of Pd, can now occur.

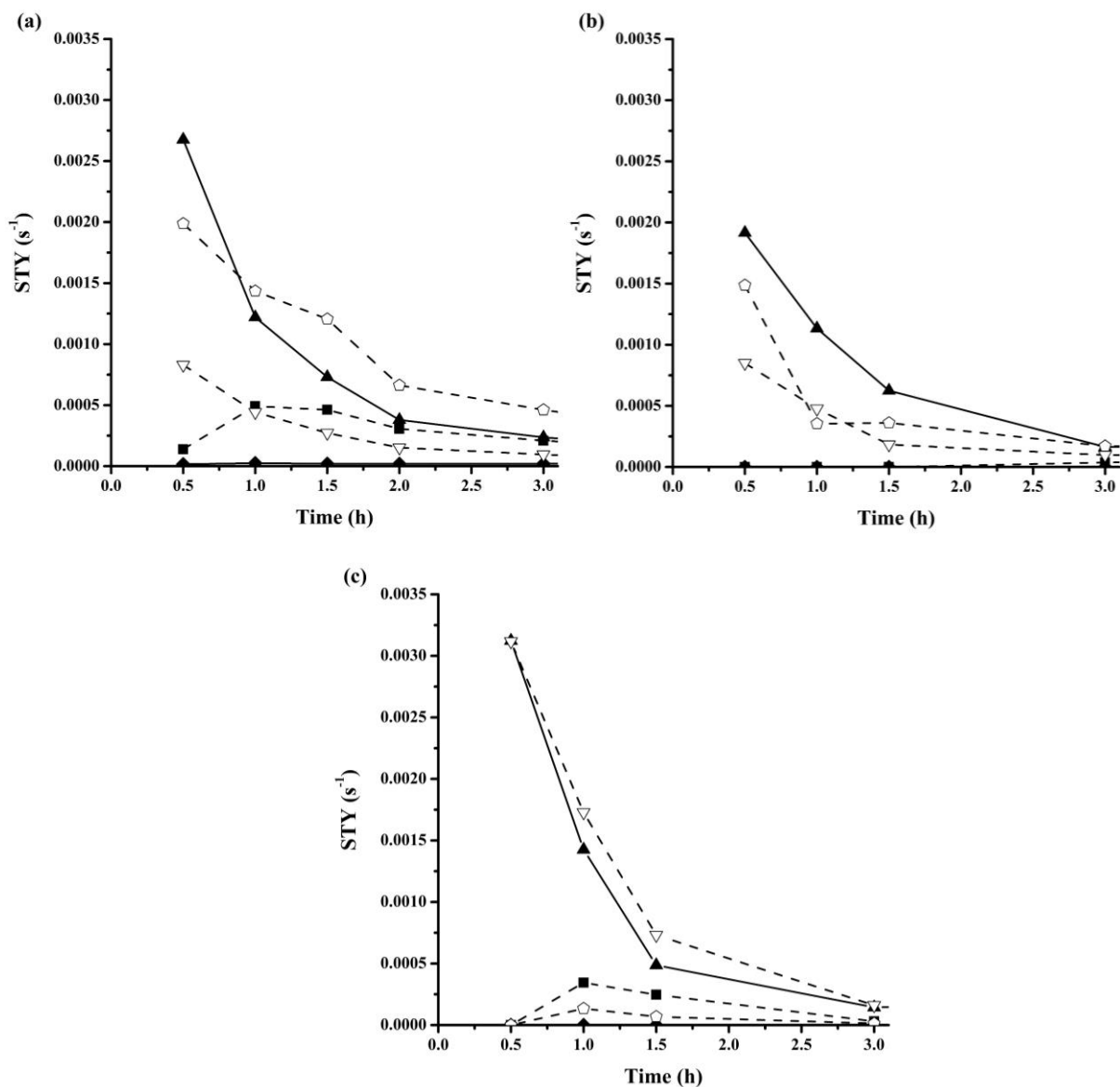
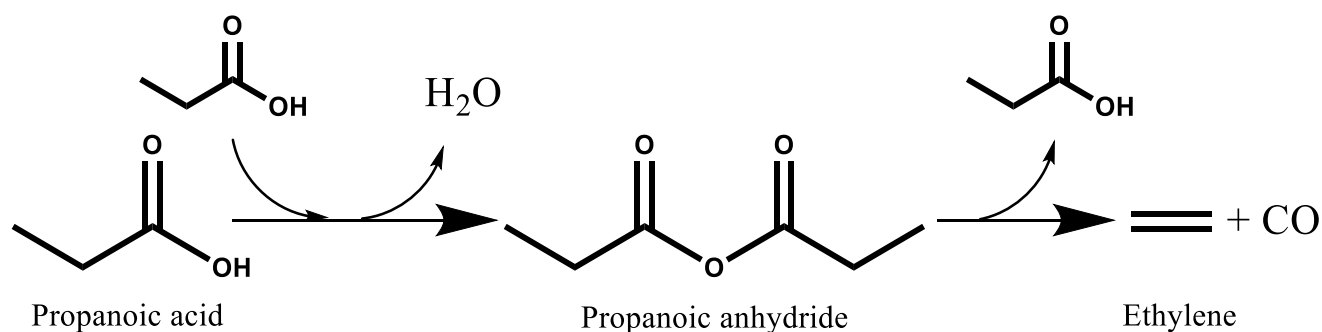


Figure 4.11. Effect of partial pressure on site time yield (STY) during the deoxygenation of propanoic acid over 20 wt% Pd/C at 533 K. The initial partial pressure of propanoic acid was (a) 1.00, (b) 0.10, and (c) 0.05 bar. ■ represents ethylene, ▲ represents ethane, ◆ represents 3-pentanone, ◇ represents CO, and ▽ represents CO₂. The STY was calculated using the Pd dispersion of the fresh catalysts.



Scheme 4.3. Propanoic anhydride as a reaction intermediate for the decarbonylation of propanoic acid.

4.3.5. Propanoic anhydride as potential reaction intermediate

The reactivity of propanoic anhydride (PAn) was compared to that of propanoic acid (PAC) over 20 wt% Pd/C at 533 K and two different partial pressures. The formation of an anhydride intermediate could provide the route for water formation observed during the decarbonylation of a carboxylic acid as shown in Scheme 4.3. In this study the site time yield (STY) was monitored during the initial 3 h of reaction to explore the kinetics on the catalysts prior to severe deactivation and the results are summarized in Figure 4.12.

At high initial partial pressure both PAC and PAn convert on 20 wt% Pd/C at 533 K with similar initial TOF, 0.0042 and 0.0040 s⁻¹ respectively. The catalyst deactivated during the first 2 h under both high and low anhydride partial pressures, but the product distribution was slightly different. As shown in Figure 4.12a, at high partial pressure, the conversion of PAn initially yielded about equal parts of PAC and deoxygenation products. Under these conditions, the catalytic conversion of both PAn and PAC proceeded mainly by decarbonylation. Whereas ethylene was initially the main product during the catalytic conversion of PAn, ethane was initially the main deoxygenation product during the catalytic conversion of PAC. The differences in production of ethylene observed at high P_{PAC} and P_{PAn} are most likely a result of the difference in formation of H₂O during reaction. As shown in

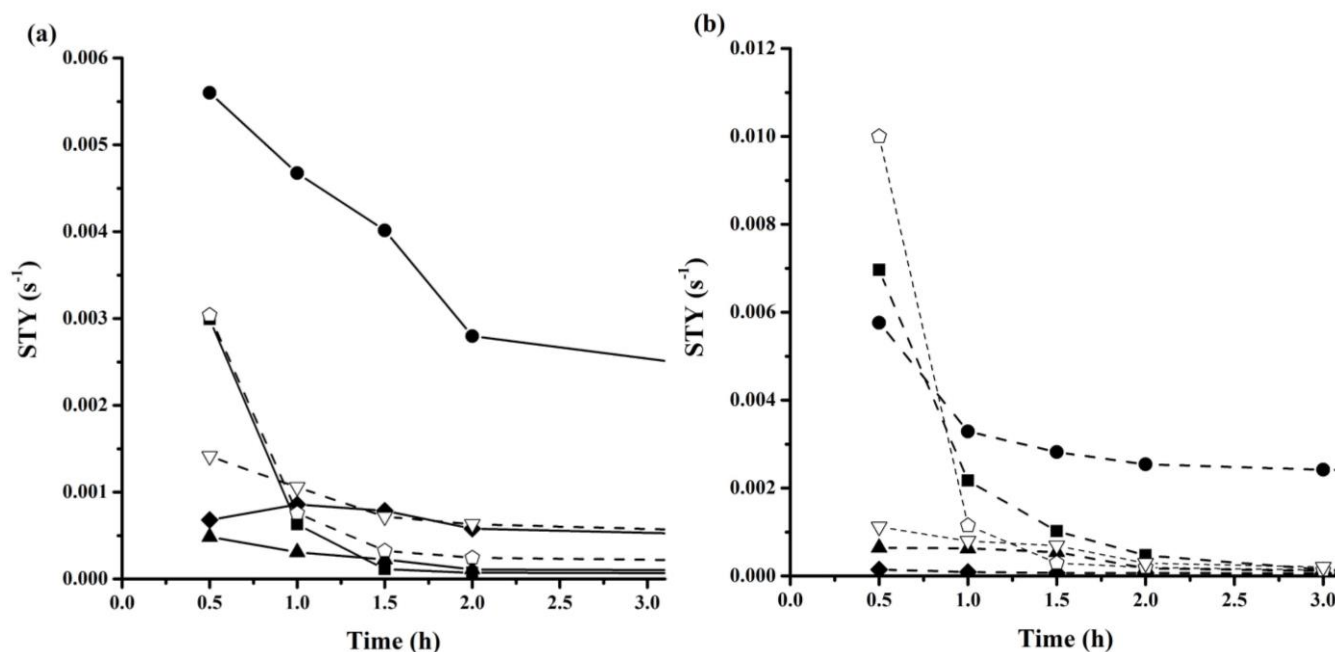


Figure 4.12. Deoxygenation of propanoic anhydride at (a) 1.00 bar for the high initial partial pressure experiment and (b) 0.025 bar for the low initial partial pressure experiment over 20 wt% Pd/Carbon at 533 K and 1 bar. ■ represents ethylene, ▲ represents ethane, ◆ represents 3-pentanone, ● represents propanoic acid, ◇ represents CO, and ▽ represents CO₂. The STY was calculated using the Pd dispersion of the fresh catalysts.

Scheme 4.3, H₂O is generated during the initial coupling of two PAc's to form PAn, but H₂O was never formed when PAn was directly fed in the reactor. In the case of PAc, H₂O is constantly formed by the decarbonylation reaction, which might contribute hydrogen for the hydrogenation of ethylene to ethane.

At low partial pressure, the initial STY values increased for the conversion of PAc and PAn as shown in Figures 4.11c and 4.12b, respectively. As already discussed in the previous section, we observed an increase in the initial TOF and a change in mechanism, from decarbonylation to decarboxylation, when the P_{PAc} was below 10 mol%. However, when partial pressure of propanoic anhydride (P_{PAn}) was below 10 mol%, we did not observe a switchover in product distribution. The main products were still CO and ethylene, similar to those observed at a high partial pressure. This

result suggests that PAn might be a surface reaction intermediate for decarbonylation only at high P_{PAC} . Furthermore, the observation that ethylene was the major product when PAn was fed together with 97.5 mol% hexane indicates little hydrogen transfer from hexane to ethylene occurs on Pd at our reaction conditions.

The very low reactivity of 3-pentanone at high and low partial pressures, 1.0 and 0.025 bar respectively, at 533 K suggests that this molecule is not a reaction intermediate in the decarbonylation or decarboxylation of propanoic acid. These results are further discussed in Appendix D.

4.4. Conclusions

Platinum, rhodium, and palladium nanoparticles were supported on Davisil SiO₂ 636 and Norit carbon, characterized by chemisorption, physisorption, X-ray diffraction, electron microscopy, and evaluated in the conversion of propanoic acid at temperatures ranging from 533 to 573 K. Results from characterization and reactivity testing confirmed that highly dispersed nanoparticles were formed on silica (dispersion \approx 49 - 79%) after a mild calcination and reduction treatment at 623 K. Reduction of Pd onto carbon resulted in a dispersion of \approx 31%. All catalysts severely deactivated during the initial 3 h of reaction over the temperature range of investigation. Palladium was found the most active metal with an initial TOF at 573 K of 0.043 s⁻¹, followed by Rh (0.027 s⁻¹), and Pt (0.007 s⁻¹). The metal nanoparticles were stable under reaction conditions as shown by XRD and TEM. However, chemisorption and physisorption showed a loss of adsorption capacity after reaction. Combined results from characterization suggest that the catalyst deactivation was not due to metal sintering but absorption of carbonaceous species.

Because Pd was the most active catalyst, the kinetics of the reaction as well as the effect of support were explored. The observed E_A over silica-supported and carbon-supported Pd nanoparticles was approximately 130 kJ mol⁻¹.

At 533K, the conversion of propanoic acid was zero order over the range of partial pressures from 0.1 to 1 bar. At lower partial pressures, the rate was negative order in acid. In the zero order regime, the main

reaction path was decarbonylation, whereas decarboxylation was the main reaction path in the negative order regime.

4.5. Acknowledgement

This material is based upon work supported by the National Science Foundation (NSF) under Award No. EEC-0813570 and by BP. Any opinions, findings, and conclusions or recommendations expressed in this material are those of the author(s) and do not necessarily reflect the views of the NSF. We acknowledge discussions with Dr. Glenn Sunley at BP, and Dr. Hien Pham and Professor Abhaya Datye at the University of New Mexico. We also gratefully acknowledge the help Mr. Matthew Schneider at the University of Virginia for his help with the TEM.

4.6. References

- [1] 2013, BP Energy Outlook 203, London, UK.
- [2] Ragauskas, A. J., Williams, C. K., Davison, B. H., Britovsek, G., Cairney, J., Eckert, C. A., Frederick, W. J., Hallett, J. P., Leak, D. J., Liotta, C. L., Mielenz, J. R., Murphy, R., Templer, R., and Tschaplinski, T., 2006, "The path forward for biofuels and biomaterials.," *Science*, **311**(5760), pp. 484–9.
- [3] Renz, M., 2005, "Ketonization of Carboxylic Acids by Decarboxylation: Mechanism and Scope," *Eur J Org Chem*, **2005**(6), pp. 979–988.
- [4] Gaertner, C. A., Serrano-Ruiz, J. C., Braden, D. J., and Dumesic, J. A., 2009, "Catalytic coupling of carboxylic acids by ketonization as a processing step in biomass conversion," *J Catal*, **266**(1), pp. 71–78.

- [5] Snåre, M., Kubičková, I., Mäki-Arvela, P., Eränen, K., and Murzin, D. Y., 2006, "Heterogeneous Catalytic Deoxygenation of Stearic Acid for Production of Biodiesel," *Ind Eng Chem Res*, **45**(45), pp. 5708–5715.
- [6] Miller, J. A., Nelson, J. A. J. A., and Byrne, M. P., 1993, "A Highly Catalytic and Selective Conversion of Carboxylic Acids to 1-Alkenes of One Less Carbon Atom," *J Org Chem*, **58**(1), pp. 18–20.
- [7] Maier, W. F., Roth, W., Thies, I., v. Rague Schleyer, P., Ragukschleyer, P., and Schleyer, R., 1982, "Gas Phase Decarboxylation of Carboxylic Acids," *Chem Ber*, **115**, pp. 808–812.
- [8] Morgan, T., Grubb, D., Santillan-Jimenez, E., Crocker, M., and Crocker, E. S. M., 2010, "Conversion of Triglycerides to Hydrocarbons Over Supported Metal Catalysts," *Top Catal*, **53**(11-12), pp. 820–829.
- [9] Santillan-Jimenez, E., Morgan, T., Lacny, J., Mohapatra, S., and Crocker, M., 2012, "Catalytic deoxygenation of triglycerides and fatty acids to hydrocarbons over carbon-supported nickel," *Fuel*, **103**(September), pp. 1010–1017.
- [10] Snåre, M., Kubičková, I., Mäki-Arvela, P., Chichova, D., Eränen, K., and Murzin, D. Y., 2008, "Catalytic deoxygenation of unsaturated renewable feedstocks for production of diesel fuel hydrocarbons," *Fuel*, **87**(6), pp. 933–945.
- [11] Mäki-Arvela, P., Snåre, M., Eränen, K., Myllyoja, J., and Murzin, D. Y., 2008, "Continuous decarboxylation of lauric acid over Pd/C catalyst," *Fuel*, **87**(17-18), pp. 3543–3549.
- [12] Rozmysłowicz, B., Mäki-Arvela, P., Lestari, S., Simakova, O. A., Eränen, K., Simakova, I. L., Murzin, D. Y., and Salmi, T. O., 2010, "Catalytic Deoxygenation of Tall Oil Fatty Acids Over a

- Palladium-Mesoporous Carbon Catalyst : A New Source of Biofuels,” *Top Catal*, **53**(15-18), pp. 1274–1277.
- [13] Immer, J. G., Kelly, M. J., and Lamb, H. H., 2010, “Catalytic reaction pathways in liquid-phase deoxygenation of C18 free fatty acids,” *Appl Catal A-Gen*, **375**(1), pp. 134–139.
- [14] Lestari, S., Mäki-Arvela, P., Bernas, H., Simakova, O., Sjöholm, R., Beltramini, J., Lu, G. Q. M., Myllyoja, J., Simakova, I., and Murzin, D. Y., 2009, “Catalytic Deoxygenation of Stearic Acid in a Continuous Reactor over a Mesoporous Carbon-Supported Pd Catalyst,” *Energ Fuel*, **23**(8), pp. 3842–3845.
- [15] Lestari, S., Simakova, I., Tokarev, A., Mäki-Arvela, P., Eränen, K., and Murzin, D. Y., 2008, “Synthesis of Biodiesel via Deoxygenation of Stearic Acid over Supported Pd / C Catalyst,” *Catal Lett*, **122**(3-4), pp. 247–251.
- [16] Snåre, M., Kubičková, I., Mäki-Arvela, P., Eränen, K., Wärnå, J., and Murzin, D. Y., 2007, “Production of diesel fuel from renewable feeds: Kinetics of ethyl stearate decarboxylation,” *Chem Eng J*, **134**, pp. 29–34.
- [17] Simakova, I., Rozmysłowicz, B., Simakova, O. A., Mäki-Arvela, P., Simakov, A., and Murzin, D. Y., 2011, “Catalytic Deoxygenation of C18 Fatty Acids Over Mesoporous Pd / C Catalyst for Synthesis of Biofuels,” *Top Catal*, **54**(8-9), pp. 460–466.
- [18] Kubičková, I., Snåre, M., Eränen, K., Mäki-Arvela, P., and Murzin, D., 2005, “Hydrocarbons for diesel fuel via decarboxylation of vegetable oils,” *Catal Today*, **106**(1-4), pp. 197–200.
- [19] Mäki-Arvela, P., Kubičková, I., Snåre, M., Eränen, K., and Murzin, D. Y., 2007, “Catalytic Deoxygenation of Fatty Acids and Their Derivatives,” *Energ Fuel*, **21**(1), pp. 30–41.

- [20] Lestari, S., Mäki-Arvela, P., Simakova, I., Beltramini, J., Lu, G. Q. M., and Murzin, D. Y., 2009, "Catalytic Deoxygenation of Stearic Acid and Palmitic Acid in Semibatch Mode," *Catal Lett*, **130**(1-2), pp. 48–51.
- [21] Simakova, I., Simakova, O., Mäki-Arvela, P., Simakov, A., Estrada, M., and Murzin, D. Y., 2009, "Deoxygenation of palmitic and stearic acid over supported Pd catalysts: Effect of metal dispersion," *Appl Catal A-Gen*, **355**, pp. 100–108.
- [22] Immer, J. G., and Lamb, H. H., 2010, "Fed-Batch Catalytic Deoxygenation of Free Fatty Acids," *Energ Fuel*, **130**(10), pp. 5291–5299.
- [23] Ford, J. P., Immer, J. G., and Lamb, H. H., 2012, "Palladium Catalysts for Fatty Acid Deoxygenation: Influence of the Support and Fatty Acid Chain Length on Decarboxylation Kinetics," *Top Catal*, **55**(3-4), pp. 175–184.
- [24] Boda, L., Onyestyák, G., Solt, H., Lónyi, F., Vályon, J., and Thernesz, A., 2010, "Catalytic hydroconversion of tricaprylin and caprylic acid as model reaction for biofuel production from triglycerides," *Appl Catal A-Gen*, **374**(1-2), pp. 158–169.
- [25] Lopez-Ruiz, J. A., and Davis, R. J., 2014, "Decarbonylation of heptanoic acid over carbon-supported platinum nanoparticles," *Green Chem*, **16**(2), pp. 683–694.
- [26] Lugo-José, Y. K., Monnier, J. R., and Williams, C. T., 2014, "Gas-Phase, Catalytic Hydrodeoxygenation of Propanoic Acid, Over Supported Group VIII Noble Metals: Metal and Support Effects," *Appl Catal A-Gen*, **469**, pp. 410–418.
- [27] Alotaibi, M. A., Kozhevnikova, E. F., and Kozhevnikov, I. V., 2012, "Deoxygenation of propionic acid on heteropoly acid and bifunctional metal-loaded heteropoly acid catalysts: Reaction pathways and turnover rates," *Appl Catal A-Gen*, **447-448**, pp. 32–40.

- [28] Hip, B. J., Duivenvoorden, F. B. M., Koningsberger, D. C., and Prins, R., 1987, "Determination of Metal Particle Size of Highly Dispersed Rh, Ir, and Pt Catalysts by Hydrogen Chemisorption and EXAFS," *J Catal*, **105**, pp. 26–38.
- [29] Pham, H. N., Pagan-Torres, Y. J., Serrano-Ruiz, J. C., Wang, D., Dumesic, J. A., and Datye, A. K., 2011, "Improved hydrothermal stability of niobia-supported Pd catalysts," *Appl Catal A-Gen*, **397**(1-2), pp. 153–162.
- [30] Boudart, M., 1995, "Turnover Rates in Heterogeneous Catalysis," *Chem Rev*, **95**, pp. 661–666.
- [31] Simakova, I., Simakova, O., Mäki-Arvela, P., and Murzin, D. Y., 2010, "Decarboxylation of fatty acids over Pd supported on mesoporous carbon," *Catal Today*, **150**(1-2), pp. 28–31.
- [32] Bernas, H., Eränen, K., Simakova, I., Leino, A.-R., Kordás, K., Myllyoja, J., Mäki-Arvela, P., Salmi, T., and Murzin, D. Y., 2010, "Deoxygenation of dodecanoic acid under inert atmosphere," *Fuel*, **89**(8), pp. 2033–2039.
- [33] Ping, E. W., Pierson, J., Wallace, R., Miller, J. T., Fuller, T. F., and Jones, C. W., 2011, "On the nature of the deactivation of supported palladium nanoparticle catalysts in the decarboxylation of fatty acids," *Appl Catal A-Gen*, **396**(1-2), pp. 85–90.
- [34] Lopez-Ruiz, J. A., Buda, C., Horlor, B. T., Shabaker, J., Braden, D., Neurock, M., and Davis, R. J., 2014, "Mechanistic Insights on the Decarbonylation and Decarboxylation of Propanoic Acid over Palladium Catalysts," *Submiss.*

Chapter 5. Conclusions and Future Work

Portions of this Introduction Chapter are based on the content of Chapters 2, 3, and 4.

5.1. Conclusions

Platinum nanoparticles were supported on Norit carbon, Vulcan carbon and silicon carbide, whereas palladium, and rhodium nanoparticles were supported on Norit carbon, Vulcan carbon, and silica. The catalysts were characterized by N₂ physisorption, H₂ chemisorption, X-ray diffraction and electron microscopy before and after reaction to evaluate the effect of reaction conditions on catalyst stability. The catalysts were studied during the liquid- and gas-phase conversion of heptanoic acid, and the gas-phase conversion of propanoic acid at temperatures ranging from 533 to 573 K. In particular, variations of metal type, metal dispersion, metal loading, support composition, synthesis method, acid concentration, space time velocities, and reaction phase were used to explore the influence of conversion on product distribution, and reaction mechanism.

In liquid-phase operation, decarbonylation was the primary reaction of heptanoic acid on Pt and Pd, producing hexene, CO and water (not measured). Some hydrogenation of the olefins to hexane and conversion of CO to CO₂ was observed, especially at higher conversions. Rapid conversion of α -olefin to internal olefin was also observed in the liquid- and gas-phase operation at high conversion. A steady-state liquid-phase TOF of 0.00070 and 0.005 s⁻¹ at 573 K was obtained for the liquid-phase conversion of heptanoic acid over Pd and Pt, respectively, which was independent of synthesis method, support composition, metal dispersion, metal loading, and acid concentration.

Operation in gas-phase allowed for extrapolation of rates to initial time in an effort to evaluate the TOF on a fresh catalyst surface. All catalysts severely deactivated during the initial 3 h of reaction over the temperature range of investigation. During the gas-phase conversion of propanoic acid over silica-

based catalysts, Pd was found the most active metal with an initial TOF at 573 K of 0.043 s^{-1} , followed by Rh (0.027 s^{-1}), and Pt (0.007 s^{-1}). Palladium nanoparticles supported on Norit carbon gave an initial TOF of $\approx 0.035 \text{ s}^{-1}$ for the gas-phase conversion of propanoic and heptanoic acid.

Because Pd was the most active catalyst, the kinetics of the reaction were explored during the gas-phase conversion of propanoic acid. The observed E_A over silica-supported and carbon-supported Pd nanoparticles was approximately 130 kJ mol^{-1} . At 533K, the conversion of propanoic acid was zero order over the range of partial pressures from 0.1 to 1 bar. At lower partial pressures, the rate was negative order in acid. In the zero order regime, the main reaction path was decarbonylation, whereas decarboxylation was the main reaction path in the negative order regime.

Propanoic anhydride was tested as a potential reaction intermediate for the decarbonylation of propanoic acid. At high and low acid partial pressure, the conversion of propanoic anhydride proceeded by decarbonylation, which suggests that propanoic anhydride may be a surface intermediate in the high pressure decarbonylation of propanoic acid.

Postmortem characterization of the catalysts revealed a decrease of surface area and almost complete loss of H_2 chemisorption capacity after the liquid-phase operation, which accounts for the low steady-state rate under liquid-phase conditions. X-ray diffraction and electron microscopy revealed that Pd nanoparticles supported on carbon sintered substantially during the liquid-phase in nearly pure acid. In contrast, carbon-supported Pd nanoparticles were quite stable during gas-phase reaction. The sintering of carbon-supported Pd nanoparticles in the liquid-phase was less significant at low acid concentrations. Interestingly, silica-supported Pd nanoparticles were able to maintain a high dispersion during the liquid-phase operation at high acid concentrations.

After gas-phase operation, x-ray diffraction and electron microscopy revealed that the metal nanoparticles were stable regardless of the metal, support composition, and acid concentration. However, chemisorption and physisorption showed a loss of adsorption capacity after reaction. Combined results

from characterization suggest that the catalyst deactivation was not due to metal sintering but absorption of carbonaceous species.

Catalyst regeneration studies were performed over spent catalyst. Whereas mild air calcination and H₂ reduction at 623 K failed to regenerate the spent catalyst after the gas-phase conversion of heptanoic acid, H₂ reduction at 623 K regenerated the spent catalyst after the gas-phase conversion of propanoic acid.

5.2. Future work and recommendations

5.2.1. Auto-sampling

In the current reaction system, gas-phase samples can only be taken manually every 30 minutes. As a result of the severe catalyst deactivation observed during the first 1 to 2 h of reaction, only 3 samples are taken are used to extrapolate reaction rates to time zero. If these gas-phase samples are not taken properly, this extrapolation can be very misleading and give inconsistent results. Recent work in our lab involving steady-state isotopic transient kinetic analysis (SSITKA) have successfully used a Valco 34-port auto-sampling valve to collect up to 16 gas-phase samples during short amount of times [1]. I recommend to use a similar set-up and automate the gas-phase sampling system to collect multiple samples during the initial 3 h of reaction and get a better resolution of the catalyst deactivation.

5.2.2. Co-feeding dihydrogen

Much of the deoxygenation literature has shown that the use of hydrogen is essential to sustain catalytic activity during liquid- and gas-phase reactions [2–16]. During the gas-phase experiments discussed in Chapters 3 and 4, we reported severe catalyst deactivation during the initial 2 hours of reaction that, in theory, could have been avoided if H₂ was co-fed during reaction. For example, Lugo-José *et al.* reported no deactivation when co-feeding 20 vol% H₂ during the gas-phase decarbonylation of propanoic acid over Pd catalysts and obtained decarbonylation and

decarboxylation products [17]. However, Alotaibi *et al.* co-fed 98 vol% H₂ during the gas-phase reaction and obtained alcohols and aldehydes as the main reaction products [18]. These reported results suggest that the amount of H₂ co-fed during reaction needs to be optimized to minimize catalyst deactivation and avoid a change in reaction mechanism from decarbonylation/decarboxylation to hydrodeoxygenation. I recommend the use and optimization of H₂ during the liquid- and gas-phase reaction to obtain constant steady-state reaction rates and make easier to quantification of turnover frequencies and estimation of observed activation energies.

5.2.3. Bimetallic catalysts

The use of bimetallic nanoparticles as catalysts for the decarbonylation of carboxylic acids is also a potential solution to the demonstrated problems of selectivity and stability with monometallic precious metal catalysts discussed in this work. The literature has shown that the overall activity of a catalyst can increase by adding a second metal. This effect can be due to many reasons such as electron donation from a metal to another, limiting the over-oxidation of the active metals, and by aiding or inhibiting side reactions, among others.

In this work I have shown that the low selectivity to decarbonylation products, α -olefins and CO, at higher conversions is the result of side reactions such as double-bond isomerization, olefin hydrogenation and water-gas shift. I recommend to try bimetallic catalysts in an effort to obtain high conversion to α -olefins by inhibiting side reactions. For example, Chiappero *et al.* [19] and Lira *et al.* [20] inhibited olefin hydrogenation by adding Sn and Cu to Pt, respectively. Furthermore, Chiappero *et al.* showed that the addition of K decreased the isomerization of the olefins [19].

Carbon monoxide is well known to strongly adsorb onto transition metals, which could be limiting the reaction rate. Therefore, I would also recommend to test the effect of adding a metal that enhances the tolerance of CO by lowering the binding energy of CO [21]. For example, Gustavo *et al.* reported that the addition of Fe to Pt increased the CO tolerance of Pt [22].

Recently our collaborators at the University of New Mexico in Professor Abhaya Datye's lab have reported enhanced catalyst stability and activity of bimetallic catalysts for the furfural hydrogenation to furfuryl alcohol compared to monometallic catalysts, when Pd was alloyed with Zn.

Assuming this proposed work is successful at identifying promising new catalysts, the characterization techniques used in this thesis will not be sufficient to characterize the active sites of a bimetallic catalysts. I recommend to use X-ray photoelectron spectroscopy (XPS) to identify the oxidation state of the metals after catalyst synthesis and reaction. I also recommend the use of electron energy loss spectroscopy (EELS) to characterize individual bimetallic particles and obtain metal composition. Furthermore, bimetallic catalysts change when exposed to reaction conditions. For example, Porosoff *et al.* reported that Pt-Ni undergoes structural changes when exposed to reaction conditions [23]. Therefore the catalyst produced here will need to be characterized under in situ reaction conditions. Previously in our lab, X-ray absorption near-edge spectroscopy (XANES) was used to characterize bimetallic catalysts surfaces in situ. I recommend to use XANES to characterize the most reactive bimetallic catalysts and correlate structural changes to catalyst activity and selectivity.

5.2.4. Reactive Distillation

As shown in this work, low conversions of heptanoic acid during the gas-phase operation favors the selectivity towards the formation of α -olefin. Since working at low conversions would require a large separation cost downstream from the reactor, I propose to work with a reactive distillation process as an alternative. The reactive distillation process integrates reaction and distillation in a single multifunctional process unit [24]. The most beneficial advantage of the reactive distillation is that the reaction products leave the reactive zone once made and, as a result, the system always works at nearly 0% conversion. This would be very beneficial since side reactions, such as double-bond

isomerization, hydrogenation and water-gas shift, would be minimized as discussed in Chapters 2 and 3.

5.3. References

- [1] Shou, H., and Davis, R. J., 2013, “Multi-Product Steady-State Isotopic Transient Kinetic Analysis of CO Hydrogenation over Supported Molybdenum Carbide,” *J Catal*, **306**, pp. 91–99.
- [2] Lestari, S., Mäki-Arvela, P., Bernas, H., Simakova, O., Sjöholm, R., Beltramini, J., Lu, G. Q. M., Myllyoja, J., Simakova, I., and Murzin, D. Y., 2009, “Catalytic Deoxygenation of Stearic Acid in a Continuous Reactor over a Mesoporous Carbon-Supported Pd Catalyst,” *Energ Fuel*, **23**(8), pp. 3842–3845.
- [3] Lestari, S., Simakova, I., Tokarev, A., Mäki-Arvela, P., Eränen, K., and Murzin, D. Y., 2008, “Synthesis of Biodiesel via Deoxygenation of Stearic Acid over Supported Pd / C Catalyst,” *Catal Lett*, **122**(3-4), pp. 247–251.
- [4] Mäki-Arvela, P., Snåre, M., Eränen, K., Myllyoja, J., and Murzin, D. Y., 2008, “Continuous decarboxylation of lauric acid over Pd/C catalyst,” *Fuel*, **87**(17-18), pp. 3543–3549.
- [5] Rozmysłowicz, B., Mäki-Arvela, P., Lestari, S., Simakova, O. A., Eränen, K., Simakova, I. L., Murzin, D. Y., and Salmi, T. O., 2010, “Catalytic Deoxygenation of Tall Oil Fatty Acids Over a Palladium-Mesoporous Carbon Catalyst: A New Source of Biofuels,” *Top Catal*, **53**(15-18), pp. 1274–1277.

- [6] Snåre, M., Kubičková, I., Mäki-Arvela, P., Eränen, K., Wärnä, J., and Murzin, D. Y., 2007, "Production of diesel fuel from renewable feeds: Kinetics of ethyl stearate decarboxylation," *Chem Eng J*, **134**, pp. 29–34.
- [7] Snåre, M., Kubičková, I., Mäki-Arvela, P., Eränen, K., and Murzin, D. Y., 2006, "Heterogeneous Catalytic Deoxygenation of Stearic Acid for Production of Biodiesel," *Ind Eng Chem Res*, **45**(45), pp. 5708–5715.
- [8] Simakova, I., Rozmysłowicz, B., Simakova, O. A., Mäki-Arvela, P., Simakov, A., and Murzin, D. Y., 2011, "Catalytic Deoxygenation of C18 Fatty Acids Over Mesoporous Pd / C Catalyst for Synthesis of Biofuels," *Top Catal*, **54**(8-9), pp. 460–466.
- [9] Kubičková, I., Snåre, M., Eränen, K., Mäki-Arvela, P., and Murzin, D., 2005, "Hydrocarbons for diesel fuel via decarboxylation of vegetable oils," *Catal Today*, **106**(1-4), pp. 197–200.
- [10] Mäki-Arvela, P., Kubičková, I., Snåre, M., Eränen, K., and Murzin, D. Y., 2007, "Catalytic Deoxygenation of Fatty Acids and Their Derivatives," *Energ Fuel*, **21**(1), pp. 30–41.
- [11] Snåre, M., Kubičková, I., Mäki-Arvela, P., Chichova, D., Eränen, K., and Murzin, D. Y., 2008, "Catalytic deoxygenation of unsaturated renewable feedstocks for production of diesel fuel hydrocarbons," *Fuel*, **87**(6), pp. 933–945.
- [12] Lestari, S., Mäki-Arvela, P., Simakova, I., Beltramini, J., Lu, G. Q. M., and Murzin, D. Y., 2009, "Catalytic Deoxygenation of Stearic Acid and Palmitic Acid in Semibatch Mode," *Catal Lett*, **130**(1-2), pp. 48–51.

- [13] Simakova, I., Simakova, O., Mäki-Arvela, P., Simakov, A., Estrada, M., and Murzin, D. Y., 2009, “Deoxygenation of palmitic and stearic acid over supported Pd catalysts: Effect of metal dispersion,” *Appl Catal A-Gen*, **355**, pp. 100–108.
- [14] Immer, J. G., and Lamb, H. H., 2010, “Fed-Batch Catalytic Deoxygenation of Free Fatty Acids,” *Energ Fuel*, **130**(10), pp. 5291–5299.
- [15] Immer, J. G., Kelly, M. J., and Lamb, H. H., 2010, “Catalytic reaction pathways in liquid-phase deoxygenation of C18 free fatty acids,” *Appl Catal A-Gen*, **375**(1), pp. 134–139.
- [16] Ford, J. P., Immer, J. G., and Lamb, H. H., 2012, “Palladium Catalysts for Fatty Acid Deoxygenation: Influence of the Support and Fatty Acid Chain Length on Decarboxylation Kinetics,” *Top Catal*, **55**(3-4), pp. 175–184.
- [17] Lugo-José, Y. K., Monnier, J. R., and Williams, C. T., 2014, “Gas-Phase, Catalytic Hydrodeoxygenation of Propanoic Acid, Over Supported Group VIII Noble Metals: Metal and Support Effects,” *Appl Catal A-Gen*, **469**, pp. 410–418.
- [18] Alotaibi, M. A., Kozhevnikova, E. F., and Kozhevnikov, I. V., 2012, “Deoxygenation of propionic acid on heteropoly acid and bifunctional metal-loaded heteropoly acid catalysts: Reaction pathways and turnover rates,” *Appl Catal A-Gen*, **447-448**, pp. 32–40.
- [19] Chiappero, M., Thi, P., Do, M., Crossley, S., Lobban, L. L., and Resasco, D. E., 2011, “Direct conversion of triglycerides to olefins and paraffins over noble metal supported catalysts,” *Fuel*, **90**(3), pp. 1155–1165.

- [20] Lira, A., and Galiasso, R., 2012, "Dehydrogenation of C 12 – C 14 paraffins on PtCu / meso-structured Al₂O₃ catalyst for LAB production : Process simulation," *Fuel*, (February).
- [21] Simonetti, D., Kunkes, E., and Dumesic, J., 2007, "Gas-phase conversion of glycerol to synthesis gas over carbon-supported platinum and platinum–rhenium catalysts," *J. Catal.*, **247**(2), pp. 298–306.
- [22] Pereira, L. G. S., Paganin, V. a., and Ticianelli, E. a., 2009, "Investigation of the CO tolerance mechanism at several Pt-based bimetallic anode electrocatalysts in a PEM fuel cell," *Electrochim. Acta*, **54**(7), pp. 1992–1998.
- [23] Porosoff, M. D., Yu, W., and Chen, J. G., 2013, "Challenges and opportunities in correlating bimetallic model surfaces and supported catalysts," *J Catal*, **308**, pp. 2–10.
- [24] Sundmacher, K., and Kienle, A., eds., 2006, *Reactive Distillation: Status and Future Directions*, John Wiley & Sons.

Appendix A. Sample calculation of Weisz-Prater Criterion

It is important to check whether mass transfer limitations are present and may be masking some of the kinetic measurement. As discussed in section 1.6, the Weisz-Prater criteria [1] was used to evaluate the possibility of internal (Φ_I) and external (Φ_E) mass transfer limitations for liquid and gas phase reaction, Equation A. 1.

$$\Phi_I = \frac{r_{\text{obs}} R_p^2 \rho_p}{D_{EA} C_{AS}} < 1 \quad \Phi_E = \frac{r_{\text{obs}} R_p \rho_p}{k_A C_{AB}} < 0.15 \quad \text{Equation A. 1}$$

where r_{obs} is the observed rate, R_p is the radius of the particle, ρ_p is the density of the catalyst pellet, D_{EA} is the effective diffusivity coefficient, k_A is the external mass transfer coefficient, C_{AS} is the surface concentration, and C_{AB} is the bulk concentration [1,2].

To evaluate the mass transport phenomena, it was used the catalyst that showed the maximum performance, which was 10 wt% Pt/Norit C, and r_{obs} was 1.03×10^{-3} and $4.25 \times 10^{-4} \text{ molh}^{-1}$ in liquid a gas-phase reaction respectively. The radius of the particle was $425 \mu\text{m}/2$ and $180 \mu\text{m}/2$, and ρ_p was 0.4 gcm^{-3} . The effective diffusivity coefficient (D_{EA}) was calculated using a porosity (ε_p) of 0.5 and a tortuosity (τ) of 3 as recommended in Davis and Davis [2], as seen in Equation 6 and 7 for liquid and gas respectively.

$$D_{EA,L} = D_{AA,L} \frac{\varepsilon}{\tau} \quad \text{Equation A. 2}$$

$$D_{EA,G} = \left(\frac{1}{D_{AA,G}} + \frac{1}{D_{KA}} \right)^{-1} \frac{\varepsilon}{\tau} \quad \text{Equation A. 3}$$

The self-diffusion coefficient (D_{AA}) for heptanoic acid was calculated using Stokes-Einstein, Equation A.4, for liquid-phase reaction and kinetic theory, Equation A.5, for gas-phase reaction. The diffusivity coefficient for Knudsen diffusion (D_{KA}) was calculated using Equation A.6.

$$D_{AA} = \frac{k_B \cdot T}{6 \cdot \pi \cdot \eta \cdot r} \quad \text{Equation A. 4}$$

where D_{AA} is the diffusion coefficient, k_B is Boltzmann constant, T is the absolute temperature, η is the viscosity of the medium, and r is the radius of the molecule. The properties for heptanoic acid in liquid phase were calculated at 573 K using the Joback and Reid contribution method [3].

$$D_{AA} = \frac{1.38 \times 10^{-16} \text{ g cm}^2 \text{ s}^{-2} \text{ K}^{-1} \times 573 \text{ K}}{6 \times \pi \times 1.86 \times 10^{-3} \text{ g cm}^{-1} \text{ s}^{-1} \times 6.28 \times 10^{-8} \text{ cm}} = 3.6 \times 10^{-5} \text{ cm}^2 \text{ s}^{-1}$$

$$D_{AA} = \frac{2}{3} \left(\frac{k_B}{\pi} \right)^{2/3} \left(\frac{N_A}{M_A} \right)^{1/2} \frac{T^{(2/3)}}{P \cdot \sigma_A^2} \quad \text{Equation A. 5}$$

where D_{AA} is the diffusion coefficient, k_B is Boltzmann constant, T is the absolute temperature, N_A is the Avogadro's constant, M_A is the molecular mass of heptanoic acid, P is the absolute pressure, and σ_A is the diameter of the molecule. The properties for heptanoic acid in gas-phase were calculated at 573 K using the Reichenberg contribution method for organic acid vapors [4].

$$D_{AA} = \frac{2}{3} \left(\frac{1.38 \times 10^{-16} \text{ g cm}^2 \text{ s}^{-2} \text{ K}^{-1}}{\pi} \right)^{2/3} \left(\frac{6.023 \times 10^{23} \text{ molecules mole}^{-1}}{130.18 \text{ g mole}^{-1}} \right)^{1/2} \frac{573 \text{ K}^{(2/3)}}{1013250 \text{ Pa} \times (12.5 \times 10^{-8} \text{ cm})^2}$$

$$D_{AA} = 1.13 \times 10^{-2} \text{ cm}^2 \text{ s}^{-1}$$

$$D_{KA} = 4850 D_P \left(\frac{T}{M_A} \right)^{1/2} \quad \text{Equation A. 6}$$

where D_{KA} is the diffusivity coefficient of Knudsen diffusion, D_P pore diameter of the catalyst pellet, T is the absolute temperature, and M_A is the molecular mass of heptanoic acid.

$$D_{KA} = 4850 \times 2.3 \times 10^{-7} \text{ cm} \left(\frac{573 \text{ K}}{130.18 \text{ gmol}^{-1}} \right)^{1/2} = 2.34 \times 10^{-3} \text{ cm}^2 \text{ s}^{-1}$$

From this, D_{EA} for liquid and gas can be calculated.

$$D_{EAL} = D_{AA} \frac{\varepsilon}{\tau} = 3.6 \times 10^{-5} \text{ cm}^2 \text{ s}^{-1} \frac{0.5}{3} = 6.00 \times 10^{-6} \text{ cm}^2 \text{ s}^{-1}$$

$$D_{EAG} = \left(\frac{1}{D_{AAG}} + \frac{1}{D_{KA}} \right)^{-1} \frac{\varepsilon}{\tau} = \left(\frac{1}{1.13 \times 10^{-2} \text{ cm}^2 \text{ s}^{-1}} + \frac{1}{2.34 \times 10^{-3} \text{ cm}^2 \text{ s}^{-1}} \right)^{-1} \frac{0.5}{3} = 3.23 \times 10^{-4} \text{ cm}^2 \text{ s}^{-1}$$

The concentration at the surface of the catalyst (C_{AS}) was calculated using a mole balance at the interface between the boundary layer and the surface of the catalyst pellet in which the flux of heptanoic acid (N_A) is equal to the observed reaction rate (r_{obs}) per gram of catalyst (Equation A.7).

$$r_{obs} = N_A \Rightarrow r_{obs} = k_A (C_{AB} - C_{AS}) S_P \Rightarrow C_{AS} = C_{AB} - \frac{r_{obs}}{k_A S_P} \quad \text{Equation A. 7}$$

where C_{AS} is the surface concentration, C_{AB} is the bulk concentration, r_{obs} is the observed rate, k_A is the external mass transfer coefficient, and S_P external catalyst particle surface area per unit reactor volume.

The external mass transfer coefficient (k_A) was obtained using a mass transfer correlation, Equation A.8, for fluid-solid interface for packed bed reactors obtained from Cussler [5].

$$k_A = 1.17 v_0 \left(\frac{d_P v_0}{\nu} \right)^{-0.42} \left(\frac{D_{AA}}{\nu} \right)^{2/3} \quad \text{Equation A. 8}$$

where k_A is the mass transfer coefficient, D_{AA} is the self-diffusion coefficient of A, v_0 is the superficial velocity which would exist without packing, ρ is the density of the fluid, d_P is the catalyst particle diameter, and ν is the kinematic viscosity of fluid.

The superficial velocities for liquid and gas phase reaction were calculated using $0.01 \text{ cm}^3 \text{ min}^{-1}$ as the feed flow rate. The densities of heptanoic were calculated at 573 K. The density of the liquid-phase acid was calculated using the Joback group contribution method and it was found to be 894 kgm^{-3} . The density of heptanoic acid in gas-phase was calculated using the ideal gas law and it was found to be 2.83 kgm^{-3} . The superficial velocity for liquid and gas phase were $1.02 \times 10^{-3} \text{ cm}^3 \text{ s}^{-1}$ and $0.33 \text{ cm}^3 \text{ s}^{-1}$ respectively.

k_{AL} for a particle size of $180 \mu\text{m}$ =

$$\begin{aligned} &= 1.17 \times 1.02 \times 10^{-3} \text{ cm}^3 \text{ s}^{-1} \left(\frac{180 \times 10^{-4} \text{ cm} \times 1.02 \times 10^{-3} \text{ cm}^3 \text{ s}^{-1} \times 0.894 \text{ gcm}^{-3}}{1.86 \times 10^{-3} \text{ gcm}^{-1} \text{ s}^{-1}} \right)^{-0.42} \left(\frac{6.00 \times 10^{-6} \text{ cm}^2 \text{ s}^{-1} \times 0.894 \text{ gcm}^{-3}}{1.86 \times 10^{-3} \text{ gcm}^{-1} \text{ s}^{-1}} \right)^{2/3} \\ &= 1.76 \times 10^{-4} \text{ cm s}^{-1} \end{aligned}$$

$$k_{A,L} \text{ for a particle size of } 425 \mu\text{m} = 1.23 \times 10^{-4} \text{ cm s}^{-1}$$

$$k_{A,G} \text{ for a particle size of } 180 \mu\text{m} =$$

$$= 1.17 \times 0.33 \text{ cm}^3 \text{ s}^{-1} \left(\frac{180 \times 10^{-4} \text{ cm} \times 0.33 \text{ cm}^3 \text{ s}^{-1} \times 2.83 \times 10^{-3} \text{ g cm}^{-3}}{1.10 \times 10^{-4} \text{ g cm}^{-1} \text{ s}^{-1}} \right)^{-0.42} \left(\frac{3.23 \times 10^{-4} \text{ cm}^2 \text{ s}^{-1} \times 2.83 \times 10^{-3} \text{ g cm}^{-3}}{1.10 \times 10^{-4} \text{ g cm}^{-1} \text{ s}^{-1}} \right)^{0.12}$$

$$= 3.49 \times 10^{-2} \text{ cm s}^{-1}$$

$$k_{A,G} \text{ for a particle size of } 425 \mu\text{m} = 2.43 \times 10^{-2} \text{ cm s}^{-1}$$

The external catalyst particle surface area per unit reactor volume, S_P , was calculated for both particle sizes, 180 and 425 μm , using Equation 13.

$$S_P = \frac{S}{V \rho} = \frac{4 \pi r^2}{\frac{4}{3} \pi r^3 \rho} = \frac{3}{r \rho} \quad \text{Equation A. 9}$$

where r is the radius of the particle and ρ is the density of the catalyst particle

$$S_{P,180} = \frac{3}{\frac{180 \times 10^{-4} \text{ cm}}{2} \times 0.4 \text{ g cm}^3} = 833.33 \text{ cm}^2 \text{ g}^{-1}$$

$$S_{P,425} = \frac{3}{\frac{425 \times 10^{-4} \text{ cm}}{2} \times 0.4 \text{ g cm}^3} = 352.94 \text{ cm}^2 \text{ g}^{-1}$$

Using Equation 11, C_{AS} for liquid ($C_{AS,L}$) and gas ($C_{AS,G}$) phase reaction were calculated. The value of k_A depends on the catalyst particle size and reaction phase. The observed reaction rate, r_{obs} , and C_{AB} depends on reaction phase, and S_P depends on the catalyst particle size.

$$C_{AS,L} \text{ for a } 180 \mu\text{m} \text{ catalyst particle} = C_{AB,L} - \frac{r_{obs}}{k_{A,L} S_P} = 6.62 \text{ molL}^{-1} - \frac{\frac{1.03 \times 10^{-3} \text{ molh}^{-1}}{0.25 \text{ g cat}} \times \frac{1 \text{ h}}{3600 \text{ s}}}{5.81 \times 10^{-4} \text{ cm s}^{-1} \times 833.33 \text{ cm}^2 \text{ g}^{-1}}$$

$$\approx 6.62 \text{ molL}^{-1}$$

$$C_{AS,L} \text{ for a } 425 \mu\text{m} \text{ catalyst particle} = 6.62 \text{ molL}^{-1} - \frac{\frac{1.03 \times 10^{-3} \text{ molh}^{-1}}{0.25 \text{ g cat}} \times \frac{1 \text{ h}}{3600 \text{ s}}}{4.05 \times 10^{-4} \text{ cm s}^{-1} \times 352.94 \text{ cm}^2 \text{ g}^{-1}} \approx 6.62 \text{ molL}^{-1}$$

$$C_{AS,G} \text{ for a } 180 \mu\text{m catalyst particle} = 2.17 \times 10^{-2} \text{ molL}^{-1} - \frac{4.25 \times 10^{-4} \text{ molh}^{-1}}{0.25 \text{ g cat}} \times \frac{1 \text{ h}}{3600 \text{ s}} \\ \approx 2.17 \times 10^{-2} \text{ molL}^{-1} - \frac{3.74 \times 10^{-1} \text{ cms}^{-1} \times 833.33 \text{ cm}^2 \text{g}^{-1}}{3.74 \times 10^{-1} \text{ cms}^{-1} \times 833.33 \text{ cm}^2 \text{g}^{-1}}$$

$$C_{AS,L} \text{ for a } 425 \mu\text{m catalyst particle} = 2.17 \times 10^{-2} \text{ molL}^{-1} - \frac{4.25 \times 10^{-4} \text{ molh}^{-1}}{0.25 \text{ g cat}} \times \frac{1 \text{ h}}{3600 \text{ s}} \\ \approx 2.17 \times 10^{-2} \text{ molL}^{-1} - \frac{2.61 \times 10^{-4} \text{ cms}^{-1} \times 352.94 \text{ cm}^2 \text{g}^{-1}}{2.61 \times 10^{-4} \text{ cms}^{-1} \times 352.94 \text{ cm}^2 \text{g}^{-1}}$$

At this point, the Weisz-Prater criteria for internal (Φ_I) and external (Φ_E) and internal mass transfer limitations can be calculated. The value of k_A depends on the catalyst particle size and reaction phase. The observed reaction rate, r_{obs} , D_{EA} , and C_{AB} depends on the reaction phase.

For a 180 μm catalyst particle:

$$\Phi_{I,L} = \frac{r_{obs} R_P^2 \rho_P}{D_{EA} C_{AS}} = \frac{1.03 \times 10^{-3} \text{ molh}^{-1}}{0.25 \text{ g cat}} \times \frac{1 \text{ h}}{3600 \text{ s}} \left(\frac{180 \times 10^{-3} \text{ cm}}{2} \right)^2 \frac{0.4 \text{ gcm}^3}{6.00 \times 10^{-8} \text{ cm}^2 \text{s}^{-1} \times 6.62 \text{ molL}^{-1}} = 0.001 < 1$$

$$\Phi_{I,G} = \frac{4.25 \times 10^{-4} \text{ molh}^{-1}}{0.25 \text{ g cat}} \times \frac{1 \text{ h}}{3600 \text{ s}} \left(\frac{180 \times 10^{-3} \text{ cm}}{2} \right)^2 \frac{0.4 \text{ gcm}^3}{3.23 \times 10^{-4} \text{ cm}^2 \text{s}^{-1} \times 2.17 \times 10^{-2} \text{ molL}^{-1}} = 0.002 < 1$$

$$\Phi_{E,L} = \frac{r_{obs} R_P \rho_P}{k_A C_{AS}} = \frac{1.03 \times 10^{-3} \text{ molh}^{-1}}{0.25 \text{ g cat}} \times \frac{1 \text{ h}}{3600 \text{ s}} \left(\frac{180 \times 10^{-3} \text{ cm}}{2} \right) \frac{0.4 \text{ gcm}^3}{5.81 \times 10^{-4} \text{ cm}^2 \text{s}^{-1} \times 6.62 \text{ molL}^{-1}} = 0.001 < 1$$

$$\Phi_{E,G} = \frac{4.25 \times 10^{-4} \text{ molh}^{-1}}{0.25 \text{ g cat}} \times \frac{1 \text{ h}}{3600 \text{ s}} \left(\frac{180 \times 10^{-3} \text{ cm}}{2} \right) \frac{0.4 \text{ gcm}^3}{3.74 \times 10^{-1} \text{ cm}^2 \text{s}^{-1} \times 2.17 \times 10^{-2} \text{ molL}^{-1}} = 0.0002 < 1$$

For a 425 μm catalyst particle:

$$\Phi_{I,L} = \frac{r_{obs} R_P^2 \rho_P}{D_{EA} C_{AS}} = \frac{1.03 \times 10^{-3} \text{ molh}^{-1}}{0.25 \text{ g cat}} \times \frac{1 \text{ h}}{3600 \text{ s}} \left(\frac{425 \times 10^{-3} \text{ cm}}{2} \right)^2 \frac{0.4 \text{ gcm}^3}{6.00 \times 10^{-8} \text{ cm}^2 \text{s}^{-1} \times 6.62 \text{ molL}^{-1}} = 0.005 < 1$$

$$\Phi_{I,G} = \frac{4.25 \times 10^{-4} \text{ molh}^{-1}}{0.25 \text{ g cat}} \times \frac{1 \text{ h}}{3600 \text{ s}} \left(\frac{425 \times 10^{-3} \text{ cm}}{2} \right)^2 \frac{0.4 \text{ gcm}^3}{3.23 \times 10^{-4} \text{ cm}^2 \text{s}^{-1} \times 2.17 \times 10^{-2} \text{ molL}^{-1}} = 0.012 < 1$$

$$\Phi_{E,L} = \frac{r_{obs} R_P \rho_P}{k_A C_{AS}} = \frac{1.03 \times 10^{-3} \text{ molh}^{-1}}{0.25 \text{ g cat}} \times \frac{1 \text{ h}}{3600 \text{ s}} \left(\frac{425 \times 10^{-3} \text{ cm}}{2} \right) \frac{0.4 \text{ gcm}^3}{4.05 \times 10^{-4} \text{ cm}^2 \text{s}^{-1} \times 6.62 \text{ molL}^{-1}} = 0.004 < 1$$

$$\Phi_{E,G} = \frac{\frac{4.25 \times 10^{-4} \text{ mol h}^{-1}}{0.25 \text{ g cat}} \times \frac{1 \text{ h}}{3600 \text{ s}} \left(\frac{425 \times 10^{-4} \text{ cm}}{2} \right) 0.4 \text{ g cm}^3}{2.61 \times 10^{-1} \text{ cm}^2 \text{ s}^{-1} 2.17 \times 10^{-2} \text{ mol L}^{-1}} = 0.001 < 1$$

The results suggest a lack of internal and external mass transfer limitations. Table A.1 summarizes the results of this analysis.

Table A.1. Summary of transport phenomena analysis

Reaction Phase	Liquid	Gas
Space velocity, v ($\text{cm}^3 \text{min}^{-1}$)	0.01	3.25
Residence time, τ (min)	90.3	0.3
Viscosity, μ ($\text{g cm}^{-1} \text{s}^{-1}$)	1.86×10^{-3}	1.1×10^{-4}
Density, ρ (kg m^{-3})	898.8	2.7
Self-diffusion coefficient, D_{AA} ($\text{cm}^2 \text{s}^{-1}$)	3.6×10^{-5}	1.1×10^{-2}
Effective Diffusivity, D_{EA} ($\text{cm}^2 \text{s}^{-1}$)	6.0×10^{-6}	3.2×10^{-4}
External Mass Transfer Coefficient For a 180 μm Catalyst Particle, $k_{A,180}$ (cm s^{-1})	5.8×10^{-4}	3.7×10^{-1}
External Mass Transfer Coefficient For a 425 μm Catalyst Particle, $k_{A,425}$ (cm s^{-1})	4.1×10^{-4}	2.6×10^{-1}
Weisz-Prater Criteria for Internal Mass Transfer Limitations for a 180 μm Catalyst Particle, $\Phi_{I,180}$	0.001	0.002
Modified Weisz-Prater Criteria for External Mass Transfer Limitations for a 180 μm Catalyst Particle, $\Phi_{E,180}$	0.001	0.0002
Weisz-Prater Criteria for Internal Mass Transfer Limitations for a 425 μm Catalyst Particle, $\Phi_{E,425}$	0.005	0.012
Modified Weisz-Prater Criteria for External Mass Transfer Limitations for a 425 μm Catalyst Particle, $\Phi_{E,425}$	0.004	0.001

Appendix B. Gas chromatography calibrations

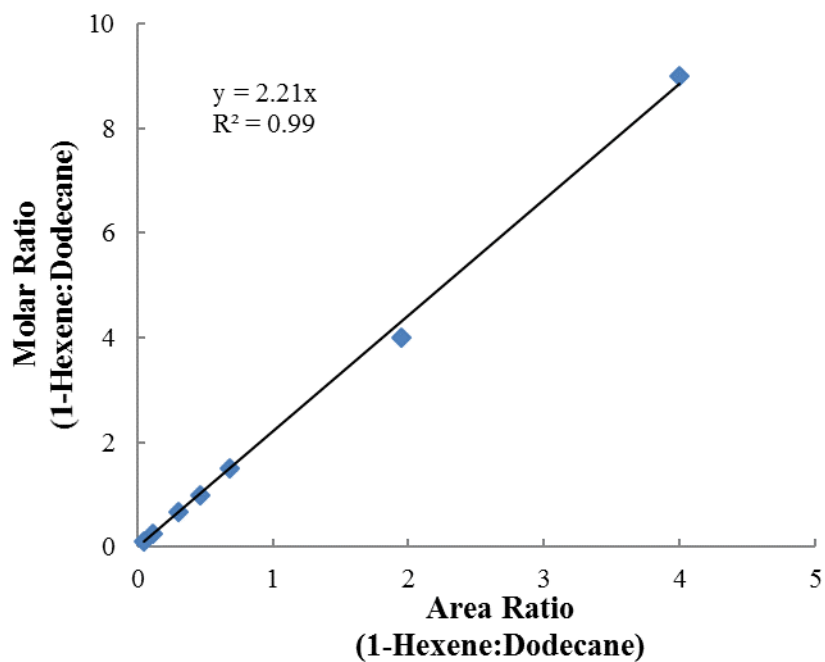


Figure B.1. Calibration curve for 1-hexene

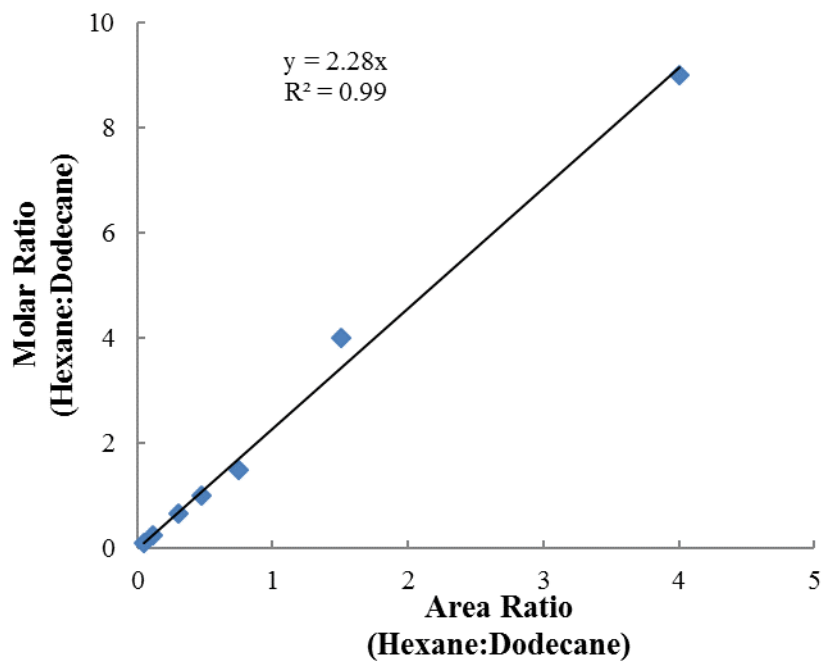


Figure B.2. Calibration curve for hexane

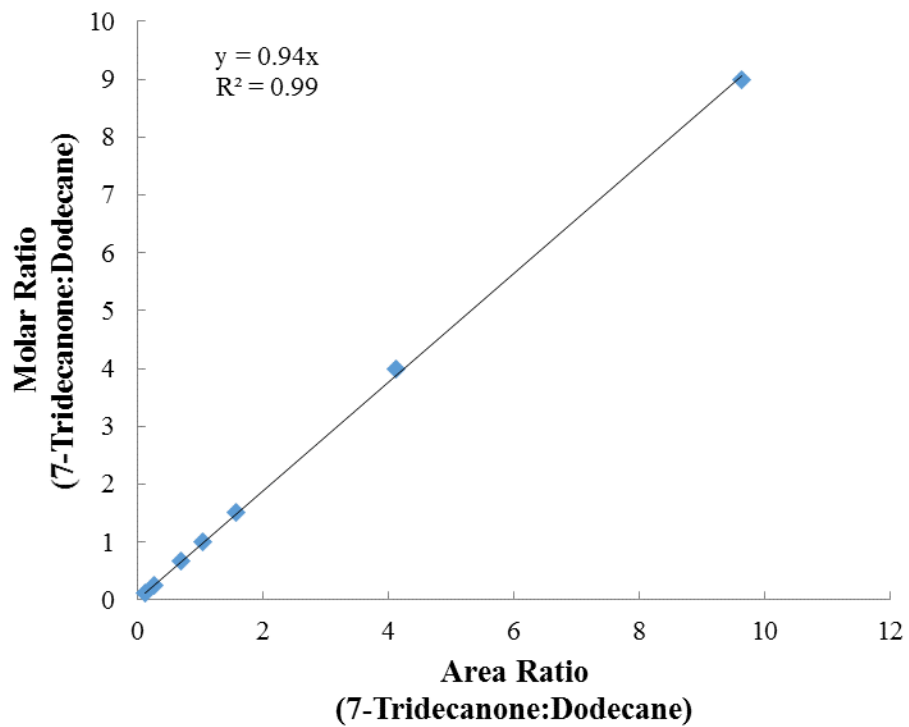


Figure B.3. Calibration curve for 7-tridecanone

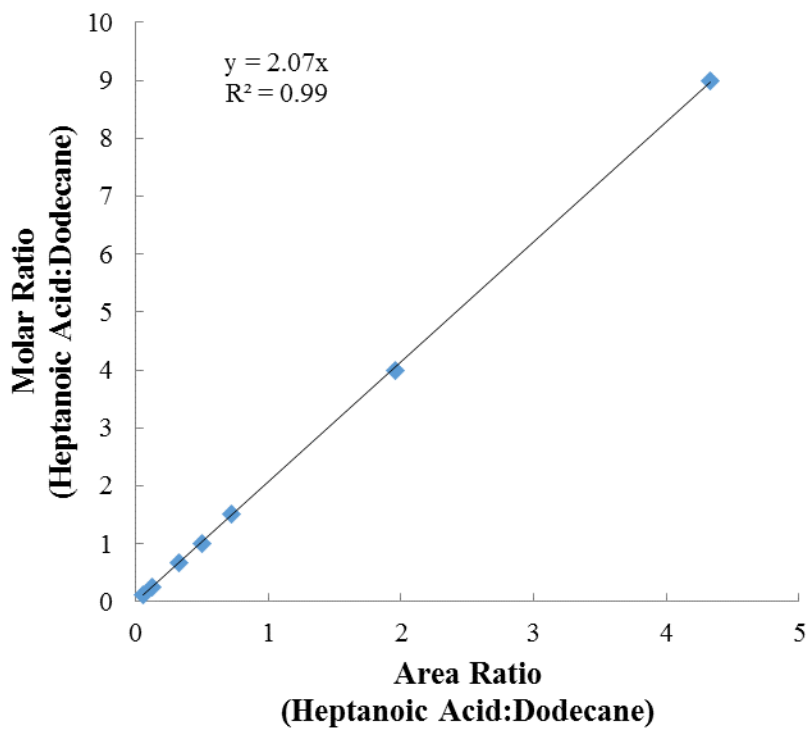


Figure B.4. Calibration curve for heptanoic acid

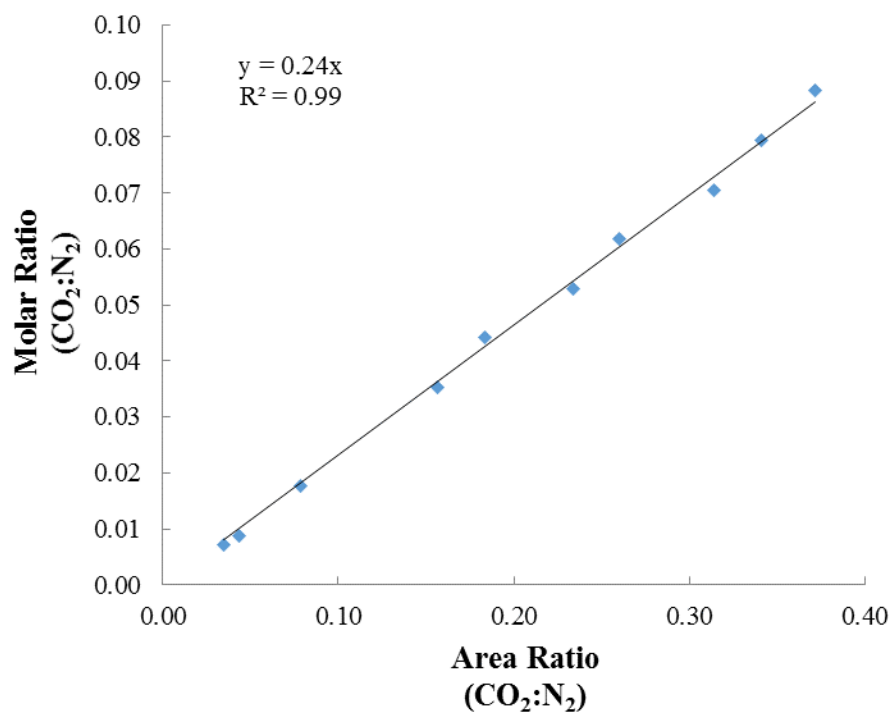


Figure B.5. Calibration curve for CO₂

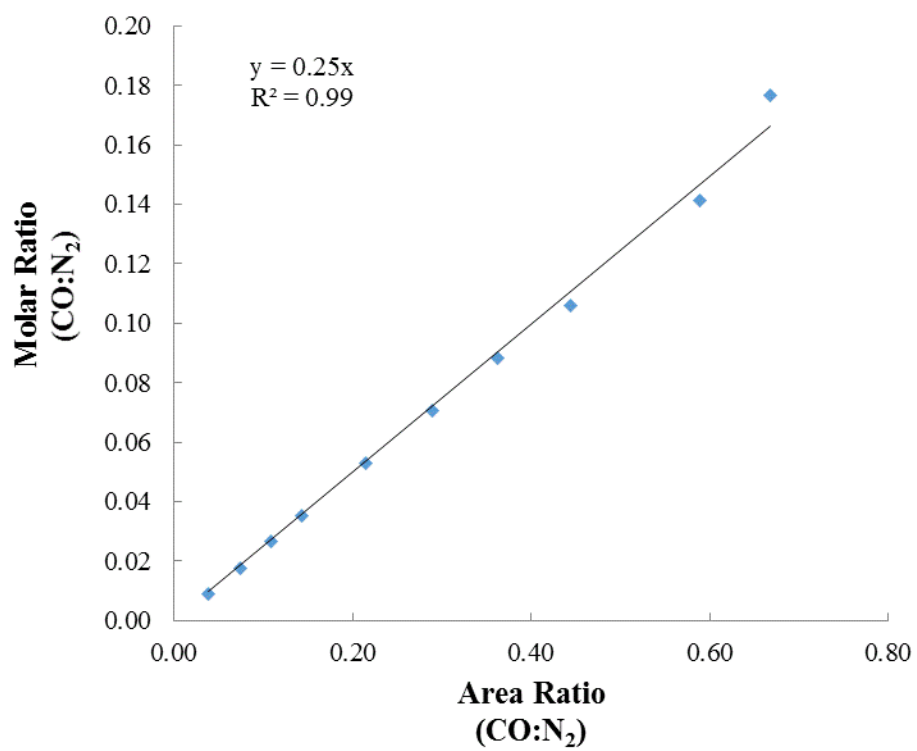


Figure B.6. Calibration curve for CO

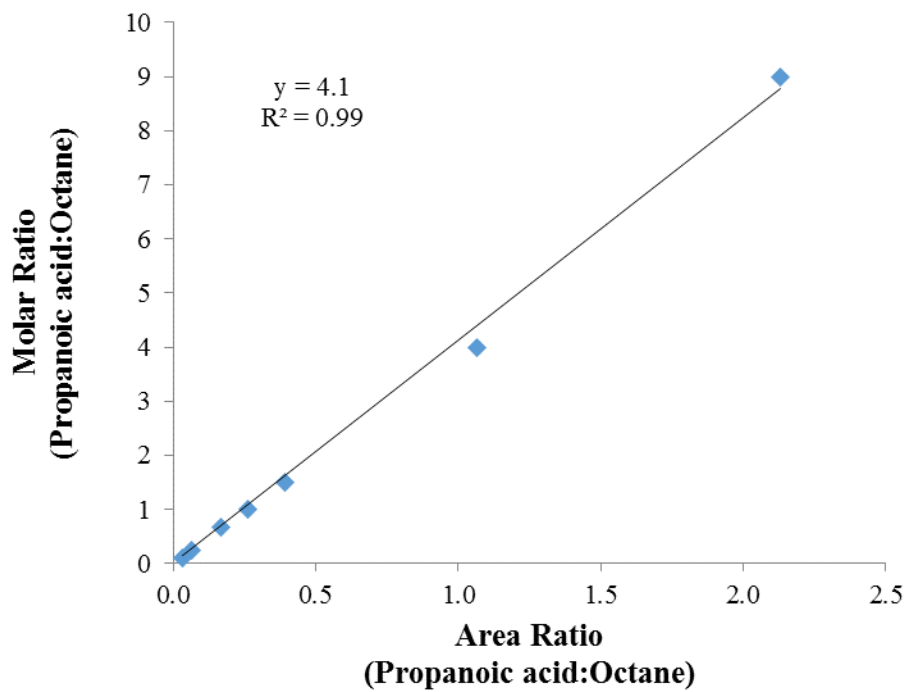


Figure B. 7. Calibration curve for propanoic acid

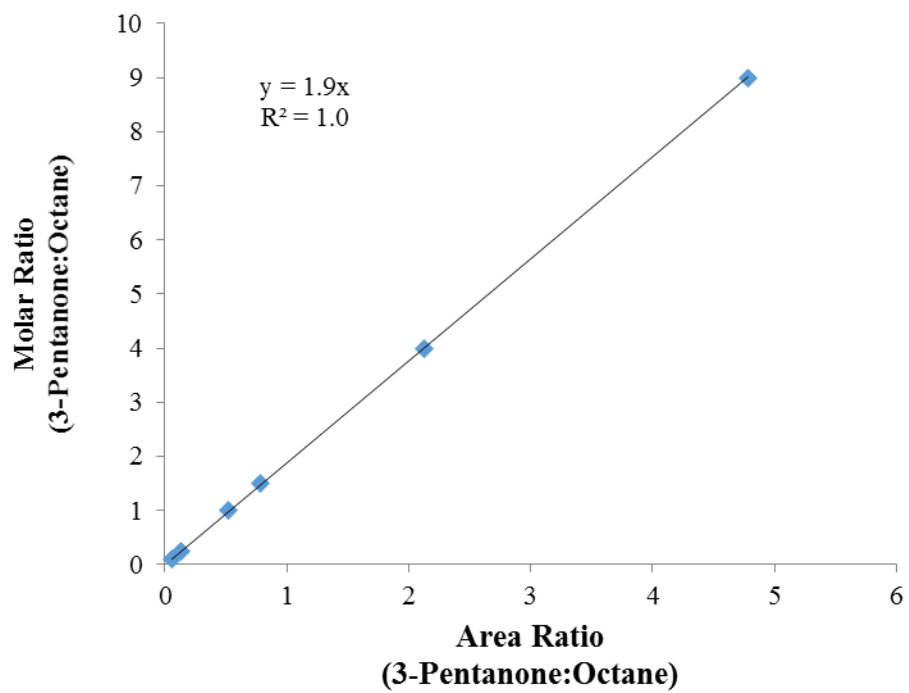


Figure B. 8. Calibration curve for 3-pentanone

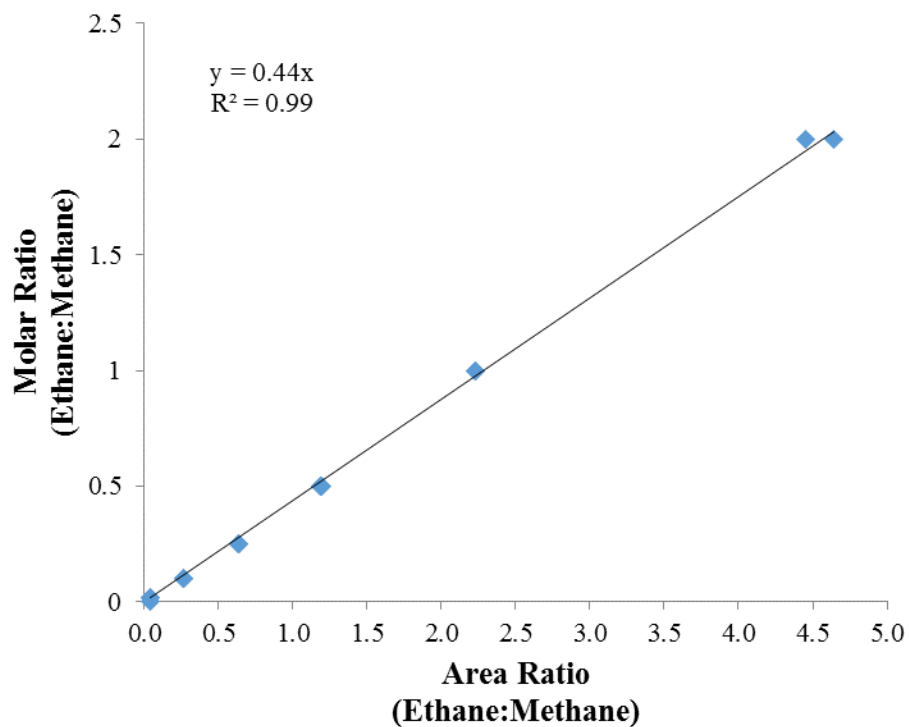


Figure B. 9. Calibration curve for ethane

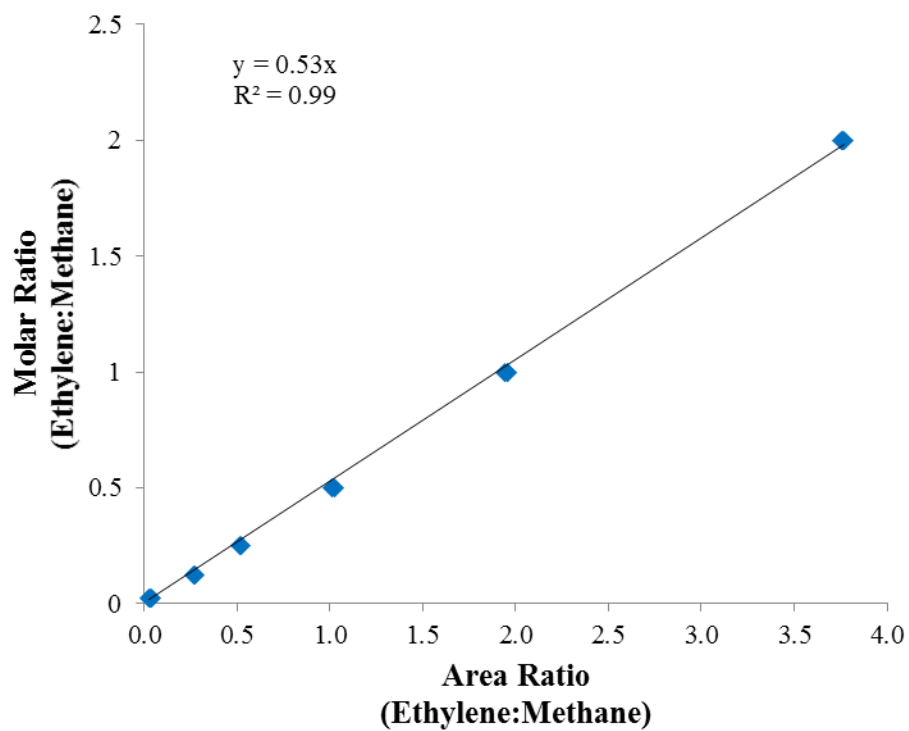


Figure B. 10. Calibration curve for ethylene

Appendix C. Effect of heptanoic acid concentration

In this section we tested the effect of acid on the TOF and product selectivity concentration during the liquid-phase conversion of heptanoic acid over 20 wt% Pd/Norit C at 40 bar and 573 K. Because of the linear relationship between conversion and product selectivity, weight of catalyst and flow rate were adjusted to have similar conversion level at different acid concentrations. Due to the catalyst deactivation observed in the previous sections, fresh catalyst was used for each acid concentration experiment. Table 3.3 shows that the liquid-phase TOF was constant at $\approx 0.00070 \text{ s}^{-1}$ independent of the heptanoic concentration. This indicated that the system was operating at zero order regime and in agreement with the observations reported by Mäki-Arvela *et al.* [6]. Furthermore, Lugo-José *et al.* also reported a zero order reaction regime during the gas-phase conversion of propanoic acid over a Pd catalyst [7]. In their work, they also reported 0.5 reaction order regime at very low concentrations of acid, however, we could not lower any further the acid concentration in our system without losing resolution because the diluent and reaction products were both in the liquid-phase.

As shown in Table C.1, whereas the selectivity to olefins (α -olefin and hexenes) decreased as the concentration of acid decreased, the CO selectivity remained $\approx 60\%$, and relatively constant, most likely because the conversion level was similar for all the experiment. Although we detected a shift in product selectivity from hexenes to hexane as reported by Immer *et al.* [8], the constancy of the CO selectivity indicated that the higher paraffin selectivity most likely due to hydrogen transfer from tetradecane to the olefins. This could explain why some studies showed that the formation rate of alkenes did not match that of CO [9,10].

The catalysts were characterized after reaction by XRD and TEM, Figures 3.12 and 3.13 respectively, and revealed that the Pd nanoparticles were stable at low concentrations of heptanoic acid. As the concentration of the acid increased above 0.4 M, Pd sintering was detected. This result suggested that high concentration of acid was responsible for the Pd sintering observed during the liquid-phase operation.

Table C.2. Summary of reactivity results for 20 wt% Pd/NoritC operated at different acid concentrations at 573 K and liquid-phase conditions.

[Heptanoic Acid]^a (mol L⁻¹)	Liquid-Phase TOF^b (s⁻¹)	Conversion^b (%)	CO Selectivity^c (%)	Hexenes Selectivity^d (%)
6.6	0.00068	8.8	54	17
2.4	0.00073	8.7	68	14
1.1	0.00072	8.7	67	5.2
0.40	0.00076	6.8	68	0.41
0.19	0.00068	9.7	63	0.0
0.10	0.00070	10	64	0.0

^a Tetradecane was used as diluent

^b Result estimated using rates of heptanoic acid after 20 h of reaction and

^c Result estimated using rates of carbon oxides after 20 h of reaction

^d Result estimated using rates of 1-hexene, i-hexenes, and hexane after 20 h of reaction

Appendix D. Catalyst deactivation during the decarbonylation of propanoic acid

Catalyst deactivation during the deoxygenation of carboxylic acids has been widely reported in the literature. Mäki-Arvela *et al.* [6] and Snåre *et al.* [11] suggested that deactivation originated from poisoning of the metal by the reactants, products (especially CO), and coking. Furthermore, Simakova *et al.* reported that deactivating aromatics are formed in reactions performed under H₂-scarce conditions [12]. The initial concentration of carboxylic acid is also proposed to influence catalyst deactivation. Mäki-Arvela *et al.* observed that deactivation was more extensive with higher initial concentration of carboxylic acid [6]. In the previous section, we observed an increase in the initial TOF when propanoic anhydride and propanoic acid were diluted, regardless of the product distribution, supporting the findings of Mäki-Arvela *et al.* [6]. However, the fact that we observed catalyst deactivation under conditions in which CO was not produced, indicates that deactivation by CO poisoning of Pd does not account for all the catalyst deactivation.

In Chapter 4, I showed that catalyst deactivation was always observed regardless of the temperature of reaction, product composition, and partial pressure of solvent. At 573 K, the catalyst deactivated when 3-pentanone appeared as a reaction product, Figure 4.2, which suggested that 3-pentanone could be responsible for the catalyst deactivation. Furthermore, the fact that the catalysts deactivated when direct decarbonylation is the main path, especially at high partial pressures of propanoic anhydride, suggests that ethylene could also be responsible for the catalyst deactivation, even at 533 K. Therefore we investigated the effect 3-pentanone and ethylene on the catalyst activity and deactivation by diluting propanoic anhydride (33 mol%) with 3-pentanone and ethylene (67 mol%) over 20 wt% Pd/Norit C at 1 bar and 533 K. Table D.1 shows that the initial TOF increased when ethylene and 3-pentanone were used to dilute propanoic anhydride.

Table D. 1. Result of reactivity of propanoic anhydride (33 mol%) co-fed with ethylene (67 mol%) or 3-pentanone (67 mol%) over 20 wt% Pd/Norit C at 533 K.

Feed	Co-Feed	Initial TOF ^a (s ⁻¹)
	Pure	0.0042
Propanoic anhydride	Ethylene	0.0105
	3-Pentanone	0.0237

^a Result estimated using extrapolated reaction rates of propanoic acid to time 0 h

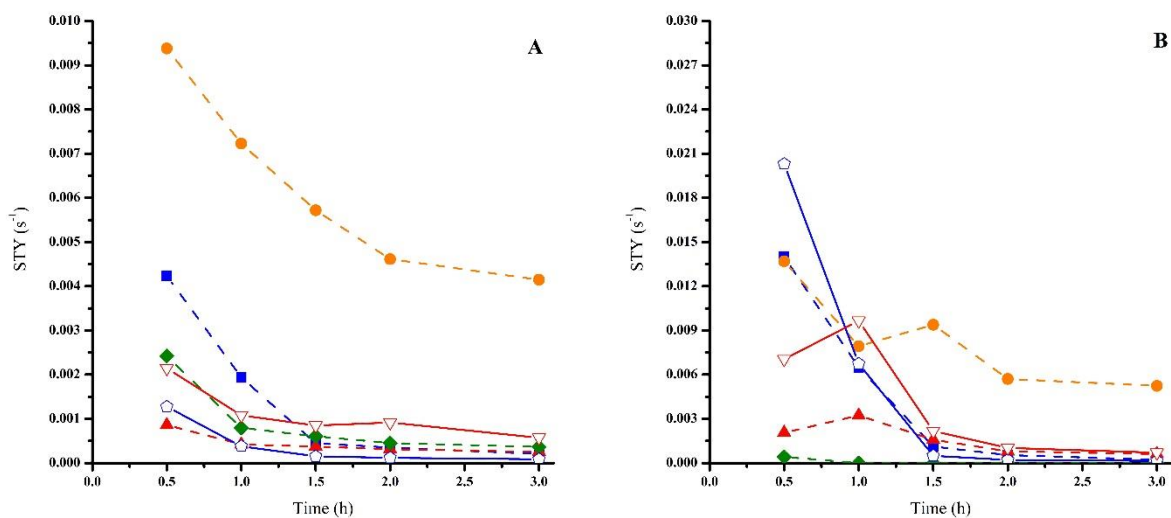
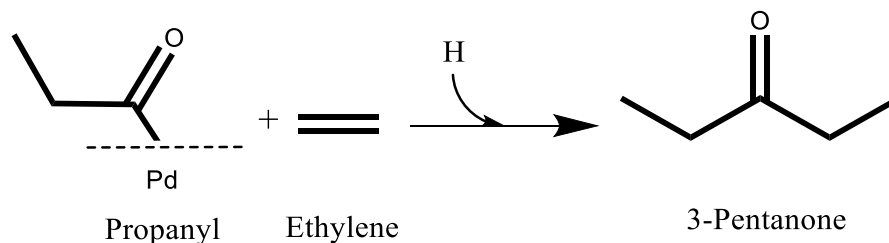


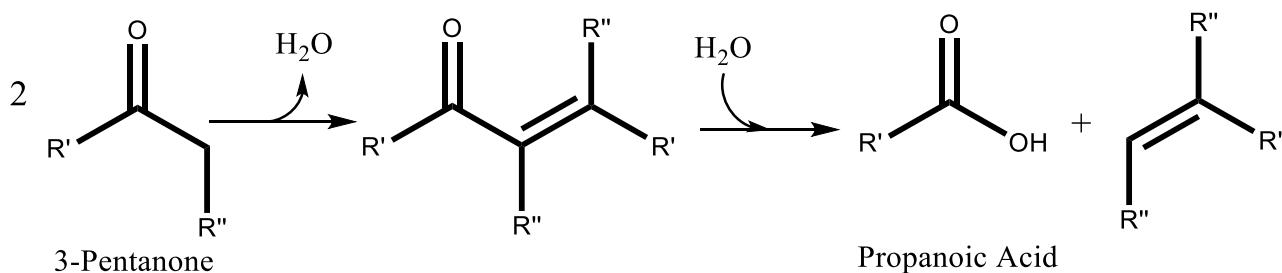
Figure D. 1. Catalytic conversion of propanoic anhydride diluted (33 mol %) with ethylene (A) and 3-pentanone (B) over 20 wt% Pd/Norit C at 573 K and 1 bar. ■ represents ethylene, ▲ represents ethane, ◆ represents 3-pentanone, ● represents propanoic acid, ◻ represents CO, and ▽ represents CO₂. The STY was calculated using the Pd dispersion of the fresh catalysts.



Scheme D. 1. Formation of 3-pentanone through a coupling reaction of propenyl and ethylene.

Figure D.1 reveals that the catalyst still showed severe deactivation during the initial 3 h of reactions. If 3-pentanone or ethylene were responsible for catalyst deactivation, we would have observed a low activity from the very beginning of the experiment. This suggests that products such as 3-pentanone and ethylene are not responsible for the initial catalyst deactivation. Furthermore, we observed an increase in production of 3-pentanone when ethylene was co-fed. This supports the idea that 3-pentanone is formed by a coupling reaction of a propenyl intermediate adsorbed on the surface, as suggested by DFT, and ethylene (Scheme D.1).

When 3-pentanone was co-fed with PAN, the production of propanoic acid and ethane increased with respect feeding pure PAN. As shown in Scheme D.2, propanoic acid could be formed as a result of the dimerization of 3-pentanone followed by thermal cracking. The ethane could be a result of the further cracking of the dimer.



Scheme D. 2. Formation of propanoic acid through the dimerization of 3-pentanone. R' represents CH₂-CH₃ and R'' represents CH₃.

Appendix E. Catalyst regeneration

In our previous study, we studied the regeneration of Pt/Norit C after the decarbonylation of heptanoic acid at 573 K with hot acid extraction at 350 K, calcination and reduction at 623 K, and we concluded that the mode of de-activation was not easily reversed by standard regeneration methods [13]. Ping *et al.* regained the catalytic activity of Pd/SiO₂ after hot extraction with solvent and subsequent reduction in H₂ at 573 K [14]. The authors concluded that the observed deactivation resulted from deposition of organic molecules onto the active sites [14]. We decided to study the regeneration of 5 wt% Pd/SiO₂ and 20 wt% Pd/Norit C after the gas-phase decarbonylation of propanoic acid at 533 K.

The catalyst regeneration was first studied over the spent Pd/SiO₂ catalyst because of its superior stability during calcination conditions and known regenerability with respect to Pd/Norit C. The spent 5wt% Pd/SiO₂ was calcined with air up to 1495 K at a heating rate of 1 K min⁻¹ to determine the main desorption temperatures of the species absorbed on the surface of the catalyst. Figure E.1 shows that there were three main desorption peaks at 473, 723, and 1195 K, and total weight loss was 8%.

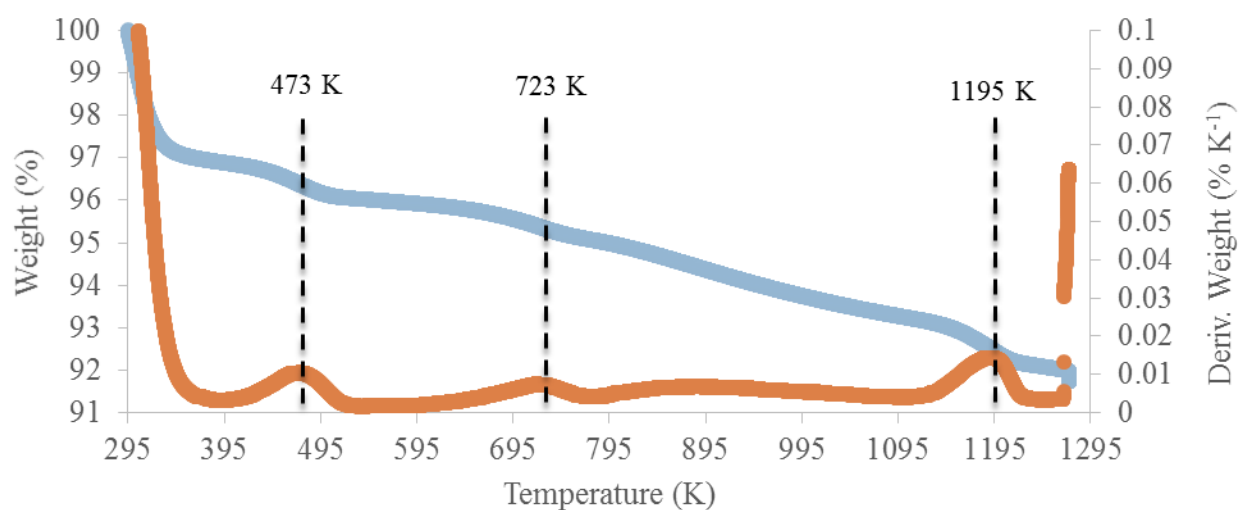


Figure E. 1. Thermogravimetric analysis of spent 5 wt% Pd/SiO₂ with air up to 1295 K. ● represents Weight (%) and can be read on the left hand axis. ● represents Deriv. Weight (% K⁻¹) and can be read on the right hand axis. The spent catalyst was recovered after the decarbonylation of propanoic acid at 533 K and 1 bar.

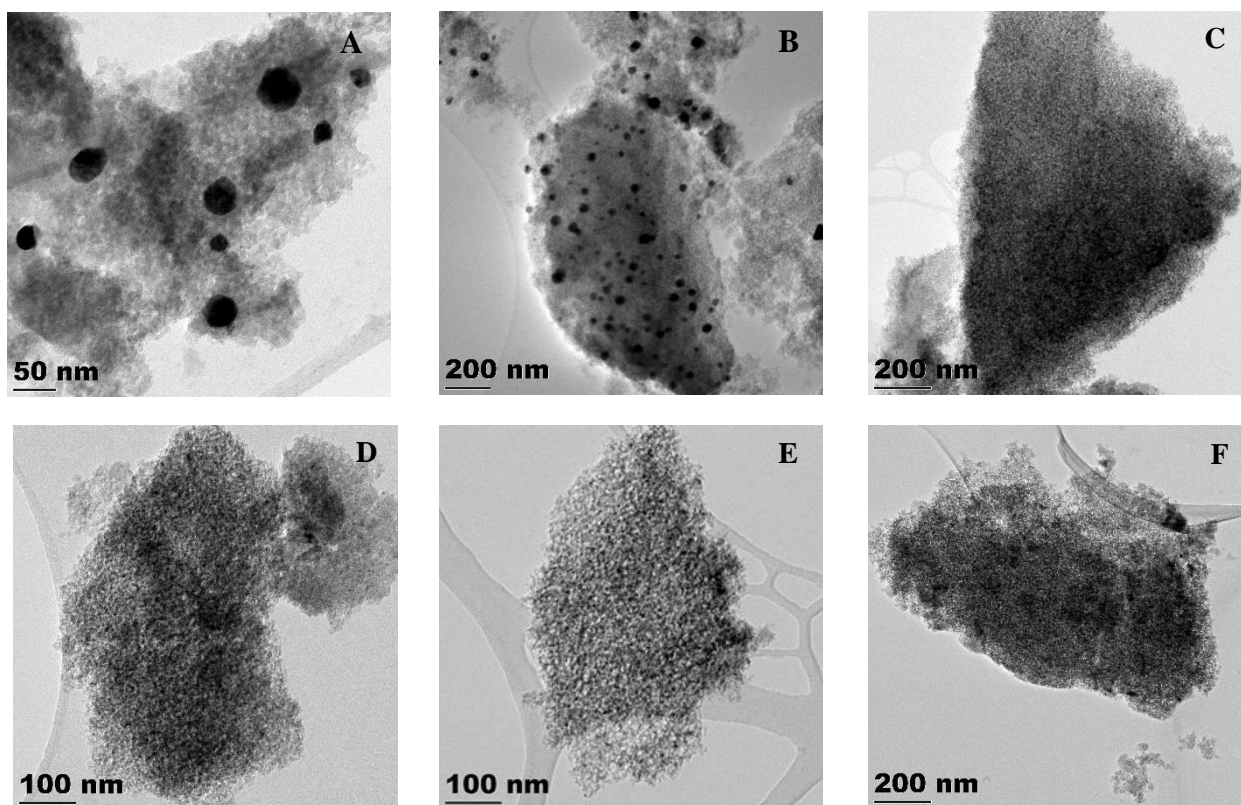


Figure E. 2. TEM images of spent 5 wt% Pd/SiO₂ after TGA analysis with air flowing at 100 cm³ min⁻¹ at 1475 K (A), 1173 K (B), 1073 K (C), 873 K (D), 773 K (E), and 623 K (D) (left) and spent 5 wt% Pd/SiO₂ (right) at 553 K (top) and 533 K (bottom).

Table 4.3 in Chapter 4 showed that the spent 5 wt% Pd/SiO₂ only lost 11% of surface area with respect to the fresh catalyst. Therefore the 8% weight loss is in agreement with the low surface area loss. Electron micrographs of the catalyst revealed that under this calcination condition, 1495 K, the Pd nanoparticles were not stable, Figure E.2.A.

The calcination experiment was repeated over new spent 5 wt% Pd/SiO₂, but lowering the calcination temperature each experiment to determine the maximum calcination temperature at which the Pd nanoparticles were stable. Figure E.2 shows that the Pd nanoparticles over SiO₂ were stable when the reduction temperature was below 1073 K (Figures E.2 C-F). Therefore the regeneration of 20 wt% Pd/Norit was attempted with Air, N₂, and H₂ at a maximum temperature of 1073 K. Figure E.3 reveals that 20 wt% Pd/Norit C showed only one desorption peak at \approx 623 K regardless of the gas used for the

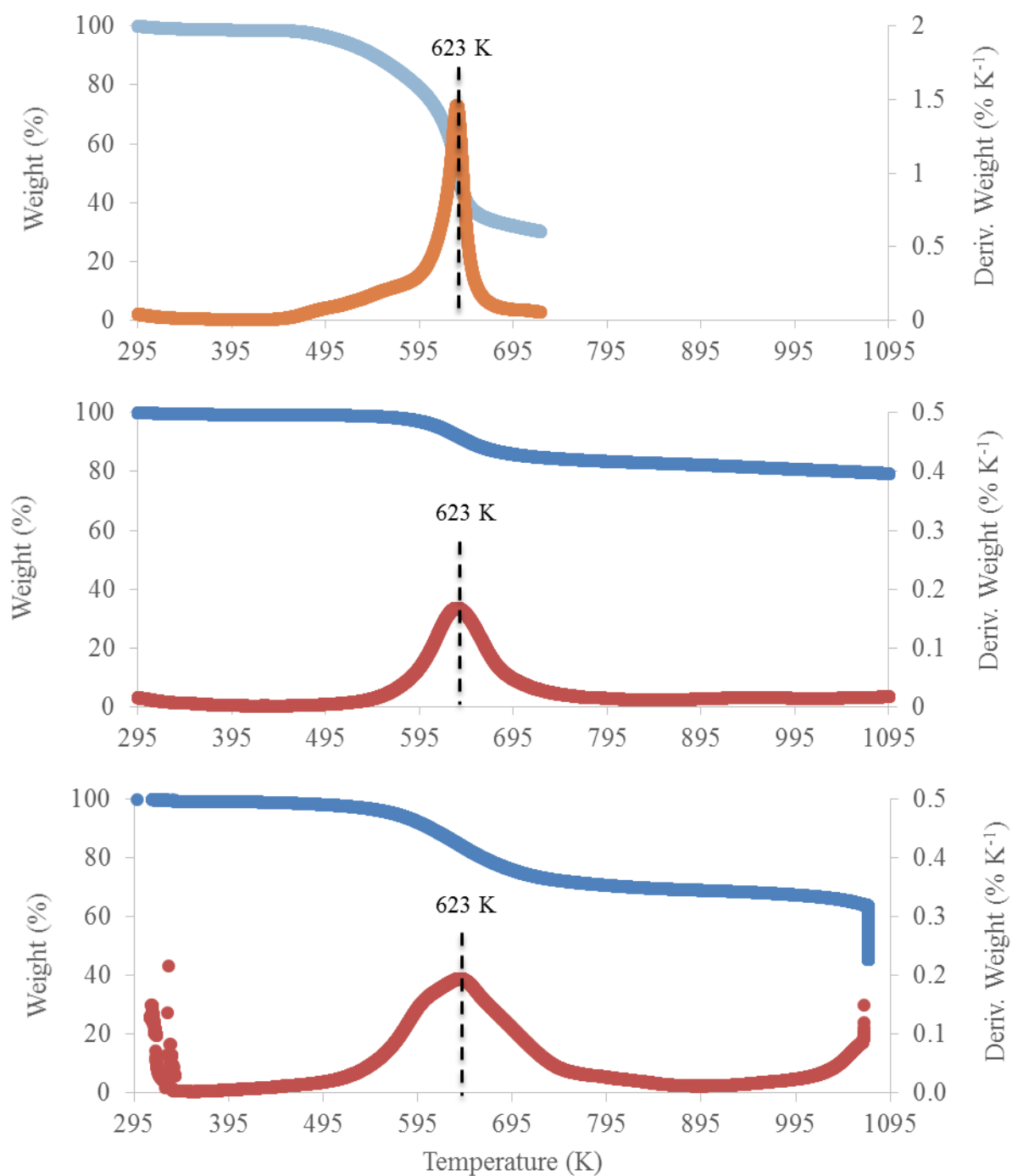


Figure E. 3. Thermogravimetric analysis of spent 20 wt% Pd/Norit C with air (top), He (middle), and H₂ (bottom) up to 1095 K. ● represents Weight (%) and can be read on the left hand axis. ● represents Deriv. Weight (% K⁻¹) and can be read on the right hand axis.

regeneration treatment, however, the weight loss strongly depended on the gas used. When Air was used, the weight loss of 20 wt% Pd/Norit was $\approx 60\%$. However, when N_2 or H_2 were used, the weight loss was 20 and 30%, respectively. Table 4.3 in Chapter 4 showed that the spent 20 wt% Pd/Norit C only lost $\approx 15\%$ of surface area with respect to the fresh catalyst. Therefore the $\approx 60\%$ weight loss suggests that Air treatment could be oxidizing the carbon support as well as the organic molecules absorbed on the surface of the catalyst. However, the 15% surface area loss is more in agreement with the weight loss observed with the N_2 and H_2 treatment. Figure E.4 shows that Pd nanoparticles were stable after both treatments at 623 K.

The catalyst was then *in situ* regenerated, as described in the Experimental Methods section, at 623 K after the conversion of PAn at 533 K and 1 bar over 20 wt% Pd/Norit C using two different treatments. One treatment used N_2 during the reactor heating step, and H_2 during the reduction step, whereas the other method used H_2 during the heating and reduction steps. The results are summarized in Table E.1 and shows that both regeneration methods successfully recovered the catalytic performance of 20 wt% Pd/Norit C. This suggests that the main cause for catalyst deactivation was deposition of organic molecules onto the active sites just like reported by Ping *et al.* [15].

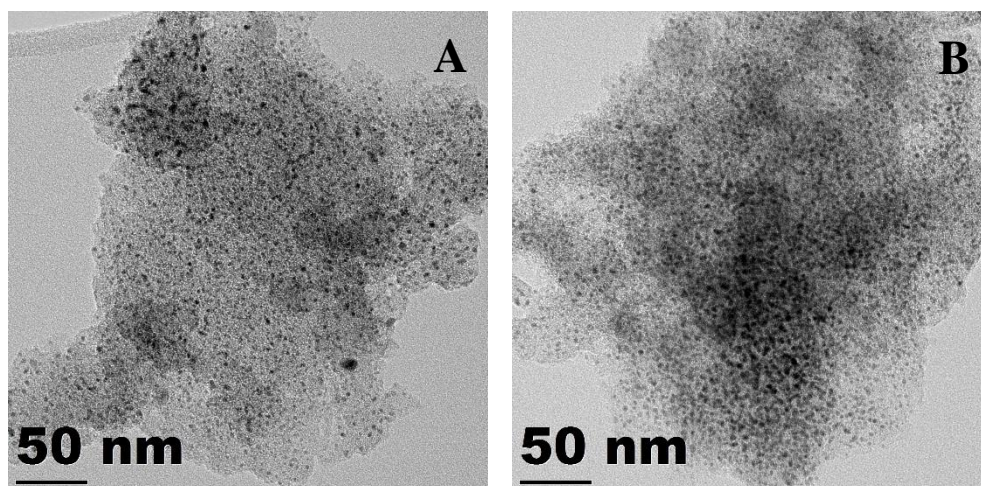


Figure E. 4. TEM images of 20 wt% Pd/Norit C after regeneration at 623 K with and N_2 plus H_2 treatment (A) and H_2 treatment (B).

Table E. 1. Result of reactivity of propanoic anhydride over 20 wt% Pd/Norit C at 533 K after regeneration with N₂ and H₂ treatments

Feed	Catalyst	Treatment	Initial TOF ^a (s ⁻¹)
Propanoic anhydride	Fresh	H ₂ at 573 K	0.0040
	Spent	He + H ₂ at 623 K	0.0039
		H ₂ at 623 K	0.0038

^aResult estimated using extrapolated reaction rates of propanoic acid to time 0 h

Appendix Bibliography

- [1] Weisz, P. B., and Prater, C. D., 1954, "Interpretation of Measurements in Experimental Catalysis," *Adv Catal*, **6**, pp. 143–196.
- [2] Davis, M. E., and Davis, R. J., 2012, *Fundamentals of Chemical Reaction Engineering*, Dover Publications, Mineola, New York.
- [3] Joback, K. G., and Reid, R. C., 1987, "Estimation of Pure-Component Properties from Group-Contributions," *Chem Eng Commun*, **57**, pp. 233–243.
- [4] Reichenberg, D., 1975, "New Methods for the Estimation of the Viscosity Coefficients of Pure Gases (with Particular Reference to Organic Vapors)," *AIChE J*, **21**(1), pp. 181–183.
- [5] Cussler, E. L., 2009, *Diffusion: Mass Transfer in Fluid Systems*, Cambridge University Press, New York.

- [6] Mäki-Arvela, P., Snåre, M., Eränen, K., Myllyoja, J., and Murzin, D. Y., 2008, "Continuous decarboxylation of lauric acid over Pd/C catalyst," *Fuel*, **87**(17-18), pp. 3543–3549.
- [7] Lugo-José, Y. K., Monnier, J. R., and Williams, C. T., 2014, "Gas-Phase, Catalytic Hydrodeoxygenation of Propanoic Acid, Over Supported Group VIII Noble Metals: Metal and Support Effects," *Appl Catal A-Gen*, **469**, pp. 410–418.
- [8] Immer, J. G., Kelly, M. J., and Lamb, H. H., 2010, "Catalytic reaction pathways in liquid-phase deoxygenation of C18 free fatty acids," *Appl Catal A-Gen*, **375**(1), pp. 134–139.
- [9] Lestari, S., Mäki-Arvela, P., Bernas, H., Simakova, O., Sjöholm, R., Beltramini, J., Lu, G. Q. M., Myllyoja, J., Simakova, I., and Murzin, D. Y., 2009, "Catalytic Deoxygenation of Stearic Acid in a Continuous Reactor over a Mesoporous Carbon-Supported Pd Catalyst," *Energ Fuel*, **23**(8), pp. 3842–3845.
- [10] Mäki-Arvela, P., Kubičková, I., Snåre, M., Eränen, K., and Murzin, D. Y., 2007, "Catalytic Deoxygenation of Fatty Acids and Their Derivatives," *Energ Fuel*, **21**(1), pp. 30–41.
- [11] Snåre, M., Kubičková, I., Mäki-Arvela, P., Chichova, D., Eränen, K., and Murzin, D. Y., 2008, "Catalytic deoxygenation of unsaturated renewable feedstocks for production of diesel fuel hydrocarbons," *Fuel*, **87**(6), pp. 933–945.
- [12] Simakova, I., Rozmyslowicz, B., Simakova, O. A., Mäki-Arvela, P., Simakov, A., and Murzin, D. Y., 2011, "Catalytic Deoxygenation of C18 Fatty Acids Over Mesoporous Pd / C Catalyst for Synthesis of Biofuels," *Top Catal*, **54**(8-9), pp. 460–466.
- [13] Lopez-Ruiz, J. A., and Davis, R. J., 2014, "Decarbonylation of heptanoic acid over carbon-supported platinum nanoparticles," *Green Chem*, **16**(2), pp. 683–694.

- [14] Ping, E. W., Pierson, J., Wallace, R., Miller, J. T., Fuller, T. F., and Jones, C. W., 2011, "On the nature of the deactivation of supported palladium nanoparticle catalysts in the decarboxylation of fatty acids," *Appl Catal A-Gen*, **396**(1-2), pp. 85–90.
- [15] Ping, E. W., Wallace, R., Pierson, J., Fuller, T. F., and Jones, C. W., 2010, "Highly dispersed palladium nanoparticles on ultra-porous silica mesocellular foam for the catalytic decarboxylation of stearic acid," *Micropor Mesopor Mat*, **132**(1-2), pp. 174–180.